Studying the environmental dependence of star formation properties of galaxies in the Abell 1437 galaxy cluster and its surrounding large scale structure.

J.P. Kotze

A thesis presented to the University of Cape Town in fulfillment of the degree:
Doctor of Philosophy in Astronomy
University of Cape Town

Supervisors: Prof. R.C. Kraan-Korteweg and A/Prof. P. A. Woudt
Co-supervisors: Dr. P. Väisänen and Dr. D. Gilbank

Abstract

It has become clear that the local galaxy environment plays a crucial role in the evolution of galaxies. Recent studies show a strong bimodal distribution of galaxy properties, with red, passive galaxies dominating the bimodal distribution in dense environments, compared to blue, actively star forming galaxies dominating the bimodal distribution in low density environments. Blue, star-forming galaxies are continuously transformed into red, passive galaxies through one or more processes while being accreted into higher density environments. The processes responsible for the observed transformation remain uncertain.

We address these issues by performing an in-depth study of large-scale structure surrounding the galaxy cluster Abell 1437 at $z = 0.135$. We consider the colour and specific star formation rate distributions of galaxies as a function of environment. In this thesis we develop techniques to derive environmental samples which consist of a cluster, groups, filament and field. The large-scale structure surrounding the cluster is characterised through the use of a Friends-of-Friends algorithm based on spectroscopic data. This provides a reference from which we construct a photometric environmental catalogue using methods developed to find groups and define filamentary structure. To accomplish this, we construct a $ugrizJHK$ multi-band dataset using a custom pipeline to derive a seeing matched photometric catalogue from Sloan Digital Sky Survey (SDSS) and UKIRT Deep Sky Survey (UKIDSS) imaging data. The photometric dataset is complemented by a near uniformly sampled spectroscopic dataset from the SDSS and Two Degree Field (2dF) survey. Stellar masses and star formation rates for the environmental samples are derived using the state-of-the-art MAGPHYS SED fitting code.

The environmental samples we derive yield, within the uncertainties, similar galaxy populations than typically found in clusters, groups and the field. Red fractions were computed for the cluster, groups, filament and field sample for which we found 0.90 ± 0.13, 0.79 ± 0.01, 0.69 ± 0.02 and 0.58 ± 0.01 respectively. This is the first filament red fraction measurement made in this way. We studied the passive fraction of galaxies as a function of environment using specific star formation rates. Passive fractions were computed using two different definitions of passiveness, $1/t_H$ ($\log(\mathrm{sSFR}) = -10.07$) and the minimum in the bimodal sSFR distribution ($\log(\mathrm{sSFR}) = -11.0$) as the division between active and passive galaxies. We found that the $\log(\mathrm{sSFR}) = -11.0$ bimodal divider is a natural division between active and passive galaxies and does not suffer from density-dependent selection effects. Quiescent fractions derived from the environmental samples reproduce previously known trends of star formation rates with environment.

The filament environment is one of the least well studied environments since their low galaxy density makes them difficult to detect. We studied the fractional excess of star forming galaxies along the filament between Abell 1437 and the neighbouring region of overdensities, and find a significant increase in star formation activity. Although there have been hints of excess star formation in filaments previously, we claim our results to be of highest significance thus far.

Acknowledgements

First, I would like to thank my UCT supervisors Prof. Renée Kraan-Korteweg and Assoc. Prof. Patrick Woudt for their support during my PhD. Your helpful comments and suggestions have always been greatly appreciated. Also, thank you to my co-supervisor Dr. Petri Väisänen for your time and support. I would like to give a special thank you to Dr. David Gilbank who took me under his wing. Your support, guidance and patience has shown me the way to becoming a better researcher. For that I will be forever grateful. To all my other colleagues at UCT, thank you for all the tearoom chats and support.

Thank you to Dr. Kevin Pimbblet who was kind enough to provide me with 2dF spectra. A massive thank you to my collaborator and friend Ralf. Your never ending support and time you devoted to this project is greatly appreciated.

To my colleagues and friends at the SAAO and SALT, thank you for your tremendous support. I would especially like to thank Amanda, Simon, Garith, Hamish, Ockert and Steve. Thank you to Dr. David Buckley for giving me the time off to finish my thesis and to play with a 10m class telescope on a regular basis.

To all my awesome friends that have supported me during my PhD, thank you so much! This is not a journey that should be taken on alone. Your love and support means the world to me. Ewald and Nicola thank you for always being there for me. Rudi, the long nights and weekends have been much easier with you here in the office, KCCO. To the other Kotze's at the SAAO, your unfailing guidance has seen me through tough times. Jannie, thank you for all the late night talks and your never-ending encouragement.

To my family, thank you for all the years of support, guidance and love. Hendrik, you and Charles have been my inspiration. Lastly, Cara, your love and support means the world to me. You have lightened the load during the final stretch of this journey. Thank you, Love.

Plagiarism Declaration

I, Johannes Paulus Kotze, know the meaning of plagiarism and declare that all of the work in the document, save for that which is properly acknowledged, is my own. References to 'we' in this thesis refers to work done by the author. Any collaborative work that was done as part of this project will be stated explicitly.

Contents

List of Figures

List of Tables

Chapter 1

Introduction

Most of the visible matter in the Universe is concentrated in galaxies, which are the basic astronomical bodies in which stars are born, evolve, and die. The gross structural properties of galaxies and their distribution in space are determined primarily by the processes of galaxy formation, while other properties such as the stellar and gas content of galaxies and their evolution with time depend mainly on the processes of star formation and stellar evolution. To separate processes of galaxy formation from those of galactic evolution is difficult. We need to consider both in an effort to understand the origin of the observed properties of galaxies and the many correlations between these properties.

This thesis is concerned with the observational study of galaxy evolution and the crucial role the environment plays in shaping the properties of galaxies. The project builds upon the most recent results which show a strong bimodal distribution of galaxy properties. We especially concern ourselves with the colour and specific star formation rate distributions of galaxies as a function of environment. New techniques are employed to derive an environmental sample which consists of a cluster, groups, filament and field. The persistent bimodality in the distribution of colour and specific star formation rate allow us to investigate the impact of these environments on galaxies as they transition from being blue and star forming, to red and passive.

1.1 Large-Scale Structure- and Galaxy Formation

A great number of advancements have been made in our understanding of the Universe as we see it today. The work on the General Theory of Relativity (GR) by Albert Einstein set the framework for cosmologists to study one of the four fundamental forces in the Universe, namely gravity (Einstein 1915). This enabled cosmologists to predict the behaviour of a model Universe and as a result, it became possible to formulate self-consistent models that describe the Universe and large-scale structure. From the work of Hoyle, Robertson, Walker, Landau, Lifshitz and Peebles, just to name a few, a theoretical picture emerged that the Universe originated from what is now called the Big Bang, where matter existed

in a hot dense state, and has been expanding and cooling ever since. It was not until the serendipitous discovery of the Cosmic Microwave Background (CMB) radiation by Penzias & Wilson (1965) that observational constraints could be placed on the theory which was predicted by Alpher & Herman (1948) and Gamow (1948). Measurements of the CMB describe the initial conditions after recombination of the very early Universe and lead the way to the standard model of cosmology.

Observations from the Cosmic Background Explorer (Bennett et al. 1992, Mather et al. 1990, Smoot et al. 1991) and the Wilkinson Microwave Anisotropy Probe (Bennett et al. 2003, Komatsu et al. 2009; 2003, Larson et al. 1980) in combination with surveys to study the large-scale structure of the Universe, for example, supernovae (Knop et al. 2003), galaxy clustering (Cole et al. 2005), gravitational lensing (Contaldi et al. 2003) and large redshift surveys (2dFGRS), (Colless et al. 1999; 2001, Percival et al. 2001) and the Sloan Digital Sky Survey (SDSS) (York et al. 2000, Stoughton et al. 2002, Abazajian et al. 2004; 2009) have led to the Λ Cold Dark Matter (ΛCDM) standard model of Big Bang cosmology and hierarchical structure formation (e.g Navarro et al. 1994). In this model, we live in a flat expanding Universe that is dominated by non-luminous components, known as dark energy and dark matter. The observable matter component, baryonic matter, accounts for only $\sim 5\%$ of the Universe's mass, the remaining $\sim 23\%$ is contained in non-baryonic matter, known as dark matter. The nature of dark energy is still unknown, but it is thought to be responsible for the observed accelerated expansion of the Universe and constitutes $\sim 72\%$ of the Universe's energy density. The success of ΛCDM is widely recognised and it is relatively simplistic, yet, provides insights into the structure and existence of the cosmic microwave background, the large-scale structure of galaxy groups and clusters, weak and strong gravitational lensing, and the accelerated expansion of the Universe.

The evidence for dark matter has been around since the 1930s when Fritz Zwicky showed that the measured velocity dispersion of galaxies in the Coma cluster (Sect. 1.3.1) requires more mass than that from the luminous matter alone (Zwicky 1930). Further evidence for the presence of dark matter came from measurements of the rotational speed of stars in disk galaxies by, e.g. Rubin et al. (1970; 1978), Clemens (1985), who showed that the rotation curve is flat at large radii. If luminous matter is the only source of mass, the rotation curve should fall off with increasing radius. Instead the measured flattening of the rotation curve infers more mass is needed to produce the constant rotation curve.

To build a picture of how the large-scale structure we observe today came to be, a realistic structure formation model can be used to describe the evolution of the density field in the Universe with time, when the field contains small fluctuations as observed in the CMB. The usual approach is to model the fluctuations as perturbations to a smooth background which is assumed to be homogeneous and isotropic. Perturbations cause overdense regions to collapse under gravity, which keep attracting more matter with the growing gravitational potential. This process gives rise to the structure we see today. Since the distribution of baryonic matter has been found to be governed by the distribution of dark matter, one can model the distribution of baryonic matter by modeling the dark matter distribution. Modeling dark

matter structural growth is relatively straightforward because it only depends on gravity. In comparison, the formation of stars and galaxies involves much more complicated gas and hydrodynamical physics. Figure 1.1 shows the dark matter structural growth from initial perturbations to the large-scale structure we observe today as a function of time on different cosmological scales.

1.2 Galaxy Formation

The observed properties of galaxies can be roughly categorised in two fairly distinct populations: early type galaxies with low to no star formation and late type galaxies with ongoing star formation (discussed in Sections 1.5 and 1.7). How these present day populations came about has been the subject of many studies and still remains a hot topic. Most of the early advancements in the field of galaxy formation have come from theoretical work by e.g. Hoyle (1953), Binney (1977), Rees & Ostriker (1977), Silk (1977), who postulated the bottom-up scenario (White & Rees 1978) where small structures form first, then merge to form larger structures.

Using this framework, the formation of galaxies can be modelled by considering small scale perturbations on collisionless dark matter which result in the formation of self gravitating dark matter halos. Since baryons only interact with dark matter via gravity, the gravitational growth of the dark matter halo leads to the gravitational collapse of the primordial gas. The gas is not collisionless, but can heat up through shocks to the virial temperature of the dark matter halo during its collapse. What happens next depends on the relative value of the cooling and collapse timescales. Masses in the range 10^{10}–10^{12} $M_{\odot}$ cool so efficiently that they always collapse at the free-fall rate, and probably quickly fragment into stars. Larger masses may, however, experience a quasistatic contraction phase where the formation time will be equal to the cooling time of the gas (Rees & Ostriker 1977). When the gas has cooled enough it can fragment into stars and form a galaxy.

The two main methods for modeling the formation and evolution of galaxies are numerical/hydrodynamical simulations and semi-analytic modelling (SAM). Numerical simulations rely on solving gravitational, hydrodynamical and radiative cooling and transfer equations for a large number of gas particles (e.g. Evrard et al. 1994, Katz et al. 1992, Navarro & Steinmetz 1997). This is a computationally complicated and time expensive task, limited to galaxy sized scales. The primary advantage of the semi-analytic approach is that it is computationally inexpensive compared to hydrodynamical simulations. One can therefore construct samples of galaxies orders of magnitude larger than is possible with hydrodynamical techniques (Henriques et al. 2009). SAMs use simplified prescriptions for the various physical processes involved in the formation and evolution of galaxies which are 'pasted' onto the dark matter simulations (e.g. Baugh et al. 2005, Benson & Bower 2010, Bower et al. 2006, Cole et al. 1994; 2000, Croton et al. 2006, Kauffmann et al. 1993, White & Frenk 1991, De Lucia et al. 2012).

One important advancement in SAM has been the successful description of the observed

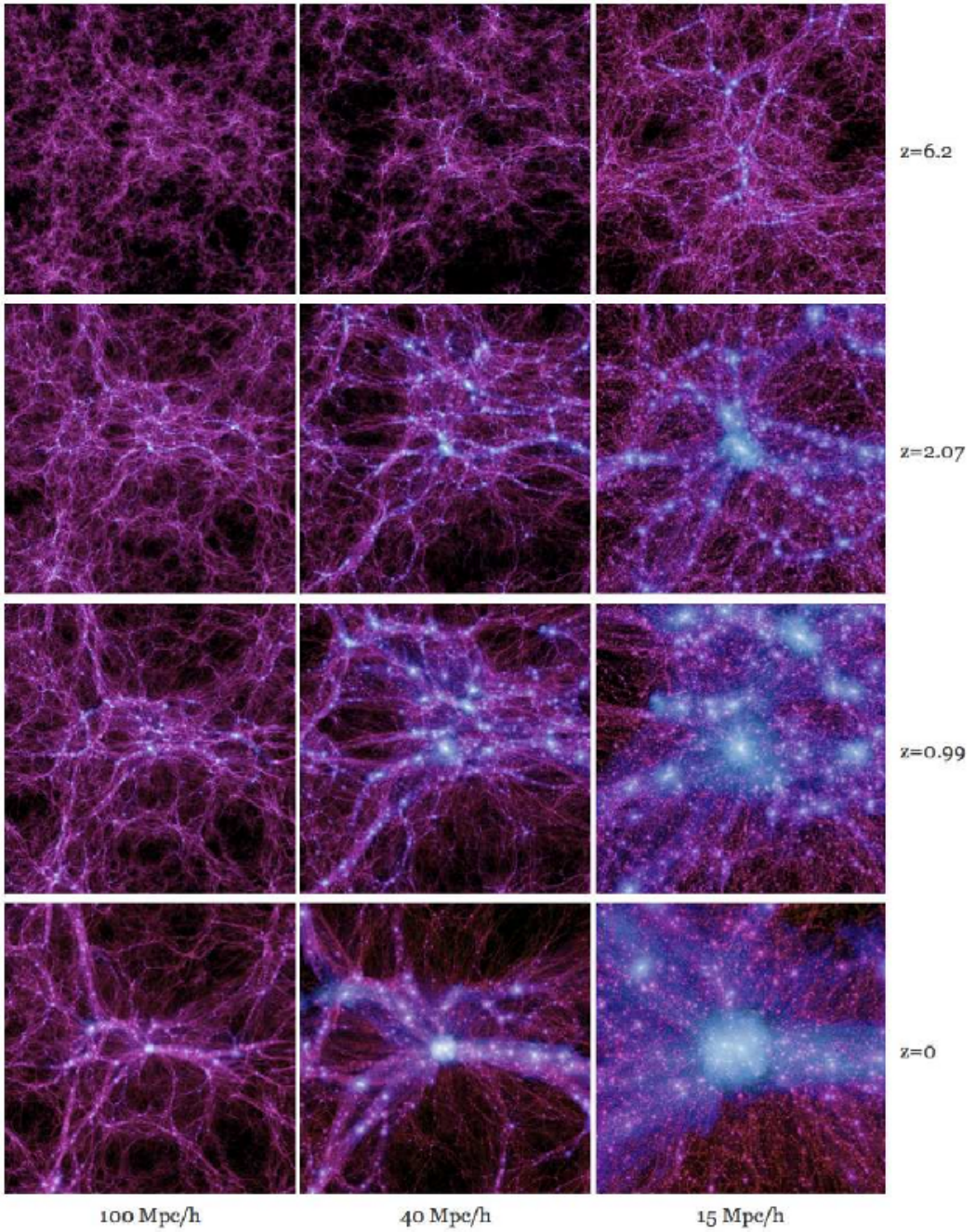

Figure 1.1: An example of dark matter large-scale structure formation taken from the Millennium-II simulation (Boylan-Kolchin et al. 2009). The large-scale structure growth is shown as a function of time, from top to bottom for three different cosmological scales ranging from large scales, on the left to smaller scales on the right.

luminosity function by the inclusion of feedback mechanisms. The observed luminosity function (number of galaxies as a function of luminosity) has a cut-off at the bright end, and has a slow increase at the faint end. If we consider stellar mass follows halo mass,

too many small faint galaxies and too many big bright galaxies are predicted in the nearby Universe from SAMs. This discrepancy with observations means the efficiency of forming stars is suppressed in high and low mass halos. Since galaxies form via the cooling of hot gas in the halo, mechanisms which would halt or quench the formation of stars in low and high mass halos have been proposed. The inclusion of supernova feedback (Benson et al. 2003, Cole et al. 2000) and photoionisation heating (Efstathiou 1992) which suppresses the cooling of the gas have been proposed as the most likely mechanism for the suppression of star formation in low mass halos. For more massive halos, a stronger energy source is needed and active galactic nuclei (AGN) are the most likely candidates (Croton et al. 2006, Peng et al. 2010). The inclusion of these feedback mechanisms has led to the successful prediction of observed galaxy properties. But, some problems still remain, e.g. the environment and its importance to both AGN formation and hot/cold gas accretion (Benson & Bower 2010). Another important component to SAM are stellar evolutionary synthesis models, originally proposed by Tinsley & Gunn (1976). Assuming an initial function which describes the distribution of masses stars are born with and a prescription for the star formation history, the evolution of a galaxy's gas and stellar component can be tracked as a function of time and the spectral energy distribution (SED) of galaxies can be extracted at any age. This is discussed in more detail in Sect. 1.10.

1.3 Observed Large Scale Structures In The Universe

1.3.1 Galaxy Clusters

In the overall picture of large-scale structural growth, galaxy clusters represent the nodes that connect filaments to form superclusters. Filaments, loosely defined as the spatially confined interconnective density enhancement between galaxy clusters, are discussed further in Sect. 1.3.3. The cores of galaxy clusters are the densest environments in the Universe and provide ideal systems to study galaxy interactions and the impact of dense environments on galaxy evolution.

In the late 1700s, both Messier (1784) and Herschel (1785) independently recognised concentrations of galaxies on the sky while trying to determine the relation between what they called "nebulae" and our own Galaxy. The fact that these nebulae were not part of our own Galaxy, but galaxies outside of the Milky Way only became apparent after the work of Edwin Hubble in the early 1920s (Hubble 1920).

Hubble attempted to quantify different galaxy populations observed in the local Universe (Hubble 1926; 1938). He classified galaxies along a morphological sequence which correlates with the relative prominence of a central bulge and disk component of a galaxy's light distribution. Galaxies dominated by an ellipsoidal bulge were classified as ellipticals, or early-type galaxies, and galaxies with a visible disk component were classified as spiral, or late-type galaxies (see Fig. 1.2). Early-type galaxies were found mostly in dense environments, and late-type galaxies in less dense environments (Sect. 1.7). This led to great interest in the

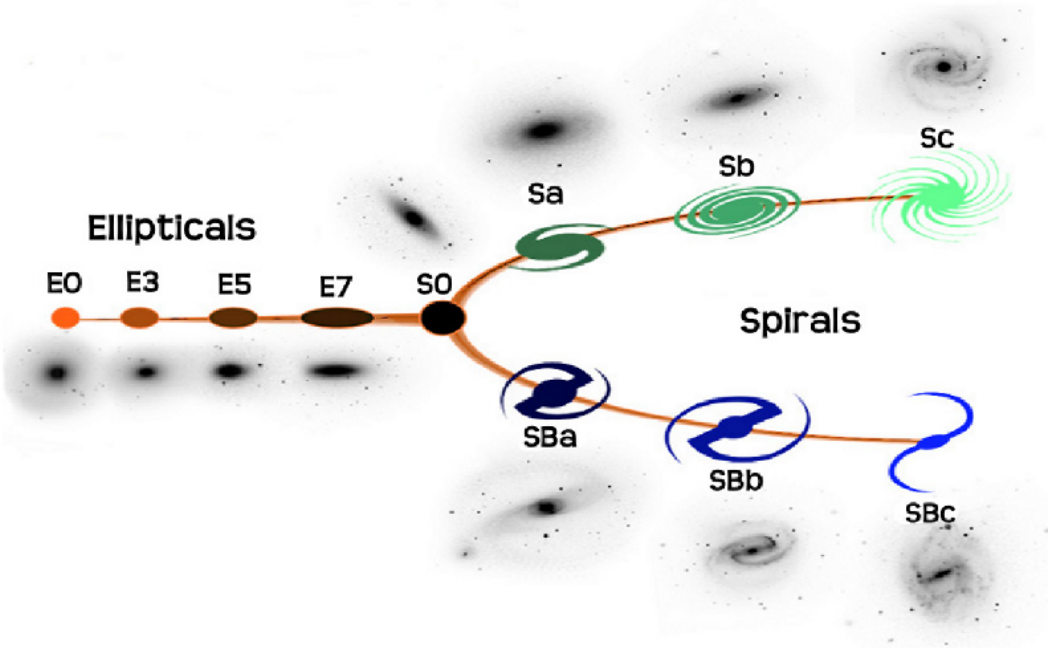

Figure 1.2: Hubble's tuning fork diagram for classifying galaxies. (*Credit: NASA & ESA, adapted by Dr. R. Kotulla)*

properties of galaxies in clusters and a number of authors began compiling catalogues of galaxy clusters to study the cluster galaxy populations.

The first to do so was George Abell who published his first catalogue of galaxy clusters in 1958 (Abell 1958), a catalogue still in use today. He visually selected cluster members by considering the redshift of the 10^{th} brightest galaxy. A circular on-sky area defined by a radius 1.72 $h^{-1}/\ z$ in arc minutes ($H_0 = 100$ km s^{-1} Mpc^{-1}) was used to search for galaxies with a magnitude $m \leq m_3 + 2$, where m_3 is the magnitude of the third brightest galaxy. Galaxies satisfying this criteria were counted as a cluster members.

Since then, a number of other techniques have been devised to optically find galaxy clusters. The matched-filter method searches for clusters by filtering optical survey data with a model that describes the luminosity and spatial distribution of galaxies in a cluster (e.g. Postman et al. 1996, Gilbank et al. 2004, Olsen et al. 2007, Milkeraitis et al. 2010). The fact that the centres of clusters are mostly occupied by early-type galaxies, which are mostly red, can be used to find galaxy clusters. Galaxies that lie on a tight red-sequence in the colour and magnitude distribution and are spatially coincident have been used to detect cluster cores (e.g. Gladders & Yee 2000). Another example of an optical cluster/group finder is the C4 algorithm (Miller et al. 2005), which uses four colours, redshift, and position information to identify overdensities of galaxies. A commonly used group/cluster finding technique is based on a Friends-of-Friends algorithm (see Sect. 2.5.1), which makes use of the three dimensional distribution of galaxies to find galaxy overdensities (e.g. Huchra & Geller 1982, Weinmann et al. 2006a, Yang et al. 2007), but requires distance information to

individual galaxies. Other cluster finding techniques do not rely on the individual cluster member galaxies but the hot gas in the intra-cluster medium (ICM). Galaxy clusters are among the brightest extragalactic X-ray sources in the Universe. The deep potential wells compress the baryonic gas and heat it to X-ray emitting temperatures (e.g. Böhringer et al. 2000, Ebeling et al. 2001, Green et al. 2004, Pacaud et al. 2007). The distortion in the observed CMB spectrum due to the scatter of CMB photons passing through the hot ICM can also be used to detect clusters, known as the Sunyaev-Zel'dovich (SZ) effect (Sunyaev & Zeldovich 1972). The large gravitational potential wells of galaxy clusters can cause weak lensing of distant background galaxies and can therefore also be used as a way to detect clusters (e.g. Wittman et al. 2001; 2006, Gavazzi et al. 2007).

The technique employed in this thesis to determine the sizes and masses of clusters and groups is termed a dynamical mass estimate. This is the technique used by Zwicky (1933) to infer the missing cluster mass, which is based on the virial theorem. The virial theorem states that for an isolated dynamical system in a stationary state of equilibrium, the kinetic energy is half the potential energy, $E_{kin} = \frac{1}{2}|E_{pot}|$. Dynamical virial radii can be estimated from kinematic data using expressions which express the virial radius as proportional to the velocity dispersion. The velocity dispersion can be calculated from:

$$\sigma_v = \sum_i \Delta v_i \quad \text{, with} \quad \Delta v_i = c(z_i - \overline{z})/(1 + \overline{z}) \tag{1.1}$$

where Δv_i are the peculiar velocities in the rest frame of the cluster and $\overline{z}$ is the mean redshift of the cluster (Carlberg et al. 1994). From the virial theorem, Carlberg et al. (1997) derived an expression for r_{200}:

$$r_{200} = \frac{\sqrt{3}\sigma_v}{10H(z)} \tag{1.2}$$

where r_{200} is the projected radius at which the mean interior overdensity is $200\rho_c$, ρ_c is the critical density and $H(z)$ is the Hubble parameter at the redshift of the cluster. It then follows that the cluster mass enclosed by r_{200} is given by (see Carlberg et al. 1994; 1997 for further details):

$$M_{200} = \frac{3r_{200}\sigma_v^2}{G} \tag{1.3}$$

Typically, less massive clusters or groups have velocity dispersions of the order of 100–500 km s^{-1} with $r_{200} \sim 0.1$–1 Mpc and total masses between $\sim 10^{12.5}$ – $10^{14.0}$ h^{-1} M$_\odot$. Massive clusters have velocity dispersions of the order of 400–1400 km s^{-1} with $r_{200} \sim 1$–3 Mpc and total masses in the range $\sim 10^{14.0}$ – $10^{15.0}$ h^{-1} M$_\odot$ (Bahcall & Oh 1996).

1.3.2 Galaxy Groups

There is no clear distinction between poor clusters and groups, the division between the two is usually based on total mass, but varies from author-to-author (and often from study-to-study

by the same author). It is thought that galaxy groups are physically bound together due to their mutual gravitational attraction and the presence of a dark matter halo. However, group members are not easy to define because dark matter haloes cannot be observed directly. Not all observed groups are confirmed physical and gravitationally bound systems as they can be a result of chance superpositions of galaxies along the line of sight. Since they contain fewer galaxies than clusters, the contrast over the background galaxy distribution is lower, making them harder to identify.

Groups of galaxies typically contain fewer than ∼30 members and are often dominated by late type galaxies. When larger groups are considered, the main constituent of galaxies usually shifts from spirals to lenticulars, but no clear cut-off in number of members exists between groups and clusters (Paz et al. 2006). Better physical quantities to discriminate between groups and clusters are mass and size, though, these are not clearly defined either. Most of the stellar mass in the present Universe is located in groups with masses a few times 10^{12} $M_\odot$ with only 2% in clusters with total masses $> 5 \times 10^{14}$ $M_\odot$ (Eke et al. 2006). Groups have been found to be present at redshifts $z > 1$ (e.g. Francis et al. 1996, Moller & Warren 1998, Gerke et al. 2005, Andreon et al. 2009, Bielby et al. 2010) and their environmental density is intermediate between that of isolated galaxies and that of the cores of rich clusters. It has become common to define groups on the basis of their inferred dark matter halo mass (e.g. Yang et al. 2005, Weinmann et al. 2006a). Group (and cluster) members can be divided into a central galaxy and satellite galaxies orbiting the central galaxy. Central galaxies are taken to be the most massive galaxies in a halo and usually reside at the gravitational potential minimum. Satellite galaxies are galaxies that are moving relative to the potential minimum having fallen in to the larger halo (e.g. van den Bosch et al. 2008, Kimm et al. 2009, Peng et al. 2010; 2012).

Different group finding algorithms have been developed and applied to identify groups using redshift information (e.g. Turner & Gott 1976, Materne 1978, Huchra & Geller 1982, Goto et al. 2002, Bahcall et al. 2003, Botzler et al. 2004, Gerke et al. 2005, Yang et al. 2007, Koester et al. 2007a, Kimm et al. 2009). Despite the vast number of grouping algorithms, the Friends-of-Friends (FoF; Huchra & Geller 1982, Yang et al. 2005; 2007) percolation algorithm and modifications thereof, remains the most widely used method for finding groups today (see Sect. 2.5.1).

1.3.3 Filaments

Galaxy filaments are the structures that make up the "cosmic web", which interconnects clusters of galaxies on scales ranging from a few to tens of Mpc. There is no official definition for what constitutes a filament, but the generally accepted definition is that a filament is a spatially-confined interconnective density enhancement between galaxy clusters (see Fig. 1.1 for an example). Due to the sparse distribution of filament galaxies, and the slight density enhancement compared to the field, filaments have not been studied in as much depth as the cluster environment (Section 1.3.1). This does not imply that filament environment is thought to be unimportant. Colberg et al. (1999) showed that filaments contain up to

$\sim$ 40% of a cluster's mass out to 4–6 Mpc. Furthermore, simulations by Fukugita et al. (1998) and Cen & Ostriker (1999) have shown that filaments could contain hot diffuse gas ($> 10^5$ K), but the surface brightness predicted are lower than can be observed with current X-ray telescopes. This led to observational studies that have tried to detect the X-ray emission resulting from gaseous filaments (Briel & Henry 1995, Kull & Böhringer 1999, Scharf et al. 2000). Other observational strategies have also been employed to detect intercluster filaments, either by ultraviolet absorption of the gas within background AGN spectra (Bergmann et al. 2004) or by gravitational strong lensing (e.g. Dietrich et al. 2005, Gray et al. 2002, Jauzac et al. 2012). Colberg et al. (2005) investigated the frequency and distribution of filaments in a ΛCDM Universe using simulations from Kauffmann et al. (1999). They show that approximately half of all intercluster filaments are warped and are statistically longer than straight filaments. Pimbblet & Drinkwater (2004) devised a morphological classification of intercluster filaments and observationally confirmed the ΛCDM predictions.

Most studies of filaments have relied on the optical detection of galaxies that populate them, using spectroscopy to map the three dimensional distribution of galaxies within filaments (e.g. Ebeling et al. 2004, Pimbblet et al. 2004, Porter & Raychaudhury 2007). Observations of the star formation properties of galaxies within filaments show that the filament plays a role in the evolution of galaxies (e.g. Porter & Raychaudhury 2007, Porter et al. 2008), to which degree this is the case is unclear. The region where the influence on individual galaxy properties in the filament turns over to be dominated by the cluster or group environment is not well established. The contribution that the filament environment makes to the overall evolution of galaxies as they are accreted from the field onto filaments and finally onto clusters remains unclear and is one of the key questions we will investigate in this thesis.

1.3.4 Superclusters

Superclusters are the largest structures in the Universe, comprising of galaxy clusters and groups interconnected by filamentary structures that build the cosmic web (de Lapparent et al. 1986, Einasto et al. 1984, Gregory & Thompson 1978, Jõeveer et al. 1978, Zeldovich et al. 1982). As we have discussed, initial fluctuations in the CMB are believed to evolve into the large-scale structure we observe today. Superclusters then, would represent the products of the largest measured fluctuations produced by large-scale density perturbations. Superclusters therefore contain information on the large-scale initial density field, and their properties can be used as a cosmological probe to discriminate between different cosmological models. The internal structure of superclusters conserves information on the galaxy formation and evolution. With this in mind, a number of investigators have compiled supercluster catalogues to help constrain the models of large-scale structure formation (e.g. Oort 1983, Bahcall et al. 1988, Einasto et al. 1997; 2001, Basilakos 2003, Einasto et al. 2007a;b; 2011).

1.4 Galaxy Evolution

One way to trace the evolution of a galaxy is through its star formation history, which is the method employed in the thesis. One of the major components in the study of galaxy evolution is the physics that lies behind the triggering of star formation (e.g. Kennicutt 1989, Madau et al. 1996; 1998, Kennicutt 1998b, Bouwens et al. 2010). In general it can be assumed that the star formation of a galaxy is limited by the availability of hydrogen (H) gas that can cool, fragment and form new stars. The surface density of gas has been found to play an important role in the star formation rate of galaxies. The Kennicutt-Schmidt law derived from the work by Schmidt (1959) and Kennicutt (1998b; 1989), showed that the surface density of HII gas is proportional to the star formation rate density, $\Sigma_{SFR} \propto \Sigma_{gas}$.

Observations of star forming galaxies point towards there being two modes in which stars are formed: i) a quiescent star formation and ii) circumnuclear star bursts. The observed star formation in local gas rich spiral galaxies is relatively low and continuous. The typical star formation e-folding time scales are $\sim$ 3–4 Gyr, much shorter than the current age of the Universe. It has been shown that spiral galaxies have a reservoir of hydrogen gas that surrounds them (e.g. Solomon & Sanders 1980, Sanders 1984, Frayer et al. 1998, Papadopoulos et al. 2001, Frye et al. 2008, Heald et al. 2011). Continuous star formation is therefore possible by the cooling of the hydrogen gas which is then accreted onto the galaxy's disk (Kormendy & Kennicutt 2004). This reservoir is likely to consist of gas that is just falling onto the halo, gas that has already fallen in and been shock heated, but which has not yet cooled radiatively and gas that has been reheated and expelled from the galaxy due to feedback processes. In addition to the infall or accretion of cold gas, mergers can bring new gas to a galaxy and induce star formation, even at late cosmic times.

1.4.1 Star Formation Rate Indicators

The presence of hot, young massive stars in a galaxy is a direct measurement of current star formation since these stars have such short lifetimes. Described below are the techniques used to derive star formation rates by quantifying the amount of flux, directly or indirectly measured from these young, hot, massive stars. We only review the star formation rate indicators relevant to the work and the discussion of results. The relationships between the SFR indicators and the actual SFR are given in, for example, Kennicutt (1998a).

Ultraviolet continuum emission

Young stars ($< 10^8$ yr) contribute most of the Ultraviolet (UV) flux of a galaxy. One can therefore use the UV continuum flux in the range 1300-2500 Å is an indicator of current star formation in a galaxy. The conversion from UV flux to SFR is based on synthesis models described in Sect. 4.1.2. This technique for deriving SFR is therefore sensitive to the underlying assumptions made in the synthesis modeling, for instance the star formation history (SFH) and initial mass function IMF. A drawback of using UV continuum emission as a SF indicator is its sensitivity to dust extinction and the contribution from evolved stellar

populations. But, with reasonable assumptions about the above mentioned parameters, the direct measurement of UV flux is one of the most powerful probes of SFR, locally, and at high redshifts (Madau et al. 1996, Ellis et al. 1997). With accurate modeling of the dust extinction, the UV continuum is the main SF indicator used to derive accurate stellar masses and SFR from optical broadband SED fitting (Sect. 1.10).

Recombination lines

Hot O and B stars photoionise the nebular hydrogen gas from which they form. The ionised H atoms recombine with free electrons which return to their ground state by the electron cascading down in energy levels. This downward cascade in energy levels is associated with the emission of a photon which will have a wavelength inversely proportional the difference in energy levels given by the Rydberg formula. The larger the energy level difference, the higher the energy level difference and therefore the shorter the wavelength of the emitted photon. The strength of the nebular emission lines, of which Hα is the strongest, are directly coupled to the UV radiation from the hot massive stars and is therefore a direct probe of current SF. However, the observed spectrum of the galaxy is a combination of the nebular emission lines and the combined spectra of the constituent stellar population. Therefore, the accurate measurement of the nebular emission lines relies on the removal of the absorption lines in the underlying stellar spectrum. The stellar spectrum can be recreated by either spectral synthesis or evolutionary synthesis models. Dust extinction is the greatest cause in systematic errors in measurements of Hα flux and it is also highly sensitive to the assumed high mass slope of the IMF.

Far-Infrared Continuum

The absorption cross section of interstellar dust is highly peaked in the UV. The absorbed UV radiation is re-emitted in the FIR and should therefore be a sensitive tracer of star formation. FIR radiation in star forming galaxies can arise from three different processes: i) emission from dust heated by young O and B stars, ii) emission from the photospheres of evolved stars as they lose mass and, iii) from dust distributed throughout the interstellar medium, which is heated by the interstellar radiation field. If it is assumed that young stars dominate the radiation field in the UV and visible bands, then the last two of these processes are negligible. The FIR luminosity can be determined by stellar population synthesis modeling and is therefore sensitive to the assumed IMF.

1.5 Bimodality Of Galaxy Properties

After the advent of wide area photometric and redshift surveys like the Sloan Digital Sky Survey (SDSS) (York et al. 2000) and the Two Degree Field Galaxy Redshift Survey (2dF-GRS) (Colless et al. 2001) large statistical significant studies of the global properties of galaxies became possible. They provide higher signal-to-noise results and insights into the

formation and evolution of galaxies. This prompted various investigators to use the large homogeneous datasets to study the effect of environment on the properties of galaxies.

A number of studies have found very strong correlations between the measurable properties of galaxies. They have shown that galaxies occupy two distinct populations: i) red massive early-type galaxies with little or no star formation, found mostly in dense environments and, ii) blue low mass late-type galaxies which are actively forming stars in less dense environments. Comprehensive studies of various physical properties of galaxies, e.g. colour, luminosity, stellar mass, stellar age and star formation rate (SFR) have found strong bimodal distributions (e.g. Strateva et al. 2001, Baldry et al. 2004, Balogh et al. 2004, Bell et al. 2004, Brinchmann et al. 2004, Kauffmann et al. 2004, Croton et al. 2005). The advent of large surveys showed the persistence of the bimodality of galaxy properties. This pointed towards there being two separate populations of galaxies, each with their own formation and evolutionary paths.

The first evidence of a possible change in SFR as a function of environment came from observations made by Butcher & Oemler (1978; 1984). They found that galaxies at higher redshift ($z = 0.4$) have a higher fraction of blue galaxies compared to local clusters, which is now known as the Butcher-Oemler effect. Dressler (1980) studied the morphologies of galaxies in 55 nearby clusters and found a correlation between the morphology of a galaxy and their local surface density, in the sense that early-type galaxies are found in denser regions than late-type galaxies (Dressler 1980, Oemler 1974, Treu et al. 2003). This is termed the morphology–density relation and it was later on shown that this relation is already in place at higher redshifts ($z \sim 0.5$), (e.g Couch et al. 1994; 1998, Dressler et al. 1997, Smail et al. 1997). The morphology-density relation was studied later in terms of galaxy colour which led to the colour–density relation; galaxies in denser environments were generally found to have redder colours than galaxies in less dense regions (e.g. Kodama et al. 2001, Cooper et al. 2006, Cassata et al. 2007, Quadri et al. 2007). The results were interpreted as a lowering in SFR (becoming redder) as density increases. Additionally, it was shown that the red galaxies in the dense environments were brighter on average than galaxies associated with the field. Subsequently it was found that the environmental impact on SFR (or colour) is stronger than that on morphology (Kauffmann et al. 2004, Blanton et al. 2005, Ball et al. 2008, Bamford et al. 2009): at fixed morphology, SFR still exhibits strong changes with environment, but at fixed SFR, there is almost no dependence of morphology on environment.

Using galaxy colours to describe a galaxy population, rather than morphological types, has the advantage that they are easily quantifiable, the measurements are robustly reproducible, and models exist that allow us to directly relate them to star formation histories with minimal assumptions. Strateva et al. (2001) found a strong bimodal distribution in the $u - r$ colour which separated galaxies into non-star forming and star forming galaxies using a colour cut. Baldry et al. (2004) quantified the colour distribution by modeling it as the sum of two Gaussian distributions. They showed the bimodal colour distribution is present irrespective of density or mass/luminosity. The fraction of galaxies on the red sequence was

found to depend strongly on both stellar mass and environment (Baldry et al. 2004, Balogh et al. 2004). The red population exhibits a tight correlation between colour and magnitude, with brighter galaxies being redder.

From the relative increase in the fraction of red galaxies as a function of density one could assume that galaxies are transformed from blue to red galaxies as a function increasing density. The fact that the red and blue populations stay well defined with no excess of galaxies in between the bimodal distribution implies that the transformation occurs rapidly ($\tau < 0.5$ Gyr) and we would expect only $\sim 1\%$ of the of the total population to be observed in the transition state (the green valley) (Balogh et al. 2004, Baldry et al. 2006). A caveat to working with a population of galaxies selected on colour alone is the non-negligible contribution of 'dusty' red star forming galaxies to the quiescent red galaxy population.

Wolf et al. (2009b) found that dusty red spiral galaxies may contribute up to 20% to the fraction of star forming galaxies in clusters with SFR down to 0.14 $M_\odot$/yr for $M_* > 10^{10}$ $M_\odot$ galaxies, and $< 10\%$ for galaxies with $M_* < 10^{10}$ $M_\odot$. The contamination of dusty star forming galaxies can be circumvented by using a more dust-insensitive proxy to measure SFR.

1.6 Global Star Formation Rate Density and Star Formation Processes

Observationally it has been established that star formation density was higher at earlier epochs in the Universe compared to what we observe today (e.g. Lilly et al. 1996, Madau et al. 1996, Hopkins & Beacom 2006). The majority of galaxies assembled most of their stars between the redshifts of $z \sim 1$–2. Between then and $z = 0$, the star formation rate density has decreased by a factor ~ 10. There is considerable evidence that active star forming galaxies experienced a decrease in their SFR and have been transformed from actively star forming galaxies to quiescent red galaxies (Noeske et al. 2007, Pozzetti et al. 2010). It was shown, in particular, that if star forming galaxies do not experience a decrease in SFR their present day stellar masses would be over produced (Baldry & Glazebrook 2003, Bell et al. 2007), which together with the increase in stellar mass of red sequence galaxies provides further evidence of the global decrease in star formation in star forming galaxies.

1.7 Star Formation - Density Relation

Balogh et al. (1998) were among the first to study the SFR away from cluster cores. They found a strong radial dependence on SFR as a function of cluster-centric distance and showed that as far out as the virial radius, the SFR was still as high as expected for the field population. With the arrival of the 2dFGRS and SDSS, Lewis et al. (2002) and Gómez et al. (2003) found a correlation between the median SFR and the local galaxy density. Additionally, they also showed that the suppression of star formation occurred at densities

much lower compared to the cluster. This prompted the investigation of SFRs even further than $\sim$ 2 virial radii from cluster centres which yielded evidence that galaxies might be 'pre-processed' or quenched of their star formation before reaching the cores of clusters (e.g. Zabludoff & Mulchaey 1998, Balogh et al. 2000, Ellingson et al. 2001, González et al. 2005, Balogh & McGee 2010).

Regions where the pre-processing of galaxies have been detected are associated with local galaxy densities similar to the densities of galaxy groups. Various studies have found a lowering of star formation rate and an increase in the fraction of early type galaxies in groups (Jeltema et al. 2007, McGee et al. 2008, Wilman et al. 2008, Balogh et al. 2009). Many recent works have found that satellite galaxies are more likely to have lower SFRs towards group/cluster centres (Balogh et al. 2000, Ellingson et al. 2001, Weinmann et al. 2006a, von der Linden et al. 2010, Prescott et al. 2011). A number of studies probed the effect density has on the observed enhancement of SF in close galaxy pairs. They showed SFR enhancement in low densities (Lambas et al. 2003, Alonso et al. 2004, Ellison et al. 2010), however the enhancement diminishes or becomes undetectable in high density environments (Alonso et al. 2004, Baldry et al. 2006, Ellison et al. 2010). Simulations have shown that galaxies are accreted mainly along large-scale structures such as filaments and sheets (Bond et al. 1996, Colberg et al. 1999). McGee et al. (2009) suggest that $\sim$ 40% of galaxies that accrete onto clusters are in groups. These observational results provide support to the idea that the pre-processing of galaxies happens on smaller scales and are more likely associated with groups as they fall in along filamentary structures towards clusters.

The role local environment plays in the quenching of star formation has been well studied. The exact mechanism responsible for this transformation, however, remains unclear, though several have been proposed. Here we discuss the main proposed mechanisms:

1.7.1 Strangulation

The most favoured mechanism that operates in the group environment is strangulation (Larson et al. 1980), also referred to as 'starvation'. Galaxies contain a halo of hot gas that can cool down and accrete onto the galaxy to form new stars. This gradual process involves the loss of an existing halo of hot gas via heating/evaporation, tidal stripping or ram-pressure stripping (Larson et al. 1980, Balogh et al. 2000, Kawata & Mulchaey 2008, McCarthy et al. 2008). As soon as a galaxy enters a more massive halo, a galaxy is stripped of its hot gas reservoir. This does not directly shut down star formation, but only the accretion of gas which could cool down and form new stars. The galaxy continues forming stars until the remaining cold gas is depleted. McGee et al. (2011) favour strangulation in their accretion model, whereby galaxies are affected $\sim$ 3 Gyr after falling in a 10^{13} $M_{\odot}$ halo/group. There are still some doubts whether strangulation can produce the strong break observed in the bimodal colour and sSFR distributions. Semi-analytic models produce too many green valley galaxies which breaks the observed bimodality (Balogh et al. 2008, Font et al. 2008, De Lucia et al. 2012). More accurate models are needed to fully understand the mechanism responsible for the observed bimodality.

1.7.2 Ram Pressure Stripping

Other mechanisms are also thought to play a role in the transformation of galaxies, especially in denser environments. Ram pressure stripping (Gunn & Gott 1972) has been proposed a viable mechanism for the transformation of galaxies since it causes the rapid removal of gas, which shuts down star formation. The main difference between ram pressure stripping and strangulation is the removal of cold gas versus hot gas respectively. Ram pressure stripping is thought to operate on gas densities which are higher, compared to strangulation, which operates on lower gas densities. If a galaxy orbits a hot gaseous halo it may experience ram pressure stripping since it only shuts down star formation, the morphology of the galaxy remains intact. This mechanism is thought to operate on the cluster periphery where infalling galaxies first experiences the hot and dense ICM (Chung et al. 2009). The effect of ram pressure stripping is thought to be more efficient in more massive halos, well illustrated in the massive Norma cluster (Sun et al. 2010, Zhang et al. 2013). Since clusters are dominated by a population of early-type galaxies, additional transformation mechanisms are thought to be at work to alter the morphology of galaxies. The high relative velocities of galaxies in clusters can subject galaxies to frequent high-speed encounters, known as harassment.

1.7.3 Harassment

'Harassment' involves high-speed, nearby encounters that tidally disturb galaxies, causing either a cessation or enhancement in star formation (Farouki & Shapiro 1981, Moore et al. 1998). More violently, galaxies can merge with one another (Makino & Hut 1997), a process that is thought to be more common in lower density regions where relative velocities are lower (Angulo et al. 2009, Wetzel et al. 2009, White et al. 2010, Cohn 2012). These dynamical interactions could potentially induce the rapid consumption of gas and therefore quench star formation. The CDM paradigm predicts that lower mass halos are scaled down versions of more massive halos. Therefore, harassment could also operate on groups sized halos. Weinmann et al. (2006a) found that if this would be the case, the late-type fraction would increase with increasing luminosity since harassment would have a bigger impact on low mass halos. This is not what they found, but more detailed studies are needed to understand the role of harassment in low mass halos.

1.7.4 Mergers

In general, mergers are considered to be rare in relaxed clusters (e.g. Makino & Hut 1997). Observationally, galaxies in massive clusters show a lower incidence of interaction than galaxies in groups or the field (McIntosh et al. 2008, Lu et al. 2009, Tal et al. 2009). In particular Heiderman et al. (2009) identified 13 morphologically disturbed galaxies with enhanced star formation, all outside the cluster cores of the A901/902 supercluster. The group environment is assumed to be the prime location for galaxy mergers. For example, Wilman et al. (2009) found S0s dominate in group environments, and Just et al. (2010) found the S0 fraction evolves most strongly in intermediate-velocity dispersion structures.

These results imply that groups are an important location for spiral mergers, in agreement with the idea of pre-processing in group environments.

1.8 Star Formation - Mass Relation

From numerous studies of the properties of galaxies as a function of environment, strong evidence has come to light that stellar mass plays a central role in determining – or at least describing – a galaxy's evolutionary state. Virtually all of the global properties commonly used to describe galaxies are strongly correlated with stellar mass, especially SFR (e.g. Kauffmann et al. 2003b, Brinchmann et al. 2004, Salim et al. 2007). Several works considered the dark matter halo masses of galaxy group/cluster catalogues, showing that a galaxy's star formation history most directly depend on the properties of their host dark matter halo (Blanton & Berlind 2007, Wilman et al. 2010, Tinker et al. 2011). However, see Peng et al. (2012) for an opposing view. The importance that stellar mass plays in the evolution of galaxies has become a topic of great interest. More importantly, the relative roles of environment and stellar mass in the evolution of galaxies have become a topic of great discussion.

Peng et al. (2010) developed an empirical method to separate the effects of stellar mass and environment on star formation. Their method is purely phenomenological and based only on observational evidence. They define two methods for the quenching of star formation, termed 'mass quenching', which is independent of environment, and 'environmental quenching' which is independent of mass. Their conclusion was that high mass ($M_* > 3 \times 10^{10}$ $M_\odot$), red, low SFR galaxies have their star formation quenched at high redshift ($z > 1$) where their star formation was quenched at a rate proportional to their stellar mass. Low mass ($M_* < 3 \times 10^{10}$ $M_\odot$), blue, star forming galaxies have their star formation quenched through either mergers, or environmental processes. Raichoor & Andreon (2012) extended their analysis to include the dependence of SFR on stellar mass as a function of cluster centric distance, and confirmed the separability of the effects that stellar mass and environment have on the quenching of star formation. Muzzin et al. (2012) also confirmed the separability of mass and environmental quenching in their study of a sample of clusters at $z \sim 1$, and reiterated that the stellar mass is the primary parameter linked to determining the stellar populations of galaxies.

Since the SFR of a galaxy is so closely related to its stellar mass, to study the star formation properties of galaxies as a function of mass and environment one can use the specific star formation rate sSFR, defined as SFR/M_*. It quantifies the current SFR with respect to the past SFR (Kennicutt et al. 1994). The sSFR has also been found to have a strong bimodal distribution which is independent of environment or mass (e.g. Weinmann et al. 2006a, McGee et al. 2011, Wetzel et al. 2012). This is consistent with the findings of Peng et al. (2010), who found no difference in sSFR in the lowest and highest density regions in the SDSS data. In addition, studies at intermediate redshifts have shown that this bimodality exists at least out to $z \simeq 1$ (e.g. Bell et al. 2004, Tanaka et al. 2005, Weiner

et al. 2005), but with different fractions of galaxies on both sides of the bimodality scale compared to $z = 0$ (Bell et al. 2004). Li et al. (2011) confirmed the same trend of a declining sSFR-mass relation for star forming galaxies from $z \sim 1$ to $z \sim 0$ and noted that the trend is primarily due to the strong dependence of SFR on mass, whereas the role of the environment is secondary and more important for lower mass galaxies. Since less massive galaxies have smaller gas reservoirs, they may be more easily affected by their environment.

1.9 Using Quiescent Fractions of Galaxies to Study Galaxy Evolution

Using the red galaxy fraction (f_r) to study the evolution of clusters and their constituent galaxies is a well used method. Previous studies span a large range in redshift and sample sizes with different selection criteria to define red galaxies. In this section we will discuss the various observed trends which could introduce differences when comparing red fractions measured in studies using different samples and methods. We also consider observed trends in the passive galaxy fraction as measured from various star formation rate indicators. This is of particular relevance to the discussion in Sect. 5.4.

1.9.1 Trends with Redshift

The most well known trend with red fraction was presented in the ground-breaking work of Butcher & Oemler (1984) (BO84). They found that the red fraction increases as a function of declining redshift. Since then, numerous studies have replicated their method in deriving red fractions and found a similar trend (e.g. Ellingson et al. 2001, Margoniner et al. 2001, De Propris et al. 2003a; 2004). For opposing findings see e.g. Fairley et al. (2002), De Propris et al. (2003b), Andreon et al. (2004). An example of typical red fraction measurements for a sample of clusters is shown in Fig. 1.3. It shows the typical scatter of cluster red fraction measurements and the observed decrease in red fraction ($f_r = 1 - f_b$) with redshift, where f_b is the blue fraction. A similar increase in the quiescent galaxy fraction have been observed for clusters as a function of declining redshift through emission line and far infra red (FIR) SFR indicators. (e.g. Haines et al. 2008, Poggianti et al. 2008)

1.9.2 Trends with Observed Photometric Bands

Because different photometric bands are sensitive to different stellar populations, an increase in the red fraction would be expected as one considers bluer to redder bands. De Propris et al. (2003a) compared a V and K band selected sample and confirmed the expected trend with pass band.

Another consideration is the colour definition when determining red fractions. Most studies adopted the prescription of BO84 to divide their sample into red and blue galaxies. The colour division was usually taken to be 0.25-0.3 magnitudes to the blue of the red

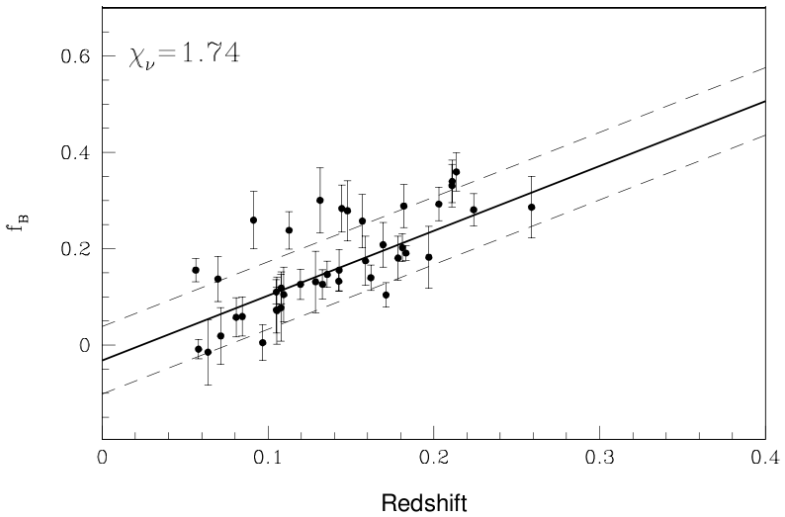

Figure 1.3: Figure 1. taken from Margoniner et al. (2001) to show the typical scatter for red/blue fraction measurements. Use $f_r = 1 - f_b$ to convert the plot to show a trend of red fraction with redshift. The fitted line is represented by the equation $f_r = 1 - [(1.34 \pm 0.11)z - 0.037]$.

sequence (e.g. Ellingson et al. 2001, Li et al. 2012) as derived from $B - V$ or $g - r$ colours. This is the intermediate colour value between typical E/S0 and Scd galaxies. Galaxies at higher redshifts have younger stars than present-day galaxies. Therefore, the reddest galaxies have a colour that becomes bluer in the rest frame with increasing redshift (e.g. Andreon et al. 2004, Kodama et al. 1998). The colour evolution of galaxies and the definition for the red fraction should therefore be taken into consideration when comparing results from studies using different redshift ranges and colour divisions. This is less of a problem in the low to intermediate redshift range ($z < 0.1$), where very little colour evolution for early type galaxies is expected (Strateva et al. 2001).

1.9.3 Trends with Magnitude Limits

Red fraction studies have relied on magnitude limited samples of different depths. The observed trend as a function of limiting magnitude is an increase in red fraction as brighter limiting magnitudes are imposed, regardless of the observed pass band (e.g. De Propris et al. 2004, Barkhouse et al. 2009). The same trend in the passive galaxy fraction is also expected.

1.9.4 Trends with Stellar Mass Limits

Since masses can be defined by a simple mass-to-light ratio, the observed trend when imposing a stellar mass limit is similar to applying a magnitude limit. An increase in the stellar mass limit results in an increase in red fraction. This is nicely depicted in Fig. 11 of Baldry et al. (2006), where they show an increase in red fraction as a function of increasing stellar

mass. In the case of our passive galaxy fraction measurements, we also expect an increase in the passive galaxy fraction as higher mass limits are imposed.

1.9.5 Trends with Sampling Radii

Red fractions have been shown to strongly depend on the sampling radius. The observed trend is a decline in the red fraction as a function of increasing radius (e.g. Ellingson et al. 2001, Pimbblet et al. 2002, Weinmann et al. 2009, Hansen et al. 2009). The same radial dependence has been shown for passive galaxies, in that there is a strong decline in the passive galaxy fraction as measured from emission line strengths with increasing radius (Lewis et al. 2002, Gómez et al. 2003).

1.9.6 Trends with Cluster Mass

When studying the evolution of galaxies using clusters, the cluster selection function should be as independent as possible of the cluster sample under consideration. Traditionally, clusters used in the study of red fractions were selected on their X-ray luminosity in an attempt to construct a homogeneous sample of clusters. This could be viewed as a mass selection due to the relation between X-ray luminosity and cluster mass. Since the X-ray luminosity only relates to the ICM, and not the properties of the constituent galaxies, this selection criteria is not well constrained. However, Andreon & Ettori (1999) showed that at a given X-ray emission, clusters rich in blue galaxies are not favoured/disfavoured at a given cluster mass. Wake et al. (2005) and Haines et al. (2009) also found no dependence on the quiescent fraction of galaxies as a function of X-ray luminosity or temperature, contrary to what was found by Popesso et al. (2007b). Several studies (Margoniner et al. 2001, Goto et al. 2003, Poggianti et al. 2006, Blanton & Berlind 2007, Gerke et al. 2007, Urquhart et al. 2010) did however find that the galaxy type fraction is a function of cluster mass. Studies of the dependence of the quiescent fraction as a function of cluster mass has been extended to groups, where it has been shown that the fraction of quiescent galaxies is a function of dark matter halo mass, in that the quiescent fraction increases with increasing halo mass (Hansen et al. 2009, Kimm et al. 2009). The observed trend with cluster mass is that the red -and passive fraction increase as a function of increasing cluster/group mass.

1.9.7 Systematics

To accurately determine red fractions when working with photometric data, it is necessary to correct for background field galaxy contamination. The field background subtraction can be a source of systematic uncertainty. A number of studies have used different methods to determine the contribution of background field galaxies, whether it be separate observations of a field sample (De Propris et al. 2003a) or using the outer edges of their sampling radii (Pimbblet et al. 2002). Since the extent of clusters are not well defined, contamination of the field sample can lead to lower red fractions. The background subtraction is an area-scaled statistical subtraction which assumes that the field population subtracted is a good

representation of the actual field population at the redshift/position of the red fraction measurement. The same discussion applies to sSFRs derived from photometry.

1.10 Evolutionary Stellar Population Synthesis Modeling

Stars and gas are the baryonic building blocks of galaxies. Most of the radiation emitted by a galaxy comes from stellar light, directly or reprocessed by the interstellar medium (ISM). Therefore, the spectral energy distribution (SED) of a galaxy contains a wealth of information regarding its stellar and gas components. To extract the physical properties contained within a galaxy's SED one needs to have an accurate understanding of how the stellar and gas components have been assembled and evolved over time to its present day state. The only way to achieve this is, is through the modeling of galaxy SEDs and by having an accurate understanding of stellar evolution and stellar spectra. This has led to the field of stellar population synthesis (SPS) modeling which aims to do just that (e.g. Tinsley & Gunn 1976, Bruzual A. 1983, Buzzoni 1989, Bruzual A. & Charlot 1993, Fioc & Rocca-Volmerange 1997, Maraston 1998, Coelho et al. 2007, Schiavon 2007, Mollá et al. 2009, Kotulla et al. 2009, Conroy et al. 2009). Key ingredients to SPS models are an accurate understanding of the phases of stellar evolution, well calibrated stellar libraries, an initial mass function (IMF) which describes how newly born stars are distributed as a function of mass, and the dust attenuation properties of the ISM. These ingredients all depend on chemical composition which complicates matters further.

1.10.1 Stellar Evolution

The evolution of a star is almost completely determined by its initial mass and chemical composition. It should therefore, in principle, be possible to predict the properties of any star after the time of its birth for a given initial mass, metallicity and stellar evolution model. Effective temperature (T_{eff}) and luminosity (L) are two of the fundamental properties that describes a star's position on the H-R (T_{eff}–L) diagram and therefore its evolutionary state. At the core of SPS modeling are the stellar evolutionary tracks that allow one to follow the evolution of any mass star from the zero-age main sequence (MS) to any later evolutionary stage on the H-R diagram. A number of groups produced publicly available isochrone libraries for a range of initial masses, metallicities and ages (e.g. Schaller et al. 1992, Bertelli et al. 1994, Cassisi et al. 2000, Girardi et al. 2000, Cioni et al. 2006, Dotter et al. 2007, Koester et al. 2007b). One of the most widely used isochrone libraries are from the Padova group (Madau et al. 1996, Marigo & Girardi 2007, Marigo et al. 2008) and includes isochrones for stars with intial masses $0.15\ \mathrm{M}_{\odot} \leq M \leq 100\ \mathrm{M}_{\odot}$, initial metallicities of $10^{-4} < Z < 0.03$ in the age range ~ 4 Myr to ~ 16 Gyr.

Later stages of stellar evolution are still not that well understood and can lead to substantial uncertainties. Some of the more critical issues are the metallicity dependent mass loss on the red giant branch (RGB) and the treatment of the thermally pulsating asymptotic

giant branch (TP-AGB) phase. The TP-AGB is one of the most difficult evolutionary phases to model while it contributes significantly to the overall luminosity of a galaxy. Maraston (2005) found that young stellar populations could also make appreciable contributions to NIR light through the TP-AGB phase which has to be taken into account to avoid substantial uncertainties in derived SPS properties.

1.10.2 Stellar Spectral Library

The position of a star for a given initial mass and chemical composition on the H-R diagram can now be predicted. The properties of an individual star are described by its spectrum. By combining a library of stellar spectra with stellar evolutionary tracks one can describe the properties of stars at any position on the H-R diagram.

There are two different methods to obtain the spectrum of a star for a given L, T_{eff} and metallicity. The first, and most straightforward, is to use a sample of local stars with measured bolometric magnitudes, T_{eff} and metallicities. From this sample one can obtain the spectrum for any star of given L, T_{eff} and Z by interpolation or extrapolation of the available spectra. This empirical method is limited by the properties sampled for stars in the local solar neighbourhood which only cover a limited range in metallicities (Gunn & Stryker 1983, Pickles 1998, Le Borgne et al. 2003).

The second method for obtaining stellar spectra is based on model stellar atmospheres, called theoretical spectra. For SPS modeling theoretical spectra are preferred because they do not have the same limitations as the empirical spectra and they can cover a much larger wavelength range. The semi-empirical BaSeL3.1 library (Lejeune et al. 1997; 1998, Westera et al. 2002) is one of the well known theoretical spectral libraries. They have compiled model atmospheres for a wide range of effective temperatures and surface gravities, covering the full range of metallicities in the Padova stellar evolution models. The library spans the wavelength range of 91 Å–160 μm at a resolving power of $\lambda/\Delta\lambda \approx 200$–$500$.

1.10.3 The Initial Mass Function (IMF)

The initial mass function (IMF), $\xi(m)$, describes the distribution in mass of a stellar population that formed in a single event, where m is the stellar mass and $\xi(m)$ is the stellar mass distribution function. The number of stars in the mass range m, $m + dm$ is given by $dN = \xi(m)dm$. The IMF has been the topic of many studies since it is fundamental to understanding star formation and for that matter, galaxy formation and evolution. Salpeter (1955) studied 0.4–10 $M_\odot$ stars in the solar-neighbourhood and derived the first estimate for the IMF. He found that the IMF could be approximated by a power law with slope $\alpha = 2.35$. The number of stars in a mass interval can therefore be represented by $dN \propto m^{-\alpha}dm$. As observational techniques improved, the same analysis was performed for volumes further than the solar-neighbourhood in the Milky Way and it was found that the IMF had roughly the same form.

For the high-mass end of the IMF the Salpeter slope of $\alpha = 2.35$ has been shown to

vary little up to 100 $M_\odot$. However, major revisions have been made to the low mass end ($0.8\ M_\odot \leq m \leq 2\ M_\odot$) of the IMF (Chabrier 2003, Kroupa 2001, Scalo et al. 1998).

The generally accepted forms of the IMF can be described either as a log-normal distribution with a power-law tail or as a series of power-laws. Kroupa (2001) found the following form of the IMF to best describe a field star sample in the solar-neighbourhood.

$$\xi(m) \propto \begin{cases} m^{-2.3} & \text{for } 0.5\ M_\odot < m < 100\ M_\odot \\ m^{-1.3} & \text{for } 0.08\ M_\odot < m < 0.5\ M_\odot \\ m^{-0.3} & \text{for } 0.01\ M_\odot < m < 0.08\ M_\odot \end{cases} \quad \text{Kroupa IMF} \tag{1.4}$$

Chabrier (2003) studied different stellar components of the Milky Way, disk stars, bulge stars and stars in young and globular clusters. He found that IMFs derived for each of these components have similar forms. The single-star IMF for disk stars is described by the following:

$$\xi(m) \propto \begin{cases} m^{-2.35} & \text{for } m > 1\ M_\odot \\ \exp -[\log(m/0.2\ M_\odot)]^2/0.6 & \text{for } m < 1.0\ M_\odot \end{cases} \quad \text{Chabrier IMF} \tag{1.5}$$

The two most influential features of the IMF are the slopes at the low and high mass ends of the stellar mass distribution. The slope at the high mass end prescribes the relative number of high mass star being formed, which in turn has the largest effect on the chemical enhancement of the ISM and kinematic feedback of star formation. The slope at the low mass end plays a very important role in the luminosity evolution of stars older than 10^9 yr with masses close to $m \approx 1\ M_\odot$.

1.10.4 Simple Stellar Populations (SSPs)

We have described the main ingredients needed to perform SPS, namely isochrones, a stellar library and an IMF. It is therefore possible to construct a composite spectrum build from the spectra of individual stars of the same age of a certain metallicity with the masses distributed according to the IMF. This is called a simple stellar population (SSP), the building blocks of SPS. The spectrum of a coeval set of stars can be represented as follows: (taken from Conroy et al. (2009)):

$$S(t, Z) = \int_{M_i^l}^{M_i^u} \Phi(M_i) \Lambda[L(M_i, Z, t), T(M_i, Z, t), Z] dM_i \tag{1.6}$$

where M_i is the initial mass, and M_i^l and M_i^u are the lower and upper mass limits of the IMF, Φ. Λ is a spectrum from the stellar library characterised by the luminosity L and temperature T which both depend on the initial mass, metallicity (Z) and time since birth. This would be a viable approximation for describing a galaxy that formed all its stars in one single burst. Considering that we still observe galaxies with ongoing star formation today, one would expect it not to be the case. We therefore need a prescription that allows us to

follow the spectral evolution of a galaxy with multiple star formation episodes.

1.10.5 Isochrone Synthesis

The isochrone synthesis technique (Charlot & Bruzual 1991, Bruzual A. & Charlot 1993) is based on the assumption that a galaxy can be described as the combination of a series of SSPs. The luminosity per unit wavelength can therefore be expressed as (Charlot & Fall 2000):

$$L_\lambda(t) = \int_0^t \Psi(t-t')S_\lambda(t')e^{-\tau_\lambda(t')}\mathrm{d}t' \tag{1.7}$$

where $\Psi(t-t')$ is the star formation rate at time $(t-t')$, $S_\lambda(t')$ is the luminosity per unit wavelength per unit mass emitted by a SSP of age t' and $e^{-\tau_\lambda(t')}$ describes the attenuation of star light by dust.

Different prescriptions for star formation rates are used in the literature. The simplest prescription for a SFR adopted today is a smooth exponentially declining SFR (e.g. Bell & de Jong 2001, Taylor et al. 2011):

$$\Psi(t) \propto e^{-\gamma t'} \tag{1.8}$$

where γ is the star-formation time-scale from the formation time to the present. Another popular method introduced by Kauffmann et al. (2003a) is based on the underlying continuous model. Random bursts of star formation are superimposed on the continuous star formation for a stochastic treatment of the SFH. The star burst is parametrised by $A = M_{burst}/M_{cont}$, where M_{burst} is the mass of stars formed in the burst and M_{cont} the total mass of stars formed from the formation time to the present. This SFR prescription is thought to be a more realistic representation of the observed SFHs of galaxies compared to the smoothly exponentially declining SFR prescription (Kauffmann et al. 2004, Salim et al. 2007).

An underlying process that is not explicitly shown in Eq. 1.7 which forms part of the SSP, is the chemical evolution of galaxies. Stars at the later stages of their evolution return a substantial fraction of their initial mass to the ISM. Stars that form from the chemically enriched ISM will have different initial metallicities, and subsequently different evolutionary paths, than the same mass stars formed at earlier epochs. It is therefore very important to track the chemical evolution of the ISM as a function of time. Stars with initial masses in the range $m \lesssim 8\mathrm{M}_\odot$ end up as white dwarfs with masses 0.4–1.4 $\mathrm{M}_\odot$ after going through the AGB phase. The convective dredge-up of heavier elements in the AGB phase enriches the ISM with the elements synthesised, namely, He, C, N and O. Stars with masses $m \gtrsim 8$ $\mathrm{M}_\odot$ enrich the ISM through stellar winds and core collapse type II supernova explosions. Heavier elements synthesised in massive stars, namely, Si, Na, Mg and Fe are returned to the ISM.

Another very important role the ISM plays in SPS modeling is the attenuation of star light by interstellar dust. Dust between the observer and stars in a galaxy redden the light from the stars. Charlot & Fall (2000) found that modeling the dust attenuation as a screen

of dust between the galaxy and observer can be represented as a power-law, $\tau_\lambda \propto \lambda^{-0.7}$, where λ is the wavelength of the emitted light. They were able to account reasonably well for the diffuse ISM attenuation observed in star bursting galaxies. It is important that the effective dust attenuation of a galaxy is dependent upon its star formation history (Calzetti et al. 1997). Charlot & Fall (2000) also found an indication of differential attenuation of different stellar populations. Young stars and their associated ionized nebula are strongly attenuated by the clouds from which the stars formed. Older stars have evolved out of their 'birth clouds' either through cloud or stellar dispersion, and are only attenuated by the diffuse ISM dust, which acts on both the young and old stars. Charlot & Fall (2000) have therefore come up with a time dependant treatment of dust:

$$\tau_\lambda(t') = \begin{cases} \tau_\lambda^{\rm BC} + \tau_\lambda^{\rm ISM} & \text{for } \; t' \leq t_0 \\ \tau_\lambda^{\rm ISM} & \text{for } \; t' > t_0 \end{cases} \tag{1.9}$$

where $\tau_\lambda^{\rm BC}$ and $\tau_\lambda^{\rm ISM}$ is the effective absorption optical depth of the dust in the birth cloud and ISM respectively. t_0 is the typical time scale, $\sim 10^7$ yr, for dense molecular clouds to dissipate.

1.11 This Thesis

The strong bimodality observed in the distribution of galaxy properties, and the close link of these properties with stellar mass has placed great importance on the use of stellar mass selected samples when studying the properties of galaxies. The separability of the role stellar mass and local environment play in the evolution of galaxies has been considered empirically, based on observations of large samples. Many open questions still remain, specifically, what environmental mechanisms are responsible for transforming blue star forming galaxies to red quiescent galaxies?

In an attempt to address some of the questions related to understanding the role environment plays in the evolution of galaxies, we set out to study, in detail, a region of the Universe centred on the massive galaxy cluster Abell 1437 at a redshift of $z = 0.135$. Sufficient photometric and spectroscopic archival data exists for this equatorial object, making such a study possible. Even though the cluster has been included in previous studies (Miller et al. 2005, Pimbblet et al. 2006, Popesso et al. 2007a), this is the first in-depth study of the star formation properties of galaxies as a function of environment for this region. An outline of how the study was conducted is given below.

In Chapter 2, the dataset is introduced. The galaxy cluster Abell 1437 at $z = 0.135$ and its surrounding large scale structure in a 64 square degree field of view is characterised and environments identified using spectroscopy and a modified Friends-of-friends algorithm.
Chapter 3 is concerned with building a consistent seeing-matched photometric dataset from SDSS and UKIDSS Large Area Survey (LAS) imaging data.
In Chapter 4, the performance of the state of the art MAGPHYS SED-fitting code is tested

against stellar masses and star formation rates derived from spectroscopic data. Thereafter, the photometric dataset is utilised to derive stellar masses and star formation rates for the complete photometric dataset.
Chapter 5 describes a new technique devised to build a photometric redshift slice at our redshift of interest. Additionally, further techniques were developed to create environmental samples from the photometric data, specifically groups and filaments. Thereafter, the environmental impact on the star formation properties of galaxies are investigated using red- and passive galaxy fractions. The validity of our methods and results are established through a detailed comparison to previous work. We also consider the filament environment in more detail by looking at the distribution of enhanced star formation activity surrounding Abell 1437 (which will be referred to as A1437 from now on). A summary of the main conclusions from the thesis, as well as interesting and exciting future work which stems from this project, is given in Chapter 6.

Throughout this work, we assume a cosmology with a present day matter density parameter $\Omega_m = 0.27$, vacuum energy density parameter $\Omega_\lambda = 0.7$, and Hubble constant $H_0 = 72$ km s^{-1} Mpc^{-1}. SDSS magnitudes are in the AB system and UKIDSS photometry is presented in the Vega magnitude system.

Chapter 2

Multiwavelength Dataset and Introduction to Abell 1437

In this chapter, we describe the assembly of our multiwavelength dataset, including spectroscopy, which is ancillary to our photometric dataset. Archival data were obtained from the Sloan Digital Sky Survey (SDSS) and UKIRT Infra-Red Deep Sky Survey (UKIDSS). For ease of reference, we have divided our data as laid out in Table 2.1.

Table 2.1: Multiwavelength dataset.

Photometric Datasets		
Dataset	Filters	Data obtained
SDSS	$ugriz$	SDSS - DR7
UKIDSS	JHK	UKIDSS
Spectroscopic Datasets		
Dataset	λ coverage	Data obtained
SDSS	3800 - 9200Å	SDSS - Early data release
2dF	4200 - 6500Å	K. A. Pimbblet†

† Private communication

2.1 SDSS Dataset

2.1.1 The Sloan Digital Sky Survey (SDSS)

The Sloan Digital Sky Survey (SDSS) was designed for a photometrically and astrometrically calibrated digital imaging survey of π sr above about Galactic latitude 30° in 5 broad optical bands. It is accompanied by a spectroscopic survey of the approximately 10^6 brightest galaxies (York et al. 2000). The 7th data-release of the SDSS data (Abazajian et al. 2009) marked the release of the final SDSS-II extended program data, which reported the

successful achievement of the goals set out more than a decade ago. The DR7 data contain photometrically and astrometrically calibrated imaging covering 11,663 deg^2, with 356×10^6 unique objects and 1,440,960 unique spectra.

The SDSS makes use of a dedicated 2.5m modified Richey-Chrétien altitude-azimuth telescope located at Apache Point Observatory in New Mexico. The telescope is equipped with two survey instruments. The first is a wide field CCD which covers 2°.5 on the sky, capable of near simultaneous imaging in 5 photometric bands, *ugriz*. The second instrument is a pair of double fibre-fed spectrographs capable of taking 640 simultaneous spectra of targets pre-selected from the imaging data (York et al. 2000). Imaging is done only in photometric and moonless conditions in mostly good seeing (median 1.5″ in r). These conditions are not required for the spectroscopy, but both the imaging and spectroscopy only takes place during moonless sky. The imaging instrument consist of 30, 2048×2048 Tektronix CCDs, configured in 6 columns and 5 rows with a pixel scale of 0.396 ″/pix. The telescope was designed to image in drift-scan mode, allowing the sky to pass over the imager, parallel to the column direction. The CCD readout is continuous, and at the same rate as the sky drifts, which results in a 53.9s integration time per filter. Images are processed through a series of interlocking pipelines which determines astrometric calibrations (Pier et al. 2003) and detects and measures the brightnesses, positions, and shapes of objects (Lupton et al. 2001, Stoughton et al. 2002). The data are calibrated to an AB magnitude system (Oke & Gunn 1983, Fukugita et al. 1996) using a 0.5m telescope, the photometric telescope (PT), located on the same site. The 95% completeness limits for point sources in each of the photometric bands are u, g, r, i, $z = 22.0$, 22.2, 22.2, 21.3, 20.5 mag respectively, depending on the seeing and sky-brightness (Abazajian et al. 2004). The quoted SDSS point source completeness limits are not directly applicable to our study however, we re-derive completeness limits for galaxies in our dataset in Sect. 3.4.5. An accuracy of 45 milliarcseconds rms is achieved for the astrometric solution of bright objects.

Objects selected for spectroscopic observations are selected from the photometric catalogue and have galactic extinction-corrected (Schlegel et al. 1998) r band magnitudes of $r \leq 17.77$. Exposure times for spectra are 15 min and three or more exposures are taken to reach a predefined signal-to-noise ratio (S/N), namely $(\mathrm{S/N})^2 > 15$ per 1.5Å pixel for stellar objects of fiber magnitude $g = 20.2$, $r = 20.25$, and $i = 19.9$. Spectra are extracted and wavelength- and flux calibrated. The flux calibration is accurate to 4% rms for point sources (Adelman-McCarthy et al. 2008) and the wavelength calibration is accurate down to 2 km s^{-1}. After calibration, spectra are classified and redshifts determined using methods described in Stoughton et al. (2002) and SubbaRao et al. (2002).

2.1.2 Data Acquisition

The SDSS observations of Abell 1437 and surrounding area were part of the SDSS Early Data Release (EDR) observations (Stoughton et al. 2002), subsequently reworked to DR7 standards (Abazajian et al. 2009). Several data products are available to the astronomy

community and designed for ease of access. The Catalogue Archive Server (CAS)* contains all measured parameters (flux, position, shape, redshift etc.) from the imaging and spectroscopy surveys. Data products, such as corrected images and calibrated spectra, are stored in the Data Archive Server (DAS)†.

Queries to the CAS database were submitted via a web interface‡ which makes use of a database language similar to the SQL§ database language. From the CAS, we obtained a number of image parameters that would enable us to identify sources of interest, perform the corrections needed to determine total magnitudes and obtain the parameters needed to download the images and spectra. To ensure uniform photometry, we obtained the SDSS images for our survey area, a 64□° field centred on A1437. To download corrected images the *run, rerun, camcol, field* and *filter* parameters are required. These parameters were submitted to the DAS and the images retrieved.

2.2 UKIDSS Dataset

2.2.1 The UKIRT Deep Sky Survey (UKIDSS)

The UKIRT Infrared Deep Sky Survey (UKIDSS) is considered to be the near-infrared (NIR) counterpart of the Sloan Digital Sky Survey. It is not a single survey, but a set of survey programmes running concurrently: The Large Area Survey (LAS), the Galactic Clusters Survey (GCS), and the Galactic Plane Survey(GPS) cover approximately 7000 deg^2 to a depth of $K \sim 18$; the Deep Extragalactic Survey (DXS) covers 35 deg^2 to $K \sim 21$, and the Ultra Deep Survey (UDS) covers 0.77 deg^2 to $K \sim 23$ (Lawrence et al. 2007).

The UKIDSS makes use of the 3.8m Cassegrain English yoke-mounted United Kingdom Infrared Telescope (UKIRT) which is located at Mauna Kea observatory. The survey instrument, the wide field camera (WFCAM), consists of four HgCdTe (HAWAII-2) near infrared arrays which covers 0.21 deg^2 on the sky with a pixel scale of 0.4 $''$/pix (Casali et al. 2007). A tip-tilt secondary mirror removes dome and windshake effects which delivers a median seeing of $\sim 0.6''$ across the whole field of view. UKIDSS makes use of five filters, $ZYJHK$, covering the wavelength range 0.83-2.37 μm. Our data originates from the Large Area Survey (LAS), the shallowest survey of the three, for which the target depths are $Y = 20.3$, $J = 19.5$, $H = 18.6$ and $K = 18.2$ (Lawrence et al. 2007) using 40 seconds integration per observation. UKIDSS imaging is taken only in seeing with a FWHM of $< 1.2''$ and the data quality requires a photometric accuracy of 0.02^{m} rms and astrometric accuracy of $< 0.1''$ rms. The goal of the LAS is to map as large as possible area of the Northern Sky (~ 4000 deg^2) that coincides with SDSS observations.

*http://casjobs.sdss.org/CasJobs/
†http://das.sdss.org/www/html/
‡http://casjobs.sdss.org/CasJobs/
§Structured Query Language

2.2.2 Data Acquisition

Data from the UKIDSS are accessed through the WFCAM Science Archive (WSA)* using a SQL interface. The archive is open to queries for detected object parameters such as right ascension, declination and magnitude in different filters etc. DR4 is the current world release of UKIDSS data, but some of the imaging for our area was taken more recently than the propriety period of 18 months. The UKIDSS imaging data are not available to non-ESO members, we therefore obtained the imaging of Abell 1437 and surrounding area via our collaborator Dr. R. Kotulla (University of Wisconsin, Milwaukee). Images are compressed using RICE compression (Pence et al. 2009; 2010) and each image is accompanied by a binary fits table containing a catalogue of sources detected by the WFCAM data processing pipeline located at the Cambridge Astronomy Survey Unit (CASU).

2.3 2dF Dataset

2.3.1 The Las Campanas Observatory and Anglo-Australian Telescope Rich Cluster Survey (LARCS)

Galaxies with a B magnitude of $B \leq 21$ were chosen for spectroscopic follow-up (Pimbblet et al. 2006). Spectroscopic observations took 12 dark nights during the period 1998–2002 for which the median seeing was $\sim 1.5''$. The aim was to obtain two pointings of ~ 9000s per cluster, which is made up of 800 fiber observations in total. The requested exposure times were chosen to obtain a S/N of 10–15 per pixel for the faintest galaxies in the sample ($R \sim 20.5$). The 600V grating provided the necessary resolution to measure key line indices and precise velocity measurements (~ 120 km s^{-1}). The rest-frame wavelength range with this grating is approximately 3700–5600 Å for the clusters, providing coverage of the major line indices of interest ([O II] λ3727 Å, [O III] λ5007 Å, Hδ, Hβ, Mgb, Feλ5270 Å).

2.3.2 Data Acquisition

Data for A1437 was obtained from Dr. K.A Pimbblet†, private communication. Spectroscopic observations for Abell 1437:

Table 2.2: 2dF observations for Abell 1437, (Pimbblet et al. 2006).

Date	Grating	Seeing	t_{exp}	$N(gal)$
2002 May 04	600V	1.2–1.4	5×1800	338
2002 May 05	600V	1.2–1.3	5×1800	339

*http://surveys.roe.ac.uk/wsa

†School of Physics, Monash University, Clayton, Melbourne, VIC 3800, Australia

2.4 Abell 1437 and surrounding area

2.4.1 Previous Work

Abell 1437 was classified as a cluster of galaxies by Abell (1958), using the following classification scheme: The redshift of the 10^{th} brightest galaxy yields the angle, α, subtended by a fixed linear size of 1.5 h^{-1} Mpc ($\text{h}^{-1} = 100$ km s^{-1} Mpc^{-1}) at the distance of the cluster. All galaxies within the radial distance α with a magnitude $m \leq m_3 + 2$, where m_3 is the magnitude of the third brightest galaxy, are counted as cluster members.

Figure 2.1: SDSS colour composite image of Abell 1437. The image is 13.5′ on a side (1.85 Mpc at the redshift of the cluster) and centred on the coordinates derived by Abell 1958, $\alpha = 12^h00^m27^s$, $\delta = 03^d21^m04^s$ (J2000). East is to the left and North is up.

Over-densities with more than 50 members were considered rich enough to be classified as part of the Abell galaxy cluster catalogue. Abell 1437 has a medium richness of 3, on a

scale ranging from 0 to 5, where the richness is defined as the number of galaxies in a cluster not fainter than $m_3 + 2$. A richness of 3 implies that one would expect 130–199 galaxies in the cluster, as defined by Abell (1958). The Abell radius for the cluster, defined by $1.72/z$ in arc minutes, is $12.8'$ for $H_0 = 100$ km s^{-1}.

Table 2.3: Properties derived for Abell 1437 obtained from literature.

Property	Value
Abell (1958)	†
RA	$12^h00^m27^s$
Dec.	$03^d20.3^m$
$\overline{z}$	0.1339
Richness	3
N(gal)[1]	154
Pimbblet. et al. (2006)	
RA	$12^h00^m25.44^s$
Dec.	$03^d21^m04^s$
$\overline{z}$	0.1345
L_X	7.72×10^{44} erg s^{-1}
$\overline{cz}$	40323 ± 77 km s^{-1}
σ_z	1152^{+59}_{-51} km s^{-1}
N(gal)	224
r_{200}	3.3 Mpc
Popesso et al. (2007)	†
$\overline{z}$	0.1341
σ_z	1497 ± 13 km s^{-1}
M_{200}	4.0×10^{15} M$_\odot$
r_{200}	3.2 Mpc
PDS	0.12
Miller et al. (2005)	†
$\overline{z}$	0.1359
σ_z	1595 km s^{-1}
Richness[2]	35
SCF[3]	0
PDS	0.18

[1] number of cluster members between m_3 and $m_3 + 2$, corrected for background.
[2] as determined by Yee & Ellingson (2003) and references therein.
[3] Structure Contamination Flag. A measure of the degree of isolation in redshift space for each cluster.
† from the CDS online catalogue.

The cluster has been studied in the X-ray quite extensively. Ebeling et al. (1996) classified it as a bright X-ray cluster as part of the X-ray-brightest Abell-type clusters of galaxies (XBACS) survey, a sub-sample of the ROSAT All-Sky Survey (RASS). They determined the X-ray luminosity (0.1–2.4 keV) to be $L_X = 7.72 \times 10^{44}$ erg s^{-1}. Schindler (2000) found that the X-ray emission is not symmetrical and strongly elongated in the SW-NE direction. They postulate that the asymmetric X-ray flux distribution is indicative of subclusters merging, which would present as intra-cluster gas ejected perpendicular to the collision axis (Schindler

& Mueller 1993). Popesso et al. (2004) combined the RASS X-ray and SDSS optical datasets to compile the RASS-SDSS cluster survey, a survey designed to study the correlation between the X-ray and optical properties of clusters. Properties derived for Abell 1437 from Popesso et al. (2004) are summarised in Table 2.3. SDSS spectra were used to determine the cluster mean redshift of $\overline{z} = 0.1341$, the rest frame velocity dispersion, $\sigma_{rest} = 1497$ km s^{-1}, cluster virial radius $r_{200} = 3.2$ Mpc and a virial mass of $M_{200} = 4.0 \times 10^{15}$ M$_{\odot}$. The PDS values referred to in Table 2.3 is the Dressler & Shectman probability that a cluster does not contain any substructures (Dressler & Shectman 1988), PDS values < 0.1 indicate clusters that are likely to contain substructures.

Pimbblet et al. (2006) found similar properties for A1437 which were derived from their 2dF spectroscopy. They confirmed a mean cluster redshift of $\overline{z} = 0.1345$, but found a slightly lower velocity dispersion of $\sigma_z = 1152^{+59}_{-51}$ km s^{-1}.

In summary, Abell 1437 is a massive cluster with a large enough combined dataset to perform an interesting study of galaxy properties associated with it, and the surrounding large scale structure. Previous studies of the properties Abell 1437 were done in the context of a larger sample of clusters. No previous study has attempted an in-depth multi-wavelength investigation of the properties of the galaxies associated Abell 1437 and its extended surrounding large scale structure.

2.4.2 Characterising large scale structure surrounding A1437

We selected a 64$\square^{\circ}$ field of view in the region defined by $176.680^{\circ} < \mathrm{RA} < 184.7893^{\circ}$ and $-0.4398^{\circ} < \mathrm{DEC} < 7.72319^{\circ}$ (Fig. 2.2), which covers Abell 1437 and the surrounding large scale structure. The area is large enough to provide regions of galaxy density ranging from clusters, to the field. A large component of the study will deal with a stellar mass selected sample, which is why the K band data defines the on-sky region for all other datasets, except for the 2dF data, which only covers the central 2°. The SDSS spectroscopic sources shown in Fig. 2.2 lie between $0.1 < z < 0.15$ and show the distribution of galaxies associated with large scale structure surrounding A1437. Figure 2.3 shows the redshift distribution of galaxies from the SDSS and 2dF datasets as a function of RA and DEC respectively. The most prominent feature is the wall-like structure at redshifts $z \sim 0.08$ and $z \sim 0.135$. These features also show up as large overdensities in Fig. 2.4, illustrating the redshift distributions of the SDSS and 2dF spectra for the whole field. The overdensity at $z \sim 0.08$ is less pronounced in the 2dF data since it was a targeted survey aimed at the redshift of A1437. The SDSS spectroscopic sample contains 7322 spectra and the 2dF sample contains 631 spectra. From the 631 2dF spectra, 177 match with SDSS spectra for which a redshift comparison is shown in Fig. 2.5. We find a systematic offset of $\langle z_{2dF} - z_{SDSS} \rangle = 89.2$ km s^{-1}. To investigate a possible magnitude dependence of the redshift offset, the comparison sample was split into galaxies brighter and fainter than the SDSS spectroscopic magnitude of $r = 17.7$. The average offsets for the bright and faint samples were found to lie within 8 km s^{-1} of the 89.2 km s^{-1} sample mean. No systematic offset as a function of magnitude

was found for the comparison sample, most probably due to the fact that the galaxies all are fairly bright. From the central limit theorem we would expect random errors to be normally distributed. The distribution is clearly narrower than a Gaussian with $\sigma = 1$ (black fitted Gaussian). The σ measured from fitting a Gaussian was found to be 0.87, which implies that the errors are over estimated by $\sim$ 13%. From private communication with K.A. Pimbblet, we believe the offset could be due to a difference in the template spectra used to compute redshifts. Since the SDSS spectra covers a larger wavelength range and have more spectral features available for template spectrum matching, we deem SDSS redshifts to be more trustworthy. We therefore apply a constant velocity offset to all the 2dF spectroscopic redshifts to remove the systematic redshift offset between the two surveys.

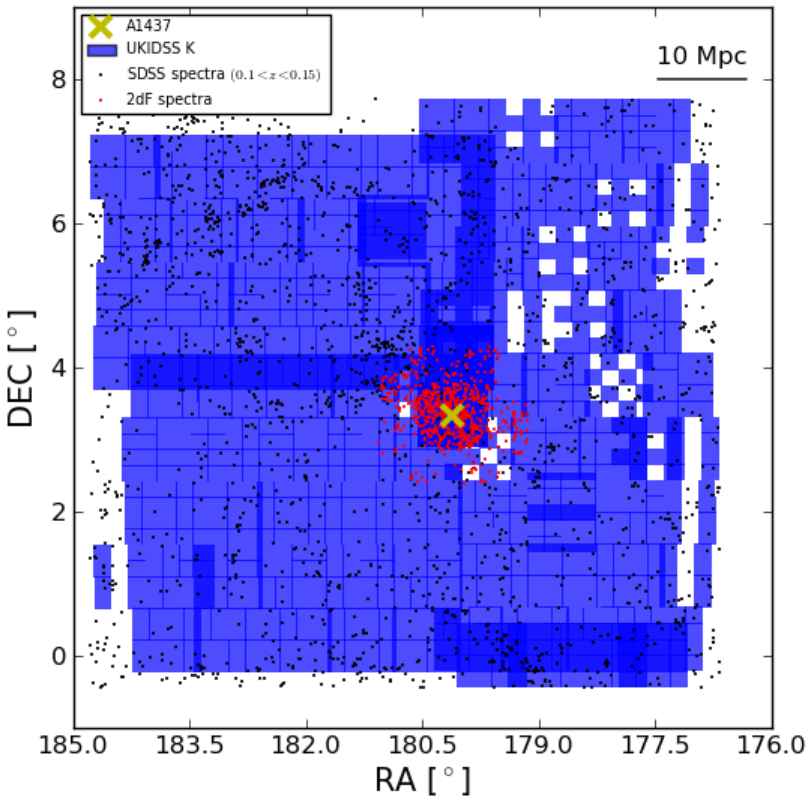

Figure 2.2: UKIDSS K band imaging on-sky coverage. The darker areas show regions of overlap or repeat observations. The empty regions have not been observed or have inadequate data quality.

A consolidated sample of spectra was constructed from the SDSS and 2dF spectra, which consists of 7953 sources. For the 177 matching galaxies, the 2dF redshift information is preferred since it has smaller random redshift errors (due to the higher S/N spectra), an average error of 40 km s^{-1} compared to the 80 km s^{-1} of the SDSS spectra.

We re-derive the velocity dispersion for the cluster from our own spectroscopic dataset.

Considering galaxies roughly within the previously found virial radius of $\sim$ 4.0 Mpc, a Gaussian is fitted to galaxies within the redshift range $0.1 < z < 0.16$. Velocity was binned into $2.5\sigma_{\rm rms}$ km s^{-1} intervals, where $\sigma_{\rm rms} = \sqrt{\sigma_{\rm 2dF} + \sigma_{\rm SDSS}} = 90$ km s^{-1}. The Gaussian fit gave a mean redshift of $\overline{cz} \approx 40000$ km s^{-1} ($\overline{z} = 0.134$) and a rest frame velocity dispersion of $\sigma_{rest} \approx 1300$ km s^{-1} (Fig. 2.6).

We use the derived velocity dispersion to define a $\pm 3\sigma_{rest}$ region centred on $\overline{z} = 0.134$ to investigate galaxies most likely to be gravitationally bound to the large scale structure surrounding A1437. Figures 2.8 and 2.9 show the redshift distribution of sources in the $\pm 3\sigma_{rest}$ range covering the 64$\square^\circ$ FoV as a function of RA and DEC respectively.

Miller et al. (2005) used the SDSS DR2 dataset to create the C4 Cluster Catalogue, which uses the C4 cluster-finding algorithm to identify clusters as overdensities. The C4 cluster finding algorithm identifies clusters in a seven-dimensional position and colour space which helps minimizing projection effects. They show that with the C4 algorithm they are able to recover 90% of Abell clusters in the redshift range $0.03 < z < 0.12$. Miller et al. (2005) found 4 overdensities in the region of our survey, two of which were identified as Abell clusters, the one being A1437. Properties derived for the clusters are shown in Table 2.4.

Sources from the C4 catalogue (Miller et al. 2005) that lie with $3\sigma_{rest}$ of $z = 0.1344$ are also indicated on Figures 2.8 and 2.9. The C4 algorithm seems to have split A1437 into two nearly overlapping overdensities with similar velocity dispersions; C4:1135 and C4:1352 lying within $\sim$ 1 and $\sim$ 2 Mpc from A1437 respectively. To investigate whether this is in fact the case, we consider Fig. 2.7 which shows the normalized velocity distribution as a function of virial radius. The virial radius for A1437 was computed from Eq. 1.2 for which we found $r_{200} = 2.94$ Mpc. Figure 2.7 shows no clear division of the cluster into two similar overdensities.

Table 2.4: C4 clustering algorithm sources within $3\sigma_{rest}$ of $z = 0.1344$.

ID	RA [°]	DEC [°]	z	σ [km s^{-1}]	richness	SCF	PDS	Other name
1135	180.2013	3.4281	0.13586	1595	35	0	0.18	ABELL 1437
1124	180.9412	4.2892	0.13462	668	36	1	0.21	ABELL 1456
1352	180.1808	3.1085	0.13409	1230	22	1	0.09	no matches
1268	180.7490	3.9049	0.13503	542	13	2	0.85	no matches

The three dimensional distribution of galaxies in Fig. 2.10 hints towards there being more interesting overdensities than previously found by Miller et al. (2005). This justifies further investigation, which leads into the next section where we look for galaxy overdensities in the spectroscopic sample.

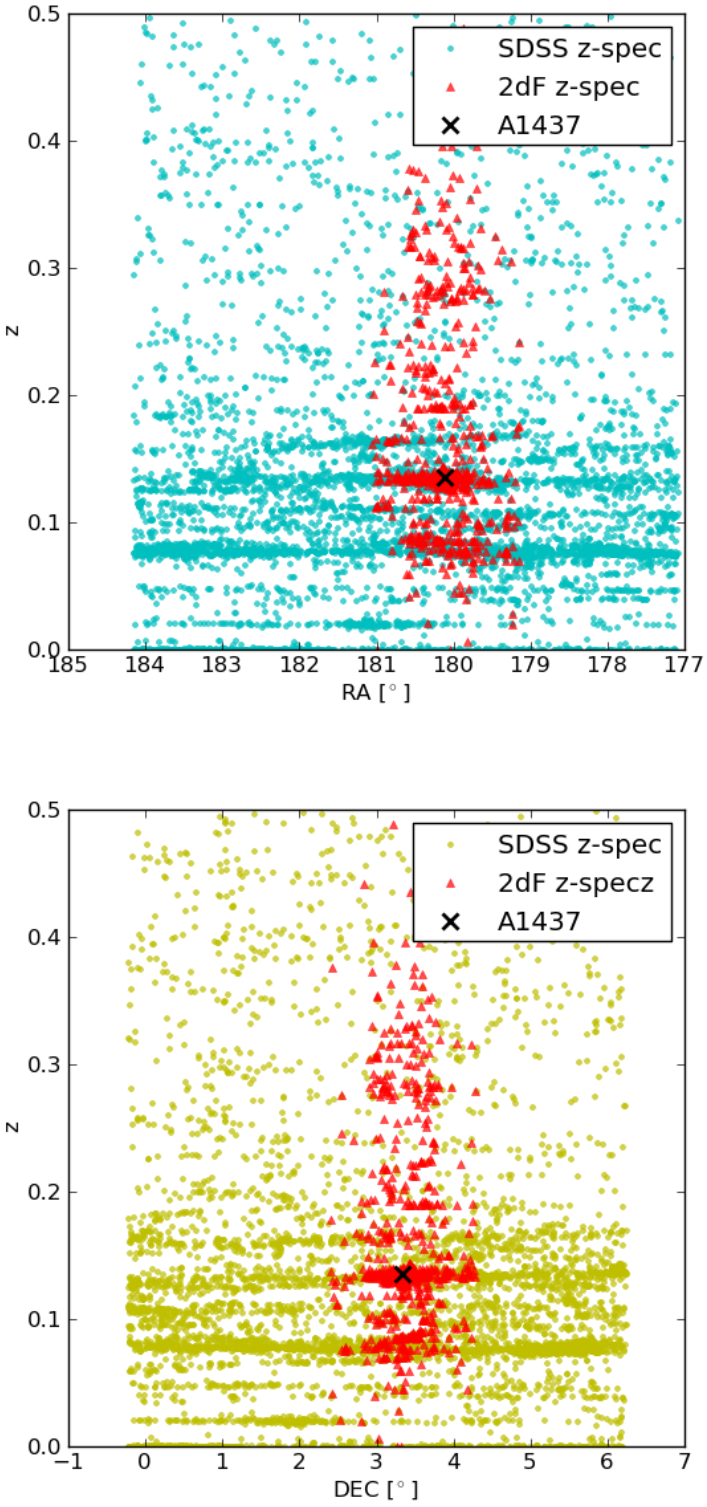

Figure 2.3: Redshift distribution of galaxies as a function of RA (top) and DEC (bottom) in the redshift range $0 < z < 0.5$. Several wall like structures can be seen at $z \sim 0.08$, $z \sim 0.135$ and $z \sim 0.16$.

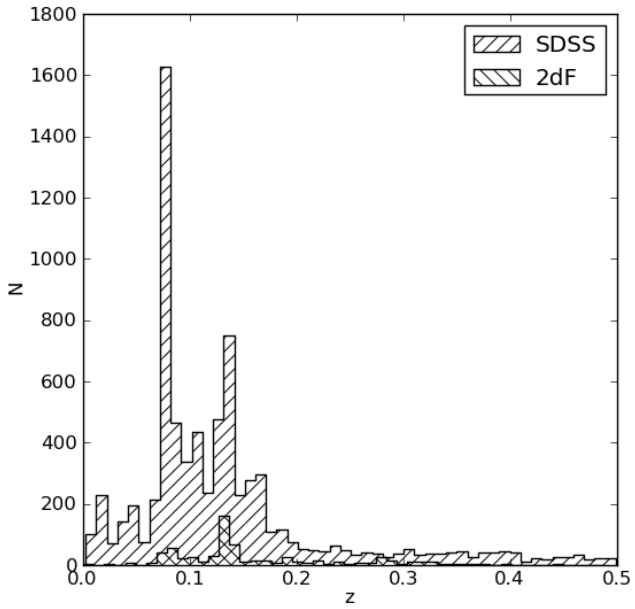

Figure 2.4: Redshift distribution of the SDSS and 2dF spectroscopic sources over the whole survey area. The SDSS redshift distribution shows the presence of a large scale structure at $z \sim 0.08$.

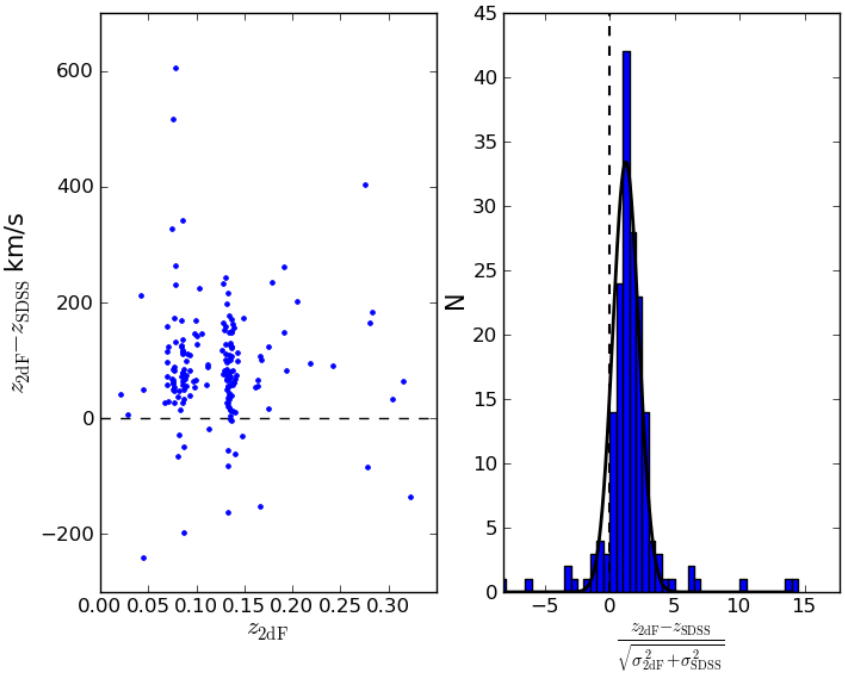

Figure 2.5: Redshift comparison of the 177 SDSS and 2dF galaxies matched within a 1″ radius. The mean redshift difference is $\langle z_{2dF} - z_{SDSS} \rangle = 89.2$ km s^{-1} with a standard deviation of $\sigma = 99$ km s^{-1}. From the central limit theorem we would expect random errors to be normally distributed. The distribution is marginally narrower than a Gaussian with $\sigma = 1$ (black fitted Gaussian). The σ measured from fitting a Gaussian was found to be 0.87, which implies that the errors are over estimated by $\sim 13\%$.

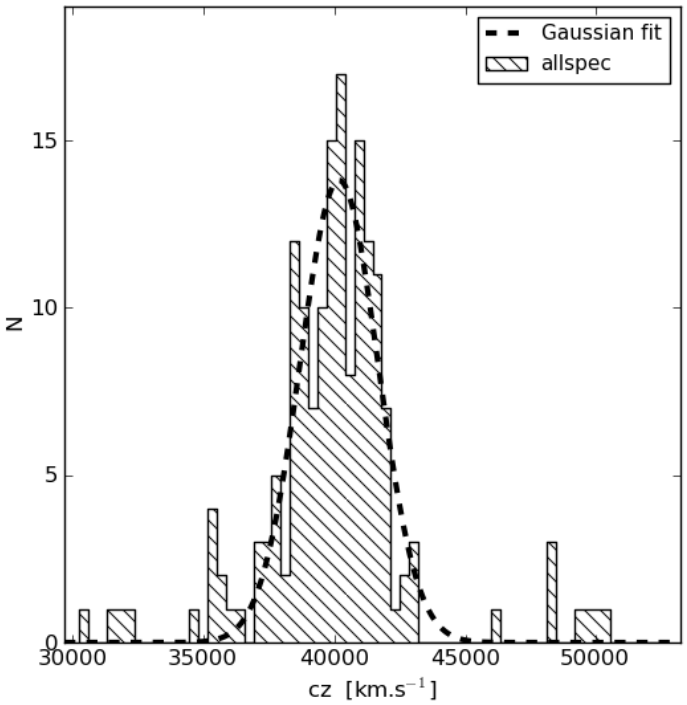

Figure 2.6: Velocity distribution of the consolidated SDSS and 2dF sample. The velocity dispersion was determined by fitting a Gaussian function to the redshift distribution of galaxies within $r_v \leq 12.6'$ of the cluster centre in the redshift range $0.1 < z < 0.16$. The mean redshift from the Gaussian fit is $\overline{z} = 0.134$ and the velocity dispersion is $\sigma_{rest} \approx 1300$ km s^{-1}.

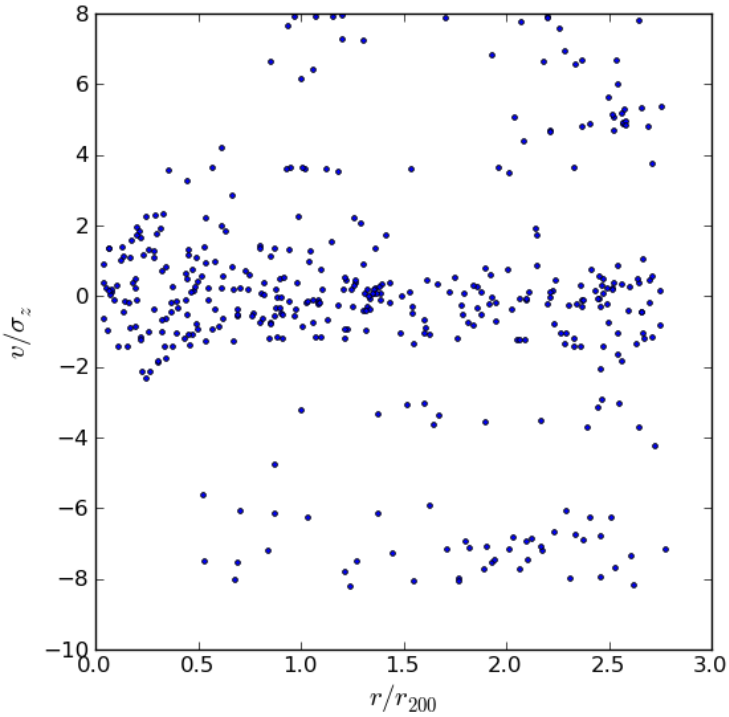

Figure 2.7: The normalised velocity distribution as a function of projected radius. By computing the relative velocities as a function of spatial distance one can look for gravitationally bound objects. Close to the zero offset there are a large number of galaxies close to the rest frame velocity of the cluster out to the virial radius.

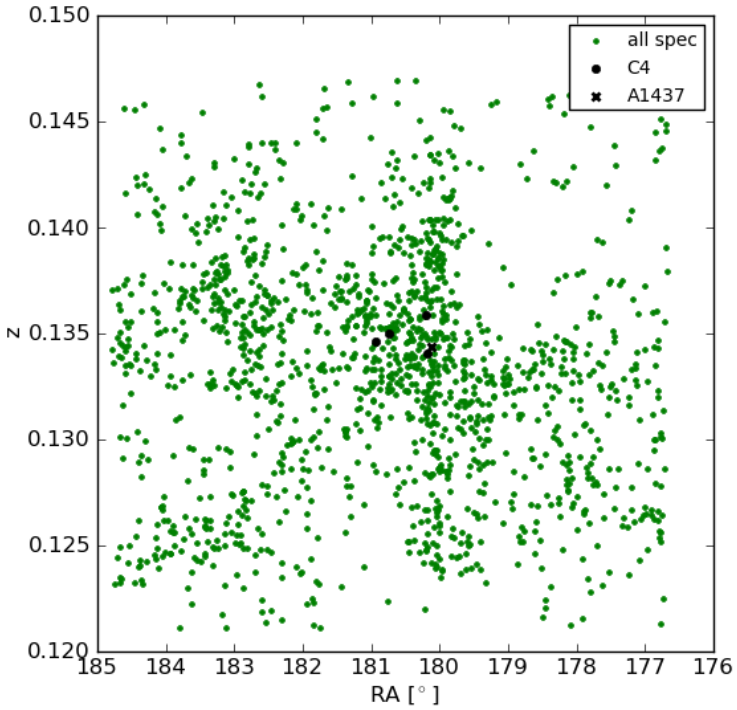

Figure 2.8: Redshift distribution of galaxies as a function of right ascension within $3\sigma_{rest} \approx$ 3900 km s^{-1} of the mean cluster redshift $\overline{z} = 0.1343$. The C4 cluster closest to the centre of A1437 (shown by the cross) is a re-identification of the A1437 in the C4 catalogue.

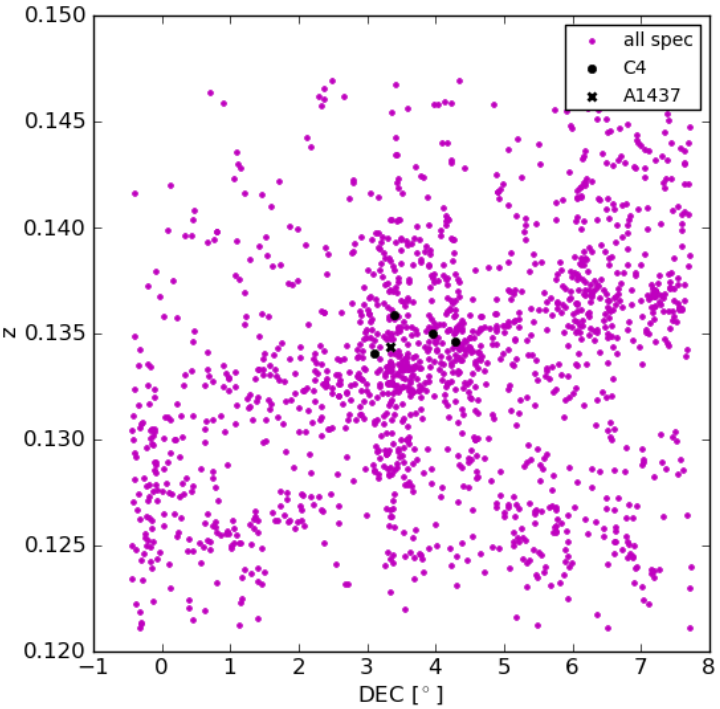

Figure 2.9: Redshift distribution of galaxies as a function of declination within $3\sigma_{rest} \approx 3900$ km s^{-1} of the mean cluster redshift $\overline{z} = 0.1344$.

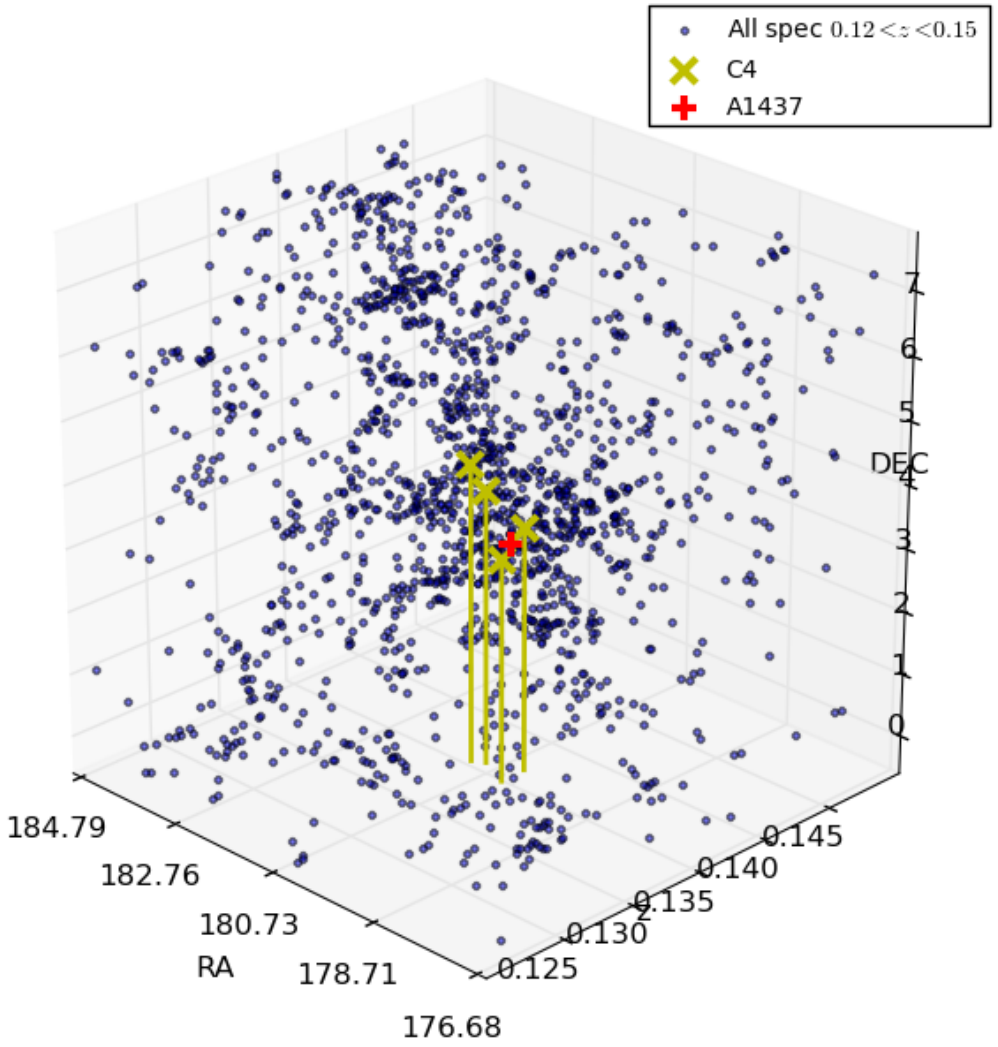

Figure 2.10: Three dimensional distribution of galaxies from our spectroscopic sample. The C4 catalogue sources that lie within the $3\sigma_{rest}$ velocity range and the full 64□° are shown as yellow crosses. The position of A1437 is shown as the red +. The two crosses nearest to A1437 indicate the positions of the C4 clusters which most likely are A1437 split into two overdensities.

2.5 The Spectroscopic Sample

The aim in the following section is to use the spectroscopic data to define galaxy environments by looking for overdensities in the three dimensional distribution of galaxies surrounding A1437. We assume that galaxies within $3\sigma_v$ of the redshift of A1437 are gravitationally bound to it, and are therefore associated with it or the surrounding large-scale structure.

2.5.1 Friends of Friends

The Friends of Friends (FoF) algorithm applied in this study is a well known technique for finding bound structures in surveys that contain redshift information. This technique was popularized by the work of Huchra & Geller (1982) who applied this technique to a whole-sky sample of galaxies to find galaxy groups. Subsequent studies by e.g. Press & Davis (1982), Einasto et al. (1984), Eke et al. (2004) and Berlind et al. (2006) have made modifications to the technique, but the basic principle remains the same. The technique is based on percolation theory which describes the behaviour of connected particles in three dimensions.

Given a catalogue of galaxies, consider the first galaxy that has not been assigned to a group. Search within a spherical volume around the galaxy using a search radius L, which we call the linking length. All the galaxies that lie within L are assigned a group id. Let's say 10 galaxies lie within L and are assigned a group id of 7. If one of the galaxies that lies within L has already been assigned to a group of 5 members with an id of 3, that galaxy and its group members will be reassigned to have a group id of 7, therefore increasing the number of galaxies in group 7 to 15 members. If no galaxies were found to lie within the linking length, the galaxy is reserved a group id defined for "field galaxies". This process is repeated for all the galaxies in the catalogue. From the example above, it is obvious that the most important parameter that governs the outcome of the FoF algorithm is the linking length, L. Many studies have considered various ways to determine the most optimal definition of the linking length (e.g. Li & Yee 2008). To simplify calculations, L is divided into a tangential component and radial component, a physical distance (D_L) and redshift (V_L) linking length respectively. D_L is a physical distance parallel to the tangential on-sky projection and the redshift of the object under consideration. It is converted to a projected on-sky distance in degrees by using the small angle approximation ($\theta = s/r$) and the angular diameter distance (Hogg 1999: Eq. 2.1):

$$\theta = \frac{D_L}{D_A}\frac{180}{\pi}, \tag{2.1}$$

where θ is the on-sky separation between two objects in degrees, D_L is the linking length in Mpc and D_A is the angular diameter distance in units of Mpc. Redshifts of galaxies are converted to rest-frame velocities $v_{rest} = cz/(1+z)$, where z is the redshift of a galaxy and c is the speed of light.

Our FoF study on the cluster and the surrounding large scale structure covers a relatively

small redshift range ($0.12 < z < 0.15$), negating the use of adaptive linking lengths in order to compensate for cosmological effects that would influence larger volume samples. We therefore chose our linking lengths, D_L and V_L to be constant for each of the environments we consider.

2.5.2 Defining Environments

Four environments for FoF analysis are defined: clusters, groups, filaments and the field. Our sample contains 1676 galaxies with redshifts from the SDSS and 2dF. The 2dF data goes ~ 5 magnitudes deeper in r than the SDSS spectroscopic limit of $r = 17.7$.

An exact determination of the linking lengths is very tricky because structures which are not physically bound together can be linked through one or two interloping galaxies with the FoF algorithm. Abell 1437 is a well established structure in 3D space which we could use to tweak the linking length parameters. Every overdensity detected was scrutinised in the RA–DEC, DEC–z and RA–z planes. Also, the rest-frame velocity distribution was considered in every case. This process was repeated until linking lengths which produced convincing physical structures were found. A range of linking lengths was considered: V_L between 200 and 2000 km s^{-1} and D_L between 0.5 and 3.0 Mpc. We found that for the cluster and groups a V_L of $\sim$ 200–500 km s^{-1} and D_L of $\sim$ 1 Mpc produced well defined structures. These values were increased beyond 1000 km s^{-1} and 2 Mpc to find filament like structures.

Clusters and Groups

Our clusters and groups catalogue was computed using an on-sky linking length of D_L = 1 Mpc and a velocity linking length of V_L = 500 km s^{-1}. We also set a lower limit on the number of galaxies needed to qualify as a group, namely $N_{min} = 5$. Figure 2.11 shows the 3D distribution of overdensities identified using our FoF method. Spatial positions of the overdensities are determined by taking the mean redshift $\langle z \rangle$, right ascension $\langle RA \rangle$ and declination $\langle DEC \rangle$. Note that the RA is not in the on-sky orientation for the 3D figures. Galaxy associations are indicated using the same colour filled circles. The dashed lines were added to help improve the depth perception of the figure and indicate group centres. The red cross symbol indicates the centre of A1437. Figure 2.12 shows the same 3D distribution, but viewed in the RA – DEC plane, again note that RA is not in the on-sky orientation. We are satisfied that the expected structures, such as A1437 and the two C4 identified overdensities, C4:1124 and C4:1268, are also identified given our parameter choice.
Discriminating between what constitutes a cluster and a group was the next step. For the larger associations, velocity dispersions are measurable and could be used to discriminate between large groups and small to medium size clusters. For small numbers of galaxies, the measurement of a Gaussian velocity dispersion is not possible. We therefore computed the standard deviation σ_v instead and used it as a proxy for the velocity dispersion (Beers et al. 1990). The standard deviation can also be problematic for samples that are too small

(e.g. Tago et al. 2008 used RMS velocities). We considered the number of members and the spatial and velocity distribution of each overdensity to aid our classification. All the overdensities with velocity dispersions less than 500 km s^{-1} were classified as groups. Their richness parameter indicates whether they are rich or poor groups. As mentioned previously, there are no set parameters to distinguish between poor clusters and rich groups. In order to simplify our analysis, we classify the overdensities identified as 12, 22 and 35 as rich groups with ID:12 previously identified as Abell 1456.

The spectroscopically derived group and cluster environments therefore contain 1 cluster and 35 groups ranging in richness from 5–35. Individual cluster and group properties are shown in Table 2.5. For each cluster and group the group id, spatial coordinates, number of members and σ_v are presented. This catalogue will be revised when considering overdensities identified with the photometric group finder in Chapter 5.

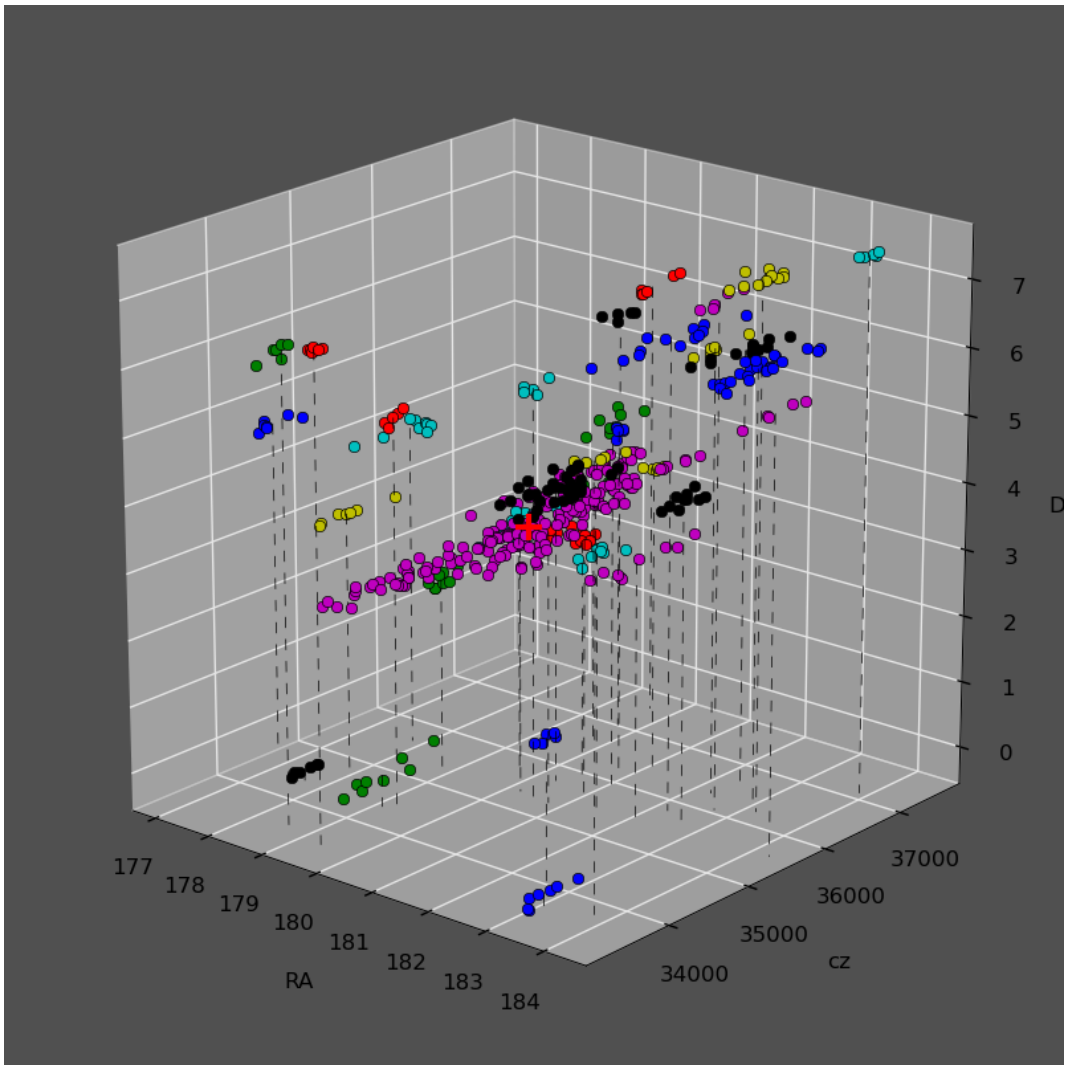

Figure 2.11: 3D distribution of clusters and groups identified using $D_L = 1$ Mpc and $V_L = 500$ km s^{-1}.

Table 2.5: Clusters and Groups identified from the spectroscopic FoF. The IDs are taken from the FoF algorithm. The mean spatial coordinates of the cluster and groups are given by $\langle RA \rangle$, $\langle DEC \rangle$ and $\langle z \rangle$. The richness N represents the number of galaxies in the cluster/groups. σ_v is the velocity dispersion determined from the standard deviation of the rest frame velocities.

Clusters						
ID	$\langle RA \rangle$	$\langle DEC \rangle$	$\langle z \rangle$	N	σ_v[km.s^{-1}]	Other Name
33	180.13	3.30	0.134	146	1002.47	Abell 1437, (C4:1135, C4:1352)*
Groups–GOF						
1	182.88	1.78	0.127	5	99.28	
6	178.26	3.57	0.130	7	256.90	
10	179.86	6.11	0.142	7	211.74	
11	178.08	4.40	0.134	9	268.77	
14	182.86	4.39	0.134	10	145.80	
15	176.81	4.56	0.130	7	192.35	
17	179.48	5.37	0.129	5	94.15	
18	180.73	5.70	0.133	5	110.35	
23	178.83	6.56	0.125	7	174.36	
24	179.64	6.83	0.125	6	89.40	
28	178.13	-0.10	0.128	6	132.40	
29	183.38	-0.17	0.125	7	228.75	
Groups–GIF						
2	179.04	2.46	0.133	8	105.90	
3	181.41	3.57	0.134	7	100.26	
4	181.78	3.50	0.133	9	143.97	
5	182.36	3.45	0.133	9	410.93	
7	181.14	6.51	0.136	5	147.31	
8	182.47	6.56	0.135	13	491.35	
9	183.98	5.73	0.126	8	128.83	
12	180.97	4.26	0.135	35	477.97	Abell 1456, C4:1124
13	181.29	4.14	0.138	5	71.81	
16	181.27	5.06	0.135	8	186.13	
19	184.53	6.06	0.134	5	269.30	
20	182.53	6.24	0.137	6	204.96	
21	182.80	6.19	0.138	12	348.14	
22	183.22	6.08	0.137	25	347.67	
25	184.10	7.59	0.140	5	89.51	
26	182.94	7.12	0.136	5	157.21	
27	183.43	7.47	0.137	11	199.03	
30	179.38	0.08	0.129	8	376.04	
31	181.04	3.67	0.133	9	190.64	
32	180.47	3.63	0.133	14	218.51	
34	180.05	3.92	0.138	6	215.61	
35	180.60	4.02	0.134	33	348.36	C4:1268
36	179.93	4.14	0.140	5	42.87	

*The C4 algorithm split Abell 1437 into two overlapping clusters.

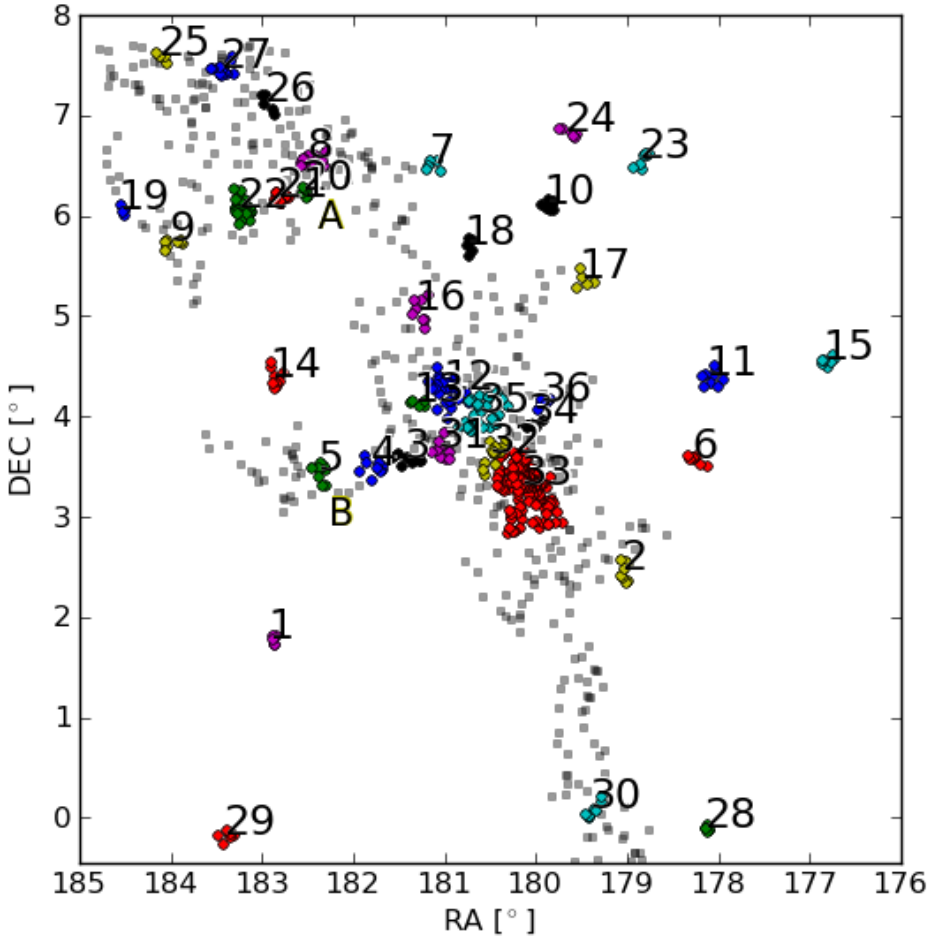

Figure 2.12: On-sky distribution of clusters and groups from Table 2.5. Filament galaxies are indicated as the grey squares. Regions marked as A and B are discussed in the text.

Filaments and the Field

There is no prescription for locating filamentary structures using FoF. To try and identify galaxies that lie in filaments, the linking lengths were increased to enable the linking together of galaxies more sparsely distributed than those in clusters and groups.

For the filament sample we used 2.3 Mpc and 1500 km s^{-1} for D_L and V_L respectively. Figure 2.14 shows the spatial distribution of the galaxies that resulted from the FoF algorithm being run with the increased linking lengths. This would also include all the galaxies identified as part of the clusters and groups overdensities as described above. The spatial distribution of galaxies belonging to clusters, groups and filaments are shown in 2.15. Cluster and rich group galaxies are represented by red-filled circles, groups by green-filled circles

and galaxies in the filaments are shown in yellow. The group sample is split into groups that lie in the filament, which we will refer to as "Groups In Filaments" (GIF) and groups that lie outside of the filament environment which we refer to as "Groups Out of Filaments" (GOF). The FoF algorithm has not been thoroughly tested in overdense regions such as filaments. We, therefore, include galaxies belonging to groups detected in the filament (GIF) as part of the filament sample.

From studies of the large-scale matter distribution and superclusters (e.g. Cole et al. 2005, Einasto et al. 2007a), it was found that filaments interconnect regions of high density, like clusters (see Fig. 1.1). In the case of the environment surrounding A1437 we find that the largest overdensity is the cluster itself, with filamentary-like extensions to the South, the East (indicated as B in Fig. 2.12) and to the North East (indicated by A). Our survey size is too small to probe regions further out, but the region marked by A is an interesting overdensity which seems to be made up of four individual groups, one of which is a rich group (ID:22). All four overdensities are $\sim$ 2 Mpc away from each other on-sky. In Fig. 2.13 we consider their normalised velocity distributions as a function of distance from group ID:22. Considering that groups ID:22, 21, 20 all lie within $\sim$ 300 km s^{-1} from each other, we suspect they are in the process of forming a cluster. Compared to the other groups, group ID:8 has a more loosely defined velocity structure and a 555 km s^{-1} mean velocity offset. It is therefore likely not associated with the groups ID:22, 21 and 20. The extension to region B is an interesting overdensity and contains 4 groups along a filamentary structure. The Southerly filamentary extension towards group ID:30 most likely connects to an overdensity outside our survey area. We consider it to be a candidate filament which remains part of the filament sample.

The field galaxy sample was constructed simply by taking the galaxies in the spectroscopic sample over the whole field in the redshift range $0.12 < z < 0.15$ and excluding all the galaxies that belong to a cluster, group or filament. Our final spectroscopic catalogue of galaxies consist of 1647 galaxies in total. 239 of those galaxies belong to the cluster environment, 239 belong to groups, 413 to filaments and 756 to the field. These environments will play an important role in the environmental definitions for the photometric sample.

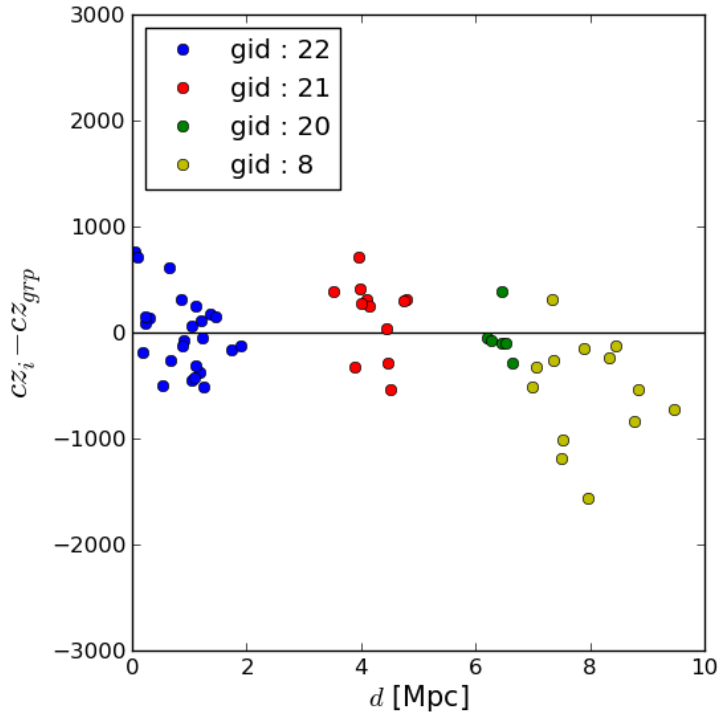

Figure 2.13: The normalised velocity distribution for galaxies in groups ID:22, 21, 20, 8, which lie close to the region marked A in Fig 2.12, shown relative to ID:22. From the normalised velocity distribution it seems like the two groups, 20, 21 and the rich group 22 are most likely a cluster in formation.

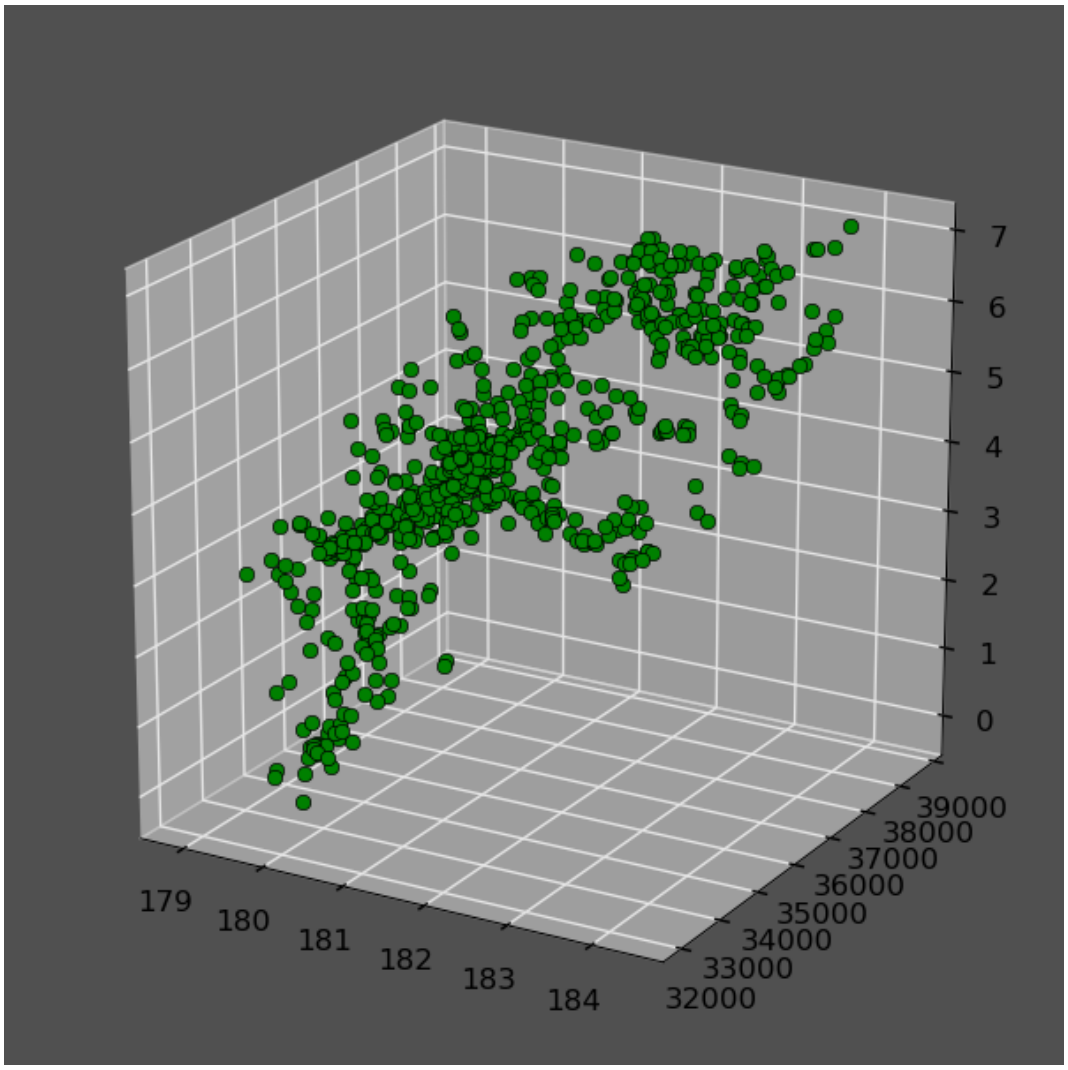

Figure 2.14: 3D distribution of galaxies that were identified with the increased linking lengths in search of filamentary structures.

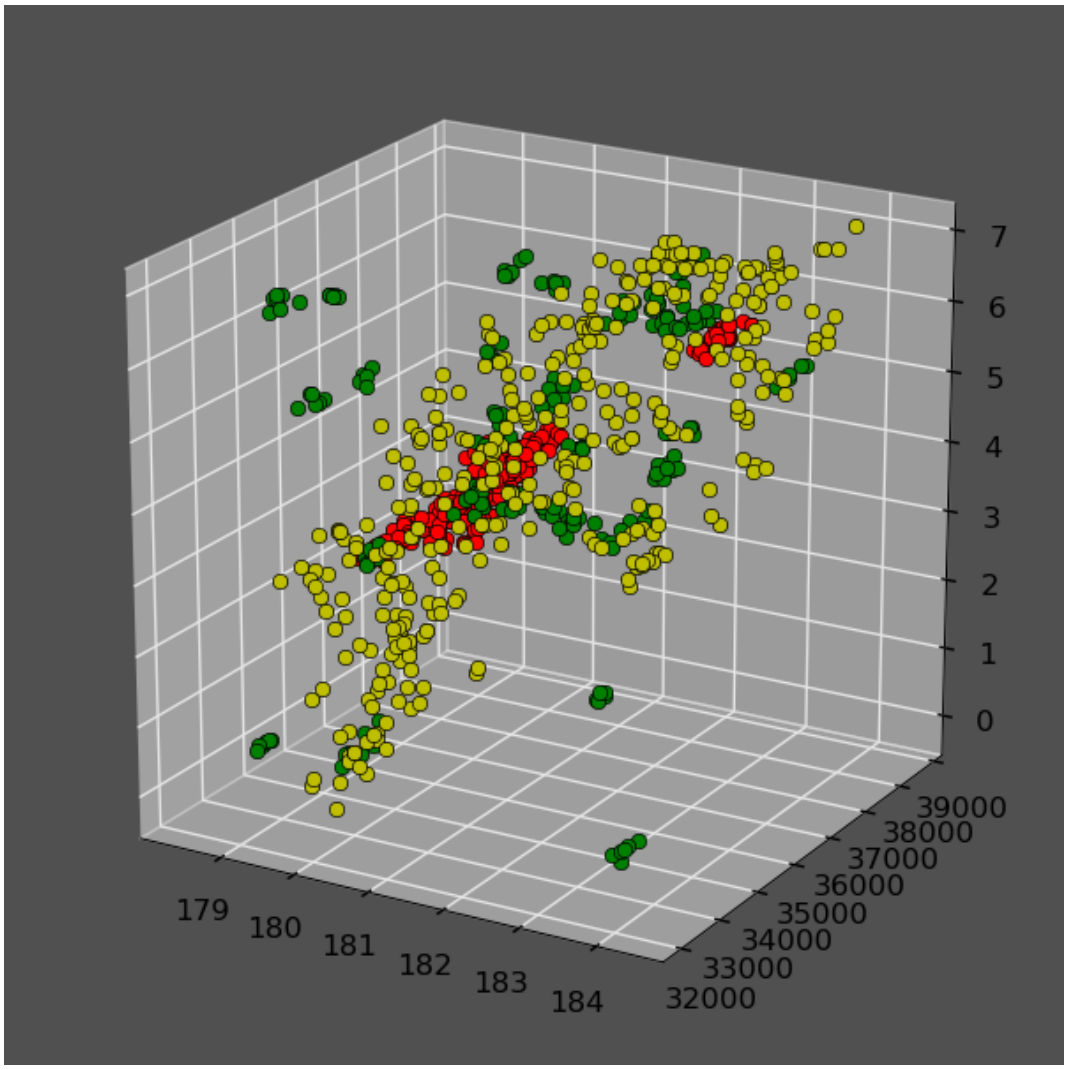

Figure 2.15: 3D distribution of galaxies belonging to clusters, shown in red, groups, shown in green and filaments, shown in yellow.

Chapter 3

Creating a Consistent Multi-Wavelength Dataset

Our aim is to construct a multicolour photometric catalogue for galaxies at the redshift of A1437 to study their properties. To do this we need accurate measurements of position, total integrated galaxy light as well as galaxy colours.

Object catalogues with extracted positions and photometry are available for both imaging surveys. UKIDSS and SDSS both use Petrosian aperture magnitudes as proxies for total integrated light. In theory, we would therefore be able to construct a multicolour catalogue for galaxies in our survey, but in practise it is not as simple. Depending on the physical properties of a galaxy, they appear different as a function of wavelength. This makes object detection and photometry over a large wavelength range difficult to deal with. Although UKIDSS and SDSS both make use of Petrosian magnitudes, the data are taken in different seeing conditions and they use different methods for raw data reduction, object extraction, deblending and photometry. Accurate measures of galaxy colours across the whole wavelength range are therefore not possible when using the catalogue photometry. An important discovery made while in the process of creating the catalogues was the unreliability of the UKIDSS photometric catalogues. A subsequent search through the literature confirmed our suspicions about the UKIDSS catalogue reliability (Smith et al. 2009, Hill et al. 2010). This is discussed in Sect. 3.2.6.

We therefore chose to implement our own photometry pipeline. No raw image processing was necessary. The pipeline was developed for detecting and extracting photometry for objects from which a consistent multi-wavelength seeing matched dataset was created. Figure 3.1 shows a diagram of how the data were obtained and the subsequent processing. The following chapter describes in detail how the multicolour catalogues were constructed.

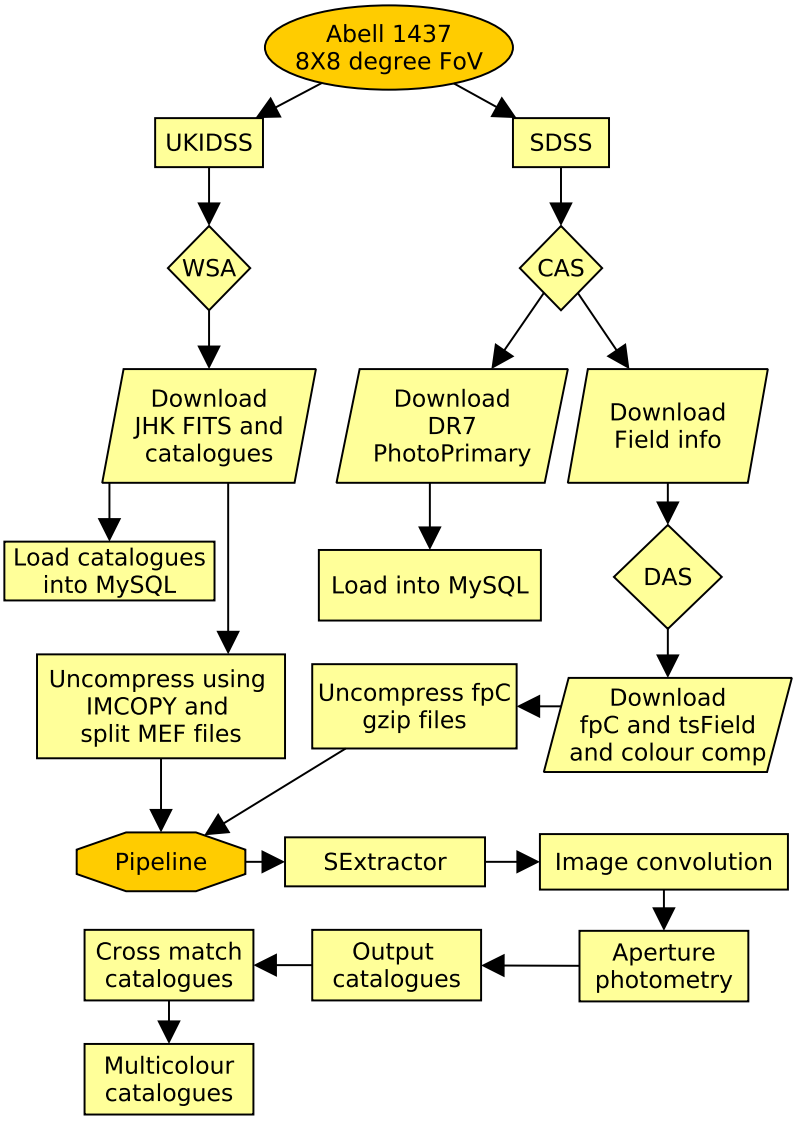

Figure 3.1: A flowchart showing the data flow.

3.1 Summary of Data

3.1.1 UKIDSS

The WFCAM detector consists of 4 detector arrays spaced by 94% in the focal plane. Four separate pointings can be tiled together to cover a 0.75 square degrees Field of View (FoV) with a pixel scale of 0.4 ″/pix. An example of what the detector focal plane looks like is shown in Fig. 3.2. In good observing conditions, WFCAM images can be under sampled, in which case microstepping is performed in an attempt to recover lost resolution. Microstepping is done by repeating an observation after having moved the telescope by an non-integral number of pixels. Output images are created by interweaving all the input pixels over a regular spaced pattern (Casali et al. 2007). Images with a 2×2 microstepping pattern has a pixel scale of 0.2 ″/pix and a 3×3 microstepping pattern produces images with a pixel scale of 0.13 ″/pix.

WFCAM images were downloaded from the WFCAM Science Archive (WSA) as RICE compressed multi-extension FITS* (MEF) files containing 4 extensions, one for each detector. Accompanying data are CASU† generated object catalogues, stored in multi extension binary FITS table format, one extension per detector or chip. Since WFCAM covers such a large FoV, there can be a significant variation in the PSF across the field. The images were decompressed using CFITSIO's IMCOPY and the MEF was split up into four separate images. The seeing variation across a single WFCAM footprint image is negligible; it is therefore more advantageous to handle a single image than the whole WFCAM MEF at once. The MEF catalogue FITS files were also split into separate files and the individual catalogues loaded into a MySQL table.

3.1.2 SDSS

SDSS fpC images are final reduced images used to perform the photometry for the ingestion into the SDSS DAS database. Together with the tsField FITS files one can reproduce calibrated photometry for observed SDSS fields. fpC FITS files have been bias subtracted, flat fielded and cleaned of bright stars. They cover the same $9.8' \times 13.4'$ area in all five filters for a particular field. The files are compressed using GZIP and named as follows: fpC-$run-$filter$camCol-$field.fit.gz, where $run is the imaging run number, $filter is the filter used (u, g, r, i, or z), $camCol is the column location in the imaging array of the CCD which acquired the data (1-6), and $field is the field number within the run. Sky subtraction is not performed on the FITS file, but a fit of the measured sky is stored in the FITS header instead. The tsField files are binary FITS tables which contains the calibration information for each observed field and named tsField-$field-$camCol-$rerun-$field.fit. An initial CAS query was used to return the run, rerun, camCol and field numbers of the images covering

*Flexible Image Transport System
†Cambridge Astronomical Survey Unit: `http://www.ast.cam.ac.uk/~mike/casu/index.html`

Figure 3.2: On-sky configuration of the WFCAM detectors. Taken from: `http://www.jach.hawaii.edu/UKIRT/instruments/wfcam/user_guide/description.html`

our survey area. The images were downloaded with WGET directly from the DAS using the relevant field information.

3.1.3 Overview

The SDSS and UKIDSS imaging coverage over the 8×8 degrees, roughly centered on Abell 1437, is shown in Fig. 3.3. The blue squares are on-sky WFCAM footprints of the UKIDSS K-band imaging coverage and the green squares are SDSS on-sky footprints of the r-band imaging coverage. Regions of overlap or repeat observations are darker shaded. There are regions of incompleteness in the K-band imaging, mostly on the Western side of the survey area. Regions of SDSS incompleteness show as light blue squares and are due to bright star contamination. The average seeing in the $ugrizJHK$ bands are given in Table 3.1 and the

seeing distribution for the u, r and K bands is shown in Fig. 3.4. The seeing in all the bands for most of the survey range between from $0.5''$ to $\sim 2''$. The u band seeing is particularly poor with an average of $\sim 1.4''$. The r and u band seeing distribution both show an extended tail towards higher seeing values and belong to imaging taken in run 000752. There is a sharp drop off in the u band is seeing at $1.8''$, which is the maximum seeing value we will use for image convolution as discussed in Section 3.2.5. Our survey consists of ~ 1080 MEF images in the J, H and K-band, which amounts to ~ 120 GB of images. The SDSS dataset contains a total of 11455 images in $ugriz$, which amounts to 70 GB of imaging data.

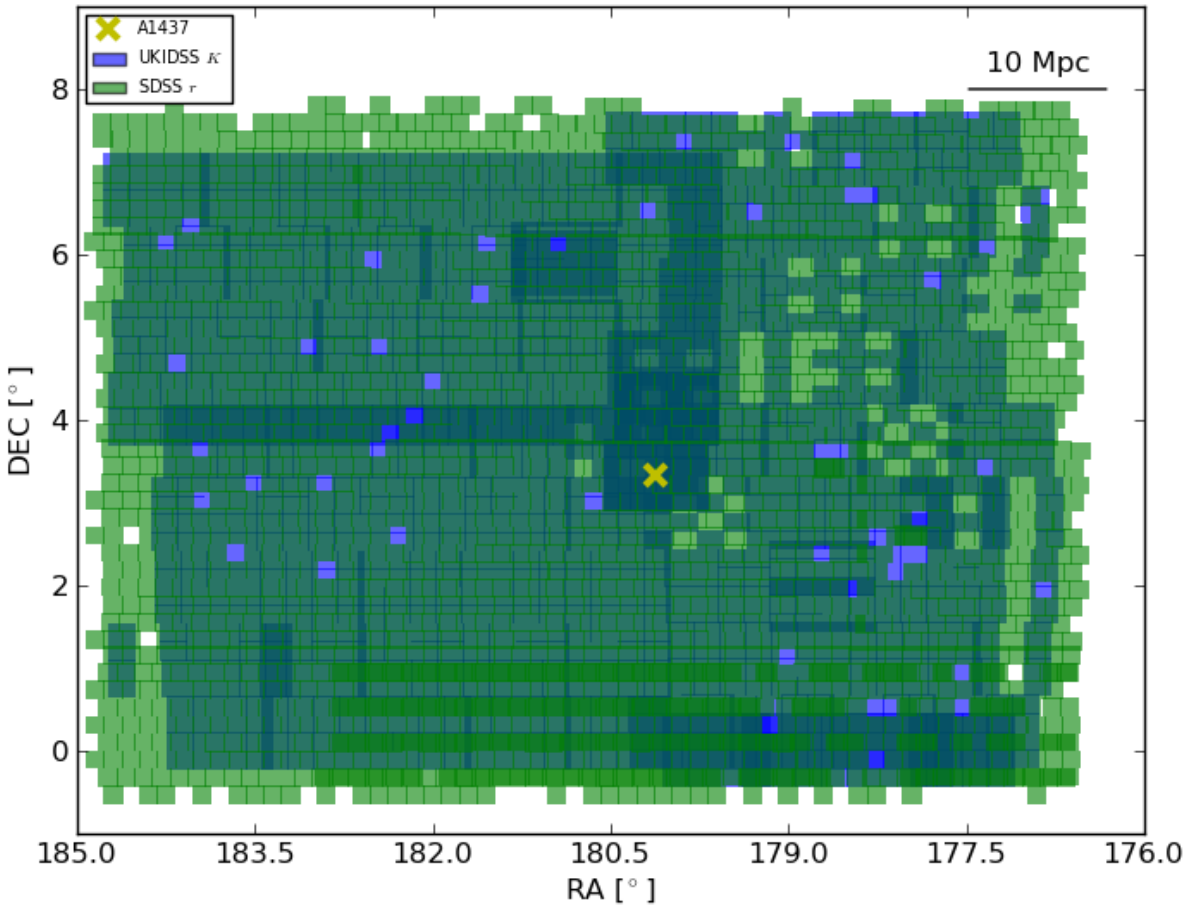

Figure 3.3: On-sky imaging coverage of the K and r-bands show in blue and green respectively. The location of A1437 is indicated by a yellow cross. Gaps in the SDSS imaging are due to bright stars, whereas the gaps in the UKIDSS imaging are due to incompleteness.

Table 3.1: Mean seeing per band for the survey area.

Band	⟨Seeing⟩[″]
u	1.38
g	1.28
r	1.17
i	1.12
z	1.15
J	0.94
H	0.91
K	0.87

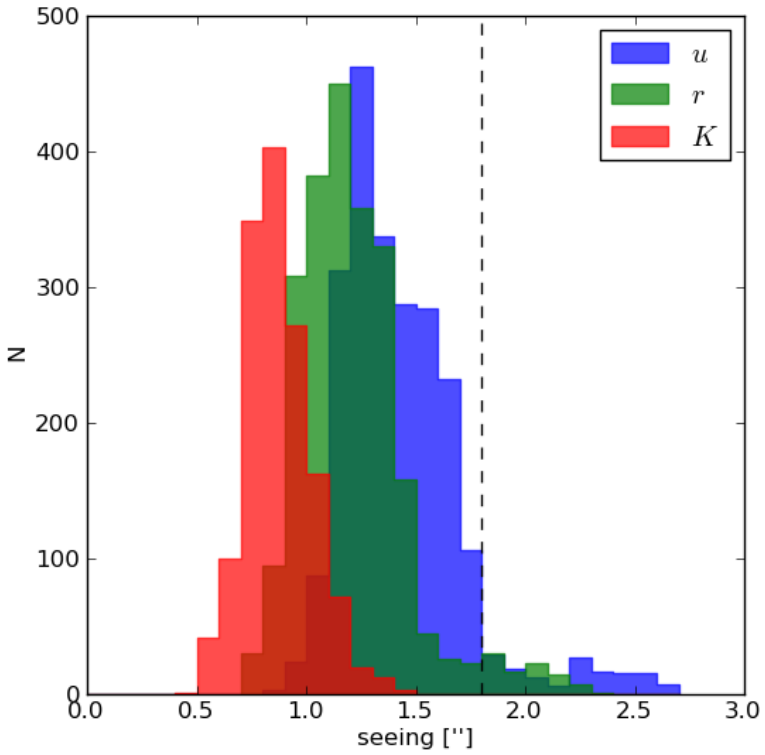

Figure 3.4: The distribution of seeing in the u, r, and K-bands. The seeing convolution value is indicated with a vertical dashed line.

3.2 Object Detection and Photometry

Extracting photometric information from an image is a two part process. Firstly, detecting objects and secondly, measuring the flux from the detected objects, e.g. Irwin (1985). Object detection is usually done by first measuring the background and background noise RMS level. User input specifies at what level pixel values above the background, and how many 'connected' pixels, constitute an object. Secondly, a centroiding algorithm determines the position of the centre of the object. To measure the flux from the detected object, a physical region around the object is defined relative to its centre, called an aperture. Flux from the object is determined by integrating the flux from all the pixels within the aperture and subtracting the background flux level.

Large imaging surveys like UKIDSS and the SDSS have designed their own software for the detection of objects ranging from stars, large nearby galaxies to quasars, and measuring flux from these objects in ways that accommodate the type of data, instrumentation and the final science goals. Other publicly available software to perform photometry usually forms part of an astronomy data reduction software packages like PHOT in IRAF, MIDAS, STARLINK, etc. SExtractor written by Bertin & Arnouts (1996) is stand-alone software developed for the fast detection and extraction of photometry for objects in large images. We have chosen SExtractor and QPHOT to perform the photometry for our survey. SExtractor to provide total magnitudes and QPHOT to determine fixed aperture magnitudes to measure galaxy colours.

For object detection SExtractor determines a background map which is a bi-cubic spline fit to image areas of the size set by the BACK_SIZE parameter. During the background map construction a σ_N (RMS noise) map of the background is constructed. SExtractor then subtracts the background map from the image and considers any pixel above $x\sigma_N$ to possibly be part of an object, where x is the factor above the RMS noise. To be considered an object, it has to consist of more than a minimum number of neighbouring pixels above $x\sigma_N$. x is set with the DETECT_THRESH parameter while the DETECT_MINAREA controls the minimum number of pixels which constitutes an object. Detected objects are then "cleaned" for contamination by neighbouring objects by use of a deblending algorithm before measuring the flux in user defined apertures. More on these apertures follow in Sections 3.2.2, 3.2.3 and 3.2.4.

QPHOT was only used to measure fluxes in fixed apertures. Photometry is performed on objects from an input list of pre-determined object positions from SExtractor. The reason for doing this is clarified in Section 3.3.

3.2.1 Galaxy Surface Brightness Profiles

Accurately measuring the sizes of galaxies is a difficult task. Galaxies typically have concentrated light distributions in their centres which can either decline fast, as is the case with elliptical galaxies, or more slowly as in the case of spiral galaxies. De Vaucouleurs (1953)

found that the light distribution of elliptical galaxies can be described by a mathematical function, know as de Vaucouleurs' law. Subsequently is was also shown that the discs of spiral galaxies are well fit by an exponential function. Sersic (1968) created a generalized form of de Vaucouleurs' law to accommodate any galaxy morphology.

$$I(r) = I_e \exp\left\{-b_n\left[\left(\frac{r}{r_e}\right)^{1/n} - 1\right]\right\} \tag{3.1}$$

where r_e is the half-light or effective radius, I_e is the surface brightness at radius r_e and the constant b_n is chosen such that half the total luminosity is emitted within radius r_e. With $n = 4$, Eq. 3.2 resembles the de Vaucouleurs' law and when $n = 1$ it resembles an exponentially declining light profile. An attempt can be made to estimate the amount lost in the background by fitting a Sérsic profile to galaxies, but even then, the method only works for larger galaxies for which a good fit to the galaxy profile can be established. The gain in accuracy is relatively small compared to other methods which are not affected by the size of the galaxies and are easier and more robust to implement in practise.

3.2.2 Kron Aperture Magnitudes

Kron (1980) developed a definition for a flexible aperture to capture most of a galaxy's flux ($> 90\%$) from the weighted mean intensities of detected objects. An object's geometry and elliptical parameters can be determined from the object's second order moments. The Kron radius is defined as follows:

$$R_1 = \frac{\Sigma R I(R)}{\Sigma I(R)} \tag{3.2}$$

This is not the original definition, but a small modification by Bertin & Arnouts (1996) for the implementation of Kron magnitudes in SExtractor. The Kron flux is measured in an aperture defined by kR_1 where $k = 2$ is used by UKIDSS and $k = 2.5$ by 2MASS. Graham & Driver (2005) found that with $k = 2$ one can expect to recover 90.6% of the total flux of an exponential profile and 87.0% for a de Vaucouleurs profile. We do not attempt to recover any lost flux and expect small systematic underestimates which is a function of profile shape.

3.2.3 Petrosian Aperture Magnitudes

Petrosian magnitudes are computed from the total amount of flux measured within a Petrosian aperture defined by the Petrosian radius (R_P). Petrosian (1976) introduced the Petrosian index as a means to study galaxy evolution, defined as the radius at which the ratio of the local azimuthally averaged surface brightness, to the mean surface brightness within that radius, is equal to 0.2. Most often the flux within $2R_P$ is used to compute Petrosian magnitudes, as is used by UKIDSS and the SDSS.

3.2.4 Fixed Aperture Magnitudes

Kron and Petrosian apertures were designed to be flexible apertures adapting to the size of objects. This makes them ideal for measuring colours for faint sources. Apertures will vary in size as a function of the observed filter for different types of galaxies. We use fixed apertures to make high S/N measurements of galaxy colours. Typically the apertures are smaller or closer to the size of the galaxies themselves ($2''$–$3''$ in diameter). Our fixed apertures were designed to sample the same area for every object in all the filters.

3.2.5 PSF Matching

Since the fixed aperture sizes we use are fairly close to the seeing in the images we need to consider the effects of differences in seeing. The flux measured for a star in $2''$ conditions will be less than the flux measured for the same star in $1''$ seeing conditions. The convolution of the stellar PSF with that of the seeing will broaden the light profile and result in more light from the PSF wings to be lost in the sky background outside the aperture. Survey data taken at different times, will not be seeing matched, as is shown Fig 3.4. Consider the K band seeing distribution for example, which varies by as much as $1''$.
A well-known technique to circumvent this problem is to degrade all the images to the same seeing. This will ensure that there are no inconsistencies when measuring the colours of galaxies and the same galaxy area will be sampled when performing the fixed aperture photometry. One important drawback of this technique is that the degrading of images decreases the brightness limit of the images. This is of particular concern for faint galaxies. Our worst measured seeing is $\sim 2.6''$, which would potentially result in a considerable number of faint galaxies to be lost in the best seeing bands like J, H and K. We have elected to set the maximum seeing degradation limit to $1.8''$. None of the UKIDSS images have seeing worse than $1.8''$. The fraction of SDSS images above the seeing limit is 0.07, 0.05, 0.04, 0.03 and 0.03 for the u, g, r, i and z bands respectively. We do not attempt to modify the seeing for the small fraction of images with seeing $> 1.8''$ and fixed aperture photometry is performed on the images regardless.

The process of seeing degradation involves the convolution of the original image with a 2D kernel to produce an image of the requested seeing. We assume that the seeing within an image follows a Gaussian distribution. Mathematically it has been shown (e.g. Bracewell 1955) that a single Gaussian can be represented as the convolution of two Gaussian distributions:

$$\sigma_f^2 = \sigma_i^2 + \sigma_k^2 \tag{3.3}$$

where σ_f, σ_i and σ_k are the Gaussian standard deviations for the final image seeing, initial image seeing and the convolution kernel respectively. Rearranging Eq. 3.4 we determine the size of the convolution kernel needed to produce the final seeing from the initial seeing:

$$\sigma_k = \sqrt{\sigma_f^2 - \sigma_i^2} \tag{3.4}$$

More detail on the technique we used to perform the image convolution is presented in the Pipeline Sect. 3.3.6. The effect of seeing degradation in our images needed to be quantified. The obvious test is to determine the effect mismatches in seeing have on the photometry of images.

To quantify the loss of stellar flux by degrading an image's measured seeing, we performed photometry on stars for a set of r-band images with a range of initial seeing. All the images were convolved to a seeing of $1.8''$ and the stellar magnitudes re-measured. Figure 3.5 shows the difference in magnitude determined within a $3''$ aperture ($r_{conv} - r$) for stars as a function of difference in final and initial seeing ($seeing_f - seeing_i$). There is a clear trend of the difference in magnitude increasing as the size of the seeing correction increases. Considering that the mean K band seeing is $\sim 0.9''$, a sizeable seeing correction will have to be applied which results in a considerable magnitude difference ($\sim 0.15^{\mathrm{m}}$). The seeing correction was therefore deemed to be a necessary step in the photometry.

As mentioned earlier, we make the assumption that the seeing profile is Gaussian. An additional test was performed to investigate whether this is a valid assumption and does not introduce any systematics in the results. We compared the light profiles of stars for an image with an initial seeing ($seeing_i = 1.8''$) to an image which had been convolved to the same seeing ($seeing_f = 1.8''$). This was done by measuring the radii at which we recover 1%, 5%, 10%, 20%, 30%, 40%, 50%, 60%, 70%, 80%, 90%, 99% of stellar flux for both images. The convolved image had a $0.9''$ seeing correction applied. The comparison between the light profiles for the two images is shown in Fig. 3.6. The comparison shows that for the inner part of the light profile a Gaussian profile compares well with a PSF. At larger radii, however, the wings of the PSF makes an increasingly larger contribution to the total flux compared to the Gaussian profile.

3.2.6 Photometry Checks

During the process of checking the convolution and the configuration of SExtractor, a comparison between the SExtractor- and UKIDSS catalogue Kron and Petrosian aperture magnitudes were made for point sources in a sub-sample of K band images, since point sources should all have the same radial profile. Even though UKIDSS defined their Kron and Petrosian apertures to be flexible circular apertures as well as limiting their size to $6''$, for star-like objects using the same definitions for Kron and Petrosian apertures, the SExtractor results should compare well with the UKIDSS catalogue values.

This is not what we discovered. Figure 3.7 shows a large scatter of $\sim 0.06^{\mathrm{m}}$ which is most worrying. A systematic offset of SEx(K_{Petro}) − CASU(K_{Petro}) $= 0.023^{\mathrm{m}}$ add to evidence that there is a problem. After thorough tests and checks to ensure the quality of our photometry, we concluded that the CASU photometric catalogues cannot be trusted, as discussed below.

As part of our investigation we looked at two randomly chosen K-band images in detail. Figure 3.8 shows the comparison between Petrosian magnitudes for point sources from these K-band images. Panel 1 shows the difference in Petrosian magnitudes (SEx(K_{Petro})

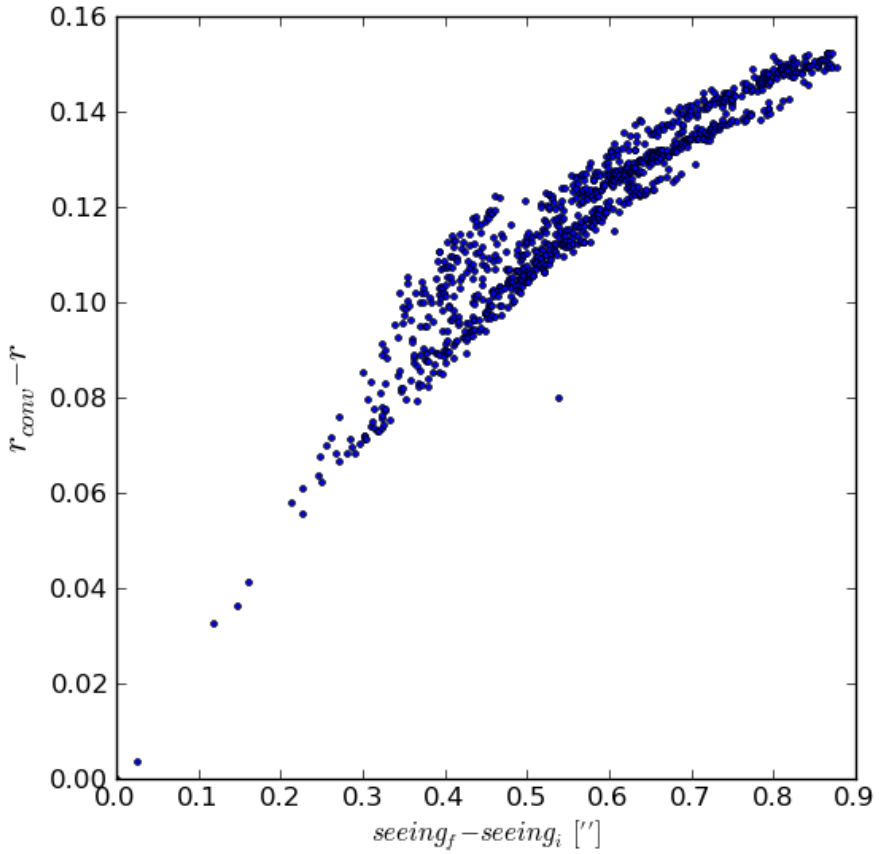

Figure 3.5: The difference in magnitude ($r_{conv} - r$) as a function of the size of the seeing correction ($seeing_f - seeing_i$). This shows that the amount of degradation applied to the seeing almost linearly diminishes the magnitude measured for the same objects in a fixed-size aperture. At the level we need to correct for seeing the decrease in flux becomes significant and therefore needs to be taken into account when measuring galaxy colours. The single outlier is most likely due to the convolution of the image smearing flux from a neighbouring object into the fixed aperture of the star used for the comparison. That would have added additional flux in the aperture and caused the deviation from the observed trend.

− CASU(K_{Petro})), where the dashed line shows an offset of zero and the solid line indicates the measured mean magnitude difference which was found to be $\langle$SEx(K_{Petro}) − CASU(K_{Petro})$\rangle = 0.046^{\mathrm{m}}$. This is larger than the $= 0.023^{\mathrm{m}}$ mean offset found for the whole CASU catalogue comparison, but shows a similar trend. Panel 2 shows the difference in the Petrosian radii (SEx($Petro_{rad}$) − CASU($Petro_{rad}$)) as a function of SEx($Petro_{rad}$). Panel 3 is the distribution of the Petrosian magnitude difference. The dashed and solid lines indicates the same as in Panel 1. Panel 4 shows the distribution of the difference in sky background for the matched objects.

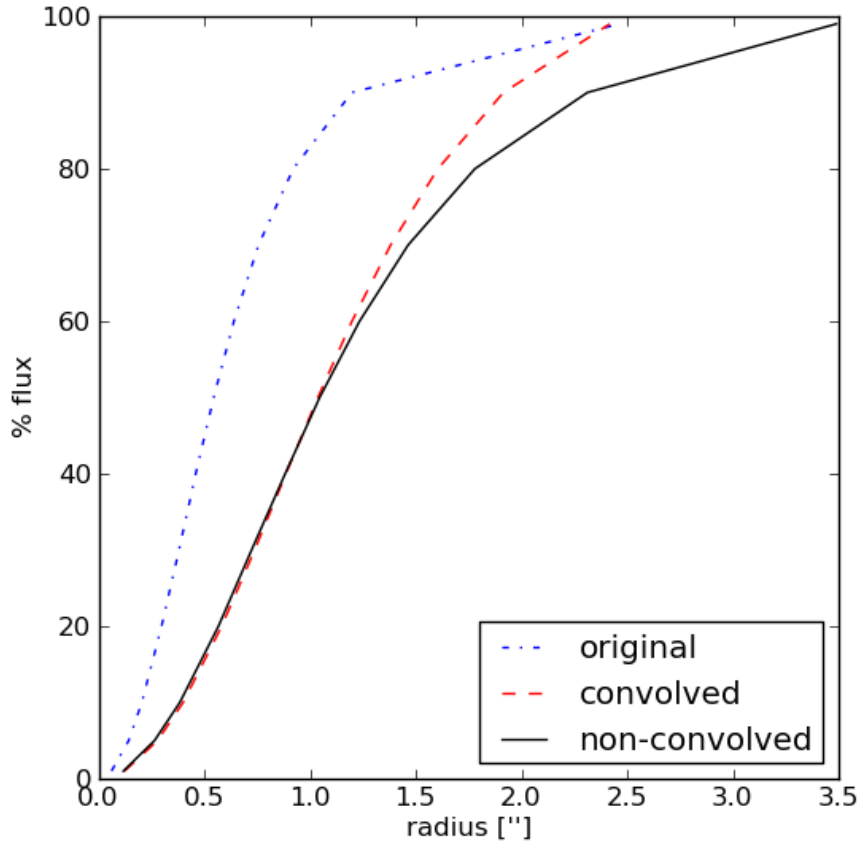

Figure 3.6: A comparison in the flux profiles of an image an initial seeing $seeing_i = 0.9''$ (broken line) seeing convolved to $seeing_f = 1.8''$ (dashed line) and an image with $seeing_i = 1.8''$ (solid line). This clearly illustrates the difference between a Gaussian and a PSF profile. Both the profiles contain the same amount of flux up to a radius of $1''$. For larger radii, the PSF still contain flux in the wings of the profile whereas the Gaussian profile is truncated at smaller radii.

There is clear offset between the two datasets, the SExtractor magnitudes are systematically fainter than the UKIDSS catalogue magnitudes with a mean offset of $\langle \mathrm{SEx}(K_{Petro}) - \mathrm{CASU}(K_{Petro}) \rangle = 0.046^{\mathrm{m}}$. The data are calibrated using the exact same method, ruling out any differences in the way measured fluxes were converted to magnitudes. Panel 2 sheds some light on what the cause of the offset could be. There is strong increase in the difference between Petrosian radii ($\mathrm{SEx}(R_P) - \mathrm{CASU}(R_P)$) as a function of increasing SExtractor Petrosian radius. An example of the different Petrosian radii is shown in Fig. 3.9. There is a magnitude offset for visually similar radii and for larger objects the difference in radii $\mathrm{SEx}(R_P) - \mathrm{CASU}(R_P)$ increases. Figure 3.9 shows no clear indication that a larger difference in radius is associated with a larger difference in magnitude for the stars in the image are all of the same order compared to the range in differences in radii.

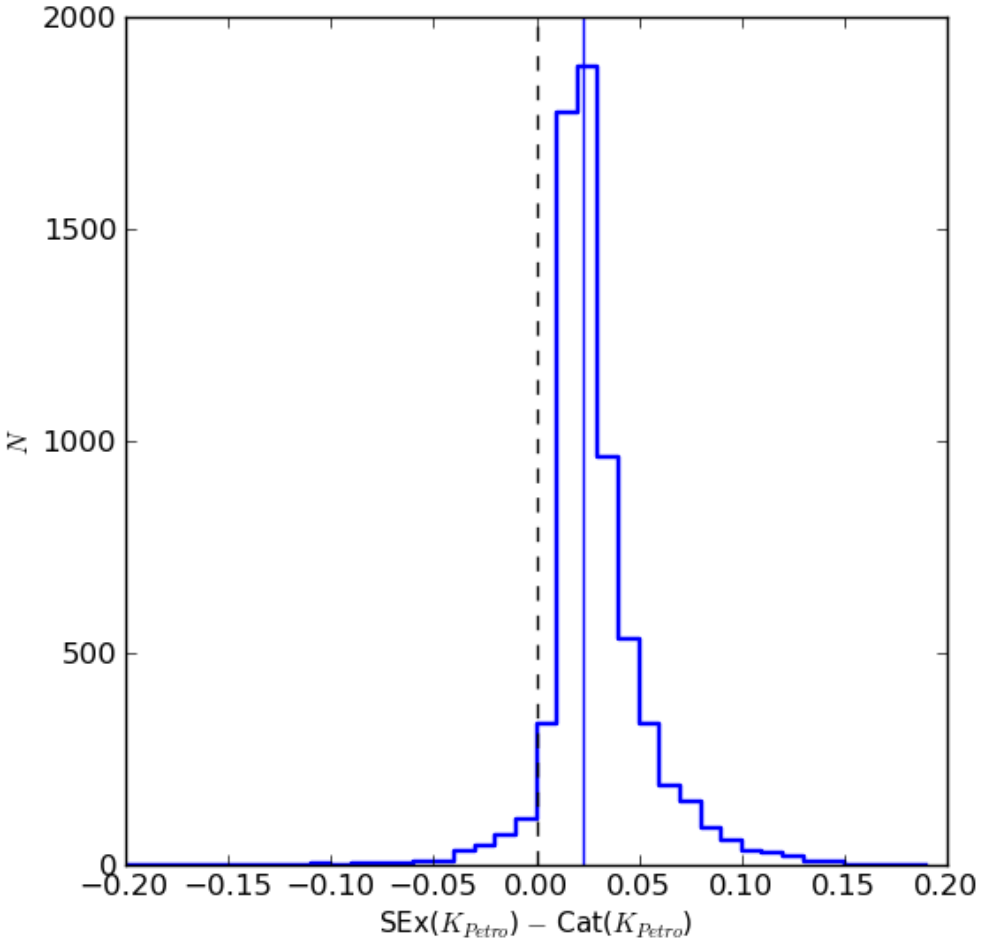

Figure 3.7: The distribution of the difference in SEx(K_{Petro}) − CASU(K_{Petro}) for objects with CLASS_STAR > 0.99 covering the whole K-band imaging sample. The offset is $\sim 0.02^{\mathrm{m}}$ less than in Fig. 3.9 but still significant at SEx(K_{Petro}) − CASU(K_{Petro}) = 0.023^{m}. The dashed line shows an offset of 0 and the solid line indicates the mean magnitude offset found.

Smith et al. (2009), who made use of CASU catalogue photometry during the course of their work, found that deblended galaxies have significantly brighter magnitudes than their parent galaxies. Subsequently a bug in the deblending algorithm was reported but the status of the bug fix is still unknown. Hill et al. (2010) found the same problem with the CASU catalogue and provides a comparison between SExtractor and CASU photometry in their Appendix A1, illustrating the deblending problem. Since there is no way to correct for this failure in the pipeline, Hill et al. (2010) decided to perform the photometry themselves using SExtractor. This supports our findings that the CASU photometry catalogues are untrustworthy and justifies the development of our own photometry pipeline.

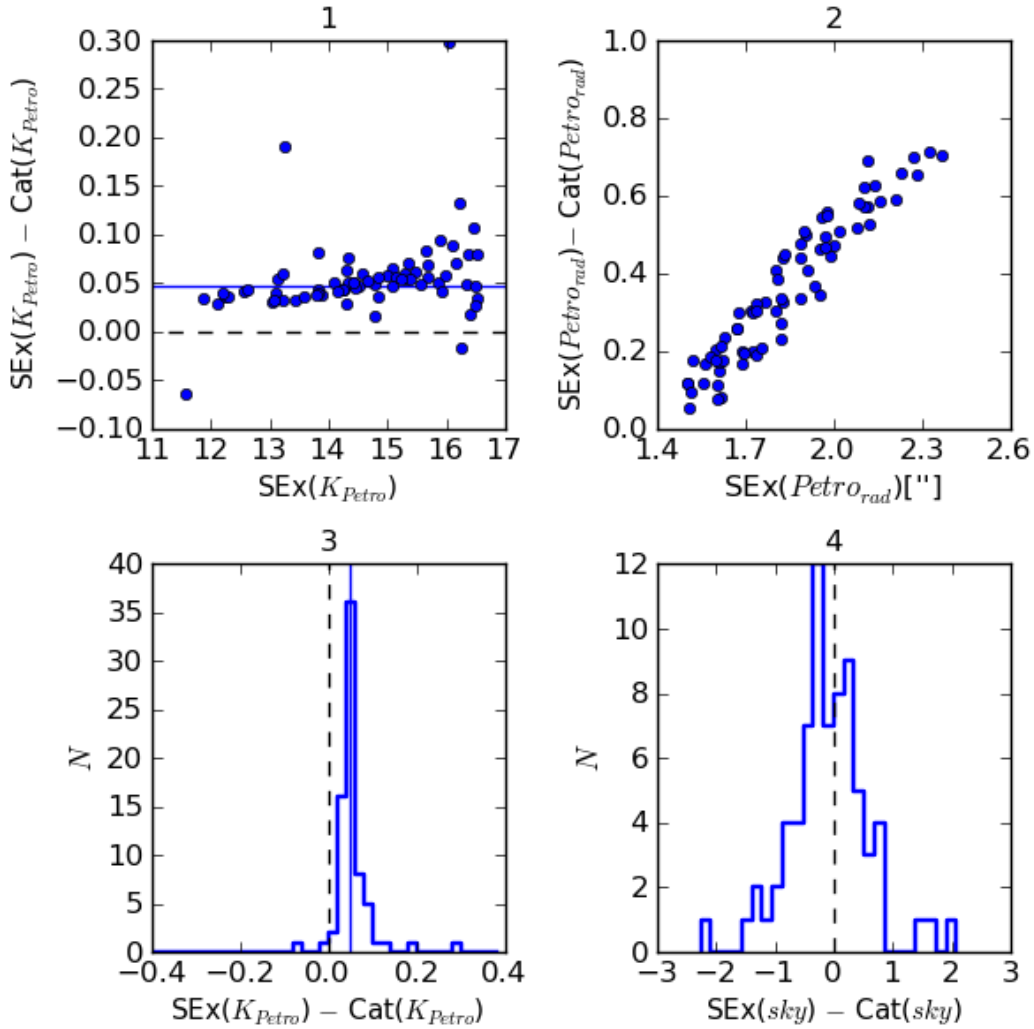

Figure 3.8: A comparison between SExtractor and UKIDSS point sources for two UKIDSS K-band images. Panel 1 shows the difference in Petrosian magnitudes (SEx(K_{Petro}) − CASU(K_{Petro})). The dashed line shows an offset of zero and the solid line indicates the mean magnitude difference which was found to be $\langle \text{SEx}(K_{Petro}) - \text{CASU}(K_{Petro}) \rangle = 0.046^{\text{m}}$. Panel 2 is a distribution of the difference in Petrosian radii in arc seconds (SEx(R_P) − CASU(R_P)). This distribution shows that for most of the stars, SExtractor measured a larger Petrosian radius compared to the UKIDSS pipeline. Panel 3 shows the distribution of magnitude differences, with the dashed an solid lines indicating the same as in Panel 1. Panel 4 shows the distribution of the difference in the sky background values measured for each source (SEx(sky) − CASU(sky)).

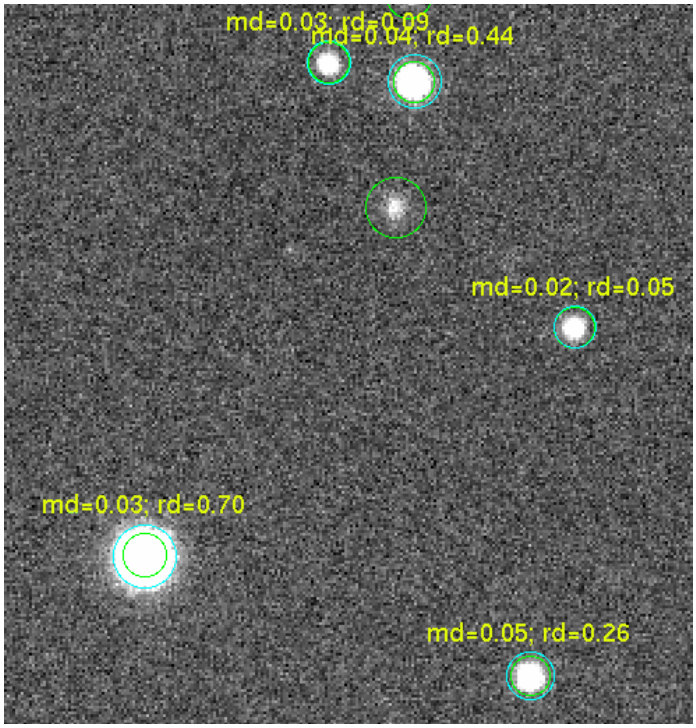

Figure 3.9: A comparison between the Petrosian apertures derived by SExtractor and UKIDSS. The cyan and green apertures are SExtractor and UKIDSS catalogue Petrosian radii respectively. The difference in magnitude is indicated by 'md' and the difference in Petrosian radius by 'rd' (in units of ″). The visual example confirms what was found in Fig. 3.8. Two concerns: for visually similar radii a magnitude offset exists even though UKIDSS claim to use the same definition as SExtractor for determining Petrosian magnitudes; for larger point sources UKIDSS seem to limit their Petrosian apertures, which, from visual inspection, would measure less flux for the same object (star in the lower left corner).

3.3 Photometry Pipeline

SExtractor is used for object detection and total flux photometry while QPHOT is used to perform circular aperture photometry on the convolved images. It is not possible to supply SExtractor with an input list of positions. A master reference image can be constructed, but this is a cumbersome and complicated procedure. QPHOT on the other hand can be provided with list of input coordinates and perform aperture photometry on those positions with little or no allowed shift in centroiding. This guarantees that we sample the same on-sky area in each band which allows us to determine accurate colours. The construction of the positional reference catalogues is described in Section 3.4.1. The reference catalogues contain 420 576 and 547 169 sources for the K and r-band respectively.

Two slightly different photometry pipelines were developed for the UKIDSS and SDSS data. The main difference between the two lies in the way the photometry is calibrated. UKIDSS images are calibrated using photometric zero point offsets derived from 'AAA' quality 2MASS point sources (Skrutskie et al. 2006) which covers our whole survey area. We follow the magnitude zero-point offset correction method described in Hodgkin et al. (2009), which also accounts for differences in filters and detector characteristics, but we deviate somewhat from the spatial distortion correction they apply, which is discussed in Section 3.5.1.

SDSS photometry is calibrated using the meta data contained in the tsField binary FITS tables, which was computed by the SDSS PHOTO pipeline for every observed field.

Several MySQL tables were set up to store the photometry and other important output. Three output catalogues per filter contain the non-referenced SExtractor output and the K and r reference QPHOT aperture magnitudes. Two tables containing the convolution information for the UKIDSS and SDSS images and thousands of tables containing the UKIDSS image calibration information were created. A master UKIDSS image calibration table contains the mean magnitude zero point offset and RA and DEC of the telescope per image. Individual 2MASS source matches per image are stored in separate tables created on the fly which is to be used for the spatial distortion correction.

The flow diagram in Fig. 3.10 illustrates the steps taken in performing the photometry and calibration of a single UKIDSS and SDSS image. Every numbered step in the diagram is described in detail in the text below.

3.3.1 Step 1. Load Images

Read in the image FITS headers, in the case of the SDSS data, the fpC and the tsField FITS files are opened. For UKIDSS images only, the pixel scale and the minimum and maximum RA and DEC of the image is determined by using the WCS information. Output MySQL table names are constructed from the filter name.

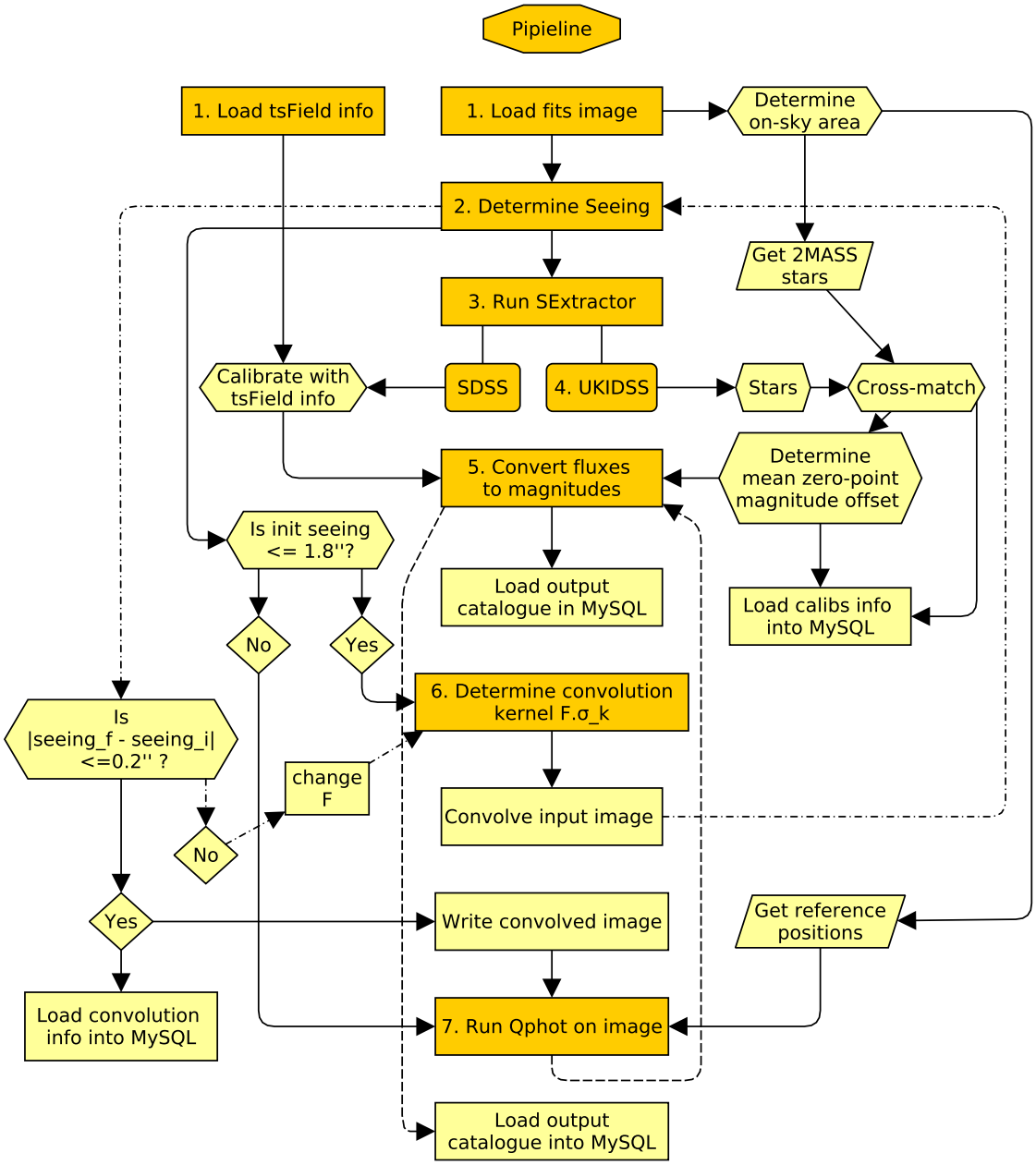

Figure 3.10: A diagram illustrating the pipeline data flow. Enumerated steps are described in the text.

3.3.2 Step 2. Determine Seeing

An accurate estimate of the seeing for each image is important for star/galaxy classification and for performing the seeing correction. It was also found that for some UKIDSS images the SEEING header keyword was an overestimation of the true seeing in the images because of the inclusion of bright close-to-saturated stars in their average PSF calculation. We calculate

the seeing by running SExtractor on the image and using the FWHM_IMAGE output parameter of stars to accurately estimate the seeing. The FWHM_IMAGE is derived from a scaled Gaussian fit to detected objects which is close enough to a PSF for our purposes. SExtractor needs an estimate of the seeing for it to calculate sensible CLASS_STAR values. The CLASS_STAR is SExtractor's object classification parameter based on Neural Network output. It can have a value between 0 (galaxy, non-star) and 1 (star). We use the seeing in the FITS header as an initial estimate, even though it may be inaccurate. This will produce a rough star/galaxy classification but will not affect the FWHM_IMAGE parameter. After running SExtractor on the image, the output catalogue is loaded into an array, from which a robust mean FWHM_IMAGE is determined for objects with a CLASS_STAR value greater than 0.9. If the number of objects with a CLASS_STAR value greater than 0.9 is less than 5, the CLASS_STAR criterion is relaxed by 0.1 until 5 or more objects can be used for the mean FWHM_IMAGE calculation. This was necessary, especially in the u band which suffers from bad seeing. Finally, the mean FWHM_IMAGE is passed back to the main script.

3.3.3 Step 3. Run SExtractor

Fluxes are computed for a range of apertures: Kron (FLUX_AUTO), Petrosian (FLUX_PETRO), FLUX_BEST and circular apertures ranging from $2''$–$10''$ in diameter. Kron and Petrosian fluxes are measured from elliptical apertures defined as $2R_{\mathrm{Kron}}$ and $2R_{\mathrm{Petro}}$, where R_{Kron} and R_{Petro} are the Kron - and Petrosian radii respectively. Additional output parameters are the position angle (THETA_J2000), ellipticity (ELLIPTICITY), full width half maximum of a Gaussian fit (FWHM_IMAGE), a range of radii containing 99% to 1% of the source flux (FLUX_RADIUS), the CLASS_STAR parameter and error flags (FLAGS). The detection limit is set to 1.7σ of the background (DETECT_THRESH) and the minimum number of pixels to constitute an object is set to 4×4 (DETECT_MINAREA). This translates into roughly $3\square''$ for SDSS and non-interleaved UKIDSS images. The BACK_SIZE and BACK_FILTERSIZE was set to 64 and 3 respectively and we set the background subtraction (BACKPHOTO_TYPE) to local mode. The SExtractor output is read into an array and passed back to the main script.

3.3.4 Step 4. UKIDSS-2MASS Source Match

To calibrate a UKIDSS image using 2MASS, we first need to determine an instrumental magnitude for the UKIDSS sources. This is done using a Pogson magnitude $m = -2.5\log(f)$, where f is the flux measured from the SExtractor $4''$ circular aperture. The predetermined RA and DEC limits of the image is used to query the 2MASS point source catalogue (which is stored locally in MySQL) and return stars which lie in that area. Sources with a CLASS_STAR parameter ≥ 0.95 are cross matched with 2MASS sources using a minimum distance criterion of $1.5''$. Magnitude offsets ($m_{\mathrm{2MASS}} - m_{UKIDSS}$) are calculated for each match from which the robust mean magnitude offset (using sigma clipping) is determined.

To investigate the effects of WFCAM field distortions the matched source's information is recorded so that corrections can be applied later. The image name, filter, RA and DEC of the telescope pointing, mean magnitude offset and the standard deviation of the magnitude offset are written to a MySQL table that stores the overall magnitude offset per image. To be able to correct the field distortions as a function of chip position, the array of matched stars is also written to a MySQL table. The table is created on the fly with the image name as the table name. The RA, DEC, x pixel coordinate, y pixel coordinate, instrument magnitude, error in instrumental magnitude, 2MASS magnitude, error in 2MASS magnitude, 2MASS colour, and magnitude offset is written into the table. The 2MASS $J-H$ colour is stored for J and H band images and $J-K$ for K-band images. The mean magnitude offset is returned to the main script to compute apparent magnitudes. An example of the offsets measured for matched 2MASS – UKIDSS point sources is shown in Fig. 3.11. The mean offset and 1σ standard deviation are indicated by the solid and dashed lines respectively.

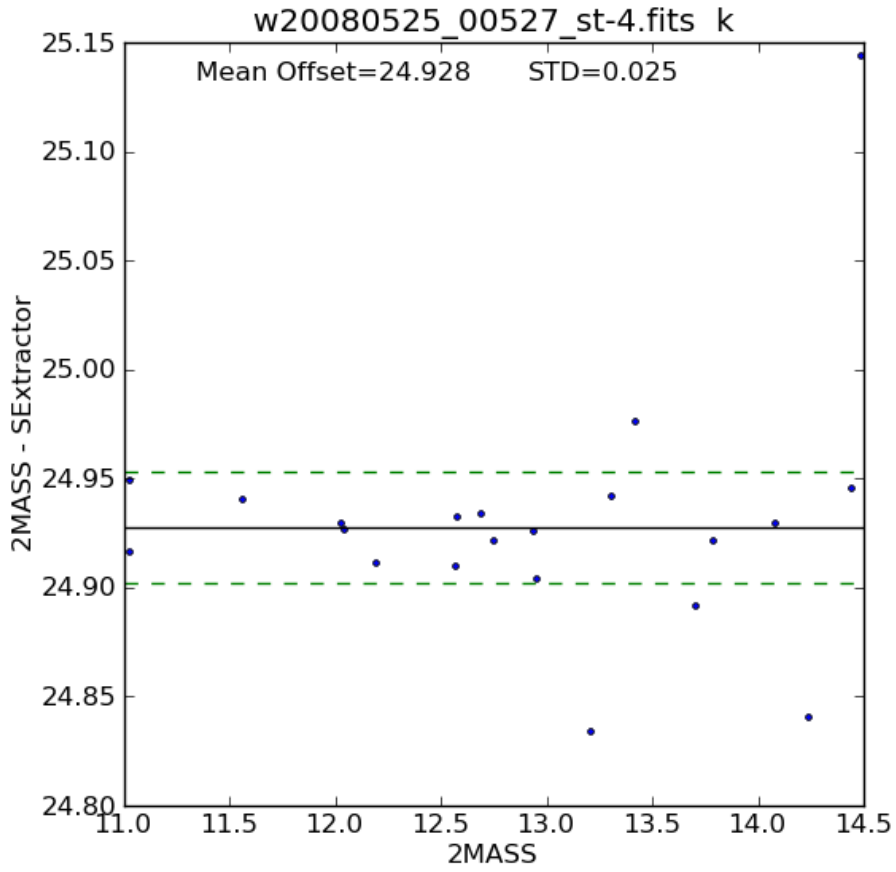

Figure 3.11: An example of the apparent 2MASS(K) − UKIDSS(K) instrumental magnitude offsets measured for matching point sources. The solid line shows the mean magnitude offset and the dashed green lines indicate the 1σ standard deviation range.

3.3.5 Step 5. Convert Fluxes to Magnitudes

The measured fluxes are converted to magnitudes. For the UKIDSS data, apparent magnitudes are computed by:

$$m = -2.5\log(f) + m_{zpt} \tag{3.5}$$

where f is the measured flux and m_{zpt} is the magnitude offset calculated in Sect. 3.3.4. The error in magnitude is computed from the error in flux by:

$$m_{err} = \frac{2.5}{\ln 10}\frac{f_{err}}{f} \tag{3.6}$$

where f_{err} is the measured error in flux.

Calibrated apparent SDSS magnitudes are computed from the measured flux and applying an exposure time and airmass correction as well as a zero point magnitude offset. The flux zero point is given by:

$$f_0 = 10^{-0.5aa} \tag{3.7}$$

where aa is the magnitude zero point. From that the flux ratio can be computed by:

$$\frac{f}{f_0} = \frac{f}{exptime}10^{0.4(aa+kk.airmass)} \tag{3.8}$$

where kk is the atmospheric extinction coefficient. The final calibrated apparent magnitude is computed from the flux ratio:

$$m = -2.5\log\left(\frac{f}{f_0}\right) \tag{3.9}$$

and the error in magnitude is computed, as before, from Eq. 3.6.

The data array containing calibrated magnitudes and all the other SExtractor output is written to the MySQL table.

3.3.6 Step 6. Image Convolution

Convolve the input image to the requested output seeing. Image convolution was performed using a 2 dimensional Gaussian filter from the SCIPY.NDIMAGE package called GAUSSIAN_FILTER. This package takes a 2D array (the input image) and convolves it in both dimensions with a 2D Gaussian kernel defined by σ, which is related to the Gaussian function FWHM by:

$$\sigma = \frac{\mathrm{FWHM}}{c}, \text{ with } c = 2\sqrt{2.\ln 2} \tag{3.10}$$

The initial seeing was determined in step 1 and the final output seeing is set to $1.8''$, we can therefore calculate the size of the convolution kernel using Eq. 3.10:

$$\sigma_k = F\sqrt{\sigma_f^2 - \sigma_i^2} \tag{3.11}$$

where σ_f was determined from the final seeing FWHM and σ_i was determined from the initial seeing FWHM. F is an adjustable parameter and is usually of the order of 0.87 for the UKIDSS and SDSS images. This arises because PSF light profiles have more flux in their wings when compared to Gaussian profiles of the same FWHM, see Fig. 3.5 for an example. However, when fitting a Gaussian to a PSF, the additional flux in the wings of the PSF profile will broaden the Gaussian fit to the light profile and FWHM of the Gaussian profile. The use of F is necessary to ensure that the FWHM of the convolved image is what we expect the final seeing to be and not larger.

We considered SExtractor's FWHM_IMAGE parameter as an estimator of the seeing. The trustworthiness of SExtractor's Gaussian approximation was tested by comparing the FWHM_IMAGE output to IRAF's IMEXAMINE task FWHM (determined from a MOFFAT profile fit) for the same point sources. We found that the two methods produced consistent results, and therefore chose to use the SExtractor FWHM_IMAGE output as a measure of the seeing. Additionally, we found that F was not constant for all images. It was therefore necessary to compute F for each image individually using an iterative method. While the difference in the requested final seeing and the measured seeing is more than $0.2''$, F is adjusted incrementally until the condition $|\text{seeing}_f - \text{seeing}_i \leq 0.2''|$ is met.

3.3.7 Step 7. Fixed Aperture Photometry

IRAF's QPHOT is part of the NOAO - DIGIPHOT - APPHOT package and is used to perform the aperture photometry. Object's fluxes are measured in $1.5''$, $2''$ and $2.5''$ radii apertures. The allowed shift in the centering box is set to 3 pixels so that the photometry is measured from the same on-sky area for all the bands. The inner radius of the sky aperture is set to $10''$ and the outer radius for the sky aperture is set to $20''$. This configuration of the sky aperture was found to be far enough from extended objects to not affect the background sky measurement, but close enough to avoid neighbouring objects being included in the sky background measurement for the majority of objects. QPHOT takes pixel positions as reference, therefore RA and DEC positions from the reference catalogue are converted to x and y pixel coordinates using the WCS object created in step 1 and the python astLib.astCoords package. IRAF's TXDUMP is used to extract the XCENTER, YCENTER, FLUX, MERR, CIER, SIER and PIER for each of the objects. QPHOT does not output RA and DEC coordinates and so the x and y output coordinates are converted back to RA and DEC. The flux measured from the three apertures is converted to magnitudes using the same method outlined in step 5 for the UKIDSS and SDSS data. We use the error in magnitude (MERR) as provided by QPHOT. CIER, SIER and PIER are error flags associated the the centering of objects, background sky determination and photometry of objects respectively. The QPHOT output for every image is loaded into a MySQL table defined by filter, which also contains the reference source ID for every object.

During every step of the pipeline DS9 region files are generated to make visual inspection of resulting detections possible.

3.4 Creating the Photometric Catalogues

3.4.1 Internal Matching - Duplicate Removal

SDSS and UKIDSS overlap neighbouring images to ensure total coverage of their respective survey areas. This results in multiple observations of the same sources as illustrated by Fig. 3.12. A procedure was developed to, firstly, identify duplicate sources. After which, a set of criteria is applied to remove all the duplicate and retain the sources with the best photometry.
From our final SExtractor catalogues we extract the unique catalogue ID, x and y pixel coordinates, RA and DEC, Kron aperture magnitude (MAG_AUTO), error in magnitude (MAGERR_AUTO) and SExtractor error flags to create a temporary catalogue. Duplicate sources were identified from the temporary catalogue using STILTS*, a command line tool designed to deal with tabular data such as astronomical object catalogues. STILTS is used to perform an internal match on our catalogues which assigns a group ID and group size for objects in a $3''$ matching radius. Objects with no duplicates are kept in the catalogue and assigned group IDs and sizes of zero. We end up with a catalogue which contains the original information from the temporary catalogue with STILTS output added for every object.

The temporary catalogue is loaded into a PYTHON script which assigns a keep flag to every object. All the objects with a group ID = 0 is automatically assigned a keep flag = 1. For each group, group members with with SExtractor error flags (FLAGS $\geq$ 7) are excluded. SExtractor produces error flags when encountering certain problems when performing photometry. Every error that occurs has a specific number value and the sum of the numerical error values provides information as to which errors occurred during the extraction of photometry of an object. The errors that sum to a SExtractor FLAG of ≤ 7 are: 1 – The object has bright neighbours, 2 – The object was originally blended with another one, 4 – At least one pixel of the object is saturated (or very close to). The errors that sum to a SEx FLAG of ≤ 7 are not catastrophic and the photometry measurements can still be used.†

Remaining group members then have their error in magnitude compared with each other and the one with the smallest error is assigned a keep flag = 1. If a group only contains members with FLAGS > 7, the member with the smallest magnitude error is assigned a keep flag = 2. The catalogues with keep flags are loaded back into MySQL to create a final reference catalogue of objects. Objects with keep flag = 1 and SExtractor error flags FLAGS ≤ 7 are kept, as well as objects with keep = 2 and FLAGS ≤ 7.

The r and K-band reference catalogues used for the QPHOT aperture photometry were constructed in the same manner outlined above. The pipeline produces three catalogues per band, a SExtractor output catalogue and a two QPHOT fixed aperture magnitude catalogue derived from the K and r positional reference catalogues. Internal duplicate-removal, using the method described above, was performed for each of these tables. With all the duplicates

*Starlink Tables Infrastructure Library
†See pages 71 and 72 of the "Guide To SExtractor" written by B. Holwerda.

removed, the tables can be combined to produce a final multicolour catalogue.

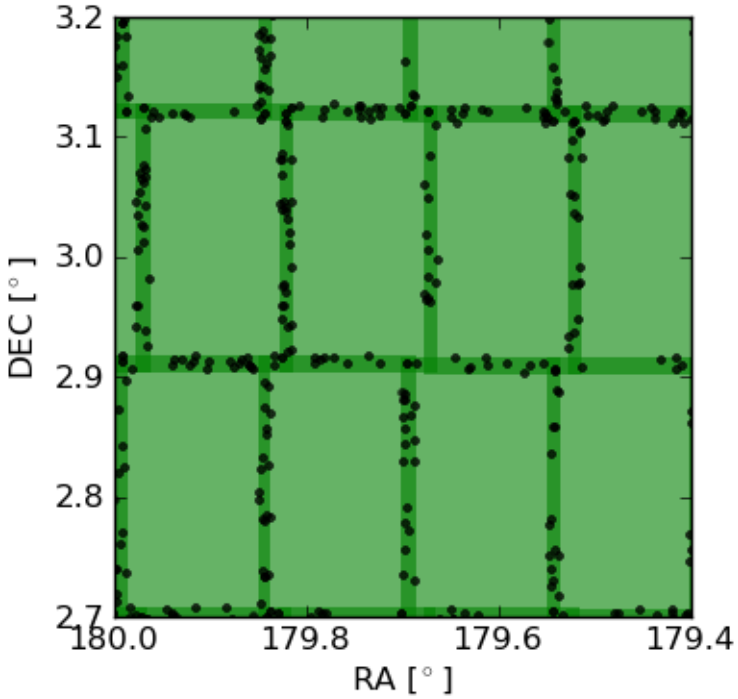

Figure 3.12: An example of duplicate sources in overlapping image areas taken from the r-band images. The green rectangles represent r-band images with the darker green sections indicating areas of overlap. The circles indicate the positions where duplicate sources were identified.

3.4.2 Table Crossmatching - Creating The Master Photometry Catalogue

The master photometry catalogue is constructed from the full SExtractor r and K-band catalogues and the u to K-band aperture photometry catalogues. The r-band catalogue is used as the reference catalogue to which sources in all other bands are matched. A normal table join (crossmatch) produces an output table containing only matched objects. For example, say table A contains 10 elements and table B contains 5 elements. If 3 of the elements match, the output catalogue will contain 3 rows of matched data. If we perform a left join (A left join B), the resulting table will have the same length as A, 10 elements, and contain 3 rows of matched data and 7 rows of unmatched data. This type of table join was used to construct the master catalogue. First, the r and K-band catalogue were joined together using a positional best match within $5''$. From the 561 765 sources in the r-band, 289 312 were matched with K-band sources. Since the reference catalogues were constructed from the SExtractor r and K-band SExtractor catalogues, the aperture catalogues contain

the same unique ID for the same object as in the SExtractor catalogues. The unique source ID is therefore used to left join the aperture photometry catalogues to the r–K matched table. For r-band left-joined sources with no match, a NULL value is assigned for the magnitude in the appropriate filter. The complete catalogue where non-NULL magnitudes are available in every band contains 267 411 sources.

3.4.3 Star / Galaxy Classification

Our star/galaxy separation is based on a combination of the CLASS_STAR parameter and the r-band half light radius. Additionally, the CLASS_STAR discriminator value was essentially calibrated using SDSS spectroscopic information. The CLASS_STAR parameter ranges between 0 and 1, with values closer to 1 indicating star-like objects and values close to 0 indicating galaxy-like objects. There is no prescribed value to discriminate between a star and a galaxy, this is left to the user to decide. We therefore tune the CLASS_STAR star / galaxy separating value by comparing it to the spectroscopic classifications from the SDSS.

We match our r-band catalogue to the SDSS spectroscopic catalogue to obtain the SpecClass value for each of the matched objects. The top panel of Figure 3.13 shows the half light radius, r_e, as a function of $r_{\mathrm{mag\_auto}}$ for the matched objects. Spectroscopically classified stars (SpecClass = 1 and 6) are shown as green star symbols and galaxies are shown as yellow squares. The double stellar locus is a result of stripe 752 having poorer seeing compared to the rest of the r-band imaging. We found that a CLASS_STAR value ≥ 0.9 gave the most comparable results. The comparison between the half light radius distribution for stars as identified from the SDSS SpecClass and objects with a CLASS_STAR value ≥ 0.9 is shown in the middle panel of Fig. 3.13. Differences in the way objects are classified could account for the small differences in the half light radius distributions, SpecClass being a spectroscopic classification while CLASS_STAR being a morphological classification. The application of the CLASS_STAR ≥ 0.9 cut on the entire r-band catalogue is shown in the bottom panel of Fig. 3.13. The bottom panel shows additional objects which were not present in the top panel, they are saturated or close to saturated stars for which the SDSS did not perform spectroscopy. There is a clear division between the saturated stars and galaxies indicated by the dashed line. The equation that best described the line was: $r_{\mathrm{mag\_auto}} = 17.4 - r_e/2.5$. Galaxies are therefore classified as objects with CLASS_STAR < 0.9 and $r_{\mathrm{mag\_auto}} > 17.4 - r_e/2.5$. Applying this criteria to the 267 411 sources with non-NULL magnitudes produced a catalogue of 161 333 objects we classify as galaxies. Note that saturated objects in Fig. 3.13, below the dividing line in the bottom panel, are not present in the top panel since no spectroscopy was performed on these sources.

To quantify how well the star/galaxy classification scheme performs, we consider the method used by Baldry et al. (2010) which is based jointly on an intensity-profile separator and a colour separator. We compute the $J-K$ versus $g-i$ colour–colour diagram in Fig. 3.14 and indicate their equation 3 with a $+0.2$ $J-K$ shift as used for their star/galaxy separator. Baldry et al. (2010) define sources below the line as stellar objects. There is

a very good, 99%, agreement between the CLASS_STAR and colour methods: we find that 1% of the morphologically selected galaxies would be classified as stars based on the colour method. Given the general agreement between the two methods, and that neither method is expected to be 100% accurate (due to e.g. photometric uncertainties), and that the inclusion of 1% erroneously identified galaxies will not alter the ultimate analysis and results, we adopt the intensity profile star/galaxy separator method in all further analysis.

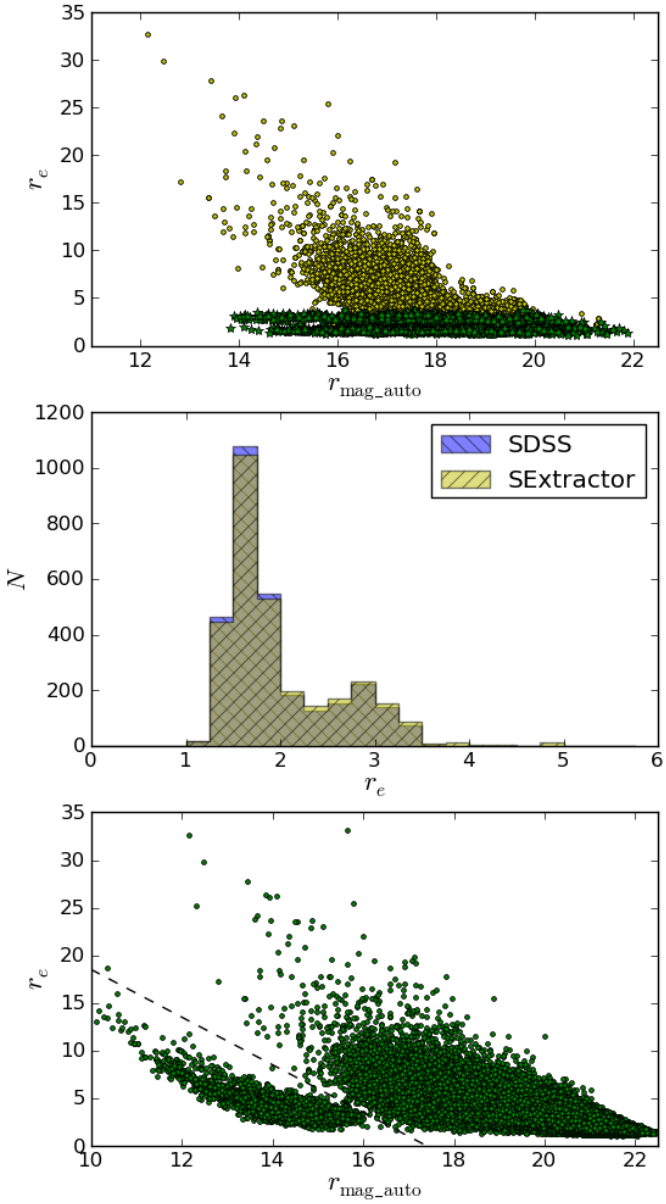

Figure 3.13: Star/galaxy separation for r-band sources, considering the size of objects as a function of magnitude. Top Panel: The green stars represent *spectroscopically* identified stars from the SDSS SpecClass value, while the yellow squares represent *spectroscopically* identified galaxies. Middle Panel: The half light radius distribution for stars as identified from the SDSS SpecClass and objects with CLASS_STAR value ≥ 0.9. Bottom Panel: Sources from the complete r-band *photometric* catalogue with stars removed. The dashed line represents the line $r_{\mathrm{mag\_auto}} = 17.4 - r_e/2.5$ which is the division between saturated stars (left of the line) and galaxies (right of the line).

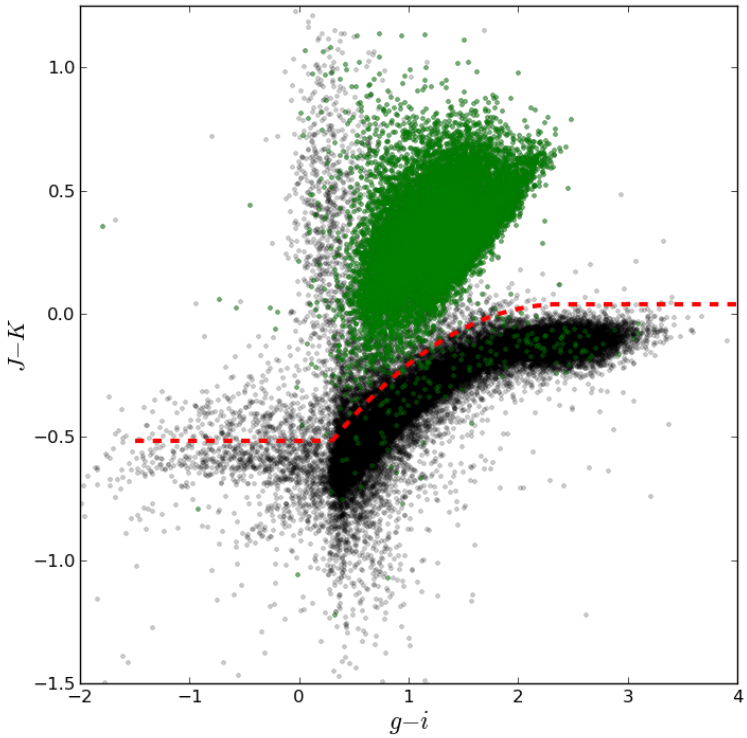

Figure 3.14: $J - K$ vs. $g - i$ is shown for a sample of sources from our catalogue taken in seeing better than $1''$. Those points overplotted with green represent sources classified as galaxies using our star/galaxy classification scheme. The red line represents Equation 3 of Baldry et al. (2010) which was used as the separator between galaxies (above the line) and stars (below the line). We found that 1% of sources we classified as galaxies lie below the Baldry et al. (2010) colour divider.

3.4.4 Survey Area

Calculating the total area covered by an imaging survey involves the calculation of image overlap between neighbouring images and careful book keeping as to how to divide the shared area. Figure 3.3 shows the on-sky footprints of all the r and K-band images which falls in our survey area. There are several areas with more than one observation and sections of missing data. To avoid these complex area computations a method was developed to approximate the total area by using the final source catalogues. The complete on-sky catalogue is sampled using a 2D grid, $30'' \times 30''$, and summing up the number of sources per bin. The 2D grid is then smoothed using a square $3' \times 3'$ kernel. All the 'pixels' with non-zero values are set to a value of 1 and summed. The total number of pixels multiplied by the area of a 'pixel' gives the total area. Since this is only an approximation, the grid is recalculated in random steps of $1'$ shifts in RA and DEC and the area computed for at least 500 realizations. The K-band area was determined to be 58.7□°, the r-band covers 69.5□° and the overlapping area covered by both bands is 57.8□°.

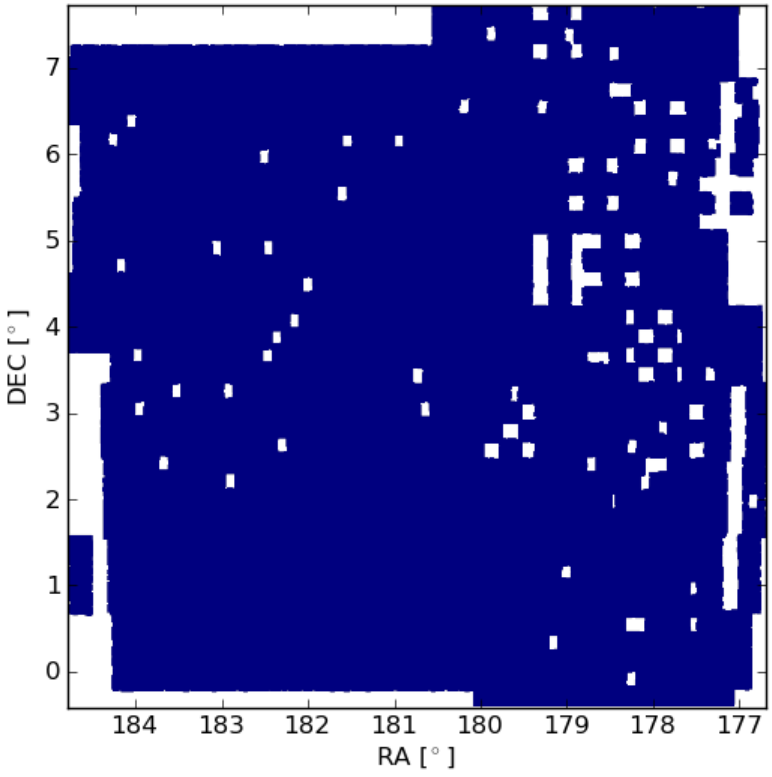

Figure 3.15: The area map of the combined r and K-band sources.

3.4.5 Completeness Limits

It is generally accepted that the Universe is homogeneous and isotropic with a flat geometry which can described by Euclidean geometry. If we make the assumption that fainter galaxies are further away, which is the case for the average galaxy, one would expect the number of galaxies to increase as one goes to fainter magnitudes due to the larger volume is being probed. This is know as the counts–magnitude relation and is usually expressed as:

$$\log(N) = A_\lambda + 0.6m \tag{3.12}$$

where N is the number of galaxies as a function of magnitude, m, and A_λ is dependent on the particular wavelength being observed. The shape of this distribution has been the topic of many studies and is linked to the evolution of galaxies (Glazebrook et al. 1994, Huang et al. 1997, Bershady et al. 1998, Väisänen et al. 2000). Recently, this method for studying galaxy evolution has fallen out of favour due to the sensitivity of the distributions to large scale galaxy distributions. The slope of the distribution has been shown to vary as a function of filter and various other parameters, but the details lie beyond the scope of the thesis. It still is a useful tool to estimate the completeness of photometric surveys. The completeness limit of a sample can be estimated by considering the magnitude at which the sample deviates from the expected number increase. The log of the number of galaxies per 0.5^{m} bin, per deg^2 for the r-band galaxy sample is shown in Fig. 3.16. The galaxies are from the r–K combined area catalogue. A straight line is fitted to the fainter end of the distribution as indicated by the solid blue line. The slope is left unconstrained. A spline is fitted to the faint end of the distribution (solid green line) to compute the 80% completeness as indicated by the vertical dashed line. The r-band completeness limit was determined to be $r \sim 20.6$. As a check of our galaxy classification we compared our results to that of Yasuda et al. (2001) using a Euclidean slope of 0.6 and fitting between the ranges $12 < r < 17$. We found that our $A_r = 5.83 \pm 0.52$ (0.5 mag)$^{-1}$ deg^{-2} is in very good agreement with the $A_r = 5.99 \pm 0.52$ (0.5 mag)$^{-1}$ deg^{-2} that they determined. We performed the same analysis for the K-band data and obtained a completeness limit of $K \sim 16.9$ (Fig. 3.17).

3.5 Catalogue Post Processing

3.5.1 UKIDSS Image Distortion Correction

There is a non-negligible radial distortion correction that needs to be applied to UKIDSS photometry (Hodgkin et al. 2009), with additional chip-to-chip variation between the 4 WFCAM detectors. The chip-to-chip variations are taking care of by calibrating each chip individually in the pipeline. To perform the radial correction we make use of the 2MASS – WFCAM matched stars recorded per image. We determine the radial distance from the centre of the detector for each of the matched stars and compute the mean offset per chip as a function of radial distance (Fig. 3.18). The blue markers are 2MASS−WFCAM offsets

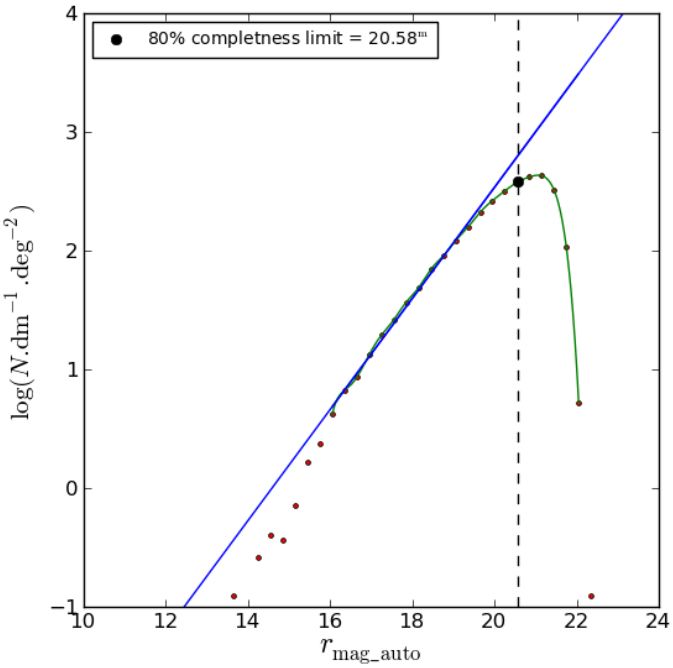

Figure 3.16: r completeness limit computed from the r-band galaxy number counts.

which lie within 2σ of the mean magnitude offset for that particular image. The red dots represent offsets binned in $1'$ bins for which the mean offset is calculated and fitted with a straight line (indicated by the solid red line). The points on the ends are excluded from the straight line fit due to low numbers in the $1'$ bins. The offset between the fitted line and 2MASS−WFCAM= 0 is taken as the radial correction as a function of distance from the centre of the detector. The radial distance for every source relative to the detector centre is computed and the corresponding chip's correction is applied it. Objects from each chip are corrected separately in every band.

Table 3.2: Minimum and maximum magnitude corrections determined for each chip in the UKIDSS filters.

Filter	Chip 1		Chip 2		Chip 3		Chip 4	
	min	max	min	max	min	max	min	max
J	-0.008	0.009	-0.014	0.016	-0.016	0.015	-0.010	0.011
H	-0.016	0.016	-0.013	0.014	-0.007	0.007	-0.012	0.014
K	-0.005	0.005	-0.016	0.019	-0.019	0.018	-0.020	0.02

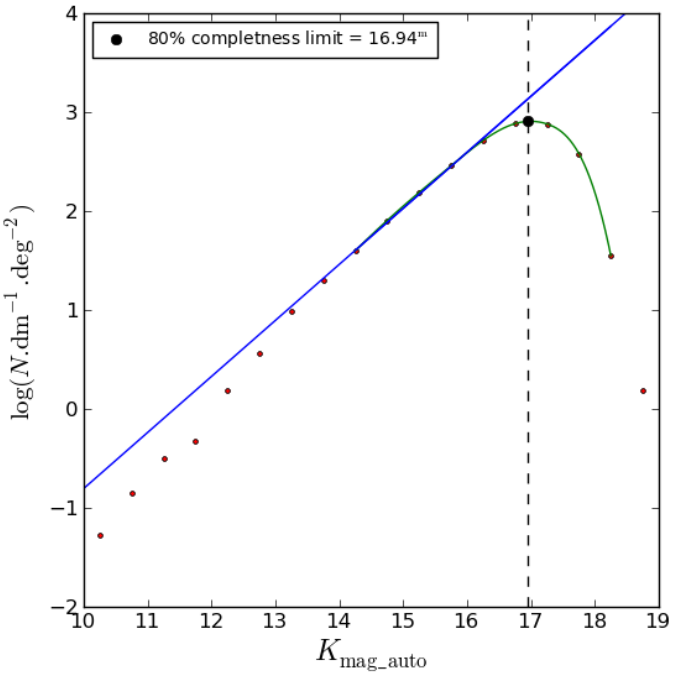

Figure 3.17: K-band completeness limit computed from the K-band galaxy number counts.

3.5.2 Galactic Extinction Correction

Galactic extinction is the attenuation of light by the scattering and absorption of photons due to interstellar dust in our own galaxy. The effect is measured along the line of sight between the observer and object and is wavelength dependent. Our galactic extinction corrections are based on the $E(B-V)$ extinction maps of Schlegel et al. (1998)* and the updated $A_b/E(B-V)$ values from Schlafly & Finkbeiner (2011), where b is the observed band. We make use of the ASTROPHYSICS python library task, obstools.get_SFD_dust, which provides an easy interface to obtain $E(B-V)$ values from the SFD dust maps for each galaxy. The average $E(B-V)$ value for the survey area is $\langle E(B-V)\rangle = 0.021$, the minimum is $E(B-V) = 0.009$ and the maximum value is $E(B-V) = 0.043$.

3.5.3 Vega and AB Magnitudes

The SDSS photometry is calibrated to the AB magnitude system as defined by Fukugita et al. (1996). UKIDSS photometry is calibrated using 2MASS, which is on the Vega magnitude system. Table 3.3 shows the absolute magnitude of the Sun in the SDSS and UKIDSS filters for the AB and Vega magnitude systems. To convert between the two magnitude systems one need only apply the relevant constant offset.

*http://www.astro.princeton.edu/~schlegel/dust/

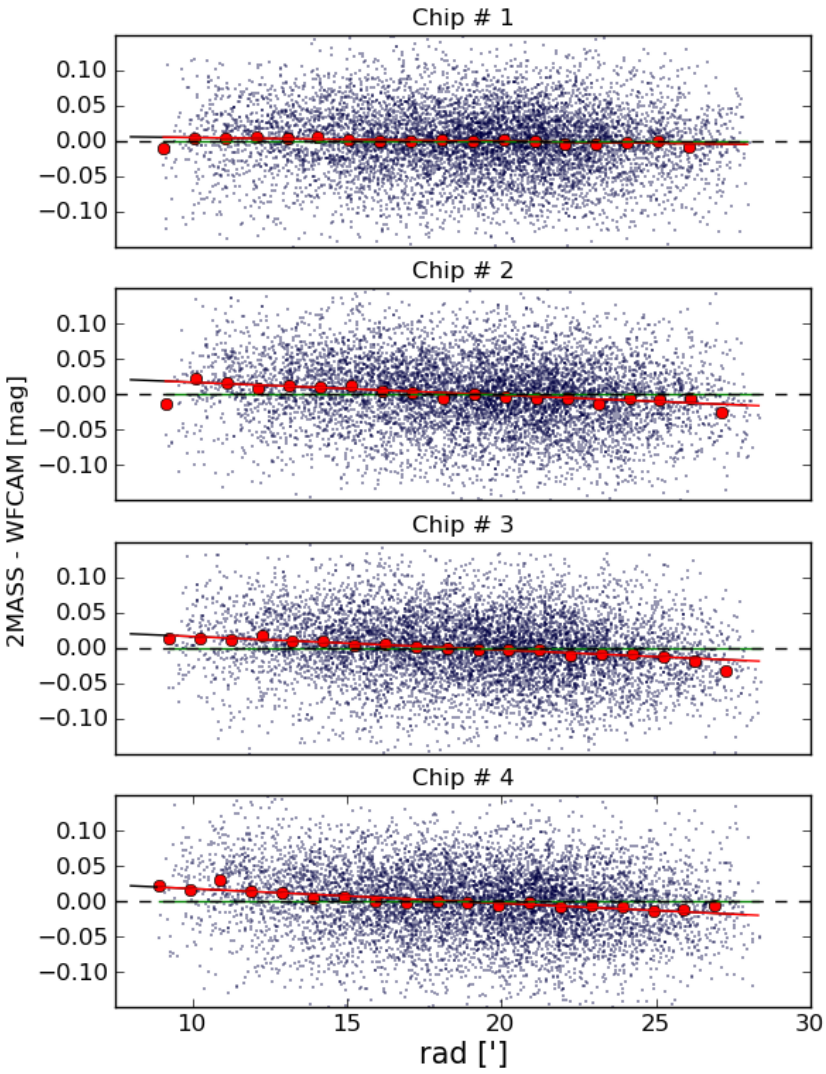

Figure 3.18: The radial distortion correction derived for the for chips in the K-band. The blue markers are the individual offsets determined by the pipeline. The red dots are the mean offsets calculated in $1'$ bins. The red line a straight line fit to the mean offsets with the end points excluded.

3.6 Additional Checks

Sources observed more than once can be used to test the reliability of the photometry. Using the catalogue constructed as part of the duplicate removal, we consider groups identified by STILTS containing 2 members and determine the difference in magnitude between the sources. To avoid using saturated sources, or sources with incomplete apertures, we only consider sources with FLAG = 0. Figures 3.19 and 3.20 show the difference in MAG_AUTO (Δm) versus MAG_AUTO for the r and K-band respectively. The dashed cyan line indi-

Table 3.3: The absolute magnitude of the Sun in the SDSS and UKIDSS filter sets in the Vega and AB magnitude systems along with the central filter wavelengths taken from Hill et al. (2010).

	$\lambda(\mu\mathrm{m})$	$\mathrm{M}_\odot$(AB)	$\mathrm{M}_\odot$(Vega)	$\mathrm{M}_\odot$(AB)$-$ $\mathrm{M}_\odot$(Vega)
u	0.3546	6.38	5.47	0.91
g	0.4670	5.15	5.23	-0.08
r	0.6156	4.71	4.55	0.16
i	0.7471	4.56	4.19	0.37
z	0.8918	4.54	4.00	0.54
J	1.2483	4.57	3.63	0.94
H	1.6313	4.71	3.33	1.38
K	2.2010	5.19	3.29	1.90

cates the mean $\langle \Delta K_{mag\_auto} \rangle$ determined from 0.3^{m} bins. The vertical yellow lines indicates the completeness limits. Note that the r-band data contains close to saturated stars which have high Δm values at bright magnitudes. The mean magnitude offsets at the completeness limit are 0.075^{m} and 0.1^{m} for the r and K-band respectively.

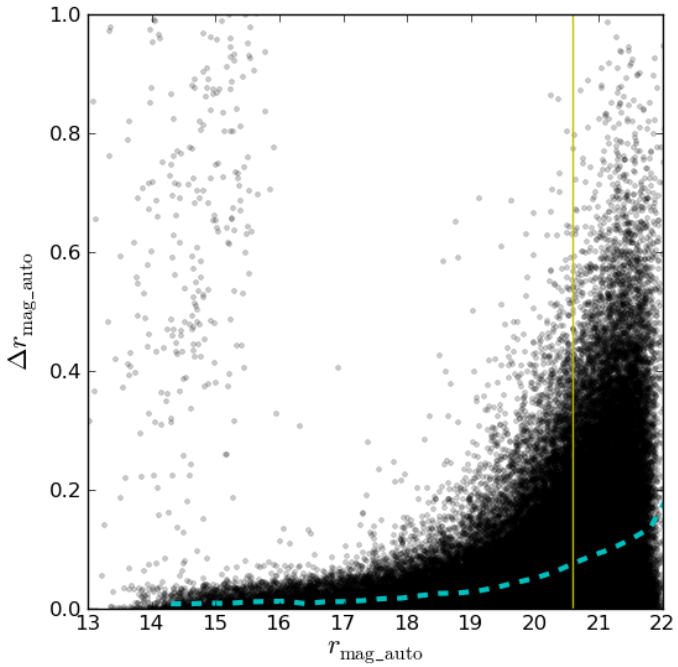

Figure 3.19: r-band photometry reliability shown as the difference in magnitude of overlapping sources. The cyan dashed line represents mean magnitude offsets determined from 0.3^{m} sized bins. At the completeness limit the mean offset is $\langle \Delta K_{mag\_auto} \rangle = 0.075^{\mathrm{m}}$. The sources with large ΔK_{mag_auto} at bright magnitudes are bright stars.

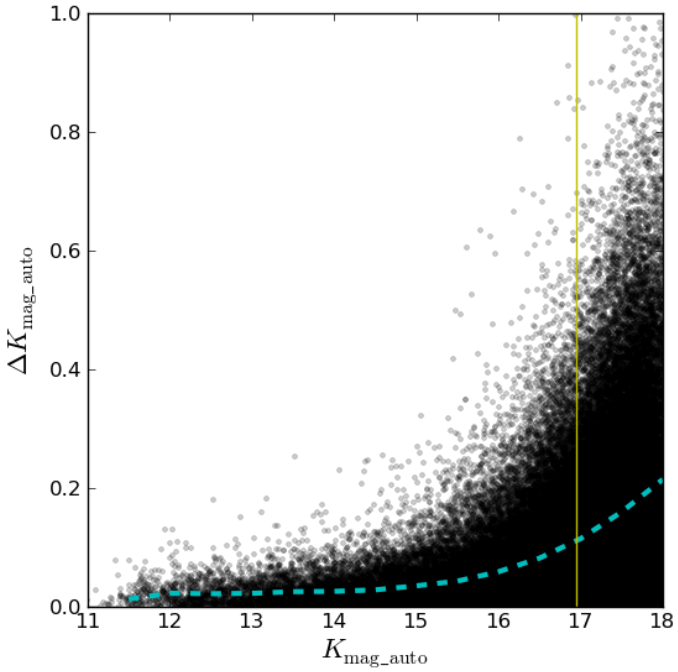

Figure 3.20: K-band photometry reliability shown as the difference in magnitude of overlapping sources. The cyan dashed line represents mean magnitude offsets determined from 0.3^{m} sized bins. At the completeness limit the mean offset is $\langle \Delta K_{mag\_auto} \rangle = 0.1^{\mathrm{m}}$.

The entire photometric sample is based on r-band detections as reference. It is therefore important to know how the derived completeness limits affect the final source catalogue. Additionally, we aim to make use of the K-band photometry to calculate stellar mass estimates. To enable us to perform a statistically sound and unbiased analysis when using a K-band selected sample we need to apply the K-band completeness limit as well. The effect on the final galaxy catalogue when applying both the r and K-band completeness limits is shown in figure 3.21. The grey circles represent the $r_{ap} - K_{ap}$ colour versus K_{mag_auto} for our 161 333 galaxies. The diagonal and vertical black solid lines indicate the r and K-band completeness limits respectively and the dashed yellow line show the r-band spectroscopic limit of $r = 17.7$. The blue circles are 2dF spectroscopic members of A1437 and the magenta triangles are SDSS spectroscopic members indicating the red sequence of the cluster. The location of the red sequence is redshift dependent and since most of our analysis will take place at $z = 0.135$, it is important to note that the completeness limits do create a selection bias on the expected colours of galaxies at the cluster redshift. The K-band completeness limit cuts off galaxies at the faint end of the spectroscopic sample, but the effect is small, of the order of 5% of the total spectroscopic sample. The application of the r-band completeness limit decreases the galaxy sample by 55% to 86 709 galaxies, additionally, the K-band completeness limit decreases the sample by a further 10% to 72 205 galaxies.

One additional feature to note in Figure 3.21 is the location of the 2dF galaxies marked with red circles. These galaxies lie at the redshift of the cluster but have $r_{ap} - K_{ap}$ colours redder than the red sequence we expect normal galaxies to have. This has also been noted by previous studies (e.g Jensen & Pimbblet 2012). These galaxies all have redshift errors $\sigma_z < 0.0015$ with photometric errors less than 0.01^{m}. To provide further insight, we took a look at the colour SDSS finding chart images for these sources, shown in Fig. 3.22. At least three of the galaxies (a, c and e) appear to have spiral like morphologies. The other galaxies appear to be quite small and of low mass. A possible explanation for their red colour could be internal dust extinction due to star formation (Wolf et al. 2009a). We will return to these interesting galaxies in a Chapter 5.

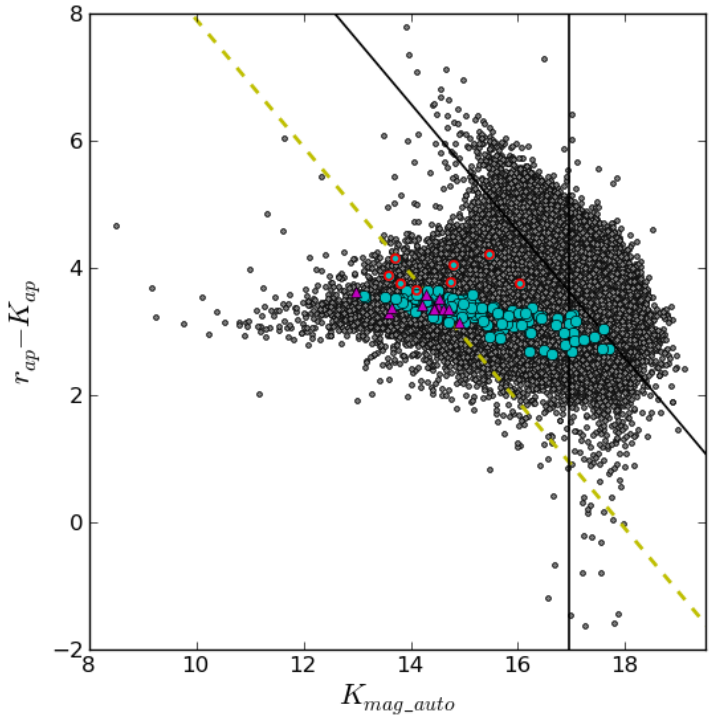

Figure 3.21: $r_{ap} - K_{ap}$ vs. K_{mag_auto} for the complete galaxy sample. The blue circles are galaxies that belong to A1437 at the redshift of the cluster ($z = 0.134$) and indicate the red sequence. There are ~ 8 cluster galaxies with $r_{ap} - K_{ap}$ colour redder than the red sequence marked with red circles. An inspection of these galaxies using the SDSS finding chart tool* show red galaxies with spiral like morphologies and Hα emission.

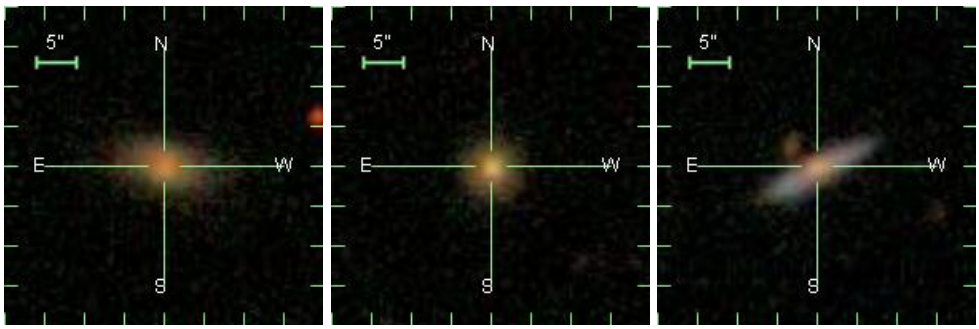

(a) (b) (c)

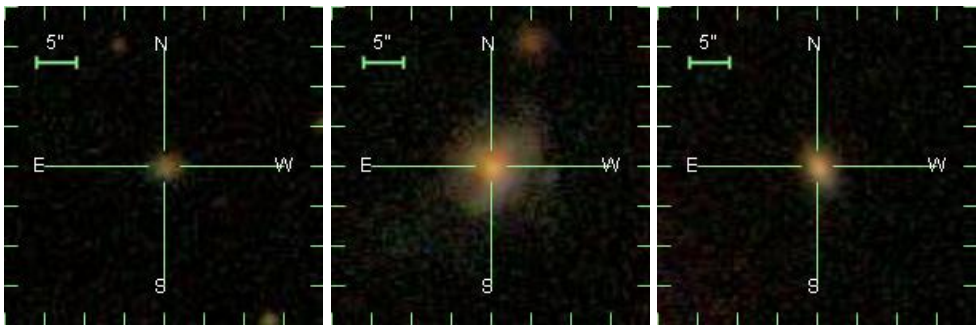

(d) (e) (f)

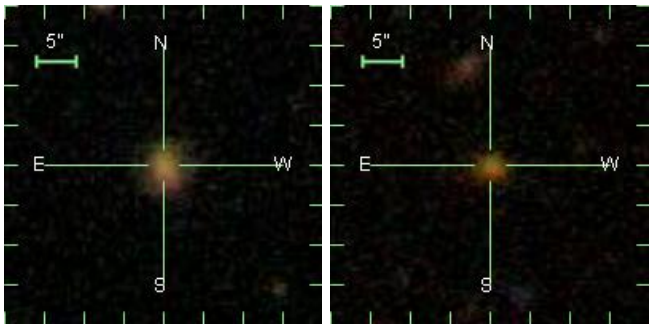

(g) (h)

Figure 3.22: Galaxies identified as having $r_{ap} - K_{ap}$ colours redder than the red sequence at the redshift of the cluster.

3.7 Summary

We have constructed a multi-colour catalogue of galaxies from SDSS *ugriz* and UKIDSS *JHK* imaging. This was accomplished by a pipeline written to perform accurate, seeing matched photometry on all the images. All aspects of constructing such a large multi-band catalogue were thoroughly tested during which time we discovered discrepancies with the UKIDSS CASU source catalogues. We have clearly shown that the CASU source catalogues are unreliable and that performing and calibrating photometry on the UKIDSS data ourselves was necessary.

The completeness limits derived for our sample are $r = 20.6$ and $K = 16.9$. Average photometric errors in the r and K-band are 0.03^{m} and 0.05^{m} respectively.

*`http://cas.sdss.org/dr7/en/tools/explore/obj.asp`

Chapter 4

Tests of Photometrically Derived Properties

In this chapter we test the quality of photometrically derived properties, in particular, stellar mass and star formation rate. The quality of derived properties is assessed by comparing them with spectroscopically derived quantities which are known to produce more accurate results. To perform the tests we use the spectroscopic FoF catalogue in the redshift range $0.12 < z < 0.15$.

A major component in the derivation of stellar masses and SFRs is the use of stellar population synthesis (SPS) models. An introduction to the inner workings of SPS was provided in Chapter 1. In this thesis we make use of the MAGPHYS SED fitting code to derive accurate stellar masses and star formation rates. The code is based on the Bruzual & Charlot (2003) and da Cunha et al. (2008) SPS models, discussed in more detail in Sect. 4.1.2. The rest of the chapter focusses on testing the MAGPHYS derived stellar masses and SFRs to those obtained using other methods, in particular methods employed by Bell et al. (2003), Kauffmann et al. (2003a) and Brinchmann et al. (2004).

We end the chapter by characterising the SDSS photometric redshifts for our sample and compare stellar masses and star formation rates derived from photometry to those derived from spectroscopy.

4.1 Stellar Mass Estimates

The important link between a galaxy's stellar mass and various other global properties e.g. luminosity, restframe colour, size, structure, SFR, mean stellar age, metallicity and local density have been discussed previously in Sect. 1.8. Stellar mass is essential in the study of various galaxy properties. Our aim in the following section is to test various methods of determining stellar masses which would ultimately lead to the method we chose to apply to our photometric galaxy sample.

4.1.1 Methods For Estimating Stellar Mass

All modern stellar mass-to-light ratio, M_*/L, estimates depend on fits to stellar population synthesis models as described above. The techniques vary from simple colour measurements (e.g. Brinchmann & Ellis 2000, Bell & de Jong 2001, Cole et al. 2001, Papovich et al. 2001, Bell et al. 2003), to UV, optical to IR SED fits (e.g. Franzetti et al. 2008, Walcher et al. 2008), to spectroscopic measurements of spectral absorption features (e.g. Kauffmann et al. 2003a, Gallazzi et al. 2005) to using the full optical spectrum (e.g. Panter et al. 2004, Cid Fernandes et al. 2007, Tojeiro et al. 2007). The aim of these techniques is to quantify the mass contributions of the older stellar population, which has been monotonically build up during the age of the galaxy, and the contribution of any recent star formation.

Our goal is to derive reliable stellar masses for galaxies in our photometric sample. The spectroscopic data afford us the opportunity to test and compare results to previous studies. Bell & de Jong (2001), Kauffmann et al. (2003a) and Brinchmann et al. (2004) derived stellar mass estimates from SDSS data using a colour estimate, spectral information and *ugriz* SED fitting respectively. We therefore only consider the methods and results from these authors, as it pertains to our dataset.

Colour Based Stellar Mass Estimate

Bell & de Jong (2001) showed, assuming various star formation histories, that the stellar M_*/L ratio is tightly correlated to the observed colour in optical bands. They found that $\log(M_*/L)$ can be approximated by:

$$\log\left(\frac{M*}{L_\lambda}\right) = a_\lambda + (b_\lambda \times \text{colour}) \tag{4.1}$$

where a_λ is the zero point and b_λ is the colour coefficient dependent on the band from which the luminosity is determined. The colour term, which is sensitive to SF, acts to correct the contribution of current SF to the overall luminosity of the galaxy. Most of the luminosity comes from a low number of high mass stars, which do not contribute to the total stellar mass significantly. The slope, b_λ, is fairly insensitive to the assumed IMF and dust reddening. The zero point, a_λ, on the other hand, depends critically on the shape of the IMF at the low-mass end, which contributes most to the stellar mass. Bell et al. (2003) present a range of a_λ and b_λ values for deriving stellar masses using the SDSS *ugriz* and 2MASS K-band. These coefficients were derived from a model grid created by the PÉGASE synthesis models (Fioc & Rocca-Volmerange 1997). They use continuous SFHs of the form:

$$\psi(t) \propto e^{-\gamma t} \tag{4.2}$$

where γ is the star formation time scale from the formation time t_{form}(Gyr) to the present. They adopt a 'diet' Salpeter IMF (Bell & de Jong 2001) and use only models of solar metallicity.

Stellar Mass Estimates From Spectral Indices

Kauffmann et al. (2003a) made a further refinement to the colour based stellar mass estimate by Bell et al. (2003) and used spectral information to derive the mass contribution of recent star formation more accurately. They show that the two spectral features, the Balmer 4000Å break strength, $D_n(4000)$, and the Balmer absorption-line index Hδ can be used to constrain the amount of stellar mass added by recent star formation (within the last $\sim$2 Gyr). $D_n(4000)$ is an indicator of mean stellar age and Hδ absorption is an indicator of recent star formation activity. They compared their z-band derived M_*/L_z to a set of models to characterise the stellar age and any recent star formation which would lead to a correction of the observed M_*/L_z from the derived dust attention and burst mass fraction.

Their models were derived from the Bruzual & Charlot (2003) (BC03) evolutionary synthesis models. A stochastic SFH prescription is used, whereby random bursts of SF are superimposed onto continuous star formation rates. They adopted a Kroupa (2001) IMF and used metallicities ranging from 0.25 $Z_\odot$ to 2 $Z_\odot$.

Brinchmann et al. (2004) made a further improvement to the Kauffmann et al. (2003a) method by adding nebular line stellar diagnostics. They use the ratio of Hα/Hβ to better constrain dust attenuation, the effect of which have been shown to cause large uncertainties in M_*/L (e.g. Fontana et al. 2004, Pozzetti et al. 2007, Poggianti et al. 2008, Zibetti et al. 2009).

Stellar Mass Estimates From SED fits

Imprinted on a galaxy spectrum is the contribution of various physical processes taking place in different wavelength regimes. Detailed fitting of the full SED should therefore lead to better estimates of a galaxy's properties. There are a number of publicly available codes that fit SEDs ranging from the UV to the NIR: e.g. STARBURST99 (Leitherer et al. 1999); GALEXEV (Bruzual & Charlot 2003); GALEV (Kotulla et al. 2009); PÉGASE (Fioc & Rocca-Volmerange 1997). A number of prescriptions for fitting model SEDs to the observed galaxies exists in the literature, of which the technical aspects lie outside the scope of the thesis. The SED fitting technique we employ is based on a Bayesian approach to parameter estimation. For a given observed galaxy, a likelihood distribution of physical parameters is constructed by evaluating how well each model in the library represents the observed properties of the galaxy. The underlying assumption is that the library of models is the distribution from which the data were randomly drawn. Therefore, the prior distribution of models must be such that the entire observational space is reasonably well sampled. The best fit parameters for a specific galaxy are computed by taking the probabilities for all models and integrating over all parameters except the one of interest. This produces a Probability Distribution Function (PDF) of which the median and width are used as the best fit estimate and uncertainty in the fit respectively. Kauffmann et al. (2003a) and Salim et al. (2007) describe the technique in more detail.

Subsequent to the Brinchmann et al. (2004) release of the MPA-JHA SDSS value added

catalogue, the MPA-JHA SDSS DR7* release has adopted the SED fitting method of Salim et al. (2007) to derive stellar masses.

4.1.2 Deriving Stellar Masses

The FoF spectroscopic sub-sample is used for our mass estimates. We can therefore test the stellar mass estimates for galaxies at the redshift we will be considering for the remainder of the study.

The Bell method

For our Bell mass estimate we have chosen the $g-r$ colour which provides reasonable sensitivity to recent SF and measure the luminosity in the z and K bands. These bands are more sensitive to the older stellar population which contributes most to the stellar mass. Luminosities are derived from absolute magnitudes by using:

$$L_\lambda/L_\odot = 10^{-0.4(M_\lambda - \mathrm{M}_\odot(\lambda))} \tag{4.3}$$

where M_λ is the absolute magnitude determined from filter λ, similarly, $\mathrm{M}_\odot(\lambda)$ is the absolute magnitude of the Sun in the same filter. The conversion from apparent to absolute magnitudes is dependent on the distance modulus $DM(z)$ and the $K(z)$-correction, which in turn is dependant on cosmology and galaxy type respectively. The Bell et al. (2003) coefficients used in our computations are shown in Table 4.1.

Table 4.1: Bell et al. (2003) coefficients for determining a M/L ratio from the $g-r$ colour and the absolute magnitude of the Sun in the z and K band. The absolute magnitude values of the Sun is taken from Table 3.3 with $\mathrm{M}_\odot(z)$ and $\mathrm{M}_\odot(K)$ band on the AB and Vega magnitude systems respectively.

	a_λ	b_λ	$\mathrm{M}_\odot$
z	-0.223	0.689	4.54
K	-0.209	0.197	3.29

MAGPHYS SED fitting

MAGPHYS – Multi-wavelength Analysis of Galaxy Physical Properties is a modeling package that enables the user to interpret observed galaxy SEDs in terms of stellar and ISM properties. The analysis of galaxy SEDs is limited to a set of multiband photometric observations and are performed in two steps. Firstly, a large library of optical galaxy spectra are built from the Bruzual & Charlot (2003) (BC03) and Bruzual 2007 (CB07) models, which both include dust attenuation as prescribed by Calzetti et al. (2000). They make use of the Padova and Geneva isochrones and a combination of stellar evolutionary tracks which

*http://home.strw.leidenuniv.nl/~jarle/SDSS/

consist of the BaSeL (Lejeune et al. 1998; 1997) theoretical and STELIB + Pickles empirical spectra (Le Borgne et al. 2003, Pickles 1998). BC03 adopts a Chabrier (2003) IMF, see Eq. 1.5 on page 22.

MAGPHYS comes with a large binary file which contain 25 000 stellar population spectra computed from BC03 models. Each spectrum was computed by randomly drawing the various adjustable model parameters from the following prior distributions.

SFHs are modelled by an underlying continuous model (Eq. 4.2) with random bursts superimposed onto this continuous model. The adjustable parameters for the SFH, t_{form}, γ and the burst time and strength are randomly drawn from prior probability distributions. The age of the galaxy, t_{form}, is uniformly distributed from 0.1 to the age of the galaxy at that redshift. The MAGPHYS model grid caters for fitting galaxies that might have experienced a star burst in the past 2 Gyr. To do so, 50% of the models are set to have experienced a stochastic star burst event. The amplitude of each burst is parametrized as $A = M_{burst}/M_{cont}$, where M_{burst} is the mass of stars formed in the burst and M_{cont} is the total mass of stars formed by the continuous model over the time t_{form}. This ratio is distributed logarithmically between 0.03 and 4.0. During a burst, stars form at a constant rate over the time t_{burst}, which is distributed uniformly between 3×10^7 and 3×10^8 yr. The metallicity is distributed uniformly between 0.02 $Z_\odot$ and 2 $Z_\odot$.

Model SEDs are computed from the stochastic model libraries at the redshift of the galaxy by convolving the model spectra with the observed filter functions. For a large catalogue it is more efficient to use a grid of redshifts from which the closest to the observed redshift will be chosen for comparison. The redshift grid is spaced in $\Delta z = 0.01$ intervals. Each model is fitted to the observed galaxy SED and a corresponding probability, $\exp(-\chi^2/2)$ is computed. This procedure builds up a likelihood distribution for all the parameters by marginalizing over all the parameters. From this, the best fit SED with associated uncertainties is computed.

Our SED stellar mass estimates are computed for three data–model combinations. We compute the stellar mass for our *ugriz* and *ugrizJHK* SEDs separately using the BC03 models as well as *ugrizJHK* SEDs with CB07. The main difference between the BC03 and CB07 models is the improved treatment of thermally pulsating - AGB stars in CB07, which have been shown to make non-negligible contributions to NIR luminosities (Maraston 2005). However, the CB07 models find the impact of the TP-AGB stars to not be as extreme as Maraston (2005).

The stellar masses and star formation rates from MAGPHYS were derived from our seeing matched aperture magnitudes. We therefore have very accurate measures of galaxy colours, which in turn enable us to better sample the shapes of SEDs. To obtain total stellar masses and total star formation rates, the MAGPHYS results are scaled by the difference in total flux and the flux measured in the aperture. We therefore scale the luminosity, L, and scale the mass accordingly through the mass-to-light ratio M_*/L. The scaling is determined from the r band photometry, which is our most sensitive band and is given by the following:

$$L_{\rm tot} = L_{\rm ap} * \times 10^{-0.4(r_{mag\_auto} - r_{ap})} \tag{4.4}$$

All the MAGPHYS derived results have this scaling applied and are quoted as total stellar masses and star formation rates.

4.1.3 Comparisons of Stellar Mass Estimates

For all of our comparisons we have corrected the estimated stellar masses to have the same IMF, which we have chosen to be the Kroupa (2001) IMF as used by Brinchmann et al. (2004). Bell masses are computed assuming a 'diet' Salpeter IMF (Bell & de Jong 2001). To convert from 'diet' Salpeter to the Kroupa IMF one subtracts a constant 0.15 dex from the 'diet' Salpeter derived $\log M_*$. The BC03 and CB07 models use a Chabrier (2003) IMF. To convert to a Kroupa (2001) IMF an addition of 0.04 dex to the Chabrier (2003) derived $\log M_*$ is needed. We show the inputs for different models we are comparing in Table 4.2.

Table 4.2: Input to the various models.

Method	Input	SPS model	SFH treatment	IMF	Z
Bell	z, K	PÉGASE	cont. no burst	'diet' Salpeter	$Z_\odot$
Kauffmann	z+D$_n$(4000), Hδ	BC03	stochastic	Kroupa	0.025–2 $Z_\odot$
Brinchmann	$ugrizK$	BC03	stochastic	Kroupa	0.025–2 $Z_\odot$
BC03	$ugriz + JHK$	BC03	stochastic	Chabrier	0.02–2 $Z_\odot$
CB07	$ugrizJHK$	CB07	stochastic	Chabrier	0.02–2 $Z_\odot$

To quantify our stellar mass estimates we use the following as a fiducial reference dataset. The latest Brinchmann derived stellar masses from the MPA-JHA* DR7 value-added catalogue are derived from full SED fits and have been well tested. As a sanity check we compared the Brinchmann to the Kauffmann stellar mass estimates and found a 0.01 dex offset with a scatter of 0.08 dex as shown in Fig. 4.1. The offset and scatter is small enough to view these datasets as equal for our purposes. We continue our comparisons with the Brinchmann stellar mass estimates. We do not view the Brinchmann results as superior to ours since there is no way to know which of the datasets contribute most to the scatter in the comparison. Both sets of results come from current state-of-the-art SPS models with similar treatments for SFH and dust extinction. The Brinchmann et al. (2004) results are well used in the literature, based on a similar dataset and therefore makes for a suitable comparative dataset.

The results of the Bell-Brinchmann mass comparison are shown in Figures 4.2 and 4.3, which are the Bell stellar mass derived from z and K-band respectively. Bell et al. (2003) predicts a scatter of 0.1 dex for optical M_*/L ratios and 0.1–0.2 dex scatter for NIR M_*/L ratios. We find a similar scatter of 0.08 dex for the z and K bands. There is a clear residual offset as a function of mass for the z-band stellar masses, the mean offset is 0.13 dex. The

*MPA: Max-Planck-Institut für Astrophysik - Johns Hopkins University

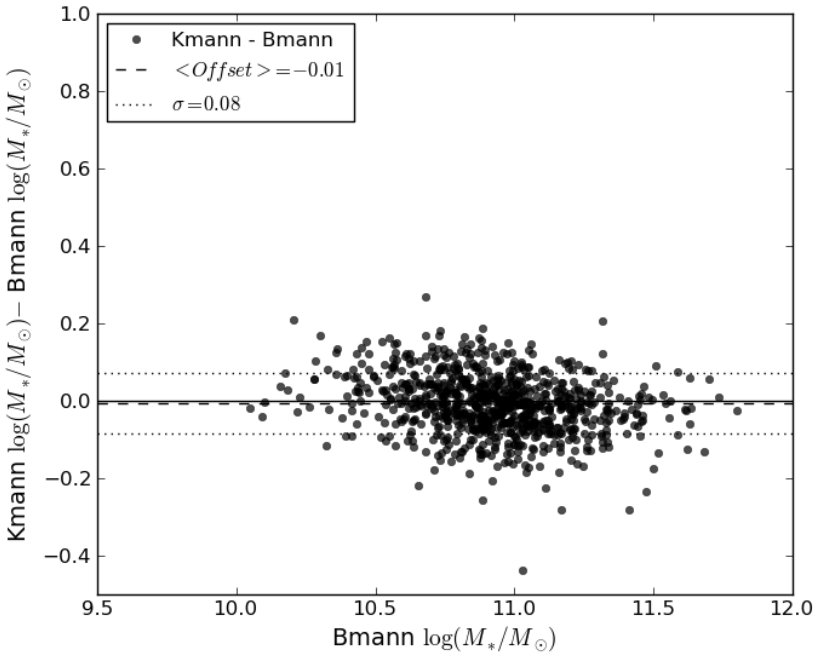

Figure 4.1: A comparison between the stellar mass estimates from Brinchmann et al. (2004) and Kauffmann et al. (2003a). We show Brinchmann $\log(M_*/\mathrm{M}_\odot)-$ Kauffmann $\log(M_*/\mathrm{M}_\odot)$ as a function of Brinchmann $\log(M_*/\mathrm{M}_\odot)$.

mean offset for the K-band is smaller, -0.013 dex, but the offset as a function of mass is more pronounced. The results point towards the Bell masses being over estimated for low mass galaxies and under estimated for high mass galaxies. The K-band luminosity derived masses seems to be more reliable than those derived from the z-band.

We now consider the stellar mass comparisons for the BC03($ugriz$), BC03($ugrizJHK$) and CB07($ugrizJHK$) models. The BC03($ugriz$)–Brinchmann comparison is shown 4.4. There is 0.02 dex residual offset present with a scatter of 0.17 dex. For the BC03($ugrizJHK$)–Brinchmann comparison the NIR data reduces the scatter to 0.13 dex, but the 0.02 dex offset still remains (Fig. 4.5). The scatter for the CB07($ugrizJHK$)–Brinchmann comparison remain at 0.13 dex, but the offset is improved to 0.01 dex. This is a marginal improvement of the offset so we will view the results of BC03($ugrizJHK$) and CB07($ugrizJHK$) as equal.

Lastly, we compare the two methods with each other. We compare the z derived stellar masses with the BC03($ugrizJHK$) masses in Fig. 4.7. For the BC03($ugrizJHK$) – Bell comparisons we subtracted 0.23 dex from the Bell masses which is the offset between the Chabrier and 'diet' Salpeter IMFs. The same non-constant offsets found in Figs.4.2 and 4.3 are present in the z and K band comparisons, shown in Figs. 4.7 and 4.8 respectively.

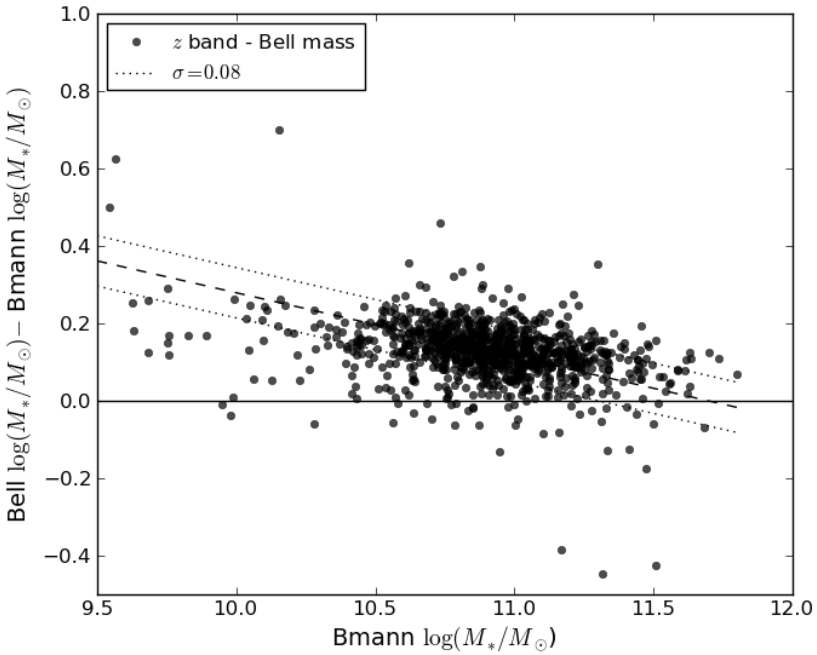

Figure 4.2: The difference in stellar masses derived from the z-band (Bell $\log(M_*/\mathrm{M}_\odot)$− Brinchmann $\log(M_*/\mathrm{M}_\odot)$) as a function of Bell derived mass. The mean offset is 0.13 dex.

4.2 Star Formation Rate Comparison

We compare the MAGPHYS derived SFRs to those obtained by Brinchmann et al. (2004). They derived SFRs using the Charlot & Longhetti (2001) SPS models to fit continuum and emission lines to their spectra. The offset between an Chabrier (2003) and Kroupa (2001) IMF derived SFR is 0.04 dex, in that the Kroupa (2001) IMF produces a slightly higher SFR. We show the BC03($ugriz$)–Brinchmann SFR comparison in Fig. 4.9 and the BC03($ugrizJHK$)–Brinchmann SFR comparison in Fig. 4.10.

The most obvious difference between the two comparisons is that the inclusion of the NIR photometry produces a much tighter distribution in SFR for star forming galaxies. The tighter distribution is most likely due to the contribution of the older stellar population, as well as dust, being better constrained by the addition of NIR photometry. This would lead to less ambiguity in which model better fits the SED, as compared to only using optical photometry for the same galaxy SED. The scatter for the star forming galaxies are 0.67 and 0.46 dex for the BC03($ugriz$)–Brinchmann and BC03($ugrizJHK$)–Brinchmann comparisons respectively. We also show the one-to-one BC03($ugrizJHK$)–Brinchmann SFR comparison in Fig. 4.11 to make a comparison easier. Conroy et al. (2009) reported a $\sim$0.3 dex uncertainty in SFR for blue galaxies when comparing different SPS codes. They also found larger errors in SFR associated with red, low SF galaxies and state that it is likely related to the long standing problem of SPS models predicting colours redder than

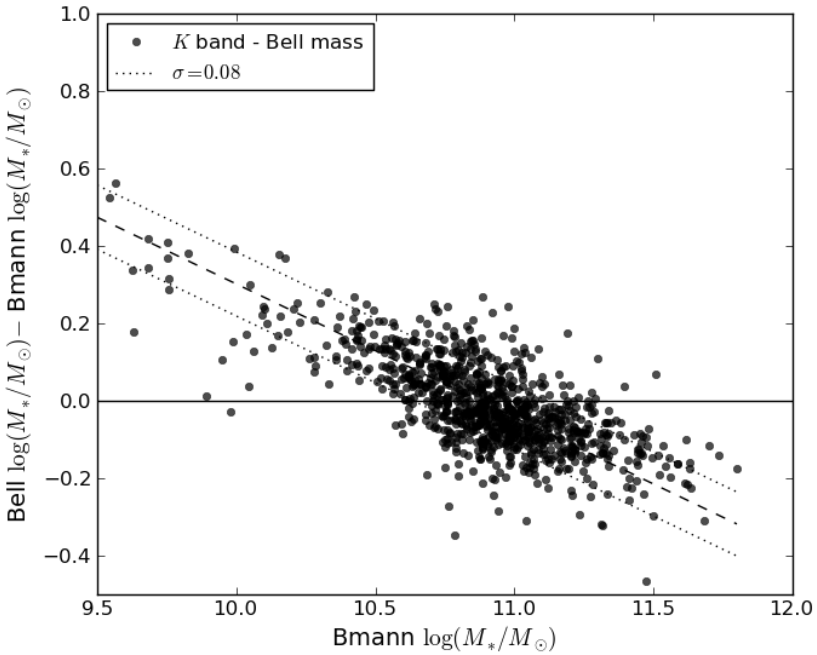

Figure 4.3: The difference in stellar masses derived from the K-band (Bell $\log(M_*/\mathrm{M}_\odot)$− Brinchmann $\log(M_*/\mathrm{M}_\odot)$) as a function of Bell derived mass. The mean offset is -0.013 dex.

observations by as much as $\sim 0.1^{\mathrm{m}}$ (Eisenstein et al. 2001, Wake et al. 2006). The scatter in the comparisons are quite large, but similar to the 0.33–0.41 dex scatter found by Salim et al. (2007) in their comparison with Brinchmann et al. (2004) SFRs. They attributed their scatter to the intrinsic differences in SFRs derived from emission lines versus the UV continuum. Star formation rates derived from emission lines are more sensitive to current star formation ($\lesssim$ 10 Myr), whereas UV continuum derived star formation is sensitive to star formation in the past $\sim$ 100 Myr. In the case of our study, our most sensitive band to "current" star formation is the u band, which is sensitive to star formation in the past $\sim$ 1 Gyr. This is the most likely cause of the observed offset and increased scatter in SFRs compared to what Salim et al. (2007) found.

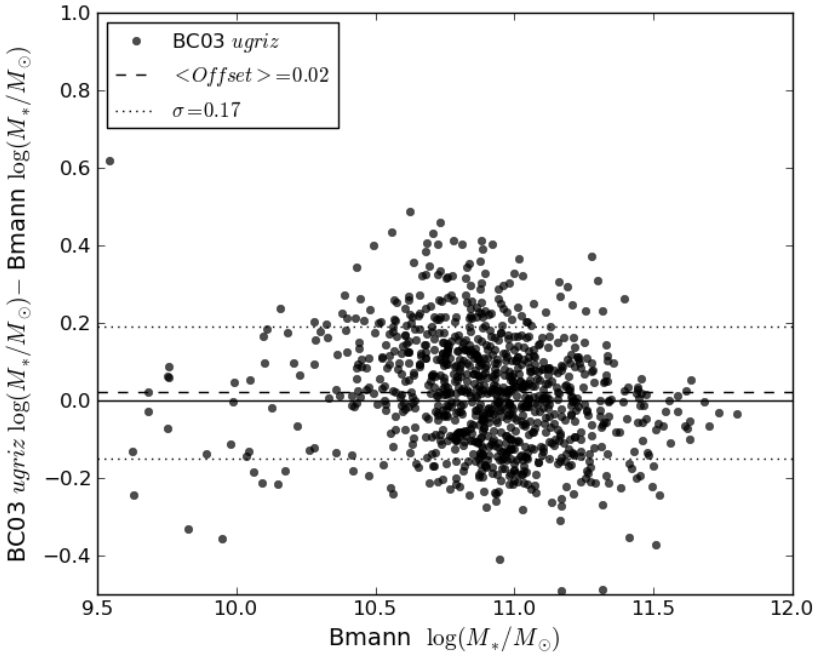

Figure 4.4: The difference in stellar masses (BC03($ugriz$) $\log(M_*/\mathrm{M}_\odot)$− Brinchmann $\log(M_*/\mathrm{M}_\odot)$) derived from using only the SDSS $ugriz$ bands for the BC03 mass estimates.

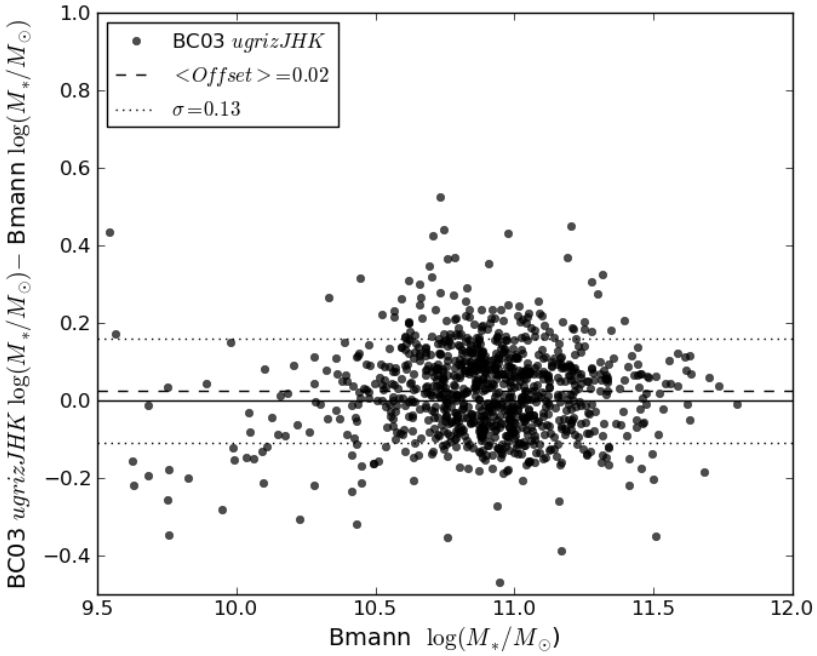

Figure 4.5: The difference in mean stellar mass (BC03($ugrizJHK$) $\log(M_*/\mathrm{M}_\odot)$− Brinchmann $\log(M_*/\mathrm{M}_\odot)$) derived from the full set of $ugrizJHK$ photometric bands.

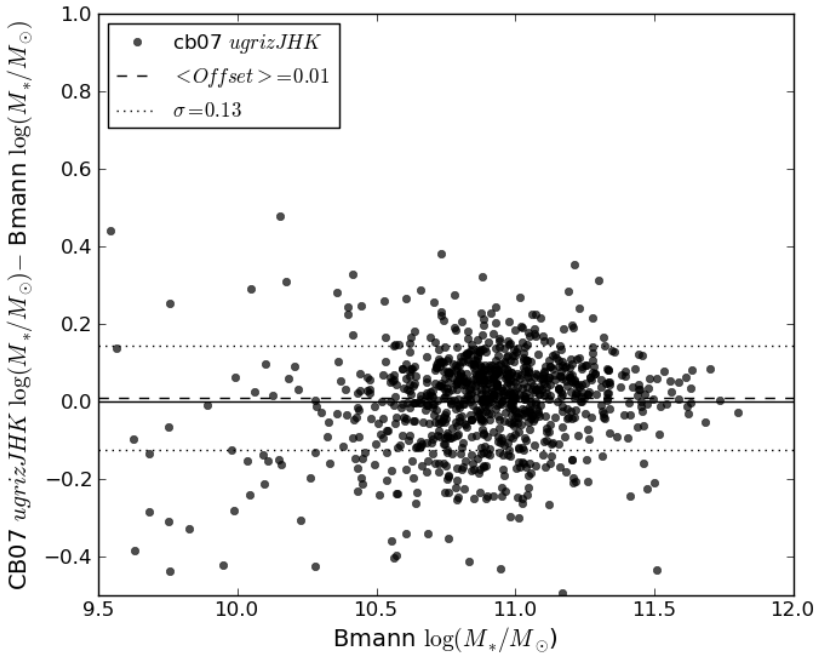

Figure 4.6: The difference in stellar mass derived from adding the UKIDSS JHK photometry to the $ugriz$ bands for the CB07 models.

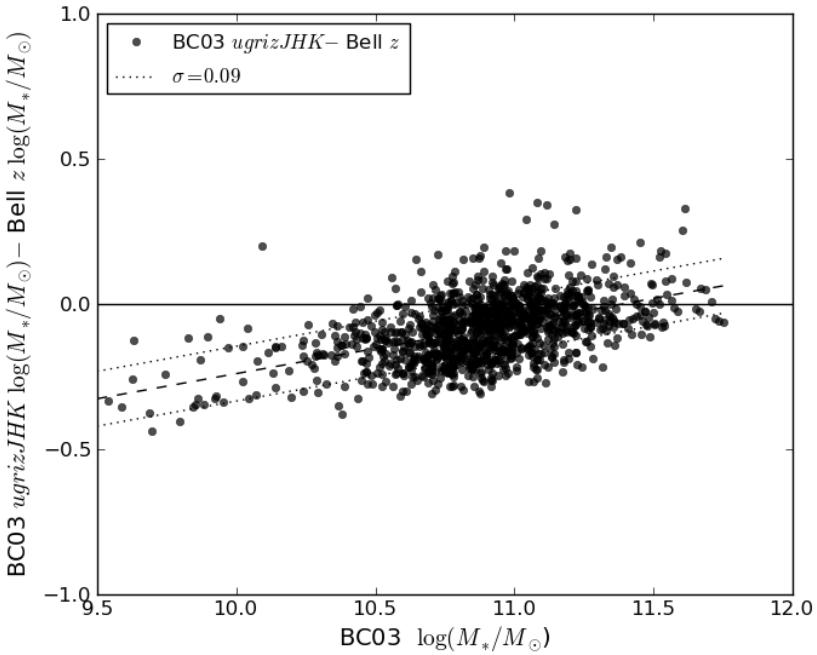

Figure 4.7: Difference in stellar mass between the two methods employed. We compare the Bell z-band derived stellar masses with the BC03($ugrizJHK$) model results. 0.23 dex was subtracted from the Bell masses to adjust for the difference in IMF. The same non-constant offset previously seen is present when compared to the BC03($ugrizJHK$) models. The dashed line is a straight line fit and the dotted lines indicate the standard deviation.

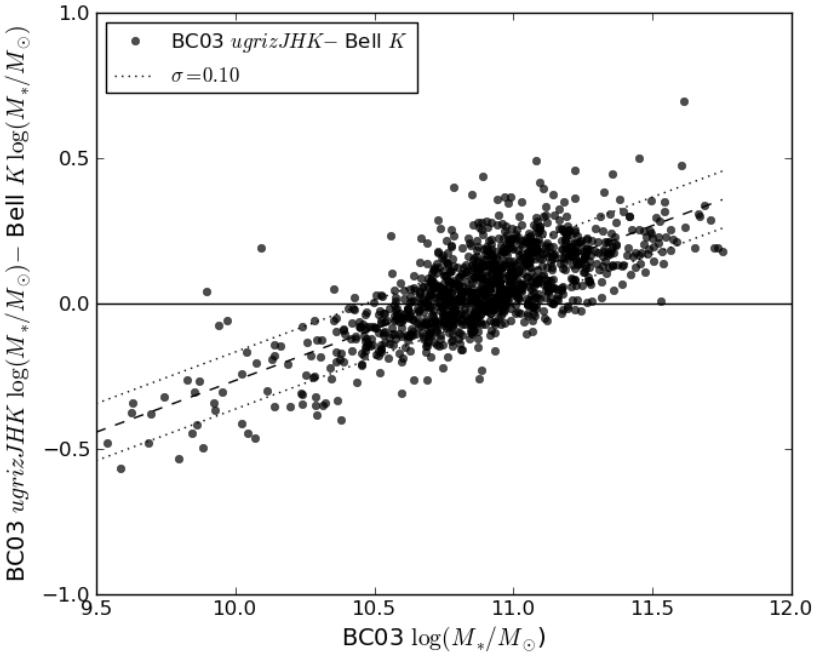

Figure 4.8: Difference in stellar mass between the two methods employed. We compare the Bell K-band derived stellar masses with the BC03($ugrizJHK$) model results. 0.23 dex was subtracted from the Bell masses to adjust for the difference in IMF. The dashed line is a straight line fit and the dotted lines indicate the standard deviation.

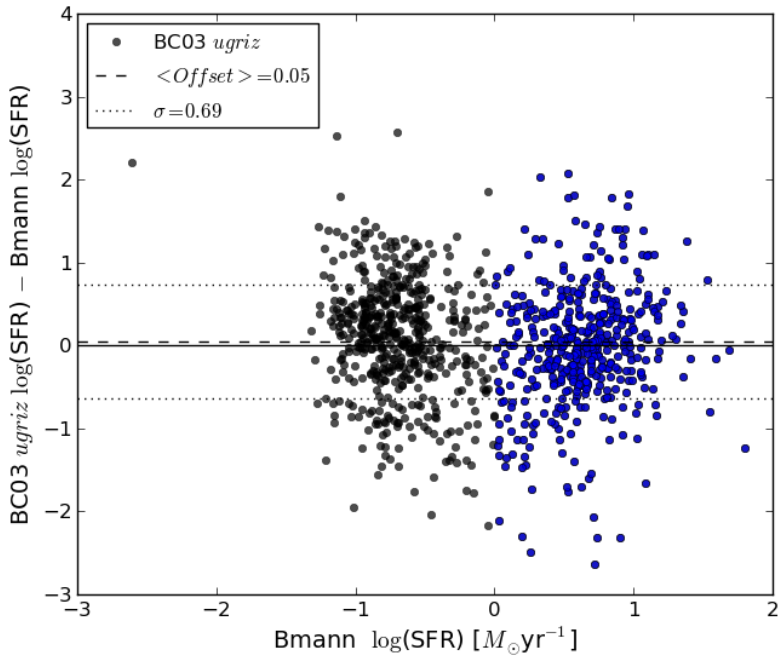

Figure 4.9: Difference in the SFRs derived from BC03(*ugriz*) and Brinchmann. There is an obvious bimodal SFR distribution with the division between passive (black circles) and actively SF galaxies (blue circles) close to log(SFR)= 0.

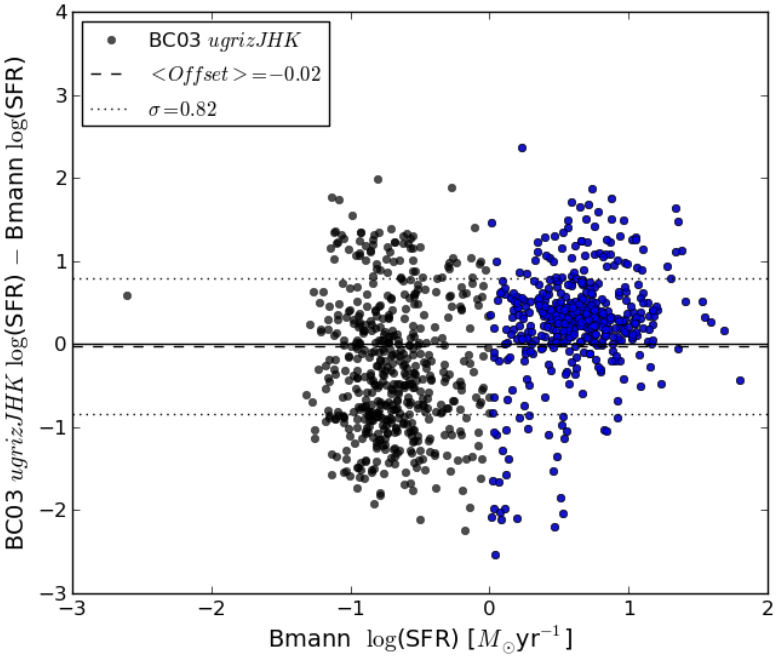

Figure 4.10: Difference in the SFRs derived from BC03(*ugrizJHK*) and Brinchmann. An obvious improvement with the inclusion of the NIR photometry is the tighter correlation in SFR for the SF galaxy comparison. However, a 0.2 dex offset is observed.

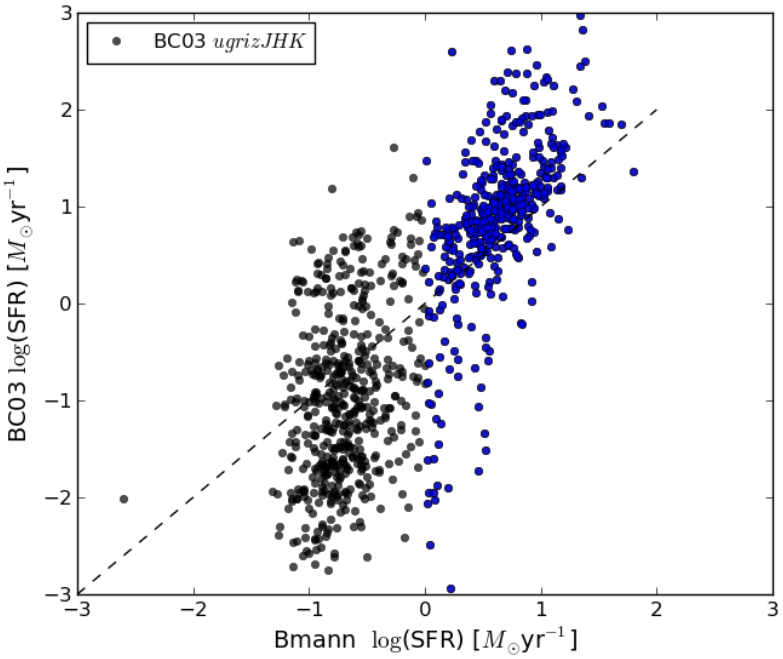

Figure 4.11: A one-to-one comparison between the Brinchmann et al. (2004) derived SFRs and MAGPHYS BC03($ugrizJHK$) SFRs. The offset and scatter are more pronounced for the non-star forming galaxies (black). The SF galaxies (blue) show a tighter correlation, but an offset 0.3 dex is present.

4.3 Photometric Redshifts

We require distance information for photometric catalogue member galaxies without spectroscopic redshifts. This will allow us to study the properties of galaxies associated with the spectroscopically defined redshift slice. The SDSS DR7 PHOTOZ table (Abazajian et al. 2009) contains photometric redshifts derived from *ugriz* photometry for galaxies in our sample. Photometric redshifts were derived using the `Photoz` code, which makes use of a hybrid method that combines template fitting (Csabai et al. 2003) and an empirical calibration using objects with both observed colours and spectroscopic redshifts. Abazajian et al. (2009) claims that the photometric redshift rms error should be good to 0.02. We independently checked this for our sample and found the median photometric redshift uncertainty for our sample to be 0.02, similar to what Abazajian et al. (2009) found. To put the size of the typical photometric redshift uncertainty into perspective: an uncertainty of 0.02 corresponds to 6000 km s^{-1}, which by spectroscopic redshift standards are classified to be a "blunder". Colless et al. (2001) classified anything with > 600 km s^{-1} difference between repeat observations to be a blunder - at this level, the majority of photometric redshifts would be classified blunders by the 2dFGRS and SDSS.

The SDSS photometric redshifts have only been tested for galaxies brighter than the spectroscopic limit $r < 17.7$. We consider the performance of the SDSS photometric redshifts by comparing redshifts from our spectroscopic sample, which contain 2dF redshifts for sources fainter than $r = 17.7$, to the SDSS photometric redshifts in Fig. 4.12. The top panel shows the one-to-one relation between z_{spec} and z_{phot}. To study the same region in z_{phot} we need to make the redshift interval larger ($0.06 < z_{phot} < 0.2$) compared to the spectroscopically defined redshift slice ($0.12 < z_{spec} < 0.15$). The mean offset for the interval was found to be $0.06 < z_{phot} < 0.2$ is $\langle z_{spec} - z_{phot} \rangle = 0.001$. This small offset could mostly be due to the large number of bright galaxies and we therefore consider the average offsets for bright ($r < 17.7$) and faint ($r \geq 17.7$) galaxies separately. For the bright galaxies we find the average redshift offset to be 0.0019 and for the fainter galaxies the average redshift offset is 0.0095.

If the photometric redshift errors are randomly distributed and there are no systematics present, the central limit theorem states that the normalised distribution of errors should be a Gaussian distribution with mean $\mu = 0$ and standard deviation $\sigma = 1$. We show the normalised error distributions for all the galaxies in the photometric redshift range as well as the normalised error distributions for galaxies brighter and fainter than $r = 17.7$ in Fig. 4.13. The distribution for all the the galaxies is close to normal, with $\sigma = 0.95$. The distribution for the brighter galaxies has a $\sigma = 0.88$. For the fainter galaxies we find that the normalised error distribution has $\sigma = 0.99$. We are therefore confident that no appreciable offsets are present in the redshift range of interest, considering the inclusion of 2dF spectra for the comparison which goes to fainter magnitudes ($R \sim 20$). The errors for the brighter galaxies might be slightly overestimated as seen from the smaller σ value.

Of the 78 311 galaxies in our photometric sample $\sim$ 3% are not in the SDSS DR7

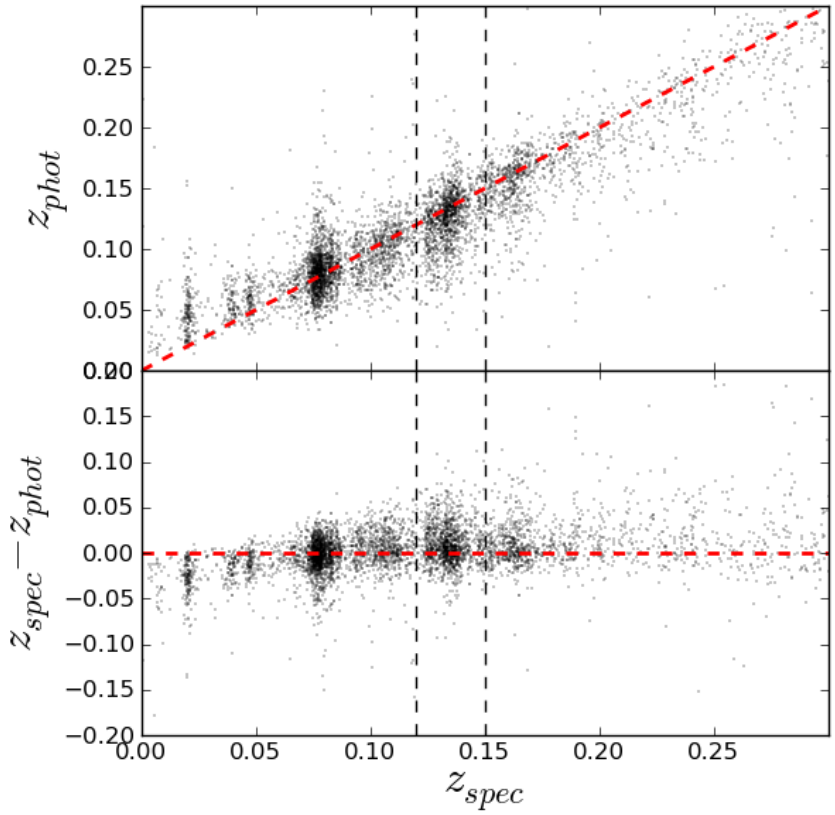

Figure 4.12: A comparison between the spectroscopic and photometric redshifts for 5482 galaxies in our survey area of which 503 are from the 2dF. The upper panel shows the one-to-one comparison between z_{spec} and z_{phot}. The lower panel shows the difference in redshift $(z_{spec} - z_{phot})$ as a function of z_{spec}. The vertical dashed lines indicates the spectroscopic redshift interval defined by three times the cluster velocity dispersion. The mean offset in the region defined by $0.06 < z_{phot} < 0.2$ is $\langle z_{spec} - z_{phot} \rangle = 0.001$.

catalogue and therefore have no photometric redshift determination.

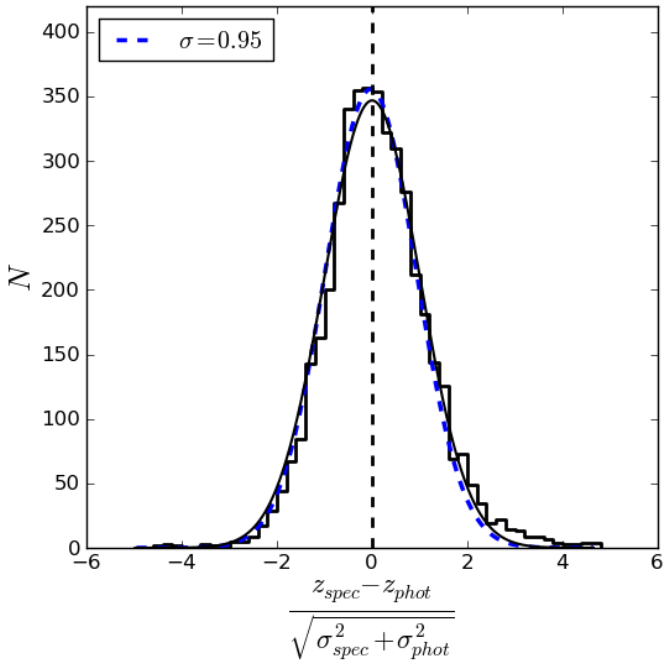

(a)

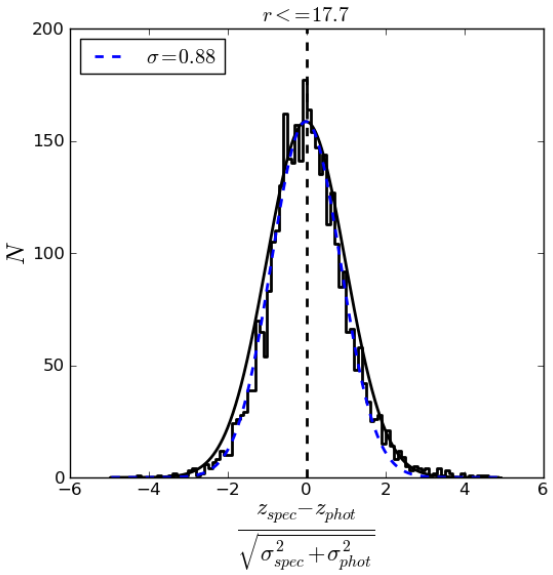

(b)

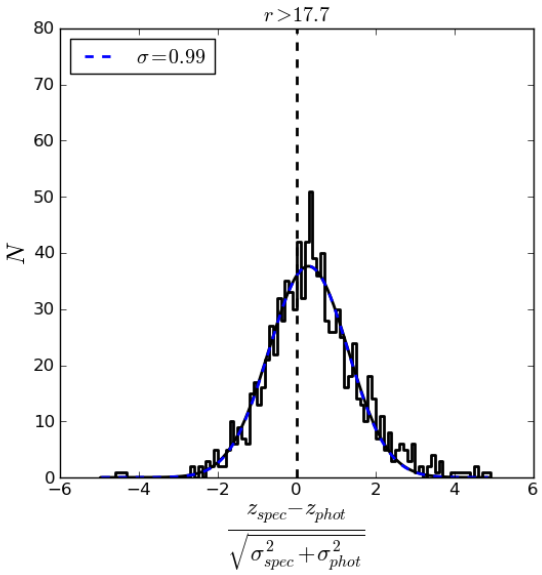

(c)

Figure 4.13: The normalized error distributions, $(z_{spec} - z_{phot})/\sigma_{z_{phot}}$, for galaxies in the range $0.06 > z_{phot} < 0.2$. The solid black curves are the expected normal distribution for a randomly selected sample with a mean $\mu = 0$ and standard deviation $\sigma = 1$. The dashed blue curves are the best fit Gaussian functions to the normalized distributions with a dispersion of $\sigma = 0.95$. The whole sample is shown in (a) and galaxies brighter and fainter than the SDSS spectroscopic limit is shown in (b) and (c) respectively. This shows that the photometric redshift errors are very close to being randomly distributed and there are no systematics present.

4.4 Stellar Masses and Star Formation Rates from Photometric Redshifts

In the following section we consider the stellar masses and star formation rates derived for the FoF spectroscopic sample using their photometric redshifts.

We compare the spectroscopically and photometrically derived quantities. It should be noted that the MAGPHYS model grid was constructed with a $\Delta z = 0.01$ spacing in redshift. The typical photometric redshift error is slightly larger than that, $z \sim 0.02$. Since MAGPHYS assumes that the redshift provided is a spectroscopic redshift with negligible error, one could expect different best fit models to be assigned to the same galaxy depending on whether the spectroscopic or photometric redshift was specified. This uncertainty in photometric redshift translate into uncertainties in stellar masses and star formation rates which have not been accounted for. The size of these of uncertainties can be gauged as follows.

The stellar mass comparison is shown in Fig. 4.14 and the star formation rate comparison is shown in Fig. 4.15. The same galaxy SEDs were used to determine the stellar masses and SFRs for the spectroscopic and photometric samples. The only difference was that in the case of the spectroscopic sample, the spectroscopic redshift was used and in the case of the photometric sample, the photometric redshift was used. Any differences in the derived stellar masses and SFRs would therefore stem from the difference in spectroscopic compared to photometric redshift. Any scatter in the comparison would therefore be a result of this. The effect of the difference in redshift is shown in the right hand panels of Figs. 4.14 and 4.15. The slight offset in stellar masses and SFRs is most likely due to the difference in redshift being slightly larger for lower mass galaxies with lower M_*/L. It is more difficult to obtain accurate photometric redshifts for such galaxies.

Lastly, we consider the stellar mass function for our photometric sample in Fig. 4.16. We compare our stellar mass function to the Bell et al. (2003) K-band stellar mass function. The Bell stellar mass function was corrected for the slope shown in Fig. 4.8 to make the comparison. The uncorrected Bell stellar mass function is also shown for reference. We consider our stellar masses to be complete close to $\log(M_*/M_\odot) \simeq 9.9$, below that our stellar mass function starts to deviate from Bell stellar mass function. Considering the ~ 0.13 dex scatter in the stellar mass comparison, we chose a hard limit of $\log(M_*/M_\odot) = 9.9$ as the stellar mass limit.

4.5 Summary

No obvious offsets were found in the comparison of the BC03 and CB07 models with the Brinchmann stellar masses and star formation rates. The scatter in the comparisons compare with what have been found by previous studies who compared to the Brinchmann results (Salim et al. 2007, McGee et al. 2011). The most note-worthy result that we find is the addition of NIR photometry to SED fits does not worsen the stellar mass estimates, contrary to what was found by Taylor et al. (2011). They attribute the worsening of the stellar mass

estimates to uncertainties in the SPS models at NIR wavelengths and/or uncertainties in calibrating the photometry between their NIR and optical datasets. Similar to our results, Banerji et al. (2013) have recently found that the addition of NIR data did not worsen their stellar mass estimates. They found that estimated stellar masses of galaxies depend on the assumptions made in the models being fitted, as well as it being sensitive to errors in the photometry and NIR templates. This could be why Taylor et al. (2011) found a worsening in their stellar mass estimates.

The Bell derived masses compare fairly well to the Brinchmann masses. The mean stellar mass offset is larger in the z-band (0.13 dex) than in the K-band (-0.013 dex). Even though the Bell offsets lie within those of the SED fits, we find a prominent slope in the mass difference. This indicates the Bell method overestimates stellar masses at lower masses and underestimates stellar masses at higher masses compared to the Brinchmann and BC03 masses, as also found by Banerji et al. (2013). The slope was also found to be steeper in the K band compared to the z-band.

The SFR comparisons show little or no overall systematic offsets even though a large scatter is observed. Taking into account that blue galaxies can have a $\sim$0.3 dex uncertainty in their SFR and given that it is very difficult to measure SF in galaxies with very low or no SF, the observed scatter seems reasonable.

These comparisons discussed above allow us to characterise the results obtained from MAGPHYS. Stellar masses derived using spectroscopic redshifts compare well to those derived using similar methods. The difficulty in deriving SFRs for galaxies with little star formation was apparent in the scatter for galaxies with $\log(\mathrm{SFR}) < 0$. A small offset of ~ 0.03 dex was found in the comparison of spectroscopically derived stellar masses and star formation rates with photometrically derived quantities. Additionally, we found that the differences are sensitive to differences in redshift, which is quite pronounced for stellar mass. MAGPHYS uses a grid spacing of $\Delta z = 0.01$ to construct model SEDs. The typical error on our photometric redshifts is 0.02. This is twice as large as the sampling grid used by MAGPHYS and this could lead to larger uncertainties in the stellar masses and SFRs derived using photometric redshifts.

The BC03 models are well used in the literature and since we demonstrated that adding NIR photometry to our SEDs does not worsen the fits, we chose to use the BC03($ugrizJHK$) for the rest of the analysis.

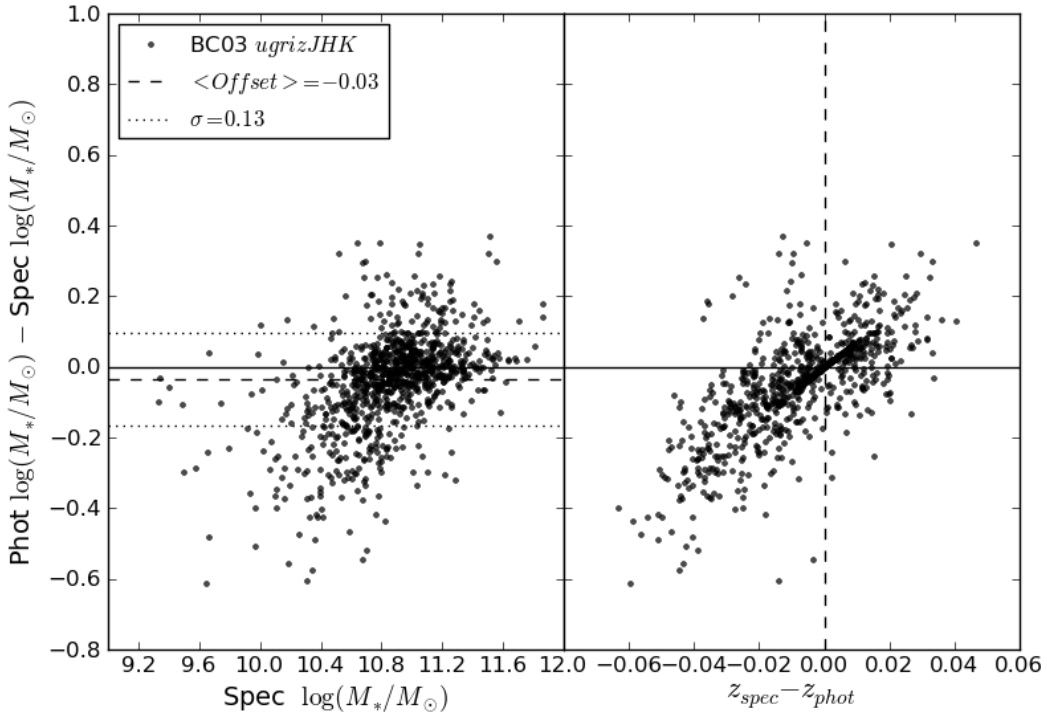

Figure 4.14: A comparison between stellar masses derived for the FoF spectroscopic sample from spectroscopic and photometric redshifts (left panel). The difference in stellar mass as a function of difference in redshift is shown in the right panel.

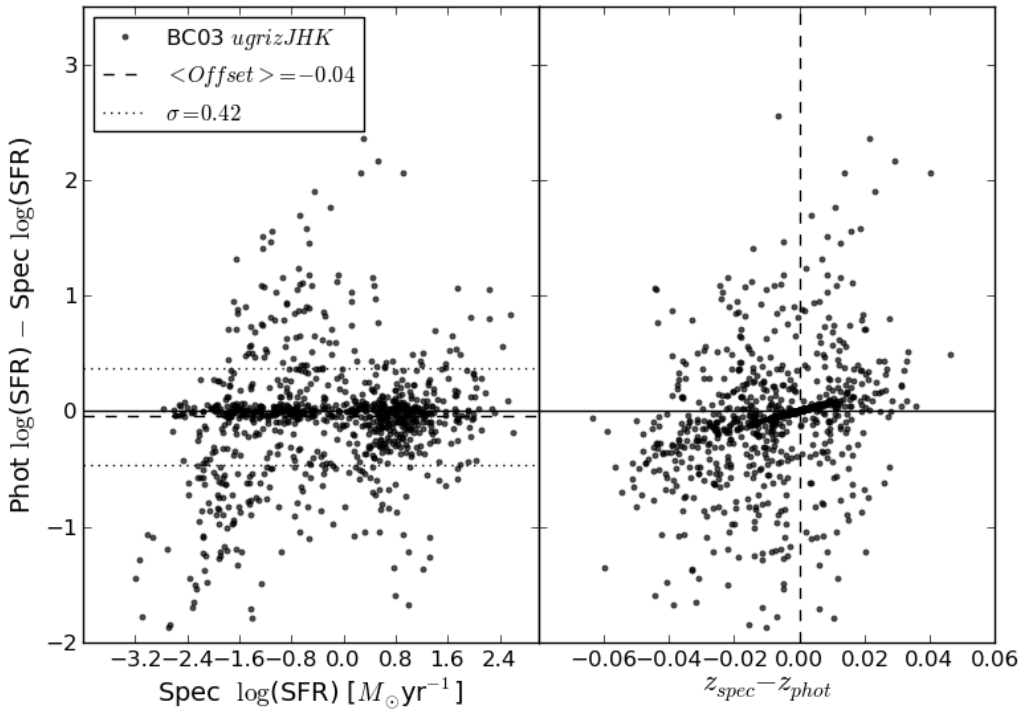

Figure 4.15: A comparison between star formation rates derived for the FoF spectroscopic sample from spectroscopic and photometric redshifts (left panel). The difference in SFRs as a function of difference in redshift is shown in the right panel. The tightly related stripes observed in the right hand panel are due to the model grid, built using discrete redshift intervals of $z = 0.01$.

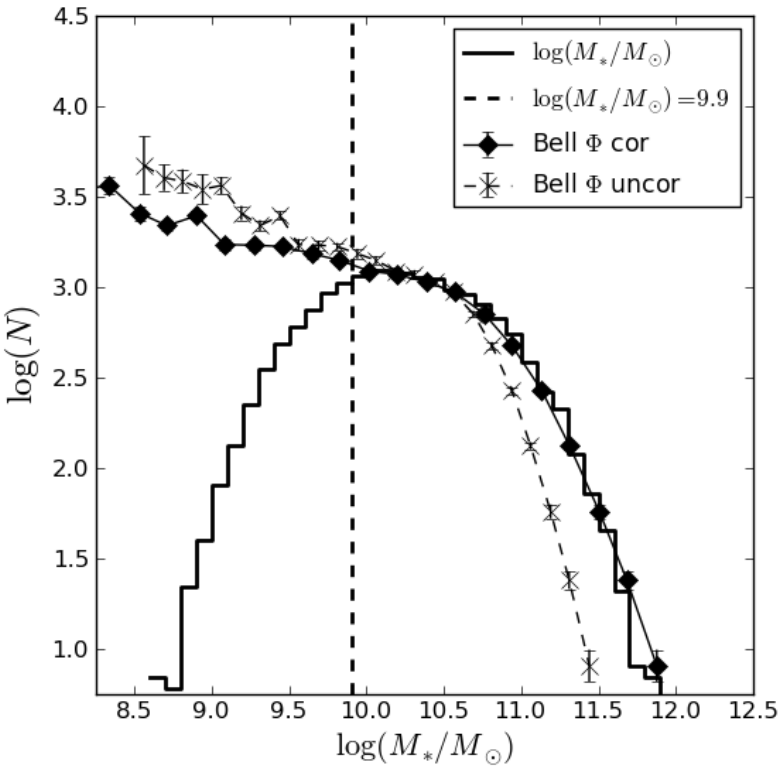

Figure 4.16: Stellar mass function for the photometric sample. The K-band stellar mass function from Bell et al. (2003) is shown for comparison. The Bell stellar mass function was corrected according to the slope found for the difference in stellar mass shown in Fig. 4.8. We consider our stellar masses to be complete up to where our stellar mass function starts deviating from the Bell stellar mass at $\log(M_*/M_\odot) \simeq 9.9$.

Chapter 5

The Effect of Environment on Star Formation

As already outlined in Chapter 1, there are several ways to observationally define a non-star forming or quiescent population of galaxies. Any quantity related to the current star formation of a galaxy can be used, such as a simple colour measurement (e.g. Bell et al. 2003, Baldry et al. 2004), the lack of a detection in star formation rate indicator (e.g. Wilman et al. 2005) as well as imposing limits on calculated SFRs or sSFRs (e.g. McGee et al. 2011). A red colour, lack of SFR indicators, or low SFRs all indicate whether a galaxy is currently not forming stars, passive, non-star forming or quiescent. As these terms are used interchangeably, we define our terminology to avoid confusion. The general population of galaxies which currently does not exhibit any signs of star formation we refer to as quiescent. Galaxies which had their SFR derived from either SED fitting, emission line strengths or any of the other SFR indicators, will be referred to as either active or passive.

Earlier we summarised the observational evidence that there is a well established bimodal colour distribution for galaxies in the local Universe (e.g. Baldry et al. 2004; 2006, Balogh et al. 2006). There is a clear division between blue/actively star forming and red/quiescent galaxies. The relative fractions between the two populations depend on both stellar mass, environment and redshift. The increase of the fraction of blue galaxies in clusters with increasing redshift was first shown by Butcher & Oemler (1984). Their work contributed to the view that clusters are active sites of galaxy evolution in which the morphology and star formation histories of member galaxies are altered. The 2dFGRS and the SDSS surveys revealed that galaxies in dense environments, i.e. clusters and groups, have substantially different properties to galaxies in the field in terms of lower average star formation rates (Lewis et al. 2002, Gómez et al. 2003) and higher red fractions (Balogh et al. 2004, Weinmann et al. 2006a) than field galaxies. The red galaxy fraction has also been observed to depend on a number of other factors, such as the luminosity limit and cluster-centric distance (Ellingson et al. 2001, Goto et al. 2003). The very tight correlation observed between SFR and stellar mass (Brinchmann et al. 2004, Salim et al. 2007) implies a strong dependence between

the star formation histories of galaxies and their stellar mass. At a fixed stellar mass, the fraction of red galaxies was found to be higher in denser environments (e.g. Kauffmann et al. 2004, van den Bosch et al. 2008). Kauffmann et al. (2003a) found a characteristic stellar mass of 3×10^{10} $M_{\odot}$ below which galaxies tend to be star forming. Moreover, red/passive fractions are lower for less massive galaxies compared to more massive galaxies, regardless of environment.

Much of the knowledge about galaxy evolution comes from the study of galaxies in clusters and groups. The contrast with respect to the field is high and spectroscopically targeted surveys have higher success rates in denser environments. These studies are therefore limited to studying the later stages of environmental processes that drive galaxy evolution in dense environments. There is increasing evidence that the pre-processing of galaxies in group environments before falling into clusters may play an important role (Balogh et al. 2000, Fujita 2004, Li et al. 2009, Balogh & McGee 2010), but this is still debated. Simulations have also pointed to the potentially important role large-scale structures play in the evolution of galaxies (e.g. Bond et al. 1996, Colberg et al. 1999). A limited number of studies have concentrated on the identification of filamentary structures and their morphologies (Einasto et al. 1984; 1994; 1997; 2007a, Smith et al. 2012). Studies on the star formation properties of galaxies in filaments are rare and mostly based on small samples (e.g. Porter & Raychaudhury 2007, Porter et al. 2008, Fadda et al. 2008, Geach et al. 2011).

In this chapter we examine the star formation properties derived from photometry of galaxies in four predefined environments: cluster, groups, filament and field. We use red and passive fractions to investigate environmental effects on these galaxy populations. The role stellar mass plays is also investigated by imposing a stellar mass limit.

Our environmental definitions are discussed in the following section, Sect. 5.1. This is followed by a description of the method used to measure red- and passive fractions in Sect. 5.2. The results of the red and passive fraction measurements as a function of environment are shown in Sect. 5.3. A detailed discussion of the results is presented in Sect. 5.4. Lastly, we consider the role of the filament in Sect. 5.4.8.

5.1 Photometric Definitions of Environment

The analysis of the spectroscopic data provides a back bone, one can say, to the large-scale structure associated with A1437. We identified four environments from the spectroscopic data which we classified as a cluster, groups, a filament and field. Our aim in the following chapter is to define a photometric sample which we can use to study the properties of galaxies residing in the different environments down to fainter magnitudes, and ultimately lower stellar masses, than is possible from the existing spectroscopy.

We developed techniques for defining groups using overdensities derived from the photometric catalogue as well incorporating the FoF spectroscopic filament distribution to define a filament sample from the photometric catalogue.

5.1.1 Building a Photometric Redshift Slice

Having characterised the photometric redshift uncertainties we can determine which galaxies in our photometric sample are most likely associated with the large-scale structures defined from spectroscopy. As we have shown, the spectroscopically defined large-scale structure surrounding A1437 lies within a redshift slice, $0.12 < z_{spec} < 0.15$, the range which covers a 3σ cluster velocity dispersion on either side of the cluster.

To construct the photometric redshift slice we assume that the photometric redshift uncertainties are Gaussian, a safe assumption to make since Oyaizu et al. (2008) showed that the photometric redshift uncertainties for the SDSS photometric redshifts are nearly Gaussian. Since our sample is taken from the same SDSS data, we showed that the photometric redshift uncertainties are nearly Gaussian in Fig. 4.13; compare this figure to figure 11 of Oyaizu et al. (2008). The size of the uncertainties represent a 1σ deviation from the best fit photometric redshift. All galaxies with photometric redshifts and uncertainties that place it within $0.06 < z_{phot} < 0.2$ are flagged as potential members of the redshift slice. Potential members are *individually* evaluated and assigned a probability of belonging to the redshift slice by integrating the overlap of their Gaussian error profile with the redshift slice. The probability is determined by:

$$P(z) = \int_{z=0.06}^{z=0.2} \exp \frac{-(z - z_{phot})^2}{2\sigma_{phot}^2} dz \tag{5.1}$$

where $\sigma_{z_{phot}}$ is the photometric redshift uncertainty and z_{phot} is the best fit photometric redshift. The photometric redshift distributions for three photometric redshift slices are shown in Fig. 5.1, illustrating the effect $P(z)$ has on the photometric redshift slice samples.

As the $P(z)$ cut-off value increases, less galaxies are assigned to the redshift slice. In general, the specific choice of $P(z)$, within a realistic range, is not critical because we employ a statistical background subtraction technique which corrects for background field galaxy contamination. This results in the subsequent quiescent fractions as a function of environment being relatively insensitive to the choice of $P(z)$ (see Sect. 5.2 for more detail). The statistical background subtraction technique does not, however, account for the presence of large-scale foreground or background structure.

Therefore, we must be particularly cautious of the large-scale structure at $z \sim 0.08$ which covers nearly uniformly the whole survey area (see Fig. 5.8 below). Due to the typical sizes of photometric redshift uncertainties, we could expect a certain level of contamination to our samples when foreground galaxies leak into our photometric redshift slice. Contamination by the $z \sim 0.08$ large-scale structure can be minimized by tuning the $P(z)$ value. This could, however, remove galaxies with larger photometric redshift uncertainties truly associated with the large-scale structure at $z = 0.135$.

We can test the performance, at least on the brighter galaxies, by comparing the photometric membership/non-membership determinations against those given by the spectroscopic redshifts. We note that this is really an upper limit to the contamination as, in practice, we also apply a background subtraction step, but this should adequately assess

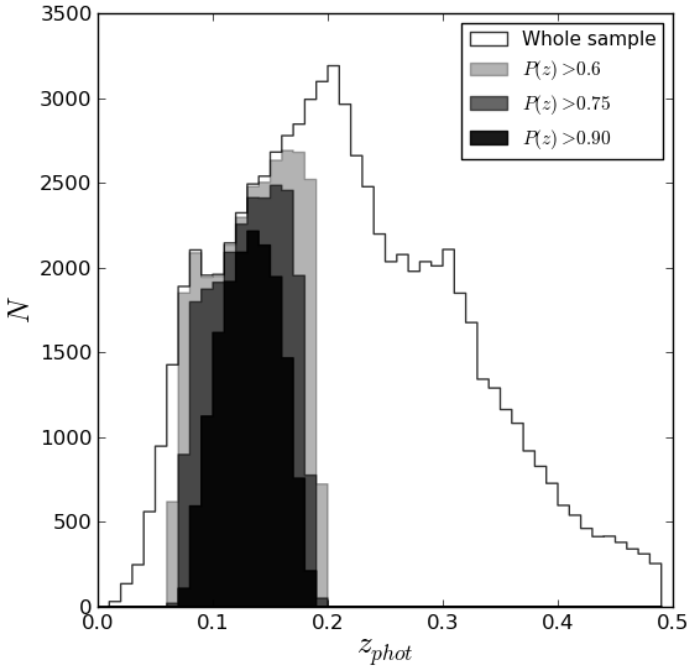

Figure 5.1: Photometric redshift distributions for the whole photometric sample and photometric redshift slices built using different $P(z)$ cuts.

the relative purity/completeness for a range of $P(z)$ thresholds. We noted in Sect. 4.3, the photometric redshift errors are comparable for r below and above 17.7, the results should therefore be equally valid below the SDSS spectroscopic limit. The purity of a group is defined as the fraction of photometric group galaxies with spectroscopic redshifts inside the range $0.11 < z < 0.16$. The completeness is defined as the number of galaxies with spectroscopic matches within the same redshift range.

The purity and completeness values were computed for a sample of seven spectroscopically well-sampled groups (Table 5.1) detected in slices derived from $P(z) > 0.75$, 0.80, 0.85, 0.90, 0.95, 0.975, 0.99. The resulting purity and completeness calculations are shown in Fig. 5.2. The purity for these groups shows little variation as a function of $P(z)$, with the purity only marginally increasing at $P(z) > 0.99$ for some of the groups. The relatively flat trend of purity as a function of $P(z)$ implies that a level of contamination is always present and that the purity has a weak dependence on $P(z)$. The mean purity for the sample groups was determined as $\sim 25\%$, which, as mentioned before, represents an upper limit to the contamination. The completeness as a function of $P(z)$ shows a different trend on the other hand. A turnover in the completeness of these groups seems to occur near $P(z) > 0.90$. The completeness is fairly constant in the $P(z)$ range 0.75 to 0.90 for most of the groups, with a decrease from 90% to 70% for $P(z)$ higher than 0.90. We therefore exclude $P(z)$ values higher than 0.90 from our analysis. Since we wished to ensure as complete a sample and the

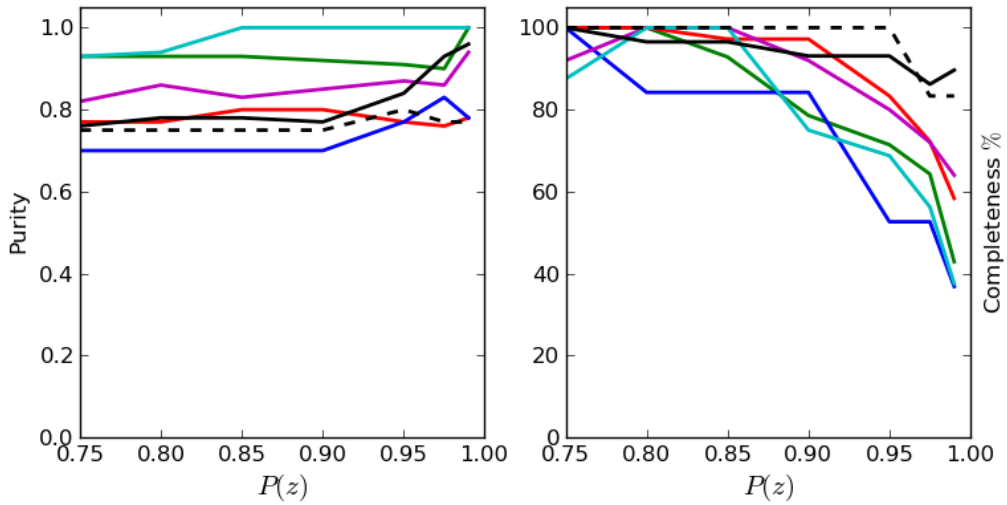

Figure 5.2: Purity (left panel) and completeness (right panel) for a sample of seven groups taken from the photometric group catalogue as a function of $P(z)$ cut-off value. Lines of similar colour in both panels represent the same group respectively. A turnover in the completeness is observed at $P(z) = 0.9$, with the purity exhibiting small variations as a function of $P(z)$.

purity only shows a weak dependence on $P(z)$, we elected to use the $P(z) > 0.75$ slice for our analysis. Furthermore, we performed our whole analysis with photometric redshift slices created with the $P(z)$ values ranging from 0.75 to 0.90, and found that the final results all lie within 1σ of the calculated quiescent fraction uncertainties for the cluster, groups and filament samples and within 2σ for the field sample. Taking into account the uncertainties on our measurements, as well as the uncertainties of the results we compare to, this variation in quiescent fractions does not affect the overall observed trends and subsequent discussion.

5.1.2 Defining Environments

We use the spectroscopically defined cluster and filament environments to define their corresponding photometric samples. The group and field environments are derived from the the photometric catalogue alone.

The Cluster Environment

The photometric cluster sample is computed by taking the central coordinates of the cluster and considering all the galaxies in the photometric redshift slice within two virial radii which is ∼6 Mpc.

The Group Environment

To locate groups in the photometric redshift slice, we use the on-sky distribution of galaxies from the photometric redshift slice to build a significance map. Galaxies in the photometric

redshift slice are placed on a 2D coordinate grid with 36″ sized pixels. The position of the galaxies are transformed from RA and DEC to X and Y using WCS information. This accounts for 1/cos(DEC) projection effects. The significance map is created by convolving the coordinate grid with a 1 Mpc circular kernel, which is the virial radius expected for a group sized overdensity with a 200–500 km s^{-1} velocity dispersion at $z \sim 0.135$. The resulting significance map is shown in Fig. 5.3. SExtractor (Bertin & Arnouts 1996) is then employed to perform peak finding and centroiding on the significance map. Since the background and the significance of detections are calculated manually (discussed in Sect. 5.1.3), SExtractor is set to perform no background subtraction. The detection threshold is set low enough to detect slight overdensities, which will be ignored if their subsequent significance is found to be too low. All the galaxies within a 2 Mpc radius from the overdensity centre are assigned to a group and the significance of the detections evaluated.

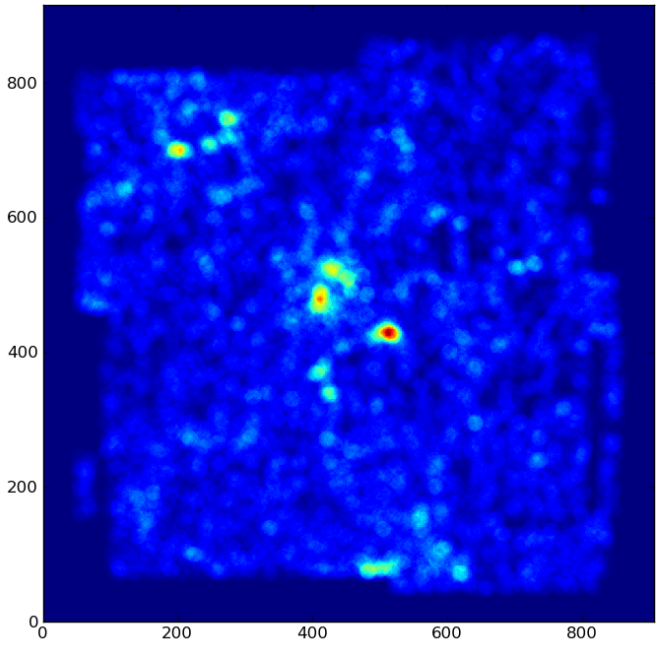

Figure 5.3: The significance map built from galaxies in our photometric redshift slice. The overdensities are peaks determined from smoothing the on-sky distribution with a 1 Mpc circular smoothing kernel to enhance 1 Mpc scale structures.

The Filament Environment

Studies of simulations (Colberg et al. 2005) and superclusters (Einasto et al. 2007a) have shown the irregular distribution of galaxies belonging to filaments, this implies that there is no set way to define a filament. Porter & Raychaudhury (2007) defined filaments as prolate spheroids with the centres of two clusters at each end, for example. We use the area defined by the on sky distribution of the spectroscopically defined filament to construct our photometric filament sample. The spectroscopic filament sample is placed on the coordinate

grid and smoothed with a 2 Mpc radius circular kernel. The low density filament environment makes it difficult to define a divide between field and filament. We use a 2 Mpc smoothing radius to closely trace the spectroscopically defined filament region but still sample enough area to build a meaningful sample. We exclude the masked 6 Mpc radius around A1437 from the filament sample to avoid contamination of the filament sample by cluster galaxies. The smoothed on-sky mask used for defining the filament sample is shown in Fig. 5.4. Again we divide groups in those that lie in the filament (GIF) and those outside the filament (GOF) as discussed in Sect. 2.5.2.

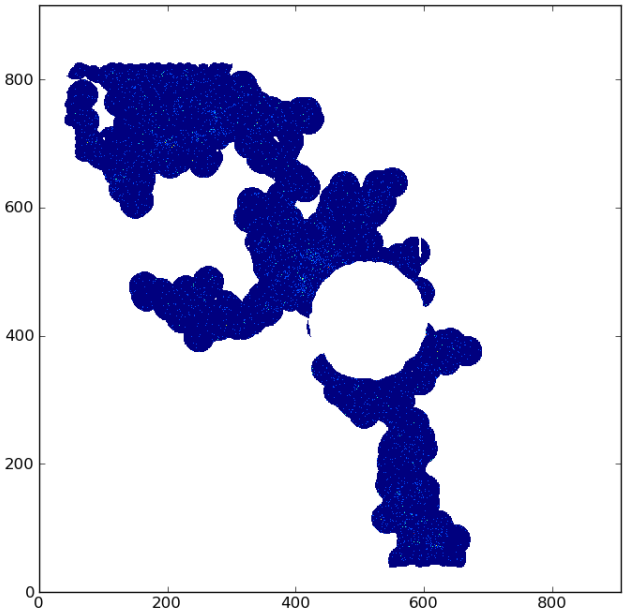

Figure 5.4: On-sky distribution of the filament mask with the cluster sample removed.

The Field Environment

The final step is to create the field sample. We construct the same 2D coordinate grid used to define the group and filament sample. Areas that define the cluster, group and filament samples are masked out and galaxies in the remaining area are considered to be part of the field sample. A map of all the environments with a 2 Mpc masking radius for the groups, 6 Mpc masking radius for the cluster and the fiducial 1 Mpc radius sampling aperture for the cluster and groups is shown in Fig. 5.5.

5.1.3 Galaxy Background Subtraction And Detection Significance

When sampling a region in the redshift slice, the total number of galaxies associated with the region is the sum of the galaxies belonging to the cluster, group or filament, and galaxies belonging to the field population. For this reason we compute the significance of the number of galaxies measured in an area compared to the background field population. To do this we

effectively compute the S/N ratio of the number of galaxies measured in the sampled area, given by the following:

$$\frac{S}{N} = \frac{N_{tot} - \bar{N}_{bg}}{\sqrt{\bar{N}_{bg\_err} + \sigma^2_{f-f} + N_{tot}}} \tag{5.2}$$

The detected signal of galaxies belonging to an overdensity is equal to $S = N_{tot} - \bar{N}_{bg}$, where N_{tot} is the total number of galaxies in the sampling area and $\bar{N}_{bg}$ is the mean background galaxy count. $\bar{N}_{bg}$ is determined by randomly sampling areas in the photometric redshift slice with a 1 Mpc radius circular aperture and computing the average of 500 galaxy count measurements. The total noise (or error), N, consists of three components, which are associated with measurement errors. Firstly, the average error associated with measuring 500 random galaxy counts $\sqrt{\bar{N}_{bg\_err}}$, the field-to-field variation in the random measurements, σ^2_{f-f}, and the Poisson counting error when determining total galaxy counts, $\sqrt{N_{tot}}$. The total noise is determined by calculating the sum of the errors in quadrature. The average background value and error for our photometric redshift slice is 11.44 ± 2.91, with the field-to-field variance being $\sigma^2_{f-f} = 2.02$.

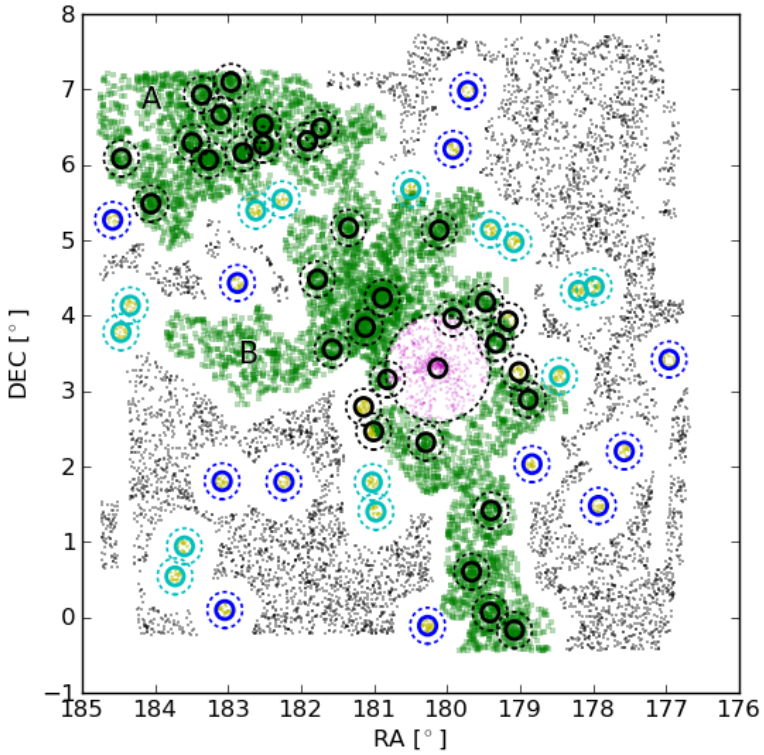

Figure 5.5: An on-sky map indicating the distribution of galaxies in the four predefined environmental samples. The solid circles indicate 1 Mpc fiducial sampling radii and the dashed circles the 2 Mpc masking radii for the groups (yellow markers) and 6 Mpc radius for the cluster (magenta markers). Black circles show candidate groups that lie in the filament (GIF) and the cyan and blue circles show groups with overlapping apertures and isolated groups respectively for GOF. Galaxies in the filament sample are shown as green squares and the field sample as black dots. The large overdensity in the North Eastern corner of the field we refer to as region A and the filamentary structure to the East as region B for future reference. Regions around the filament and groups devoid of galaxies were masked to avoid these samples being contaminated by galaxies in other environments.

5.1.4 Checks On Detected Groups

To confirm that the detected groups are in fact bound in velocity space, we consider the photometric redshift distribution of the groups normalised to their average photometric redshift as a function of radius from the group centre. We have already established an upper limit to the possible foreground contamination of $\sim 25\%$ for spectroscopically well-sampled groups. However, there is the possibility that a detected group belongs to the foreground structure.

Some groups are sparsely sampled spectroscopically, making it difficult to quantify their purity. We therefore inspected the group velocity distributions visually as well. Figure 5.6 is an example of a group sparsely sampled spectroscopically with a well defined photometric redshift overdensity, but low purity.

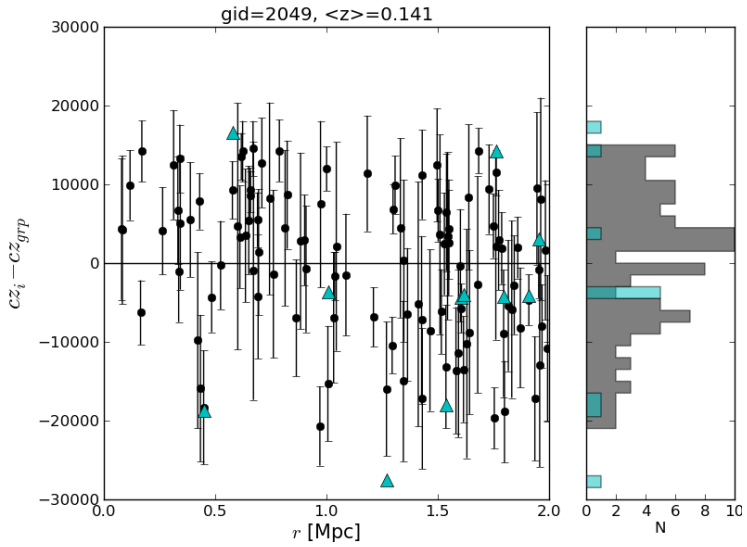

Figure 5.6: An example of the normalised redshift distribution as a function of radius in Mpc for a group with a well defined photometric redshift overdensity, but sparsely sampled spectroscopically. The black circles represent group members with their photometric redshift uncertainties indicated by the error bars. The cyan triangles are sources in the photometric group matched to spectroscopy. Note that some level of foreground contamination remains. The grey and cyan histograms show the photometric and spectroscopically matched redshift distributions respectively.

The top panel in Fig. 5.7 is an example of a group well sampled spectroscopically (solid black line in Fig. 5.2). In this case too, a level of foreground contamination remains. The bottom panel of Fig. 5.7 shows the normalised redshift distribution for a detected group which clearly belongs to the foreground structure. We found 13 groups with similarly low purity that belong to the foreground structure. Our final photometric group catalogue contains 58 groups, of which 13 were identified as foreground groups, which is roughly $\sim 23\%$ of our detected groups. The foreground groups were removed from further analysis, but are still listed in the catalogues below.

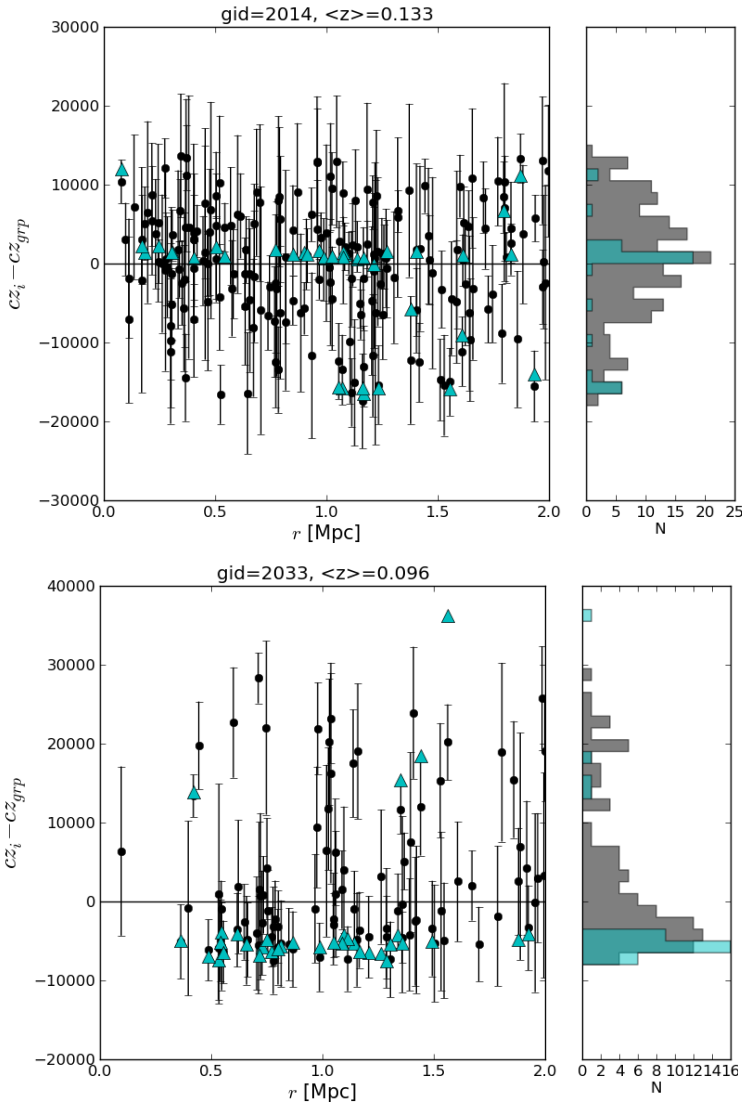

Figure 5.7: Examples of the normalised redshift distributions as a function of radius in Mpc for a spectroscopically well sampled group (top panel) and a foreground group (bottom panel). The black circles represent group members with the error bars indicating the size of individual photometric redshift uncertainties. The cyan triangles are sources in the photometric group matched to spectroscopy.

A map that contains all the positions for the cluster and groups derived from the FoF and photometric group finder is shown in Fig. 5.8. Additionally, we show spectroscopic sources belonging to the foreground structure, defined by $0.06 < z_{spec} < 0.1$. Groups identified as belonging to the foreground structure clearly lie in regions where overdensities in the $0.06 < z_{spec} < 0.1$ structure are located. The significant overdensities of the foreground galaxy distribution show little correlation with the $z = 0.135$ large-scale structure. We therefore do not expect foreground structures to impact our results. The final catalogues of photometric groups are given in Tables 5.1, 5.2 and 5.3. Again we separated groups that lie in the filament (GIF) from those outside the filament (GOF) as discussed in Sect. 2.5.2.

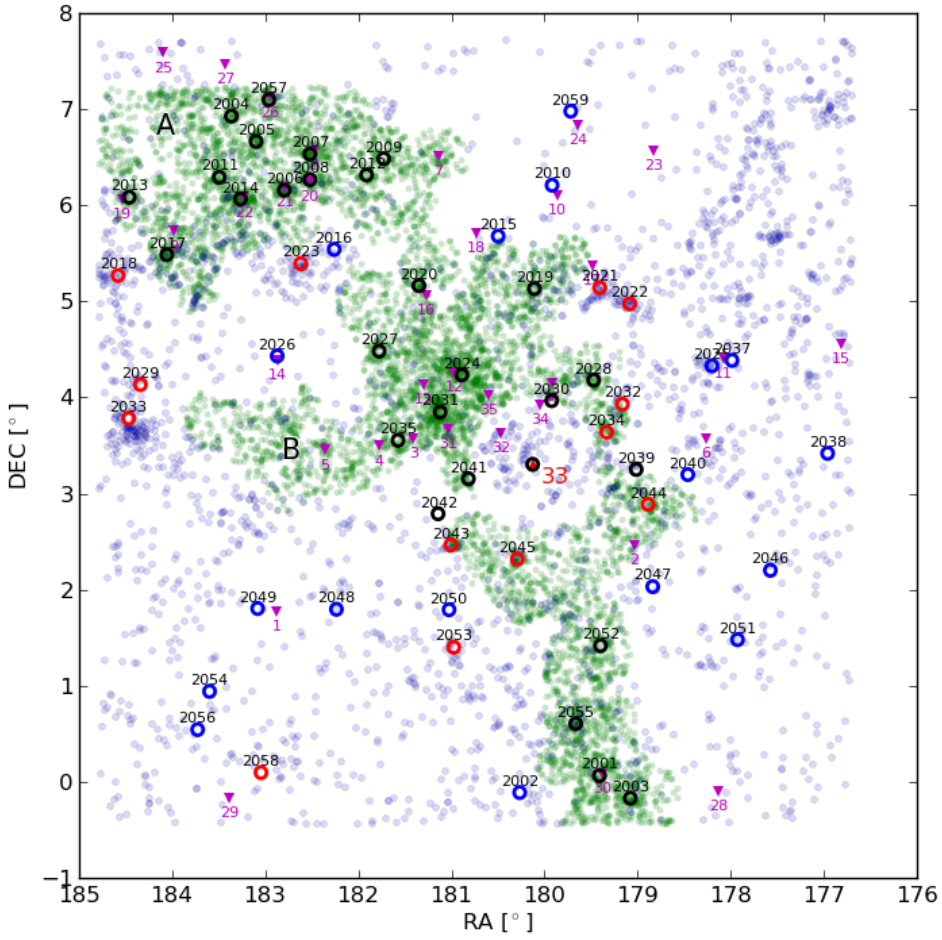

Figure 5.8: A map showing the location of the detected groups and cluster from the spectroscopic FoF and the photometric group finder. The spectroscopically defined cluster is indicated in red; spectroscopic groups are shown as magenta triangles; photometric groups are shown as open black and blue circles for GIF and GOF respectively. Spectroscopic foreground galaxies in the rage $0.06 < z_{spec} < 0.1$ are indicated by the blue dots. Groups identified as belonging to the foreground structure (red circles) clearly lie in regions where overdensities in the $0.06 < z_{spec} < 0.1$ structure are located.

Table 5.1: Catalogue of the groups inside the filament. The internal ID number from the photometric group finder is shown, as well as the mean coordinates of the group galaxies and the background subtracted number of group members, N. Sources cited in the column labelled Other Name are either matches to the FoF catalogue, in which case the FoF ID is cited, or matches to sources in the C4 catalogue.

Groups– GIF				
ID	$\langle RA \rangle$	$\langle DEC \rangle$	N	Other Name
2001	179.41	0.06	35	s:30
2003	179.08	-0.17	47	
2004	183.36	6.93	29	
2005	183.10	6.66	40	
2006	182.80	6.16	62	s:21
2007	182.52	6.53	69	s:8
2008	182.52	6.27	44	s:20
2009	181.73	6.48	30	
2011	183.50	6.29	39	
2012	181.91	6.32	27	
2013	184.46	6.08	25	s:19
2014	183.27	6.07	92	
2015	180.50	5.68	34	
2017	184.06	5.49	44	
2019	180.11	5.13	28	
2020	181.35	5.16	27	
2024	180.89	4.24	65	Abell 1456, C4:1124, s:12
2027	181.78	4.48	41	
2028	179.47	4.18	26	
2030	179.92	3.97	25	
2031	181.12	3.85	110	
2035	181.57	3.55	35	
2039	179.02	3.25	29	
2040	178.46	3.20	29	
2041	180.82	3.15	33	
2042	181.14	2.79	67	
2044	178.89	2.89	27	
2052	179.40	1.42	29	
2055	179.66	0.61	41	
2057	182.96	7.10	36	s:26

Table 5.2: Catalogue of the cluster and the groups outside the filament. The internal ID number from the photometric group finder is shown, as well as the mean coordinates of the group galaxies and the background subtracted number of cluster/group members, N. Sources cited in the column labelled Other Name are either matches to the FoF catalogue, in which case the FoF ID is cited, or matches to sources in the C4 catalogue.

Cluster				
ID	$\langle RA \rangle$	$\langle DEC \rangle$	N	Other Name
33	180.13	3.30	126	Abell 1437, C4:1135
Groups– GOF				
ID	$\langle RA \rangle$	$\langle DEC \rangle$	N	Other Name
2002	180.27	-0.11	68	
2010	179.92	6.21	39	
2016	182.26	5.54	27	
2025	178.20	4.33	42	
2026	182.87	4.43	30	s:14
2037	177.99	4.39	36	s:11
2038	176.96	3.42	26	
2046	177.57	2.20	27	
2048	182.24	1.80	29	
2049	183.08	1.80	33	
2050	181.03	1.79	29	
2051	177.93	1.48	34	
2054	183.60	0.94	27	
2056	183.73	0.54	30	

Table 5.3: Catalogue of the groups detected in the foreground structure. The internal ID number from the photometric group finder is shown, as well as the mean coordinates of the group galaxies and the background subtracted number of group members, N.

Groups– GIF			
ID	$\langle RA \rangle$	$\langle DEC \rangle$	N
2018	184.58	5.27	30
2021	179.41	5.14	37
2022	179.08	4.97	31
2023	182.62	5.39	32
2029	184.34	4.13	26
2032	179.16	3.93	26
2033	184.47	3.78	30
2034	179.33	3.64	26
2043	181.01	2.46	64
2045	180.29	2.32	26
2047	178.84	2.03	30
2053	180.98	1.40	25
2058	183.05	0.10	32

5.2 Measuring Quiescent Fractions

To recap: galaxies which had their SFRs derived from either SED fitting, emission line strengths, or any of the other SFR indicators will be referred to as either active or passive, and the general population of non-star forming galaxies will be referred to as quiescent.

The fraction of quiescent galaxies as a function of environment is calculated using two methods. The first is a simple colour measurement derived from the observed $u-r$ colour distribution. The second method makes use of the sSFR derived from the star formation rates and stellar masses obtained from our MAGPHYS SED fitting.

5.2.1 Quiescent Fraction

The quiescent galaxy fraction is defined as the ratio of quiescent galaxies observed, s, out of a total number of n galaxies, the quiescent fraction is given by:

$$f_{r/p} = \frac{s}{n}, \tag{5.3}$$

where $f_{r/p}$ represents the red or passive galaxy fraction. Under the assumption that s and n obey Poisson statistics, the uncertainty on $f_{r/p}$ is approximated by:

$$\sigma^2(f_{r/p}) = \frac{s(n-s)}{n^3} \tag{5.4}$$

this does not hold for $s = 0$, in which case the error is approximated by $1/(2n)$ (De Propris et al. 2004). For the group sample we compute the standard error of sample means by $\sigma(f_{r/p})/\sqrt{N}$, where N is the number of groups.

5.2.2 Red Fraction Definition

Strateva et al. (2001) showed that the $g-r$ vs. $u-g$ colour-colour distribution is strongly bimodal with an optimal colour separator of $u-r = 2.22$. Through visual inspection they found that the peaks of the bimodal distribution corresponds roughly to early -and late type galaxies, as defined by their concentration parameters, i.e. morphology.

We define red and blue galaxies by using a $u-r$ vs. r_{mag_auto} colour-magnitude diagram (CMD) for the galaxies in our photometric sample. The $u-r$ colour is measured from our fixed aperture magnitudes. Figure 5.9 shows the $u-r$ vs. r_{mag_auto} CMD for photometric redshift slice member galaxies. The dashed red line represents a straight line fit to the Gaussian mean values determined for $u-r$ distributions in $0.^{\mathrm{m}}1$ r_{mag_auto} bins for the red sequence (RS). The Strateva et al. (2001) $u-r$ colour divider is indicated on Fig. 5.9 as the yellow dashed line for comparison. Even though the difference is small, their straight $u-r$ colour divider was based on data limited to $z \sim 0.1$, whereas our sample lies at $z \sim 0.135$.

Instead of defining the red and blue galaxy population with a constant colour cut, we adjust the $u-r$ CM distribution to have a $u-r$ vs. r_{mag_auto} slope of zero. The fitted $(u-r)_{fit,RS}$ colour is subtracted from the red sequence of the observed $(u-r)_{obs}$ colour

for all galaxies. This makes it possible to determine the bimodal colour distribution for the whole sample and define a single $(u-r)_{cor}$ colour discriminator. The minimum of the bimodal distribution was chosen as the $u-r$ colour discriminator. This is shown in Fig. 5.10 by the vertical dashed line at $(u-r)_{obs} - (u-r)_{fit,RS} = -0.50$. The error bars indicated are Poisson number count errors calculated per magnitude bin.

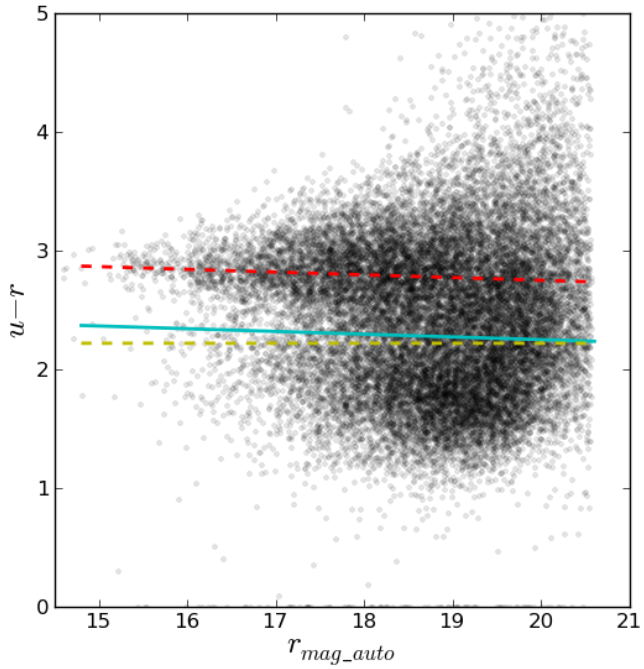

Figure 5.9: $u-r$ vs. r_{mag_auto} for redshift slice members. The dashed red line is a straight line fit to Gaussian mean values determined for $u-r$ distributions in $0.^{\mathrm{m}}1$ r_{mag_auto} bins, which is represented by the following equation: $u-r = -0.023 r_{mag\_auto} + 3.2$. The solid cyan line is the colour divider obtained in Fig. 5.10. The Strateva et. al 2001 $u-r = 2.22$ colour divider is shown as the yellow dashed line.

To correct the cluster, groups and filament sample for background field galaxy contamination we subtract an area scaled $(u-r)_{cor}$ distribution from the cluster, groups and filament $(u-r)_{cor}$ distributions. The $(u-r)_{cor}$ colour distribution as a function of environment is shown in Fig 5.11. The original colour distribution, field subtracted colour distribution and area scaled colour distribution for the field are shown as the magenta histogram, solid black histogram and green histogram respectively. f_r as a function of environment is determined by applying the $(u-r)_{cor} = -0.50$ colour divider on the field galaxy background subtracted histograms.

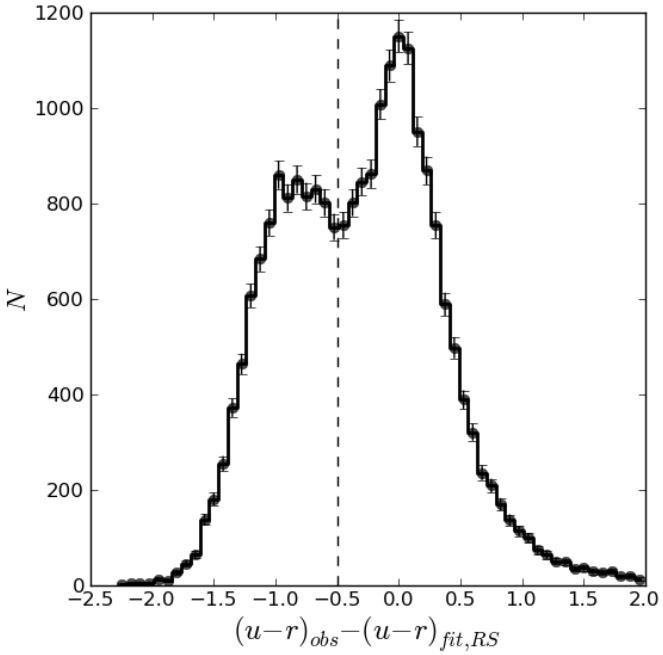

Figure 5.10: The corrected $(u-r)_{cor}$ colour distribution for the whole sample. The vertical dashed line indicates the minimum in the $(u-r)_{cor}$ distribution at $(u-r)_{cor} = -0.50$.

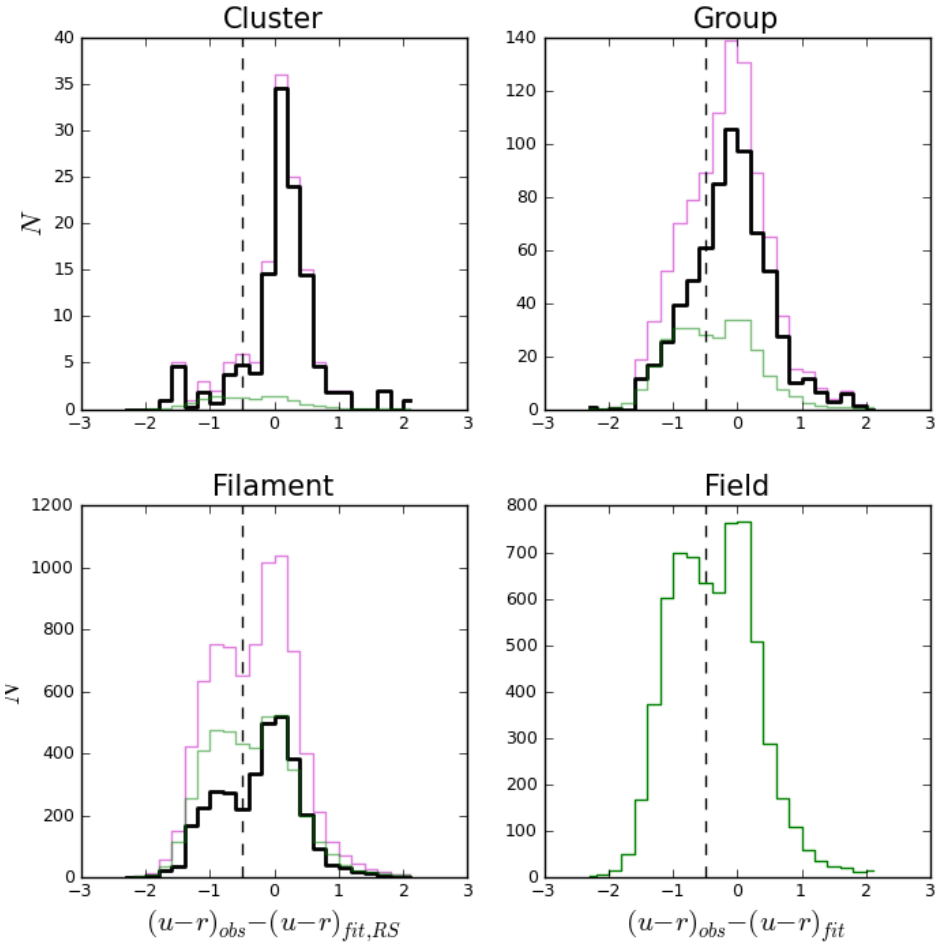

Figure 5.11: Corrected $(u-r)_{cor}$ colour distributions as a function of environment. The black histogram shows the colour distribution after the field histogram (green) has been subtracted from the original colour distribution (magenta). The vertical dashed line indicates the colour divider used to split the distribution into red and blue galaxies.

5.2.3 Stellar Mass Limit

The stellar mass completeness limit of $\log(M_*/M_\odot) = 9.9$ for the photometric sample was derived in Sect. 4.4 and is shown in Fig. 4.16. The effect of imposing the stellar mass limit on the $u - r$ colour–$\log M_*/\mathrm{M}_\odot$ distribution is shown in Fig. 5.12. The stellar mass limit is indicated by the solid vertical line while the slope of the red sequence is indicated by the dashed magenta line.

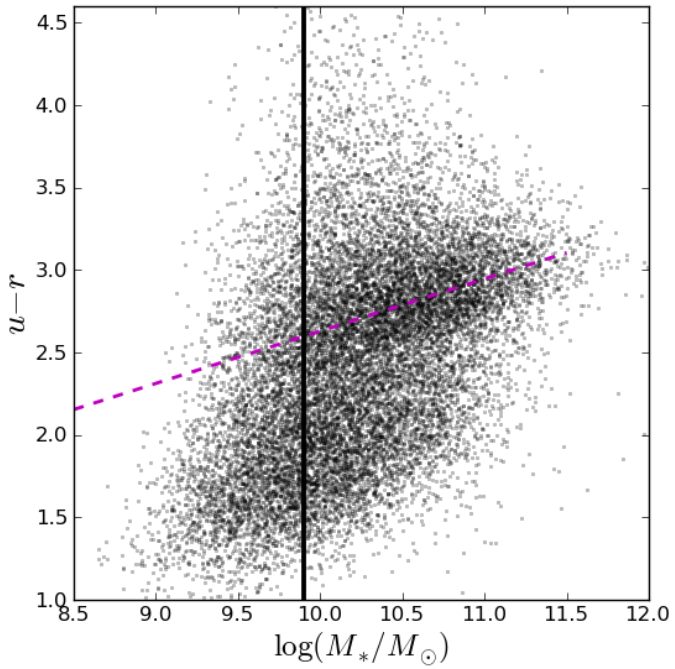

Figure 5.12: The colour-stellar mass diagram for our photometric redshift sample. The diagonal dashed line shows the centre of the red sequence. The solid vertical line indicates the lower mass limit.

5.2.4 Passive Galaxy Fraction Definition

The SFR of a galaxy is a key indicator of galaxy evolution, and for active galaxies there is a strong correlation between star formation rate and stellar mass (e.g. Kauffmann et al. 2003b, Brinchmann et al. 2004, Pence et al. 2010). A useful method to study the SF properties of galaxies is the specific star formation rate, defined as sSFR=SFR/M_*, which is in units of time^{-1}. The sSFR quantifies the current SFR with respect to the past SFR (Kennicutt, Tamblyn & Congdon 1994). To compute the passive galaxy fraction as a function of environment we need to derive similar criteria to what was used when computing red fractions. Assuming all galaxies have formed their stars at a constant rate over the age of the Universe, consider the Hubble time (t_H) at the redshift of interest. Galaxies with a

sSFR less than $1/t_H$ are converting gas into stars at a rate which is higher than their past average over the age of the Universe. These galaxies are classified as actively star forming with $\log(\mathrm{SFR}/M_*) > -10.07$. McGee et al. (2011) used the minimum in their bimodal sSFR distribution, similar to our $(u-r)_{cor}$ distribution, to divide their sample into passive and actively star forming galaxies. Their sample was at a slightly lower redshift, $z \sim 0.08$, for which we expect a 0.64 Gyr age difference. We show the sSFR distribution for our sample in Fig. 5.13 and find the same dividing value of $\log(\mathrm{sSFR}) = -11$ yr^{-1} that McGee et al. (2011) derived.

To determine the passive galaxy fraction as a function of environment, we apply the two passive galaxy fraction dividers and use the same area scaled histogram subtraction method employed to derive the red fractions as a function of environment.

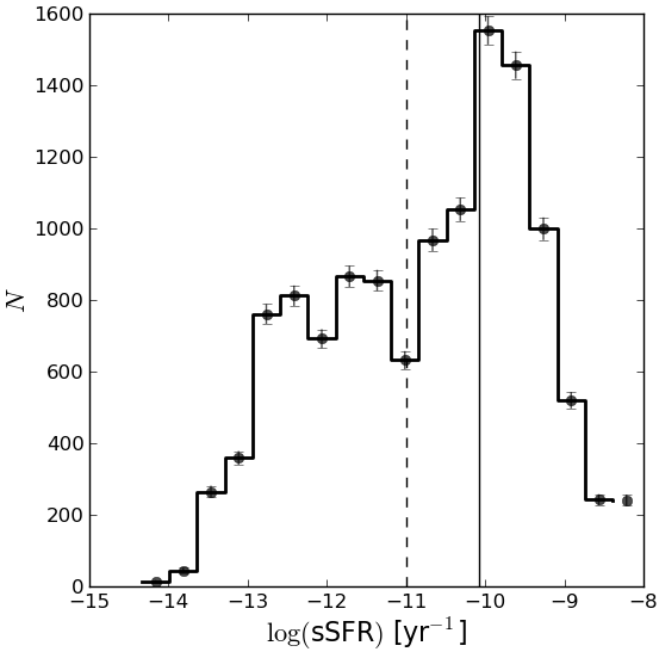

Figure 5.13: sSFR distribution with the minimum indicated by the vertical dashed line at $\log(\mathrm{sSFR}) = -11$ yr^{-1}, which is the same value used by McGee et al. (2011) for their passive galaxy fraction analysis. The $1/t_H$ sSFR divider, $\log(\mathrm{sSFR}) = -10.07$ yr^{-1} is indicated by the vertical solid line.

5.3 Results

The derived red fractions as function of environment for different sampling radii are shown in Fig. 5.14. The results derived using the $P(z) = 0.90$ photometric redshift slice are also indicted on the plot.

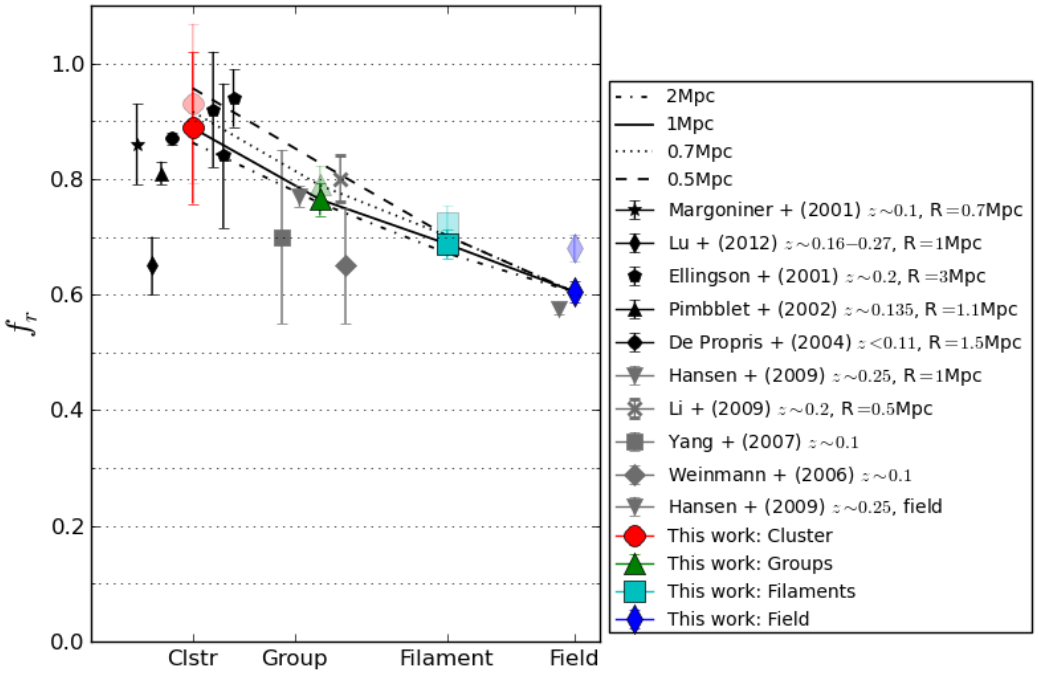

Figure 5.14: f_r calculated for galaxies in the each of the environments. A 1 Mpc radius aperture was used to derive the cluster and group red fractions. Filament and field red fractions were derived from the environmental definitions described in the text. The literature references are summarised in Table 5.4 for comparison in redshift range, sampling radius size, volume limit and measured f_r. f_r derived for the $P(z) = 0.90$ photometric redshift slice are also indicated as the lighter coloured symbols.

To investigate the effect stellar mass selection has on our sample, we impose the earlier derived stellar mass limit on the photometric redshift slice sample. The resulting red fractions as a function of environment are shown in Fig. 5.15. We also indicate the red fraction as a function of environment without the imposed mass limit for reference. The passive galaxy fractions as a function of environment derived from the $1/t_H$ and bimodal sSFR dividers are shown in 5.16. For both these measurements the stellar mass limit was imposed.

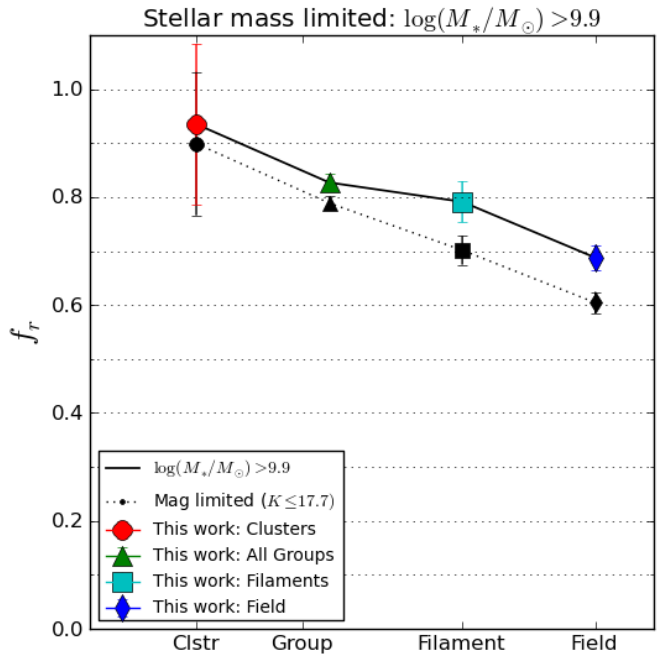

Figure 5.15: Stellar mass limited red fraction as a function of environment, determined from our fiducial 1 Mpc sampling radii. The dotted black line represents the fiducial f_r measurement without an imposed stellar mass limit.

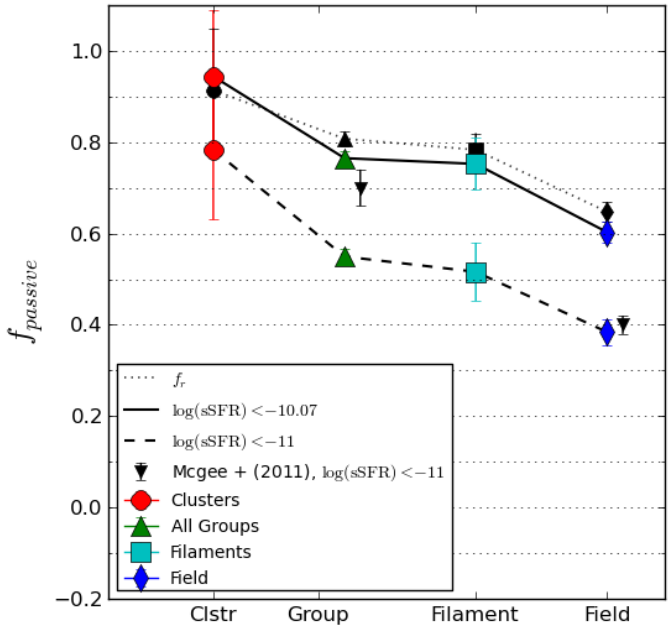

Figure 5.16: Passive galaxy fraction as a function of environment. The passive galaxy fraction was determined by using the $1/t_H$ divider of $\log(\mathrm{sSFR}) = -10.07$ yr^{-1} (solid line) and the bimodal sSFR divider of $\log(\mathrm{sSFR}) = -11$ yr^{-1} (dashed line). The dotted black line shows the red fraction trend as a function of environment for reference. The upside down triangles indicate passive fractions for groups and the field, estimated from McGee et al. (2011).

5.4 Discussion

Previous studies of quiescent fractions of galaxies have typically relied on magnitude limited samples. These studies concentrated largely on clusters and probed a large range of redshifts, typically between $0.1 \lesssim z \lesssim 0.5$. They mostly relied on the colour-magnitude relation (CMR) of red sequence galaxies for the identification of clusters. Studies of group quiescent fractions relied on FoF based algorithms to find associations of galaxies (e.g. Yang et al. 2007). The group finding algorithms generally make use of spectroscopy, but some photometric redshift based techniques have been developed (e.g. Li et al. 2012). Keeping in mind the expected trends with various parameters mentioned in the previous section, we compare our red fraction measurements to those in the literature. It should be made clear that some of these studies determined blue fractions, in which case they were converted to red fractions in order to make comparisons possible. This applies to the Margoniner et al. (2001) results, for example, where we use their blue fraction as a function of redshift to aid in the discussion of trends in red fraction with redshift (Fig. 1.3). Further, we use the trend of red fraction with limiting magnitude found by De Propris et al. (2004) for reference. They showed that a 1 magnitude increase in their limiting magnitude decreased their red fractions by $\sim 5\%$. A summary of the studies used in the comparison is provided in Table 5.4. The observed magnitude limits used in the comparison studies were converted to absolute r band magnitudes using results published by Fukugita et al. (1995).

5.4.1 Red Fraction Dependence on $P(z)$

In Fig. 5.14 we have shown that red fractions derived from 1 Mpc radii for the $P(z) > 0.75$ and $P(z) > 0.90$ photometric redshift slices lie within 1σ for the cluster, groups and filament environments. The difference between the red fractions derived for the field environments are somewhat larger, but still lie within 2σ of the respective measurements. The red fractions as a function of environment therefore only weakly depend on $P(z)$, hence supporting our choice of a more complete group sample by using the $P(z) > 0.75$ slice for the analysis.

5.4.2 Cluster Red Fraction Comparison

We measure a red fraction of $f_{r_c} = 0.9 \pm 0.13$ for our cluster sample using a 1 Mpc sampling radius down to $M_r = -18.7$. The large error on the cluster red fraction will be the dominant cause of uncertainty in our comparison with previous studies, as shown in Fig. 5.14.

We first compare our cluster red fraction to results obtained by Margoniner et al. (2001). They considered a sample of 295 clusters in the redshift range 0.03–0.25. Red fractions were measured using a fixed 0.7 Mpc sampling radius. They derived a parametric form of the red fraction dependence on redshift of $f_r = 1 - [(1.34 \pm 0.11)z - 0.037]$, based on a best fit straight line to their data. This roughly predicts a $\sim 10\%$ decrease in f_r per $0.1z$ increase in redshift. Using their parametric form we obtain a red fraction of 0.86 ± 0.07 at $z = 0.135$. This compares well to our red fraction within the given uncertainties. From

Hansen et al. (2009) we estimated that a 0.5 Mpc decrease in sampling radius could increase the red fraction by $\sim 5\%$. We therefore expect them to have a higher red fraction. The observed difference shown in Fig. 5.14 is most likely due to their sample including higher redshift clusters.

The red fraction result of De Propris et al. (2004) was derived for a sample of 60 clusters in the redshift range $0.02 < z < 0.11$. Their cluster red fraction of 0.87 ± 0.01 was measured using a $r_{200}/2$ (1.5 Mpc) sampling radius. The median redshift of their sample is $z = 0.06$, from which we would have expected a higher red fraction compared to ours. This is most likely offset by their survey being b_j selected and nearly 2 magnitude fainter.

In our comparison with the red fraction measurements of Ellingson et al. (2001), we considered the average red fraction of the three clusters in their lowest redshift bin ($z = 0.2$), as indicated in Fig. 5.14. The three clusters were plotted separately to show the reader what the typical scatter and uncertainties of individual cluster red fraction measurements are like. Their red fractions were measured in a 0.85 Mpc sampling radius for spectroscopically confirmed members only. Taking the observed trends in redshift and radial dependence into account, we expected their red fractions to be lower than ours. A comparison of their red fractions with Margoniner et al. (2001) (Fig. 1.3) also revealed that their red fractions are higher than expected at a redshift of $z = 0.2$. Their higher than expected red fraction could be accounted for by their slightly smaller sampling radius, but is more likely due to their data being shallower than ours by almost 2 magnitudes.

Lu et al. (2012) measured red fractions for a sample of 120 clusters down to a completeness limit of $r = 24$. We only considered their results for the $0.16 < z < 0.27$ redshift bin in which 43 clusters were stacked. They considered the radial dependence of their red fractions from which we estimated a red fraction of 0.65 ± 0.05 at 1 Mpc. This value is much lower than our red fraction, but given the large uncertainties on the measurements we can only classify it as a 2σ difference. The mean redshift of their sample is at $z \sim 0.22$, for which we expected a slightly lower red fraction compared to ours. Additionally, their survey went ~ 1.5 magnitudes deeper than ours which will also tend to lower red fractions.

The most direct comparison in red fraction for our cluster sample comes from the work of Pimbblet et al. (2002). They derived red fractions for a sample of 11 X-ray selected Abell clusters in the redshift range $0.07 < z < 0.16$, which included A1437. They employed a similar method to Butcher & Oemler (1984) for deriving red fractions by limiting their sample to $M_V = -20$ and using a R_{30} (1.1 Mpc) sampling radius. R_{30} is defined as a circular radius containing 30% of the cluster's projected galaxy distribution. After determining which galaxies lie in R_{30}, they perform a statistical background subtraction and determine a richness, N_{30}, for the remaining galaxies. Their colour divider, defined as $\Delta(B-V) = -0.2$ bluer than the fitted red sequence, is then applied to measure a red fraction. Other than a small difference in the definition of colour divisions, our studies essentially measured red fractions for the same galaxies. We expect little difference in the cluster red fraction measurements. Their 0.81 ± 0.02 red fraction, however, is lower than $f_{r_c} = 0.9 \pm 0.13$, which is a considerable difference considering we measured a red fraction from the same galaxy

population. A comparison between the Pimbblet et al. (2002) and De Propris et al. (2004) results shows a lower than expected red fraction as well. Additionally, the small error derived for a sample of $N_{30} = 47$ galaxies seems unrealistically low taking into account that it was derived as a Poissonian number count error, similar to the number of galaxies we measured the red fraction from. The exact reason for the offset is unknown.

5.4.3 Group Red Fraction Comparison

Our group red fraction measurement was derived from 23 groups, defined as GOF in Sect. 5.1.4 and shown in Fig. 5.5. The red fraction measured from our fiducial 1 Mpc sampling radius for the 23 GOF groups is $f_{r_g} = 0.79 \pm 0.01$.

Our first group comparison was to two studies that used similar group finding methods. The red fractions from Weinmann et al. (2006b) are based on a group finding method developed by Yang et al. (2005). The Yang group finder was based on spectroscopic data from the 2dFGRS. They use a modified FoF algorithm that estimates dark matter halo masses from mass-to-light ratios and velocity dispersions of galaxies. Weinmann et al. (2006b) used the group finder to identify 53 229 systems from the SDSS DR2 data. The sample spanned a redshift range of $0.01 < z < 0.2$ and was limited by an absolute magnitude of $M_r > -22.5$. They studied the red fractions of galaxies as a function of luminosity in six dark matter halo mass bins. A group red fraction was estimated from their red fraction vs. luminosity distribution. We estimated a red fraction of 0.65 ± 0.1 by considering an average luminosity and halo mass from their distribution. The uncertainty on their measurement was estimated from the range their red fractions spanned over the halo mass range. Considering the fairly large estimated uncertainty, their red fraction is comparable to our group fraction measurement. The Yang et al. (2008) red fraction measurements were based on SDSS DR4 data with the same observational limits in redshift and magnitude as Weinmann et al. (2006b). Yang et al. (2008) studied the red fraction as a function of halo mass for central and satellite galaxies separately. Their group red fractions were derived by dividing the number of red centrals (satellites) by the number of all centrals (satellites) in a given halo mass bin. The same consideration was not made for our sample. We therefore estimated the average red fraction from their central and satellite red fraction vs. halo mass distribution. Taking the upper and lower red fraction values which fall within the halo mass range, we approximated a red fraction of 0.7 ± 0.15. Considering the estimated error, their red fraction is comparable with our group fraction measurement.

Next, we compared our group red fraction to Hansen et al. (2009). They considered red fractions of 165 597 systems derived using the MaxBCG algorithm (Koester et al. 2007a) in the redshift range $0.1 \leq z \leq 0.3$. The MaxBCG algorithm does not rely on spectroscopy to identify groups. Instead, it only uses photometry and the clustering of galaxies on the sky, in magnitude, and in colour to identify groups. This method has been shown to successfully identify clusters and groups down to low richnesses. For the Hansen et al. (2009) study, magnitudes were k-corrected to $z = 0.25$ and they limited their sample to $i < 21.3$ in

apparent magnitude. To enable a comparison, we had to determine which richness bin closely resembles a typical group in our sample. Equation 10 in Hansen et al. (2009) relates the cluster/group mass to their definition of richness, N_{200}. The typical group velocity dispersion from our spectroscopic FoF groups are $\sim \sigma_v = 350$ km s^{-1}. The typical dynamical mass as derived from Eq. 1.3 is 0.85×10^{14} M$_\odot$. This placed our typical group sample in their $20 \leq N_{200} \leq 29$ bin. Using this richness bin we estimated a group red fraction from their red fraction vs. virial radius distribution. To make a fair comparison to our single 1 Mpc sampling radius we compute the average red fraction for their radial bins out to $r/r_{200} = 1$. The average red fraction uncertainty was divided by the number of radial bins used. Finally, we estimate a red fraction of 0.77 ± 0.02, measured inside $r/r_{200} = 1$ (1 Mpc). This compares well, within the respective uncertainties, to our group red fraction measurement.

Our final group comparison was with Li et al. (2012). They conducted a study of 905 galaxy groups in the redshift range $0.15 < z < 0.52$ down to $M_{R_c} > -19.41$. Their group catalogue was constructed from photometric redshifts using an adapted FoF algorithm developed by Li & Yee (2008), called the probability FoF (pFoF) algorithm. The pFoF algorithm uses an adjustable on-sky linking length which scales with redshift to find galaxies in on-sky associations. Their photometric redshift probability method works on the following principle (see Li & Yee (2008) for details): If one assumes that there is no uncertainty in the redshifts of galaxies consider a redshift z_0. The occurrence of a galaxy or group at z_0 is a δ function. For galaxies with photometric redshifts, consider that galaxy A, galaxy B, ..., n with photometric-redshift probability densities PA(z),PB(z), ..., and Pn(z) form a group at z_0. The group redshift density is the likelihood for all these n members to occur at the same redshift, $\mathrm{P_{group}}(z) = \mathrm{PA}(z)\mathrm{PB}(z) \ldots \mathrm{Pn}(z)$. By joining more galaxy-group members to a group, one can bring down the photometric redshift uncertainty of $\mathrm{P_{group}}(z)$. This method is not too dissimilar from the method employed in our photometric group finder. We, however, pre-selected the redshift we are interested in. Group members were assigned to groups based on the probabilities derived from their photometric redshift errors. Our on-sky distribution smoothing technique is analogous to their on-sky linking length definition. Similar to our method, they have to statistically subtract background galaxies from their groups using an area scaled method. Even though their group redshift errors go down as more group members are assigned to a group, they still have to subtract a background sample which covers all the likelihoods of the galaxies in their sample. Having a redshift slice circumvents this problem since the field galaxies in the slice already cover all likelihoods of those galaxies associated with groups in the slice. From these similar methods one could expect similar results.

We estimated a red fraction from their red fraction vs. radius distribution for the redshift range $0.15 < z < 0.35$. Their red fraction measurement was split into three group mass bins. At a radius of 0.5 Mpc we estimated the average red fraction and divided the average error by $\sqrt{3}$ to obtain 0.8 ± 0.04. This value compares well to our group red fraction within the estimated uncertainties.

5.4.4 Filament Red Fraction Comparison

No comparisons for our filament red fractions are available in the literature. Our filament red fraction measurement of 0.69 ± 0.02 is a new result. No other study has considered the red fraction of galaxies identified as belonging to a filamentary structure. We will return to the filament results in Sect. 5.4.8 of the discussion.

5.4.5 Field Red Fraction Comparison

Considering the respective uncertainties, we find the Hansen et al. (2009) global field red fraction estimate, 0.58 ± 0.01, consistent with our field red fraction $f_{r_f} = 0.60 \pm 0.02$. Their possibly slightly lower field red fraction is mostly likely due to our sample being K band limited.

The large uncertainties on our measurements prevented us from performing a more quantitative comparison to what have been found by previous large studies. Any comparison on a quantitative basis would be difficult, however, due to the different methods employed. These studies also have large internal scatter associated with them, as is apparent from Fig. 1.3. Large surveys that construct 'homogeneous' samples are never truly homogeneous since cluster properties vary considerably, even when stringent selection criteria are applied.

Barring these large uncertainties, we have shown that the methods that were employed in deriving red fractions produced results comparable to previous works. Since Butcher & Oemler (1984), many studies have replicated their result on much larger datasets. More sophisticated methods have made it possible to extend these studies to groups. Throughout these studies, the field galaxy population has been the reference to which the effects of the environments have been measured against. Even though we only have one comparison for the field sample, which compares well, we do not expect any large discrepancies in the field red fraction measurements because the on-sky area we sample is large enough to be representative of the field galaxy population at $z = 0.135$.

Table 5.4: Literature comparison for f_r results. N is the number of clusters/groups in the sample; z range for the redshift considered in the study; Obs. lim. is the quoted magnitude limit for the study; Conv. Lim. is the observed magnitude limit converted to the absolute r band magnitude; f_r is the red fraction measured by the study.

Author	N	R_{sample}	z range	Obs. Lim.	Conv. Lim.	f_r	Comments
This work: Cluster f_r	1	1 Mpc	0.135	$M_K = -21.2$	$M_r = -18.7$	0.9 ± 0.13	K band limited
Margoniner + (2001)	295	0.7 Mpc	0.03–0.25	$M_r = -19.6$	$M_r = -19.8$	0.85 ± 0.07	
Ellingson + (2001)	15	$\sim$0.85 Mpc	0.18–0.55	$M_r = -21.0$	$M_r = -20.0$	0.85 ± 0.12	Spectroscopic members
Pimbblet + (2002)	1	1.1 Mpc	0.135	$M_V = -21.0$	$M_r = -20.1$	0.81 ± 0.02	Abell 1437
De Propris + (2004)	60	1.5 Mpc	$<$0.11	$M_{b_j} = -18.5$	$M_r = -16.5$	0.87 ± 0.01	
Lu + (2012)	43	1 Mpc	0.16–0.27	$r = 24$	$M_r = -16.1$	0.65 ± 0.05	M_r derived at the mean $z = 0.22$.
This work: Group f_r	23	1 Mpc	0.135	$M_K = -21.2$	$M_r = -18.7$	0.79 ± 0.06	
Hansen + (2009)	165 597	$\sim$ 1 Mpc	0.1–0.3	${}^{0.25}M_i = -18.2$	$M_r = -18.6$	0.77 ± 0.02	
Li + (2009)	304	$r_{200}/2$	0.15–0.35	$M_{R_c} = -19.41$	$M_r = -19.14$	0.81 ± 0.04	$\log(M_*/M_\odot) > 10.2$
Weinmann + (2006)	53 229	r_{200}	0.1	${}^{0.1}M_r = -22.5$	${}^{0.1}M_r = -22.5$	0.6 ± 0.10	
Yang + (2007)	301 237	r_{200}	0.1–0.2	${}^{0.1}M_r = -22.5$	${}^{0.1}M_r = -22.5$	0.7 ± 0.15	

5.4.6 Imposing A Stellar Mass Limit On The Red Fraction

The importance of stellar mass in the evolution and observable properties of galaxies has become more evident in recent years. Kauffmann et al. (2003a) showed that SFR and colour strongly depend on stellar mass. A stellar mass-limited survey would therefore be a more physical approach in studying galaxy populations. The effect of applying a stellar mass limit on red fractions as a function of environment are considered in the following section.

We do this by imposing the stellar mass completeness limit derived earlier. The resultant red fractions as a function of environment is shown in Fig. 5.15, with the magnitude limited red fraction indicated for reference.

Imposing the stellar mass limit marginally affects the cluster and group red fractions. The cluster red fraction increased from 0.90 ± 0.13 to 0.93 ± 0.15, while the group red fraction increased from 0.79 ± 0.01 to 0.83 ± 0.02. The stellar mass limited red fractions for the cluster and groups stay well within the respective uncertainties of the magnitude limited red fractions. The effect on the filament and field red fractions were more significant. The filament red fraction increased from 0.70 ± 0.03 to 0.78 ± 0.04 and the field red fraction increased from 0.60 ± 0.02 to 0.69 ± 0.02. The increase in the filament and field red fractions lie outside their respective 1σ uncertainties, which is not statistically significant. The observed trend after imposing the stellar mass limit is an overall increase in red fraction as a function of environment, but more so for the filament and field environments.

To help understand the origin of this trend we refer back to the $u-r$ colour–stellar mass relation in Fig. 5.12, which shows that the imposed stellar mass limit mostly affects galaxies bluer that the red sequence. Comparing the colour space occupied by these galaxies in the CMR (Fig. 5.9), one finds that they roughly populate the fainter end of the magnitude distribution. From both these figures we see that these galaxies occupy regions of low mass-to-light ratios. We therefore speculate that the increasing trend with red fraction is due to a blue, low M_*/L population being excluded, more so in the filament and field samples as compared to the cluster and group samples. A difficulty in relating our results to other studies in terms of environment is that environment is usually defined as a density, whether it be surface or spatial density. No distinctions of environment based on galaxy density were made in our study. We know however, that galaxies in clusters occupy regions of highest galaxy density and galaxies in the field occupy the lower density regions. Our results show an apparent monotonic decrease in red fraction as one steps from our cluster towards field environments. We compare this trend in red fraction with results from Baldry et al. (2006). In figure 11 of Baldry et al. (2006) they show that red fractions for their sample increase almost linearly as a function of increasing density. A direct comparison between our results and theirs is not possible since different parameters were used to derive red fractions. An attempt is made to approximate densities for our environments by assuming that our environmental definitions follow the same trend where the cluster represents the highest density environment, and the field sample the lowest. Adding actual densities to our sample will not aid any of the further discussions. However, we can now refer to galaxies as being in environments of high, intermediate and low density, whereby clusters are classified as a

high density environment, groups as intermediate density environments and the filament and field sample as the low density environments.

The loss of this blue, low M_*/L population after imposing a stellar mass limit seem to happen preferentially in the filament and field environments, i.e. low density environments. The increase in red fractions for the clusters and groups are much smaller and less significant. It is obvious that if a change is due to blue galaxies, it will have little effect in environments with high red fractions.

The fact that we see a similar trend in the cluster and group red fractions implies that these galaxies are either preferentially found in low density environments, or these galaxies do reside in denser environments, but do not have blue colours. If the latter was the case, we would expect to see red low M_*/L galaxies in the colour-mass relation (Fig. 5.9), which is not what we observe. From our results we can conclude that blue, low M_*/L galaxies are preferentially found in less dense environments. For our small sample this effect is not highly significant, but the results for the low density filament and field are convincing enough with increases in red fractions larger than 1σ.

To put our results into perspective, we consider the analysis of De Propris et al. (2004) who found that their red fraction measurements were highly correlated with cluster-centric radius. The field red fraction was found to smoothly increase with increasing density towards clusters. From this evidence they concluded that cluster specific processes could not be responsible for the change in red fraction observed. The more likely explanation would therefore be that local mechanisms, whose efficiency increases with density, plays an important role in the transformation of the blue population of galaxies with increasing density.

Studies using much larger samples have confirmed this trend. Baldry et al. (2006) and Peng et al. (2010), for example, show that this blue low M_*/L galaxy population, known as blue dwarf galaxies, reside mostly in low density environments. Using an empirical approach to study the observed properties of galaxies, Peng et al. (2010) puts forward the idea that for galaxies at $z < 1$ one can separate the evolutionary effects of stellar mass and environment. For galaxies with stellar masses below $\log(M_*/\mathrm{M}_\odot) < 10.0$, environmental processes are thought to play a larger role in the evolution of galaxies, compared to stellar mass. The same is seen in our results.

Even though the trend has been shown before, the fact that we can draw the same conclusion from our sample gives confidence to the methods that were developed to study the galaxy populations as a function of environment. Many previous studies have used NIR luminosity limits, especially K band, to create "stellar mass limited" samples. But, as we have demonstrated, a notable difference between K band and stellar mass selected samples exists.

5.4.7 Passive Galaxy Fraction

We now consider the passive galaxy fraction as a function of environment for our stellar mass limited sample. Figure 5.16 shows the results from using two sSFR divisions to determine passive fractions. The stellar mass limited red fraction results are also indicated for com-

parison. The group passive fraction we obtained is compared to measurements from McGee et al. (2011). They considered passive fractions of galaxies derived from sSFRs. Their study is based on SDSS and CNOC2 photometry and spectroscopy, from which we only consider the results of their SDSS group sample at a median redshift of $z \sim 0.08$. They probed a similar mass range to ours, but did not state any clear stellar mass limit on their sample.

Their group finder is based on a percolation algorithm developed by Carlberg et al. (2001). Their group radius was defined as $1.5r_{200}$, where r_{200} was derived from velocity dispersions of group galaxies. Stellar masses and SFRs for their sample were derived using SED-fitting, similar to ours. Model galaxy SEDs were created using the Bruzual & Charlot (2003) models with a Chabrier (2003) IMF. They also used similar evolutionary tracks, spectral libraries and SFH prescription. The SED fitting on the other hand was performed with code written by McGee et al. (2011).

Their SDSS photometric sample was complemented with GALEX photometry. The break in their sSFR distribution was used as the passive galaxy fraction divider, which was found to be $\log(\mathrm{sSFR}) = -11.0$, similar to what we found. McGee et al. (2011) considered passive fractions as a function of stellar mass from which we estimated an average passive fraction of 0.7 ± 0.04. This is higher than the 0.53 ± 0.018 group passive fraction we computed using $\log(\mathrm{sSFR}) < -11.0$.

The difference in passive fractions is of the order of $\sim 5\%$ when taking the errors into account. Their median redshift at $z = 0.08$ is lower compared to our sample at $z = 0.135$, a viable reason to expect their passive fraction to be higher than ours. Additionally, their SDSS dataset was limited to $M_r \lesssim -20.0$, of the order of 3 magnitudes brighter than our sample at $z = 0.08$. From the observed trends seen in red fractions, we could expect them to measure a higher passive fraction. More subtle effects could also play a role which would not be explained by trends seen in quiescent fractions. For instance, differences in the way sSFRs were derived. The FUV is more sensitive to recent ($\lesssim 100$ Myr) star formation compared to the u band, which is sensitive to star formation on time scales of $\lesssim 1$ Gyr. The difference in sensitivity to recent star formation could therefore imply that we define different populations as passive, which prevents a meaningful comparison between our results. A direct comparison and analysis of where differences can occur lies outside the scope of this thesis. To be able to understand where differences can arise, a full comparison of parameters used to derive stellar masses and star formation rates will have to be done. Even then, the large typical scatter of ~ 0.2–0.3 dex in derived star formation rates could hide small systematic differences.

We now consider the differences in the passive fractions determined using the two sSFR divisions introduced earlier. To aid in the discussion we consider Fig. 5.17. It shows the $\log(\mathrm{sSFR})$ vs. $(u-r)_{cor}$ distribution with the $(u-r)_{cor} = -0.5$ colour divider indicated as the solid vertical line and the sSFR dividers indicated by horizontal dashed lines. The passive fractions derived from the $\log(\mathrm{sSFR}) < -10.07$ divider is systematically higher than the passive fractions derived using $\log(\mathrm{sSFR}) < -11.0$. The obvious explanation for this is that more star forming galaxies are classified as passive when using the $\log(\mathrm{sSFR}) < -10.07$

divider compared to log(sSFR) < -11.0 (see Fig. 5.13), therefore the passive fraction is higher. From Fig. 5.17 one can see that the log(sSFR) < -10.07 divider includes more galaxies that were classified as blue galaxies. This in itself would not be a problem when considering a sample of galaxies belonging to the same environment. Our sample on the other hand consists of a range of environments and therefore densities.

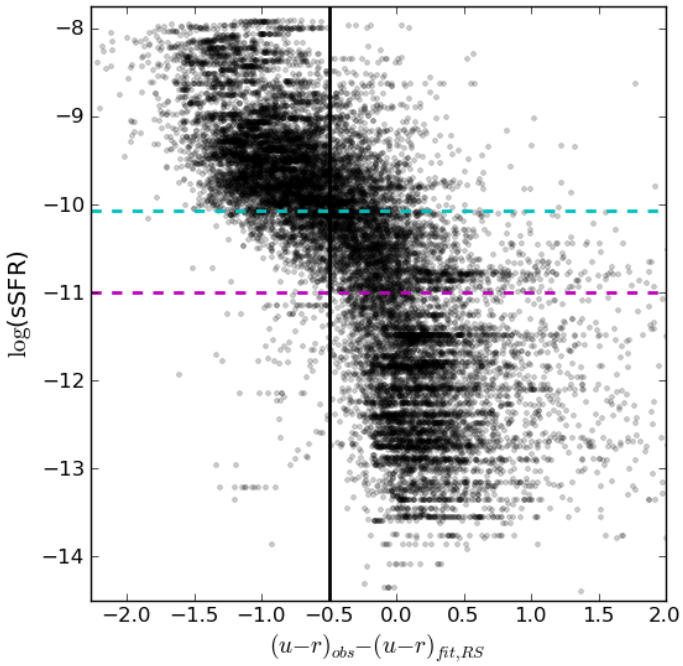

Figure 5.17: log(sSFR) vs. $(u-r)_{cor}$ for the photometric redshift slice sample. The $(u-r)_{cor} = -0.5$ colour is indicated by the vertical black solid line. The $\log(\text{sSFR}) = -10.07\ \text{yr}^{-1}$ passive fraction divider is show by the dashed horizontal cyan line and the bimodal sSFR divider, $\log(\text{sSFR}) = -11\ \text{yr}^{-1}$, is shown as the dashed horizontal magenta line.

In Sect. 5.4.6 we showed that imposing a stellar mass limit has a larger effect on low density environments. The apparent flattening in trend of the passive fraction as a function of environment for the log(sSFR) < -10.07 passive fractions compared to the log(sSFR) < -11.0 passive fractions provides evidence of this. More galaxies are classified as passive in the lower density environments compared to the higher density environments when using log(sSFR) < -10.07. If these two divisions had the same effect on the overall population of galaxies the trend would be exactly the same but just offset from one another. Which one of these passive galaxy fraction definitions is preferable to use when probing a range of densities? As shown by Baldry et al. (2006), the strongly bimodal distribution of the galaxy population persists as a function of density. Only the relative number of galaxies in the bimodal distribution changes. It would therefore seem that this bimodal distribution is the natural division between the populations of galaxies independent of stellar mass or

density. In their study, Wetzel et al. (2012) showed that the bimodal distribution of the sSFR persisted when they considered the halo mass and radial dependence of cluster and group satellite galaxies. Their sample which was drawn from the SDSS showed a similar minimum in sSFR distribution ($\log(\mathrm{sSFR}) \simeq -11.0$). The fraction of galaxies around $\log(\mathrm{sSFR}) \simeq -11.0$ remained unchanged while the relative fractions in their active and passive populations varied relative to each other. Using the observed bimodality of galaxy properties therefore seem like a more natural way to divide galaxy populations and are less susceptible to selection criteria.

It should be noted, however, that imposing a stellar mass limit on the sSFR distribution will have a similar effect to what we found when imposing a stellar mass limit on the colour distribution. One would preferentially increase the passive fraction of less dense environments.

A stellar mass limited sample has been highlighted as being a more physical way to study galaxy populations. What difference does it then make to include star formation information when studying a galaxy population when a colour can be used as a proxy thereof? The answer lies in Fig. 5.17. It shows the contribution of star forming galaxies to the red galaxy population. If one considers galaxies in the region defined by $(u-r)_{cor} > -0.5$ and $\log(\mathrm{sSFR}) < -11.0$, we find that $\sim 30\%$ of the galaxies on the red sequence are star forming.

Haines et al. (2008) found that $\sim 30\%$ of galaxies that lie on the red sequence are actively forming stars, as measured from Hα equivalent widths. Wolf et al. (2009b) confirmed that dusty red galaxies can contribute up to $\sim 30\%$ of the red sequence population as seen in their study of the A901/2 supercluster at $z = 0.17$. Red fraction measurements would therefore be contaminated by dusty red star forming galaxies since they have similar colours as quiescent galaxies on the red sequence. This could be of particular importance when measuring red fractions for individual systems like clusters, where the contribution of red star forming galaxies would be unknown. Much larger samples, as used by Baldry et al. (2006), would average these effects out and lead to the smooth trends observed by these investigators. Even when most precautions against observational biases are taken, the dust content of galaxies will be unknown when using colour to study a star forming galaxy population. One would therefore not be able to obtain the level of accuracy needed to study the underlying galaxy population of these systems, since the unknown number of dusty red galaxies would add additional uncertainties to the results. This is true for our sample. A small number of galaxies identified as having colours redder than the red sequence at the cluster redshift was identified in Fig. 3.21. These galaxies presumably are dusty red star forming galaxies. The smaller galaxies in Fig 3.22 were too faint for spectroscopy. Galaxies labelled as b, e, and g have faint signatures of star formation. The galaxy labelled as c was most probably labelled as red, because only the central region of the galaxy was sampled.

Contamination from dusty star forming galaxies could be negated by knowing the dust content of galaxies. This is the power of SPS modeling. It provides an estimate of the dust content of galaxies. It is therefore a more physical method to study the properties of galaxies.

However, as with any other technique, one needs to understand the uncertainties associated with it. Even though SPS modeling is a powerful technique to study the properties of galaxies, it does rely on a fair amount of assumptions and priors that might not be well understood.

As we have shown in this thesis, special care has to be taken in building a multi-band dataset in order to derive accurate stellar masses and SFRs when using SPS models. A photometric pipeline was specifically developed to perform accurate photometry on a seeing matched dataset. The importance of having a seeing matched dataset was shown, especially when measuring the colours of galaxies in different bands, across different datasets. This will avoid the introduction of biases in galaxy colours. The same applies when only using colours to study galaxy populations. The accuracy of the photometry is very important.

When using colours to study galaxy populations, at least two photometric bands are necessary. SPS modeling on the other hands requires more bands to improve the SED fitting. Including bands more sensitive to recent star formation is beneficial to improving derived star formation rates, but this does imply that large optical surveys need to include rest-frame UV and FIR data, which are better indicators of current star formation (e.g. Salim et al. 2007, Zheng et al. 2007, Bell et al. 2007, da Cunha et al. 2008, McGee et al. 2011, Lu et al. 2012).

Even with a very accurate photometric dataset, a number of assumptions and sometimes not so well understood uncertainties remain when performing SPS modeling. Section 1.10.3 outlined the crucial role the IMF plays in the study of galaxy populations. Still, it remains one of the least well understood parameters in galaxy evolution. Conroy & van Dokkum (2012), van Dokkum & Conroy (2012) and Smith et al. (2012) found evidence that the IMF varies as a function of velocity dispersion, with a steeper (more bottom-heavy) IMF found for more massive galaxies. Davé (2008) considered the implications of an evolving IMF. Still, it remains one of the hottest debated topics in astronomy today, but also one of the most difficult to constrain observationally. The underlying assumption that all galaxies have the same universal IMF has major implications, not only for SPS modeling, but also studies that rely on SAM to predict properties of galaxies. A lot of effort has been spent in trying to determine the universality of the IMF, but this has proven to be a difficult task.

Other parameters that SPS modeling are built upon, the later stages of stellar evolution, stellar libraries and the modeling of the dust content of galaxies all carry a range of assumptions and uncertainties with it. For example, using a Bayesian approach to model the star formation histories already assumes that a population of galaxies can be described by the chosen range or priors which does not necessarily apply to the galaxy population in question.

The above listed uncertainties are inherent in the current state of the art SPS modeling, as the case with the MAGPHYS code used in this project. We attempted to quantify the uncertainties of our derived stellar masses and SFRs by comparing our results to those obtained from methods known to have produced similar estimates of stellar masses and SFRs. We found, that in the best case scenario, when spectroscopic redshifts were used,

our uncertainties were of the order of 0.13 dex in stellar mass and 0.8 dex in SFR. Since the scatter in such a comparison is dependent on the internal scatter of both datasets being compared, we could not conclusively state which dataset made the largest contribution to the scatter.

The difficulty in measuring SFRs for galaxies with very low SFRs contributes to scatter in derived SFRs. The star formation rate indicator used to derive SFRs also plays a role. Brinchmann et al. (2004) derived SFRs from nebular emission lines, which is much more sensitive to recent star formation ($\lesssim$ 10 Myr) compared to the UV continuum measured in the u band ($\lesssim$ 1 Gyr). McGee et al. (2011) found a smaller scatter than we did in their comparison with the Brinchmann et al. (2004) SFRs and ascribed their scatter to the fact that the FUV is only sensitive to star formation in the past $\lesssim$ 100 Myr. When deriving SFR from emission lines, a certain amount of AGN contamination can take place which could also lead to an increase in scatter when comparing results (see Brinchmann et al. (2004) for a further discussion). Considering the comparison of our star forming galaxies to Brinchmann et al. (2004), we found a scatter in SFR of 0.48 dex. The scatter is most likely internal to our SFRs since we are less sensitive to recent star formation, but we cannot rule out a contribution from the Brinchmann SFRs.

Using colour information to study the properties of galaxies is a well used method. As we have shown, there is a certain degree of uncertainty when it comes to red star forming galaxies. It is not as an expensive method, in observing and computing time, as compared to SPS modeling. But, the accuracy required to quantitatively study galaxy populations has made it necessary to seek alternative methods. It is therefore beneficial to compile large multi-band datasets and make use of SPS models to derive stellar masses and star formation rates in order to gain more insight into the evolution of galaxies. However, more effort is required to decrease the uncertainties associated with SPS modeling, otherwise the additional accuracy needed to progress the study of galaxy evolution will always be outside our reach.

5.4.8 The Role Of The Filament Environment

Recently, studies investigating the effects large-scale structure around clusters have on galaxy populations have been intensifying. ΛCDM cosmological simulations predict the continuous growth of rich clusters through the accretion of matter along filaments and smaller scale structures (e.g. Bond et al. 1996, Suhhonenko et al. 2011). Evidence that galaxy transformation occurs at large cluster-centric radii (Lewis et al. 2002, Gómez et al. 2003, Rines et al. 2005, Verdugo et al. 2008) have motivated studies of filaments and their role in the evolution of galaxies. Only a few such studies have been performed, in particular, studies concerned with the effect large-scale structure has on star formation. Porter & Raychaudhury (2007) studied a single filament at $z \sim 0.1$, this study was subsequently extended to 52 filaments in Porter et al. (2008); Fadda et al. (2008) considered a single filament sample at a slightly higher redshift of $z = 0.23$. At much higher redshifts, Geach et al. (2011) and Coppin et al. (2012) considered the inter-connecting large-scale structures between clusters at $z = 0.55$

and $z = 0.9$ respectively.

The studies by Porter & Raychaudhury (2007) and Porter et al. (2008) are the most similar to ours in redshift. They used a spectroscopic survey to study regions between pairs of clusters. They defined star formation activity from the spectral type classification η-parameter (Colless et al. 2001). Their main result concerning the enhancement of star formation is an increase in the average star formation activity (the average spectral type) along filaments between 2–3 Mpc from cluster centres. However, their results based on passive fraction (again derived from η) do not show such an effect, in fact their environmental dependence of passive fraction is extremely comparable to our results (compare their figure 3 of Porter et al. (2008) to our Fig. 5.16).

Fadda et al. (2008) determined SFRs from $ugrizJHK + 24$ μm SED fitting for galaxies with spectroscopic redshifts over half the filament connecting Abell 1770 and Abell 1763. They found that the fraction of active galaxies (starburst from their definition) is higher in the filament compared with both cluster core and cluster outskirts away from the filaments. Our results (Fig. 5.4.7) show good agreement with their passive fractions (1 - active fraction), however, their boundary between active and passive, $\log(\mathrm{sSFR}) = -8.61$, is significantly different from ours ($\log(\mathrm{sSFR}) = -11$).

When comparing to results derived at higher redshift one should be cautious of evolutionary effects. With this in mind we consider the results of Geach et al. (2011), who studied the supercluster Cl 0016+16 using photometric redshifts and separately considered NUV and FIR as star formation indicators. They essentially studied the spatial distribution of actively star forming galaxies defined by these two indicators. They define a fractional excess, Ψ, by dividing this local active fraction by the active fraction of the field. They found a handful of very localised excesses of star forming galaxies.

Finally, at $z = 0.9$ the study by Coppin et al. (2012) measured a lower limit total FIR star formation rate for galaxies in a candidate filament between two clusters. Confirming this as an excess in star formation is complicated by systematic differences from available field samples.

In order to investigate the claimed enhancement of star formation activity in filament environments, we constructed a spatially smoothed map of the cluster and surrounding galaxies which belong to the photometric redshift slice. Additionally, the distribution of actively star forming galaxies across the survey area was considered by computing the fraction of actively star forming galaxies, similar to the Ψ parameter derived by Geach et al. (2011), defined as a fractional excess of star forming galaxies:

$$\Psi = \frac{\text{Local fraction of star forming galaxies}}{\text{Average fraction of star forming field galaxies}} \tag{5.5}$$

We remind the reader that Ψ indicates the location where the probability of any one galaxy undergoing star formation is enhanced ($\Psi > 1$). The average fraction of star forming field galaxies was taken as 1−(field passive fraction)= 0.6, computed in Sect. 5.4.7. A surface overdensity map for galaxies belonging to the photometric redshift slice is shown in

Fig. 5.18, similar to figure 2 of Geach et al. (2011). We reminder the reader that the regions around the filament and groups were masked to avoid the samples being contaminated by field galaxies, which is the reason for these regions being devoid of galaxies. Also, a 6 Mpc masking radius around the cluster ensured a clean filament sample. Groups in the filament (GIF) are indicated by solid circles with 1 Mpc radii. Groups outside of the filament area (GOF) are indicated by dotted circles with 1 Mpc radii. The position of A1437 and two nearby overdense regions, located to the North East (NE) of A1437, are indicated by crosses. The black dotted circle around A1437 represents its $r_{200} \sim 3$ Mpc virial radius. The maps were constructed with a grid scale of $180''$ pixel^{-1} and convolved with a 1 Mpc circular kernel.

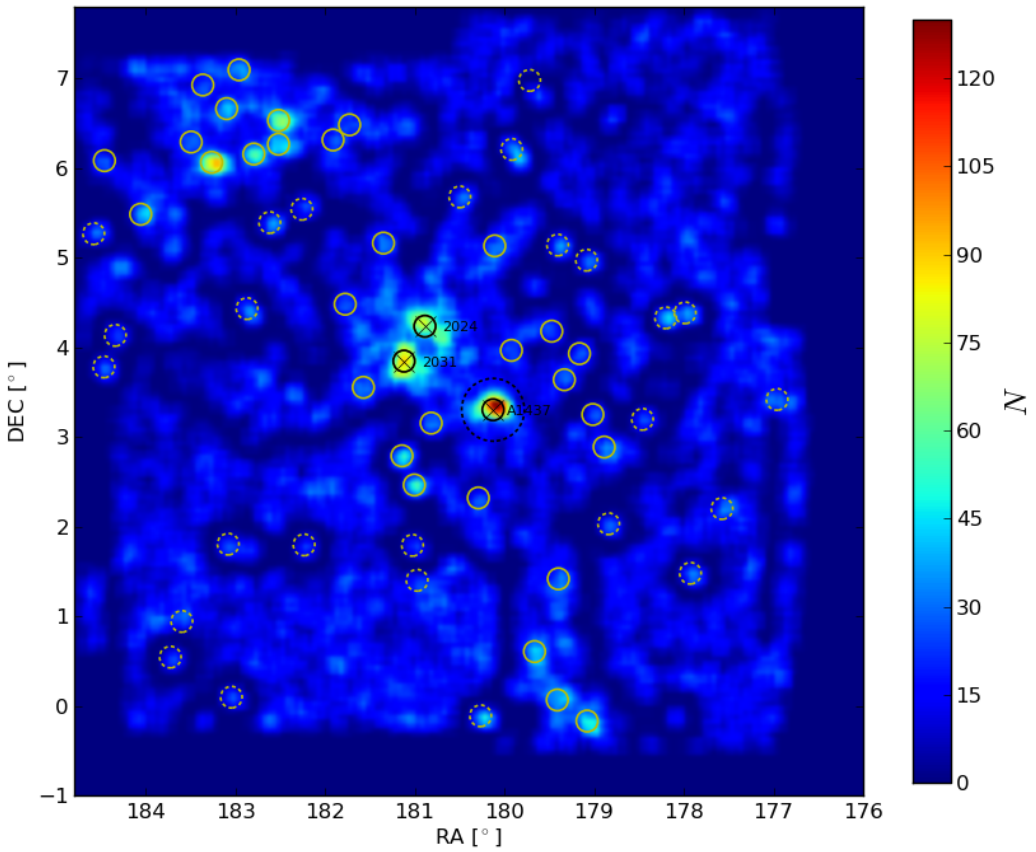

Figure 5.18: Galaxy surface density map for all the galaxies belonging to the photometric redshift slice. Magenta circles with 1 Mpc radii indicate the location of groups residing in the filament (GIF). Groups outside the filament environment (GOF) are indicated by cyan circles. The position of A1437 is indicated by the cross with the dashed circle indicating its $r_{200} \sim 3$ Mpc virial radius. Regions around the filament and groups devoid of galaxies were masked to avoid these samples being contaminated by galaxies in other environments.

Of particular interest is the region connecting A1437 and the two overdensities to the NE. This region shows a fair enhancement in the number density of galaxies connecting the three

overdensities, making it a good candidate for being a supercluster with an interconnecting filament. The NE overdensities were identified as photometric groups: ID:2024 and ID:2031. Group ID:2024 was previously classified as the cluster Abell 1456 (from now on referred to as A1456) (Abell 1958), whereas group ID:2031 has no prior classification. Additionally, A1456 is located in the filament and was treated as part of the filament sample. To ensure that the addition of A1456 to the filament sample, and it being omitted from the group sample does not skew the previously derived results, we recomputed the quiescent fractions and found the results to be consistent.

In Fig. 5.19 we consider the active galaxy fraction, Ψ values greater than 1, as contours on the galaxy density map. The contour values start at $\Psi = 1$ and indicate where there is an increased probability of a galaxy exhibiting ongoing star formation. By considering the fractional excess one takes care of the fact that overdense environments naturally have more galaxies. Regions showing an increase in the probability of finding galaxies with ongoing star formation ($\Psi > 1$) are scattered over the whole survey the area. Groups are indicated by red and black dashed circles to avoid confusion with contours. The groups show no, or very low signatures of excess in the fraction of star forming galaxies within 1 Mpc. Regions with $\Psi > 1$ mostly seem to be anti-correlated with regions of high galaxy density, like the cluster and higher density groups. A region where there is a notable enhancement in the probability of finding galaxies with ongoing star formation is associated with the three significant overdensities in the centre of the survey area: A1437 and the groups identified as ID:2024 and ID:2031 (A1456). The $\Psi > 1$ region seems to follow the interconnecting filamentary structure. We consider a close-up view of this region in Fig. 5.20.

The most striking feature is the region of fractional excess in star formation activity surrounding group ID:2031 which connects the group ID:2024 and A1437 along a filamentary structure. The excess is not smoothly distributed across the region, but seems to be concentrated in pockets smaller than the size of a typical group. There is also an excess on the edge of the virial radius of A1437 which connects to a low density group to the East. This is most likely where the filamentary structure from the NE connects to the cluster as well, as the density profile of the cluster seems somewhat extended in an Easterly direction. The galaxy distributions surrounding the two groups extend in a South Westerly direction towards A1437, and cover a fairly large region of intermediate galaxy density. The positions of individual star forming galaxies with $\log(\mathrm{sSFR}) > -11.0$ are also indicated.

We observe no overlap of the foreground structure with the region of enhanced star formation activity (Fig. 5.8), confirming the enhancement is associated with the large-scale structure at $z = 0.135$. Judging by the number of galaxies enclosed by the contours, it is unlikely that the enhancement in star formation activity is entirely due to shot noise. We asses this by determining the significance of the enhancement from 5000 bootstrap resamplings of Ψ. Ψ was computed for two circular regions with ~ 2 Mpc radii, indicated in Figs. 5.20 and 5.21, which contains the region defined by the $\Psi = 1$ contours. The mean Ψ for the region was found to be 1.04 with an uncertainty of 0.04, making the enhancement significant above the 3σ level.

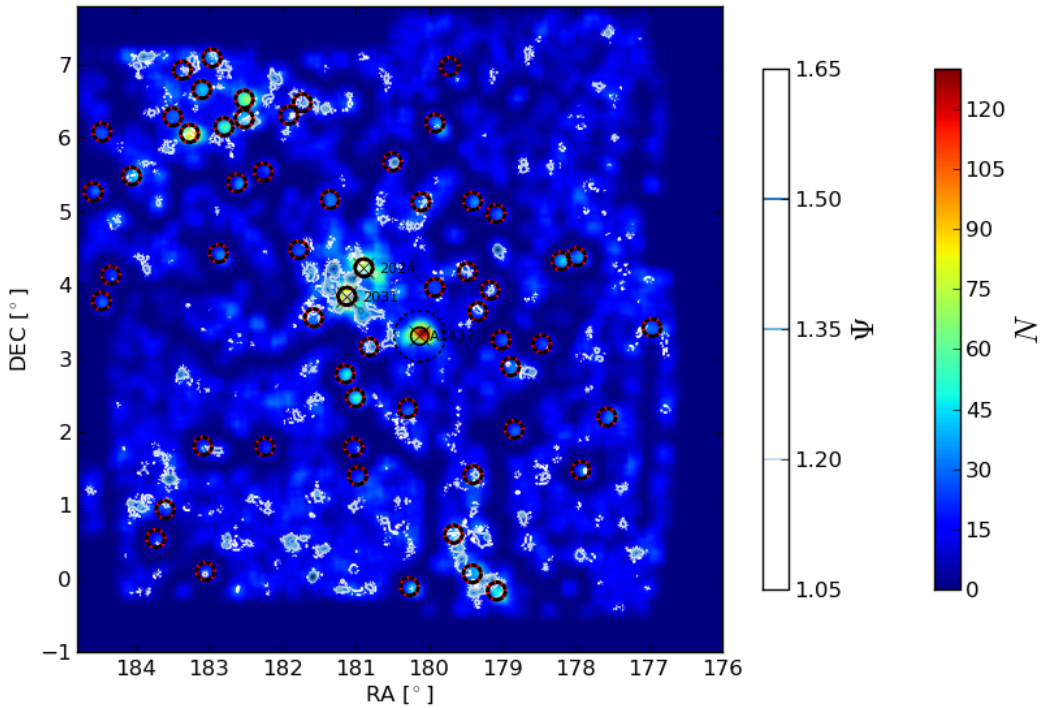

Figure 5.19: Active galaxy fractional excess ($\Psi > 1$) overlaid on the galaxy density map. As in Fig. 5.18, GIF are indicated by magenta circles with 1 Mpc radii and the GOF are indicated by cyan circles. The dashed circle again indicates the $r_{200} \sim 3$ Mpc virial radius of A1437. One of the obvious features is the lack of star forming galaxies in overdense regions, particularly A1437 and two significant overdense group North East (NE) of A1437. Most groups also show very low levels of star formation activity which is consistent with the current picture where the cessation of star forming galaxies takes place in overdense regions. Regions around the filament and groups devoid of galaxies were masked to avoid these samples being contaminated by galaxies in other environments.

How does the enhancement relate to what has been found by other studies? Porter et al. (2008) found an increase in the average spectral type towards more actively star forming galaxies at a distance of 2–3 Mpc from cluster cores. However, this measurement cannot be directly compared to either of the measures in our plots, nor with any of the other paper's measurements. This excess is only seen in one of their radial bins with large errors bars. The large errors bars seen in this one radial bin is puzzling, considering that they constructed bins with equal number of galaxies for their analysis. It is difficult to disentangle whether the enhancement they observe is due to the cluster or the filament since no comparative measurement was taken on the opposite site of the cluster from the filament (as was done, for example by Fadda et al. 2008).

Fadda et al. (2008) found an increase in the starburst galaxy fraction along filaments. They measured this in the cluster outskirts along filaments and at the same distance for the cluster outskirts off-filament. Even though their passive fraction in the cluster core and

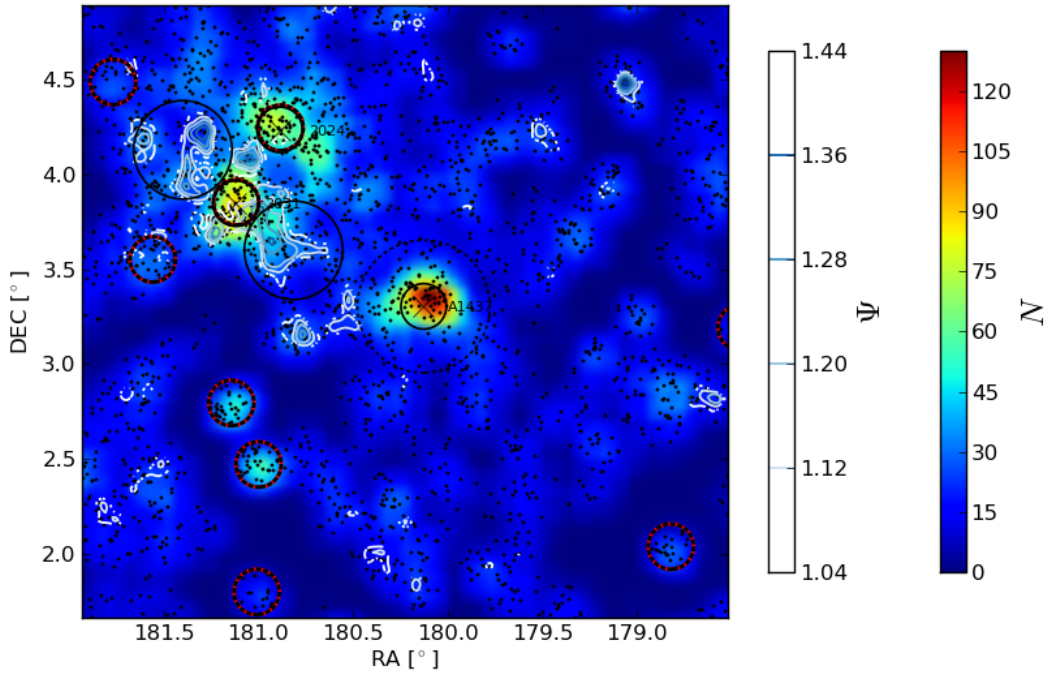

Figure 5.20: A zoomed in version of Fig. 5.19 centred on A1437. Also indicated in the figure are the positions of two fairly significant galaxy overdensities in a NE direction from A1437; the group with ID: 2031 and the group ID: 2024, previously identified as A1456. There is a definite galaxy overdensity between A1437 and the NE overdensity with low levels of fractional excess of star forming galaxies along the interconnecting filamentary structure. The square indicates the region used to determine the significance of the excess in star formation activity.

filament compare well with ours, as described above, they interpret this as an enhancement in star formation in the filament due to their comparison in starburst fractions on and off filament. From their figure 1, counting their galaxies, their relatively small error bars on starburst galaxy fraction are underestimated. Just using Poisson statistics, their filament and outskirts off-filament values becomes consistent. It is therefore difficult to interpret these results as enhancement in star formation activity along the filament.

In contrast, the findings of Geach et al. (2011) do not show any preferential enhancement in the star forming fraction in the direction along filaments. Instead, they find small localised enhancements of the probability of a galaxy exhibiting star formation, which are distributed across their whole survey area. Some of these excesses are based on as few as two galaxies and their significance assessed by bootstrap re-sampling the data. We find similar enhancements across our survey area. Our measurements are essentially the same, except for a normalising factor, but we are cautious of making a direct comparison. Evolutionary effects could play a role since their sample is at a much higher redshift. Their NUV method should be fairly comparable to our SED-fit SFRs. However, they separately consider FIR star formation

which we cannot compare to. It is interesting to note that very few of their enhancements are seen both in the NUV and FIR and they seem to select completely disjoint enhancements.

We have found an excess in star formation activity associated with a filament region as claimed by previous studies. It is difficult, however, to directly compare our results to what was found previously. We therefore also consider work by Verdugo et al. (2012) and Haines et al. (2006), who conducted surveys of superclusters using galaxy colours. They considered galaxy properties as a function of local galaxy density. Haines et al. (2006) studied the fraction of blue galaxies as a function of galaxy density in the Shapley supercluster at $z = 0.05$. They found regions with high fractions of blue galaxies which were anti-correlated with regions of high galaxy density. Regions with high blue galaxy fractions were not preferentially distributed along filamentary structures, but scattered over the survey area (see their Fig. 5). Verdugo et al. (2012) also confirmed a low number of blue galaxies in high-density environments in their study of large scale structure surrounding the massive cluster, $\mathrm{RXJ1347}-1145$ at $z = 0.45$. Additionally, they traced un-obscured star formation using GALEX NUV photometry over their survey area and found that the fraction of GALEX NUV sources as a function of galaxy number density follows the colour-density relation closely. They found regions with larger fractions of blue and/or star-forming galaxies at moderate densities, and considered it evidence that some preprocessing is occurring in the large-scale structure. They stress that they did not find any evidence of enhanced star formation activity in the large scale structure as claimed by Porter et al. (2008) and Fadda et al. (2008). Instead, they find similar pockets of concentrated, but normal, star formation as Geach et al. (2011) did. (see figures 10 and 11 in Verdugo et al. 2012).

Geach et al. (2011) and Verdugo et al. (2012) showed that the average SFRs of star forming galaxies in their respective large scale structures were comparable to the their field samples. This too was shown for spectroscopic surveys, e.g. Verdugo et al. (2008) and Poggianti et al. (2008) used emission line strengths ([OII] and Hα) and found the same; that the mean line strengths of the star forming population is independent of environment. We compared the average sSFRs of our filament and field samples and found average sSFRs of $\langle \log(\mathrm{sSFR}) \rangle = -9.70$ and $\langle \log(\mathrm{sSFR}) \rangle = -9.67$ for the filament and field respectively. These values lie within the scatter of the sSFRs for our sample, we can therefore support the previous findings. We do note, however, that the scatter in our sSFR measurements is reasonably large. Additionally, we calculated the average sSFR for galaxies in the region around group ID:2031, demarcated by the $\Psi = 1$ contours, and found $\langle \log(\mathrm{sSFR}) \rangle = -9.74$. This indicates that there is no appreciable increase in the sSFRs for galaxies in this region and are, on average, comparable to galaxies in the field.

It is interesting to note that the filament in the South Westerly (SW) direction from group ID:2024 shows very little excess in star formation activity compared to the filament extending SW from the group ID:2031, even though they seem to have similar galaxy densities. To investigate the observed difference, we consider a passive fraction density map in Fig. 5.21 with Ψ indicated as before. The filament extending SW from the group ID:2024 contains a region with fairly high passive fractions. This is indicative of a fairly established

population of galaxies which experienced cessation in their star formation. Regions around group ID:2031 where an excess in star formation activity were detected, border on regions with increased passive fractions. These border regions could be where the cessation of star formation takes place and see galaxies being transformed from blue, star forming, to red, quiescent galaxies.

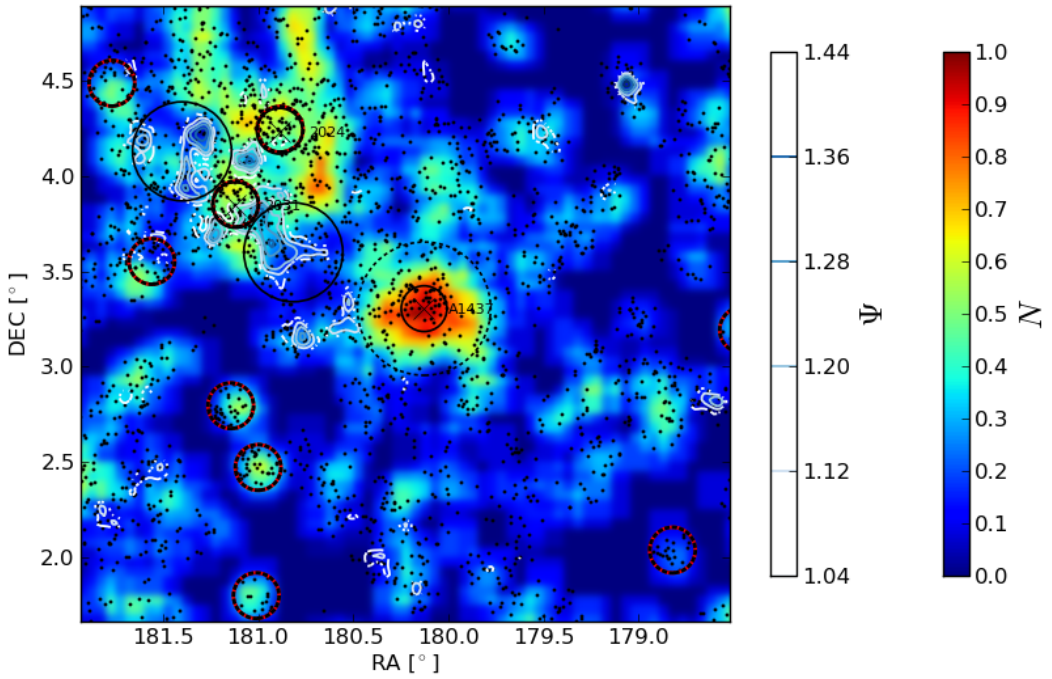

Figure 5.21: A zoomed in view of a passive fraction (f_p) density map with the fractional excess in active galaxies (Ψ) shown as contours. Contour values start at $\Psi = 1$. This figure highlights the high fraction of passive galaxies in the region South West of the group ID: 2024 (A1456). This region is occupied by a population of galaxies which underwent a cessation in star formation. The border between the region were we detect an excess in star formation activity and the region of high passive fraction is potentially interesting. In this region we could expect galaxies to be transformed from blue, star forming galaxies to red, quiescent galaxies. The square indicates the region used to determine the significance of the excess in star formation activity.

A reasonable explanation for the observed enhancement in star formation activity could be the tidal interactions of galaxies. Tidal interactions are thought to operate in low- to intermediate density environments where the relative velocities of galaxies are low. Galaxies passing close enough to each other can interact gravitationally, disturbing their cold gas disk. This can drive gas into their central regions or cause molecular clouds to collapse, triggering bursts of star formation (e.g. Toomre & Toomre 1972, Negroponte & White 1983, Barnes & Hernquist 1991, Barnes 1992, Mihos & Hernquist 1994, Barnes & Hernquist 1996, Mihos & Hernquist 1996). Star bursts, however, are usually associated with substantially enhanced star formation rates compared to that of field galaxies. We have shown there is

no such enhancement in the individual sSFRs for galaxies in the region surrounding the group ID:2024 and filament. We could, alternatively, be seeing regions where galaxies with star formation rates similar to field galaxies are in the process of being accreted onto denser environments. The local galaxy densities could be too low for the cessation of star formation to take place and we therefore observe an increase in the concentration of star forming galaxies. This would show up as a fractional excess in star formation activity according to our definition.

Our study of the filament shows that the filament environment around, and connected to A1437, plays a definite role in the evolution of galaxies. We have found evidence of pre-processing of galaxies in the large-scale structure. This pre-processing appears heterogeneous and is likely to be dependent on particular conditions where multiple mechanisms of transformation are at play.

Chapter 6

Conclusions and Future Work

6.1 Conclusions

This thesis provides the first in-depth study of the galaxy cluster Abell 1437 at $z = 0.135$ and its extended surrounding large-scale structure. Through the use of techniques developed for this project, we have characterised the large scale structure and star formation properties of galaxies in a 64 $\square^{\circ}$ area centred on Abell 1437. The distribution of galaxies in the large-scale structure was used to construct samples of galaxies as a function of their local environment. Photometric redshifts provide distance information, which together with the on-sky distribution of galaxies, allowed us to detect group-sized overdensities at the cluster redshift. We used spectroscopically identified large-scale structures to define a region from which a photometric filament sample was built. This is the first time a filament sample has been constructed in such a way. Four environmental samples were constructed; a cluster sample, which contains Abell 1437; a group sample, containing 58 groups; a filament sample and a field sample. The most exciting discovery were filamentary structures that connect A1437 with a pair of overdensities which shows significant enhancement in the fractional excess of star forming galaxies.

To carry out this investigation we made use of a large area multi-band imaging dataset covering the $ugrizJHK$ bands obtained from the SDSS and UKIDSS surveys. The imaging dataset was complemented by a spectroscopic dataset from the SDSS and 2dF which provided a near uniform coverage over the whole survey area. Most of the analysis was dependent on high accuracy photometry. A photometry pipeline was developed to produce seeing-matched aperture magnitudes for galaxies in order to obtain accurate colours for galaxies. During the development of the pipeline it was found that the photometric catalogue for the UKIDSS data contained spurious photometry. It was therefore decided that the photometry pipeline would incorporate the photometric calibrations of the UKIDSS data as well.

In order to characterise the large-scale structure surrounding A1437, an adapted FoF algorithm was employed to firstly identify clusters and groups of galaxies, and secondly, to

identify larger scale structures like filaments. We were successful in identifying groups that have not been catalogued before, as well as a filamentary structure linked to A1437.

Because the spectroscopic data were limited in depth, a meaningful study of the properties of the galaxies identified from the spectroscopy was not possible due to the bright completeness limit. We developed further techniques to study the galaxies associated with the spectroscopically identified environments using photometric data. SDSS photometric redshifts provided distance information, together with the on-sky distribution of galaxies associated with the large-scale structure allowed to identify overdensities of galaxies. Photometric redshifts have large errors which is problematic for identifying which galaxies belong at the redshift of the spectroscopically identified large scale structure. A method was developed to assign probabilities ($P(z)$) to galaxies. Based on their photometric redshift error it was decided whether they belong to the large scale structure or not. We investigated the influence of $P(z)$ on groups detected in the photometric redshift slice. Our analysis, however, was not critically dependant on the specific choice of $P(z)$, within a realistic range, because we employed a statistical background subtraction technique which compensates for background field galaxy contamination. We were, however, cautious of the large-scale structure at $z \sim 0.08$. The purity and completeness values for a sample of spectroscopically well-sampled groups were determined for photometric redshift slices created using a range of $P(z)$ values. It was found that the contamination due to the foreground structure was 25% at its worst. Because we could not completely remove the foreground contamination by increasing $P(z)$, we decided to ensure a complete sample instead and elected to use the $P(z) > 0.75$ photometric redshift slice for our analysis.

Stellar masses and star formation rates were derived using the state-of-the art SED fitting code, MAGPHYS, fitting to the Bruzual & Charlot (2003) SPS models.

- Within our observed uncertainties, we were able to confirm that the methods developed to create the environmental samples yielded representative populations of galaxies typically expected in these environments. This was done by first establishing the observed trends of red and passive fractions over a range of observed parameters. Previous results obtained for similar studies were then compared to our values on an environment-by-environment basis, taking into account the observational differences. Not only were we able to successfully compare our results with others, we also found that the samples produced previously known trends in red and passive fractions. The significance of our results are however limited by our small sample size. We found consistently that our defined environments follow a trend of decreasing local galaxy density from cluster to group, group to filament, and filament to field environment. This allowed a qualitative comparison of the observed trends as a function of density.

- The importance of having a stellar mass-limited sample was investigated by studying the effect of imposing a stellar mass limit on the red fractions as a function of environment. The results we obtained showed that imposing a stellar mass limit preferentially increases the red fractions measured for less dense environments, in our case,

the filament and the field environments. The increase in red fraction was due to the exclusion of blue dwarf galaxies which are more numerous in less dense environments. The change in red fractions after imposing the stellar mass limit showed that a K-band limited sample cannot be viewed as being a stellar mass limited sample. Even though it samples more of the older stellar population, and therefore is a better estimate of stellar mass compared to the r or V band limited samples, it still is not a truly stellar mass limited selection criterion. It is therefore important to study the fundamental properties of galaxies i.e. their stellar mass and star formation rates to gain better insight into the evolution of galaxies and the role environment plays in shaping the properties of galaxies.

- We studied the passive fraction of galaxies as a function of environment using specific star formation rates. Passive fractions were computed using two different definitions of passiveness. Firstly, we computed red fractions using $1/t_H$ where t_H is the age of the Universe at the redshift of the cluster. This is a well known method used to study starburst galaxies. Galaxies with a $\log(\mathrm{sSFR}) < 1/t_H$ were classified as being passive. At the redshift of the cluster $1/t_H = -10.07$. Secondly, passive fractions as a function of environment were computed using the minimum in the bimodal sSFR distribution as the division between active and passive. The minimum was found to be at $\log(\mathrm{sSFR}) = -11.0$. The impact of the two definitions was assessed and we found that the $\log(\mathrm{sSFR}) = -10.07$ division preferentially excludes actively star forming galaxies from the low density environments. We find that the $\log(\mathrm{sSFR}) = -11.0$ bimodal divider is a natural division between active and passive galaxies and does not suffer from density-dependent selection effects.

- We found that a considerable amount ($\sim 30\%$) of galaxies classified as red are still actively forming stars according to their sSFRs. This is similar to what was found previously in studies using spectroscopically derived star formation rates (e.g. Haines et al. 2008, Wolf et al. 2009b).

- For the filament sample we considered the fractional excess of star forming galaxies, Ψ, which indicates the location where the probability of any one galaxy undergoing star formation is enhanced. We confirmed the findings of previous studies: a region where there is a notable enhancement in the probability of finding galaxies with ongoing star formation. The $\Psi > 1$ region seem to follow the interconnecting filamentary structure between A1437 and the groups identified as ID:2024 and ID:2031 (A1456). A reasonable explanation for the observed enhancement in star formation activity could be the tidal interactions of galaxies triggering bursts of star formation. Star bursts, however, are usually associated with substantially enhanced star formation rates compared to that of field galaxies. We found no enhancement in the individual sSFRs for galaxies in the region surrounding the group ID:2024 and filament. We alternatively speculate that we could be seeing regions where galaxies with star formation rates similar to field galaxies are in the process of being accreted onto denser environments. The local

galaxy densities could be too low for the cessation of star formation to take place and we therefore observe an increase in the concentration of star forming galaxies. This would show up as a fractional excess in star formation activity according to our definition.

- Our study has pushed the limits of what is observationally possible with data from the SDSS. We developed software and new methods to make use of the state of the art SPS models. From our results, we have shown that the effort in deriving stellar masses and SFRs pays off in the form of having a better handle on the fundamental properties of galaxies.

6.2 Future Work

- An observational program aimed at obtaining multi-object spectroscopy for galaxies of interest has been awarded time on the Southern African Large Telescope (SALT). We therefore have the opportunity to perform an in depth study of the galaxies located along the filament connecting A1437 and A1456 and the surrounding area. This will allow us to build a detailed three dimensional picture of the galaxy distribution surrounding A1437 and the filament to much higher precision than is possible with photometric redshifts. We will also attain more accurate star formation rates and stellar masses for these galaxies using spectroscopy. A spin off of the SALT data would be that we can better characterise the performance of the MAGPHYS models at lower luminosities as well as help improve the photometric group finder.

- Extending our wavelength coverage to the NUV and FIR will provide us with a better handle on the total SFRs of galaxies, especially for galaxies with highly obscured SFR, which as we showed make up a considerable fraction of our sample. Publicly available data from GALEX and WISE will therefore be integrated into our future dataset.

- The techniques that have been developed for this project are scalable to larger samples. Our aim is to construct a larger sample of supercluster environments and perform an in depth study similarly to what was done in this thesis. We have shown that the cutting edge techniques employed in this study yield new and interesting results. The discovery of the significant excess in star forming galaxies along the filament makes for a very interesting future project. Increasing our sample size to $\sim$ 10 filaments could provide us with significant enough results to address questions pertaining to the drivers behind the evolution of galaxies in these rarely studied environments.

Bibliography

Abazajian, K., Adelman-McCarthy, J. K., Agüeros, M. A., Allam, S. S., Anderson, K., Anderson, S. F., Annis, J., Bahcall, N. A., Baldry, I. K., Bastian, S., Berlind, A., Bernardi, M., Blanton, M. R., Bochanski, Jr., J. J., Boroski, W. N., Briggs, J. W., Brinkmann, J., Brunner, R. J., Budavári, T., Carey, L. N., Carliles, S., Castander, F. J., Connolly, A. J., Csabai, I., Doi, M., Dong, F., Eisenstein, D. J., Evans, M. L., Fan, X., Finkbeiner, D. P., Friedman, S. D., Frieman, J. A., Fukugita, M., Gal, R. R., Gillespie, B., Glazebrook, K., Gray, J., Grebel, E. K., Gunn, J. E., Gurbani, V. K., Hall, P. B., Hamabe, M., Harris, F. H., Harris, H. C., Harvanek, M., Heckman, T. M., Hendry, J. S., Hennessy, G. S., Hindsley, R. B., Hogan, C. J., Hogg, D. W., Holmgren, D. J., Ichikawa, S.-i., Ichikawa, T., Ivezić, Ž., Jester, S., Johnston, D. E., Jorgensen, A. M., Kent, S. M., Kleinman, S. J., Knapp, G. R., Kniazev, A. Y., Kron, R. G., Krzesinski, J., Kunszt, P. Z., Kuropatkin, N., Lamb, D. Q., Lampeitl, H., Lee, B. C., Leger, R. F., Li, N., Lin, H., Loh, Y.-S., Long, D. C., Loveday, J., Lupton, R. H., Malik, T., Margon, B., Matsubara, T., McGehee, P. M., McKay, T. A., Meiksin, A., Munn, J. A., Nakajima, R., Nash, T., Neilsen, Jr., E. H., Newberg, H. J., Newman, P. R., Nichol, R. C., Nicinski, T., Nieto-Santisteban, M., Nitta, A., Okamura, S., O'Mullane, W., Ostriker, J. P., Owen, R., Padmanabhan, N., Peoples, J., Pier, J. R., Pope, A. C., Quinn, T. R., Richards, G. T., Richmond, M. W., Rix, H.-W., Rockosi, C. M., Schlegel, D. J., Schneider, D. P., Scranton, R., Sekiguchi, M., Seljak, U., Sergey, G., Sesar, B., Sheldon, E., Shimasaku, K., Siegmund, W. A., Silvestri, N. M., Smith, J. A., Smolčić, V., Snedden, S. A., Stebbins, A., Stoughton, C., Strauss, M. A., SubbaRao, M., Szalay, A. S., Szapudi, I., Szkody, P., Szokoly, G. P., Tegmark, M., Teodoro, L., Thakar, A. R., Tremonti, C., Tucker, D. L., Uomoto, A., Vanden Berk, D. E., Vandenberg, J., Vogeley, M. S., Voges, W., Vogt, N. P., Walkowicz, L. M., Wang, S.-i., Weinberg, D. H., West, A. A., White, S. D. M., Wilhite, B. C., Xu, Y., Yanny, B., Yasuda, N., Yip, C.-W., Yocum, D. R., York, D. G., Zehavi, I., Zibetti, S., & Zucker, D. B. 2004, AJ, 128, 502

Abazajian, K. N., Adelman-McCarthy, J. K., Agüeros, M. A., Allam, S. S., Allende Prieto, C., An, D., Anderson, K. S. J., Anderson, S. F., & et al. 2009, ApJS, 182, 543

Abell, G. O. 1958, ApJS, 3, 211

Adelman-McCarthy, J. K., Agüeros, M. A., Allam, S. S., Allende Prieto, C., Anderson, K. S. J., Anderson, S. F., Annis, J., Bahcall, N. A., Bailer-Jones, C. A. L., Baldry, I. K., Barentine, J. C., Bassett, B. A., Becker, A. C., Beers, T. C., Bell, E. F., Berlind, A. A., Bernardi, M., Blanton, M. R., Bochanski, J. J., Boroski, W. N., Brinchmann, J., Brinkmann, J., Brunner, R. J., Budavári, T., Carliles, S., Carr, M. A., Castander, F. J., Cinabro, D., Cool, R. J., Covey, K. R., Csabai, I., Cunha, C. E., Davenport, J. R. A., Dilday, B., Doi, M., Eisenstein, D. J., Evans, M. L., Fan, X., Finkbeiner, D. P., Friedman, S. D., Frieman, J. A., Fukugita, M., Gänsicke, B. T., Gates, E., Gillespie, B., Glazebrook, K., Gray, J., Grebel, E. K., Gunn, J. E., Gurbani, V. K., Hall, P. B., Harding, P., Harvanek, M., Hawley, S. L., Hayes, J., Heckman, T. M., Hendry, J. S., Hindsley, R. B., Hirata, C. M., Hogan, C. J., Hogg, D. W., Hyde, J. B., Ichikawa, S.-i., Ivezić, Ž., Jester, S., Johnson, J. A., Jorgensen, A. M., Jurić, M., Kent, S. M., Kessler, R., Kleinman, S. J., Knapp, G. R., Kron, R. G., Krzesinski, J., Kuropatkin, N., Lamb, D. Q., Lampeitl, H., Lebedeva, S., Lee, Y. S., Leger, R. F., Lépine, S., Lima, M., Lin, H., Long, D. C., Loomis, C. P., Loveday, J., Lupton, R. H., Malanushenko, O., Malanushenko, V., Mandelbaum, R., Margon, B., Marriner, J. P., Martínez-Delgado, D., Matsubara, T., McGehee, P. M., McKay, T. A., Meiksin, A., Morrison, H. L., Munn, J. A., Nakajima, R., Neilsen, Jr., E. H., Newberg, H. J., Nichol, R. C., Nicinski, T., Nieto-Santisteban, M., Nitta, A., Okamura, S., Owen, R., Oyaizu, H., Padmanabhan, N., Pan, K., Park, C., Peoples, Jr., J., Pier, J. R., Pope, A. C., Purger, N., Raddick, M. J., Re Fiorentin, P., Richards, G. T., Richmond, M. W., Riess, A. G., Rix, H.-W., Rockosi, C. M., Sako, M., Schlegel, D. J., Schneider, D. P., Schreiber, M. R., Schwope, A. D., Seljak, U., Sesar, B., Sheldon, E., Shimasaku, K., Sivarani, T., Smith, J. A., Snedden, S. A., Steinmetz, M., Strauss, M. A., SubbaRao, M., Suto, Y., Szalay, A. S., Szapudi, I., Szkody, P., Tegmark, M., Thakar, A. R., Tremonti, C. A., Tucker, D. L., Uomoto, A., Vanden Berk, D. E., Vandenberg, J., Vidrih, S., Vogeley, M. S., Voges, W., Vogt, N. P., Wadadekar, Y., Weinberg, D. H., West, A. A., White, S. D. M., Wilhite, B. C., Yanny, B., Yocum, D. R., York, D. G., Zehavi, I., & Zucker, D. B. 2008, ApJS, 175, 297

Alonso, M. S., Tissera, P. B., Coldwell, G., & Lambas, D. G. 2004, MNRAS, 352, 1081

Alpher, R. A. & Herman, R. 1948, Nature, 162, 774

Andreon, S. & Ettori, S. 1999, ApJ, 516, 647

Andreon, S., Lobo, C., & Iovino, A. 2004, MNRAS, 349, 889

Andreon, S., Maughan, B., Trinchieri, G., & Kurk, J. 2009, A&A, 507, 147

Angulo, R. E., Lacey, C. G., Baugh, C. M., & Frenk, C. S. 2009, MNRAS, 399, 983

Bahcall, N. A., Batuski, D. J., & Olowin, R. P. 1988, ApJ, 333, L13

Bahcall, N. A., McKay, T. A., Annis, J., Kim, R. S. J., Dong, F., Hansen, S., Goto, T., Gunn, J. E., Miller, C., Nichol, R. C., Postman, M., Schneider, D., Schroeder, J., Voges, W., Brinkmann, J., & Fukugita, M. 2003, ApJS, 148, 243

Bahcall, N. A. & Oh, S. P. 1996, ApJ, 462, L49

Baldry, I. K., Balogh, M. L., Bower, R. G., Glazebrook, K., Nichol, R. C., Bamford, S. P., & Budavari, T. 2006, MNRAS, 373, 469

Baldry, I. K. & Glazebrook, K. 2003, ApJ, 593, 258

Baldry, I. K., Glazebrook, K., Brinkmann, J., Ivezić, Ž., Lupton, R. H., Nichol, R. C., & Szalay, A. S. 2004, ApJ, 600, 681

Baldry, I. K., Robotham, A. S. G., Hill, D. T., Driver, S. P., Liske, J., Norberg, P., Bamford, S. P., Hopkins, A. M., Loveday, J., Peacock, J. A., Cameron, E., Croom, S. M., Cross, N. J. G., Doyle, I. F., Dye, S., Frenk, C. S., Jones, D. H., van Kampen, E., Kelvin, L. S., Nichol, R. C., Parkinson, H. R., Popescu, C. C., Prescott, M., Sharp, R. G., Sutherland, W. J., Thomas, D., & Tuffs, R. J. 2010, MNRAS, 404, 86

Ball, N. M., Loveday, J., & Brunner, R. J. 2008, MNRAS, 383, 907

Balogh, M. L., Babul, A., Voit, G. M., McCarthy, I. G., Jones, L. R., Lewis, G. F., & Ebeling, H. 2006, MNRAS, 366, 624

Balogh, M. L., Baldry, I. K., Nichol, R., Miller, C., Bower, R., & Glazebrook, K. 2004, ApJ, 615, L101

Balogh, M. L., McCarthy, I. G., Bower, R. G., & Eke, V. R. 2008, MNRAS, 385, 1003

Balogh, M. L. & McGee, S. L. 2010, MNRAS, 402, L59

Balogh, M. L., McGee, S. L., Wilman, D., Bower, R. G., Hau, G., Morris, S. L., Mulchaey, J. S., Oemler, Jr., A., Parker, L., & Gwyn, S. 2009, MNRAS, 398, 754

Balogh, M. L., Navarro, J. F., & Morris, S. L. 2000, ApJ, 540, 113

Balogh, M. L., Schade, D., Morris, S. L., Yee, H. K. C., Carlberg, R. G., & Ellingson, E. 1998, ApJ, 504, L75

Bamford, S. P., Nichol, R. C., Baldry, I. K., Land, K., Lintott, C. J., Schawinski, K., Slosar, A., Szalay, A. S., Thomas, D., Torki, M., Andreescu, D., Edmondson, E. M., Miller, C. J., Murray, P., Raddick, M. J., & Vandenberg, J. 2009, MNRAS, 393, 1324

Banerji, M., Glazebrook, K., Blake, C., Brough, S., Colless, M., Contreras, C., Couch, W., Croton, D. J., Croom, S., Davis, T. M., Drinkwater, M. J., Forster, K., Gilbank, D., Gladders, M., Jelliffe, B., Jurek, R. J., Li, I.-h., Madore, B., Martin, D. C., Pimbblet, K., Poole, G. B., Pracy, M., Sharp, R., Wisnioski, E., Woods, D., Wyder, T. K., & Yee, H. K. C. 2013, MNRAS, 431, 2209

Barkhouse, W. A., Yee, H. K. C., & López-Cruz, O. 2009, ApJ, 703, 2024

Barnes, J. E. 1992, ApJ, 393, 484

Barnes, J. E. & Hernquist, L. 1996, ApJ, 471, 115

Barnes, J. E. & Hernquist, L. E. 1991, ApJ, 370, L65

Basilakos, S. 2003, MNRAS, 344, 602

Baugh, C. M., Lacey, C. G., Frenk, C. S., Granato, G. L., Silva, L., Bressan, A., Benson, A. J., & Cole, S. 2005, MNRAS, 356, 1191

Bell, E. F. & de Jong, R. S. 2001, ApJ, 550, 212

Bell, E. F., McIntosh, D. H., Katz, N., & Weinberg, M. D. 2003, ApJS, 149, 289

Bell, E. F., Wolf, C., Meisenheimer, K., Rix, H.-W., Borch, A., Dye, S., Kleinheinrich, M., Wisotzki, L., & McIntosh, D. H. 2004, ApJ, 608, 752

Bell, E. F., Zheng, X. Z., Papovich, C., Borch, A., Wolf, C., & Meisenheimer, K. 2007, ApJ, 663, 834

Bennett, C. L., Halpern, M., Hinshaw, G., Jarosik, N., Kogut, A., Limon, M., Meyer, S. S., Page, L., Spergel, D. N., Tucker, G. S., Wollack, E., Wright, E. L., Barnes, C., Greason, M. R., Hill, R. S., Komatsu, E., Nolta, M. R., Odegard, N., Peiris, H. V., Verde, L., & Weiland, J. L. 2003, ApJS, 148, 1

Bennett, C. L., Smoot, G. F., Hinshaw, G., Wright, E. L., Kogut, A., de Amici, G., Meyer, S. S., Weiss, R., Wilkinson, D. T., Gulkis, S., Janssen, M., Boggess, N. W., Cheng, E. S., Hauser, M. G., Kelsall, T., Mather, J. C., Moseley, Jr., S. H., Murdock, T. L., & Silverberg, R. F. 1992, ApJ, 396, L7

Benson, A. J. & Bower, R. 2010, MNRAS, 405, 1573

Benson, A. J., Bower, R. G., Frenk, C. S., Lacey, C. G., Baugh, C. M., & Cole, S. 2003, ApJ, 599, 38

Bergmann, M. P., Forestell, A., Gebhardt, K., & Jorgensen, I. 2004, in IAU Symposium, Vol. 220, Dark Matter in Galaxies, ed. S. Ryder, D. Pisano, M. Walker, & K. Freeman, 175

Berlind, A. A., Frieman, J., Weinberg, D. H., Blanton, M. R., Warren, M. S., Abazajian, K., Scranton, R., Hogg, D. W., Scoccimarro, R., Bahcall, N. A., Brinkmann, J., Gott, III, J. R., Kleinman, S. J., Krzesinski, J., Lee, B. C., Miller, C. J., Nitta, A., Schneider, D. P., Tucker, D. L., Zehavi, I., & SDSS Collaboration. 2006, ApJS, 167, 1

Bershady, M. A., Lowenthal, J. D., & Koo, D. C. 1998, ApJ, 505, 50

Bertelli, G., Bressan, A., Chiosi, C., Fagotto, F., & Nasi, E. 1994, A&AS, 106, 275

Bertin, E. & Arnouts, S. 1996, A&AS, 117, 393

Bielby, R. M., Finoguenov, A., Tanaka, M., McCracken, H. J., Daddi, E., Hudelot, P., Ilbert, O., Kneib, J. P., Le Fèvre, O., Mellier, Y., Nandra, K., Petitjean, P., Srianand, R., Stalin, C. S., & Willott, C. J. 2010, A&A, 523, A66

Binney, J. 1977, ApJ, 215, 483

Blanton, M. R. & Berlind, A. A. 2007, ApJ, 664, 791

Blanton, M. R., Eisenstein, D., Hogg, D. W., Schlegel, D. J., & Brinkmann, J. 2005, ApJ, 629, 143

Böhringer, H., Voges, W., Huchra, J. P., McLean, B., Giacconi, R., Rosati, P., Burg, R., Mader, J., Schuecker, P., Simiç, D., Komossa, S., Reiprich, T. H., Retzlaff, J., & Trümper, J. 2000, ApJS, 129, 435

Bond, J. R., Kofman, L., & Pogosyan, D. 1996, Nature, 380, 603

Botzler, C. S., Snigula, J., Bender, R., & Hopp, U. 2004, MNRAS, 349, 425

Bouwens, R. J., Illingworth, G. D., González, V., Labbé, I., Franx, M., Conselice, C. J., Blakeslee, J., van Dokkum, P., Holden, B., Magee, D., Marchesini, D., & Zheng, W. 2010, ApJ, 725, 1587

Bower, R. G., Benson, A. J., Malbon, R., Helly, J. C., Frenk, C. S., Baugh, C. M., Cole, S., & Lacey, C. G. 2006, MNRAS, 370, 645

Boylan-Kolchin, M., Springel, V., White, S. D. M., Jenkins, A., & Lemson, G. 2009, MNRAS, 398, 1150

Bracewell, R. N. 1955, Australian Journal of Physics, 8, 54

Briel, U. G. & Henry, J. P. 1995, A&A, 302, L9

Brinchmann, J., Charlot, S., White, S. D. M., Tremonti, C., Kauffmann, G., Heckman, T., & Brinkmann, J. 2004, MNRAS, 351, 1151

Brinchmann, J. & Ellis, R. S. 2000, ApJ, 536, L77

Bruzual, G. & Charlot, S. 2003, MNRAS, 344, 1000

Bruzual A., G. 1983, ApJ, 273, 105

Bruzual A., G. & Charlot, S. 1993, ApJ, 405, 538

Butcher, H. & Oemler, Jr., A. 1978, ApJ, 226, 559

—. 1984, ApJ, 285, 426

Buzzoni, A. 1989, ApJS, 71, 817

Calzetti, D., Armus, L., Bohlin, R. C., Kinney, A. L., Koornneef, J., & Storchi-Bergmann, T. 2000, ApJ, 533, 682

Calzetti, D., Meurer, G. R., Bohlin, R. C., Garnett, D. R., Kinney, A. L., Leitherer, C., & Storchi-Bergmann, T. 1997, AJ, 114, 1834

Carlberg, R. G., Yee, H. K. C., & Ellingson, E. 1994, ApJ, 437, 63

Carlberg, R. G., Yee, H. K. C., Ellingson, E., Morris, S. L., Abraham, R., Gravel, P., Pritchet, C. J., Smecker-Hane, T., Hartwick, F. D. A., Hesser, J. E., Hutchings, J. B., & Oke, J. B. 1997, ApJ, 485, L13

Carlberg, R. G., Yee, H. K. C., Morris, S. L., Lin, H., Hall, P. B., Patton, D. R., Sawicki, M., & Shepherd, C. W. 2001, ApJ, 563, 736

Casali, M., Adamson, A., Alves de Oliveira, C., Almaini, O., Burch, K., Chuter, T., Elliot, J., Folger, M., Foucaud, S., Hambly, N., Hastie, M., Henry, D., Hirst, P., Irwin, M., Ives, D., Lawrence, A., Laidlaw, K., Lee, D., Lewis, J., Lunney, D., McLay, S., Montgomery, D., Pickup, A., Read, M., Rees, N., Robson, I., Sekiguchi, K., Vick, A., Warren, S., & Woodward, B. 2007, A&A, 467, 777

Cassata, P., Guzzo, L., Franceschini, A., Scoville, N., Capak, P., Ellis, R. S., Koekemoer, A., McCracken, H. J., Mobasher, B., Renzini, A., Ricciardelli, E., Scodeggio, M., Taniguchi, Y., & Thompson, D. 2007, ApJS, 172, 270

Cassisi, S., Castellani, V., Ciarcelluti, P., Piotto, G., & Zoccali, M. 2000, MNRAS, 315, 679

Cen, R. & Ostriker, J. P. 1999, ApJ, 514, 1

Chabrier, G. 2003, PASP, 115, 763

Charlot, S. & Bruzual, A. G. 1991, ApJ, 367, 126

Charlot, S. & Fall, S. M. 2000, ApJ, 539, 718

Charlot, S. & Longhetti, M. 2001, MNRAS, 323, 887

Chung, S. M., Gonzalez, A. H., Clowe, D., Zaritsky, D., Markevitch, M., & Jones, C. 2009, ApJ, 691, 963

Cid Fernandes, R., Asari, N. V., Sodré, L., Stasińska, G., Mateus, A., Torres-Papaqui, J. P., & Schoenell, W. 2007, MNRAS, 375, L16

Cioni, M.-R. L., Girardi, L., Marigo, P., & Habing, H. J. 2006, A&A, 452, 195

Clemens, D. P. 1985, ApJ, 295, 422

Coelho, P., Bruzual, G., Charlot, S., Weiss, A., Barbuy, B., & Ferguson, J. W. 2007, MNRAS, 382, 498

Cohn, J. D. 2012, MNRAS, 419, 1017

Colberg, J. M., Krughoff, K. S., & Connolly, A. J. 2005, MNRAS, 359, 272

Colberg, J. M., White, S. D. M., Jenkins, A., & Pearce, F. R. 1999, MNRAS, 308, 593

Cole, S., Aragon-Salamanca, A., Frenk, C. S., Navarro, J. F., & Zepf, S. E. 1994, MNRAS, 271, 781

Cole, S., Lacey, C. G., Baugh, C. M., & Frenk, C. S. 2000, MNRAS, 319, 168

Cole, S., Norberg, P., Baugh, C. M., Frenk, C. S., Bland-Hawthorn, J., Bridges, T., Cannon, R., Colless, M., Collins, C., Couch, W., Cross, N., Dalton, G., De Propris, R., Driver, S. P., Efstathiou, G., Ellis, R. S., Glazebrook, K., Jackson, C., Lahav, O., Lewis, I., Lumsden, S., Maddox, S., Madgwick, D., Peacock, J. A., Peterson, B. A., Sutherland, W., & Taylor, K. 2001, MNRAS, 326, 255

Cole, S., Percival, W. J., Peacock, J. A., Norberg, P., Baugh, C. M., Frenk, C. S., Baldry, I., Bland-Hawthorn, J., Bridges, T., Cannon, R., Colless, M., Collins, C., Couch, W., Cross, N. J. G., Dalton, G., Eke, V. R., De Propris, R., Driver, S. P., Efstathiou, G., Ellis, R. S., Glazebrook, K., Jackson, C., Jenkins, A., Lahav, O., Lewis, I., Lumsden, S., Maddox, S., Madgwick, D., Peterson, B. A., Sutherland, W., & Taylor, K. 2005, MNRAS, 362, 505

Colless, M., 2DF Galaxy Redshift Survey Team, Ellis, R., Bland-Hawthorn, J., Cannon, R., Cole, S., Collins, C., Couch, W., Dalton, G., Driver, S., Efstathiou, G., Folkes, S., Frenk, C., Glazebrook, K., Kaiser, N., Lahav, O., Lewis, I., Lumsden, S., Maddox, S., Peacock, J., Peterson, B., Price, I., Sutherland, W., & Taylor, K. 1999, in Looking Deep in the Southern Sky, ed. R. Morganti & W. J. Couch, 9

Colless, M., Dalton, G., Maddox, S., Sutherland, W., Norberg, P., Cole, S., Bland-Hawthorn, J., Bridges, T., Cannon, R., Collins, C., Couch, W., Cross, N., Deeley, K., De Propris, R., Driver, S. P., Efstathiou, G., Ellis, R. S., Frenk, C. S., Glazebrook, K., Jackson, C., Lahav, O., Lewis, I., Lumsden, S., Madgwick, D., Peacock, J. A., Peterson, B. A., Price, I., Seaborne, M., & Taylor, K. 2001, MNRAS, 328, 1039

Conroy, C., Gunn, J. E., & White, M. 2009, ApJ, 699, 486

Conroy, C. & van Dokkum, P. 2012, ApJ, 747, 69

Contaldi, C. R., Hoekstra, H., & Lewis, A. 2003, Physical Review Letters, 90, 221303

Cooper, M. C., Newman, J. A., Croton, D. J., Weiner, B. J., Willmer, C. N. A., Gerke, B. F., Madgwick, D. S., Faber, S. M., Davis, M., Coil, A. L., Finkbeiner, D. P., Guhathakurta, P., & Koo, D. C. 2006, MNRAS, 370, 198

Coppin, K. E. K., Geach, J. E., Webb, T. M. A., Faloon, A., Yan, R., O'Donnell, D., Ouellette, N., Egami, E., Ellingson, E., Gilbank, D., Hicks, A., Barrientos, L. F., Yee, H. K. C., & Gladders, M. 2012, ApJ, 749, L43

Couch, W. J., Barger, A. J., Smail, I., Ellis, R. S., & Sharples, R. M. 1998, ApJ, 497, 188

Couch, W. J., Ellis, R. S., Sharples, R. M., & Smail, I. 1994, ApJ, 430, 121

Croton, D. J., Farrar, G. R., Norberg, P., Colless, M., Peacock, J. A., Baldry, I. K., Baugh, C. M., Bland-Hawthorn, J., Bridges, T., Cannon, R., Cole, S., Collins, C., Couch, W., Dalton, G., De Propris, R., Driver, S. P., Efstathiou, G., Ellis, R. S., Frenk, C. S., Glazebrook, K., Jackson, C., Lahav, O., Lewis, I., Lumsden, S., Maddox, S., Madgwick, D., Peterson, B. A., Sutherland, W., & Taylor, K. 2005, MNRAS, 356, 1155

Croton, D. J., Springel, V., White, S. D. M., De Lucia, G., Frenk, C. S., Gao, L., Jenkins, A., Kauffmann, G., Navarro, J. F., & Yoshida, N. 2006, MNRAS, 365, 11

Csabai, I., Budavári, T., Connolly, A. J., Szalay, A. S., Győry, Z., Benítez, N., Annis, J., Brinkmann, J., Eisenstein, D., Fukugita, M., Gunn, J., Kent, S., Lupton, R., Nichol, R. C., & Stoughton, C. 2003, AJ, 125, 580

da Cunha, E., Charlot, S., & Elbaz, D. 2008, MNRAS, 388, 1595

Davé, R. 2008, MNRAS, 385, 147

de Lapparent, V., Geller, M. J., & Huchra, J. P. 1986, ApJ, 302, L1

De Lucia, G., Weinmann, S., Poggianti, B. M., Aragón-Salamanca, A., & Zaritsky, D. 2012, MNRAS, 423, 1277

De Propris, R., Colless, M., Driver, S. P., Couch, W., Peacock, J. A., Baldry, I. K., Baugh, C. M., Bland-Hawthorn, J., Bridges, T., Cannon, R., Cole, S., Collins, C., Cross, N., Dalton, G. B., Efstathiou, G., Ellis, R. S., Frenk, C. S., Glazebrook, K., Hawkins, E., Jackson, C., Lahav, O., Lewis, I., Lumsden, S., Maddox, S., Madgwick, D. S., Norberg, P., Percival, W., Peterson, B., Sutherland, W., & Taylor, K. 2003a, MNRAS, 342, 725

De Propris, R., Colless, M., Peacock, J. A., Couch, W. J., Driver, S. P., Balogh, M. L., Baldry, I. K., Baugh, C. M., Bland-Hawthorn, J., Bridges, T., Cannon, R., Cole, S., Collins, C., Cross, N., Dalton, G., Efstathiou, G., Ellis, R. S., Frenk, C. S., Glazebrook, K., Hawkins, E., Jackson, C., Lahav, O., Lewis, I., Lumsden, S., Maddox, S., Madgwick, D., Norberg, P., Percival, W., Peterson, B. A., Sutherland, W., & Taylor, K. 2004, MNRAS, 351, 125

De Propris, R., Stanford, S. A., Eisenhardt, P. R., & Dickinson, M. 2003b, ApJ, 598, 20

de Vaucouleurs, G. 1953, MNRAS, 113, 134

Dietrich, J. P., Schneider, P., Clowe, D., Romano-Díaz, E., & Kerp, J. 2005, A&A, 440, 453

Dotter, A., Chaboyer, B., Ferguson, J. W., Lee, H.-c., Worthey, G., Jevremović, D., & Baron, E. 2007, ApJ, 666, 403

Dressler, A. 1980, ApJ, 236, 351

Dressler, A., Oemler, Jr., A., Couch, W. J., Smail, I., Ellis, R. S., Barger, A., Butcher, H., Poggianti, B. M., & Sharples, R. M. 1997, ApJ, 490, 577

Dressler, A. & Shectman, S. A. 1988, AJ, 95, 985

Ebeling, H., Barrett, E., & Donovan, D. 2004, ApJ, 609, L49

Ebeling, H., Edge, A. C., & Henry, J. P. 2001, ApJ, 553, 668

Ebeling, H., Voges, W., Bohringer, H., Edge, A. C., Huchra, J. P., & Briel, U. G. 1996, MNRAS, 281, 799

Efstathiou, G. 1992, MNRAS, 256, 43P

Einasto, J., Einasto, M., Frisch, P., Gottlober, S., Muller, V., Saar, V., Starobinsky, A. A., Tago, E., Tucker, D., & Andernach, H. 1997, MNRAS, 289, 801

Einasto, J., Einasto, M., Saar, E., Tago, E., Liivamägi, L. J., Jõeveer, M., Suhhonenko, I., Hütsi, G., Jaaniste, J., Heinämäki, P., Müller, V., Knebe, A., & Tucker, D. 2007a, A&A, 462, 397

Einasto, J., Klypin, A. A., Saar, E., & Shandarin, S. F. 1984, MNRAS, 206, 529

Einasto, M., Einasto, J., Tago, E., Dalton, G. B., & Andernach, H. 1994, MNRAS, 269, 301

Einasto, M., Einasto, J., Tago, E., Müller, V., & Andernach, H. 2001, AJ, 122, 2222

Einasto, M., Einasto, J., Tago, E., Saar, E., Liivamägi, L. J., Jõeveer, M., Hütsi, G., Heinämäki, P., Müller, V., & Tucker, D. 2007b, A&A, 464, 815

Einasto, M., Liivamägi, L. J., Saar, E., Einasto, J., Tempel, E., Tago, E., & Martínez, V. J. 2011, A&A, 535, A36

Eisenstein, D. J., Annis, J., Gunn, J. E., Szalay, A. S., Connolly, A. J., Nichol, R. C., Bahcall, N. A., Bernardi, M., Burles, S., Castander, F. J., Fukugita, M., Hogg, D. W., Ivezić, Ž., Knapp, G. R., Lupton, R. H., Narayanan, V., Postman, M., Reichart, D. E., Richmond, M., Schneider, D. P., Schlegel, D. J., Strauss, M. A., SubbaRao, M., Tucker, D. L., Vanden Berk, D., Vogeley, M. S., Weinberg, D. H., & Yanny, B. 2001, AJ, 122, 2267

Eke, V. R., Baugh, C. M., Cole, S., Frenk, C. S., & Navarro, J. F. 2006, MNRAS, 370, 1147

Eke, V. R., Frenk, C. S., Baugh, C. M., Cole, S., Norberg, P., Peacock, J. A., Baldry, I. K., Bland-Hawthorn, J., Bridges, T., Cannon, R., Colless, M., Collins, C., Couch, W., Dalton, G., de Propris, R., Driver, S. P., Efstathiou, G., Ellis, R. S., Glazebrook, K., Jackson, C. A., Lahav, O., Lewis, I., Lumsden, S., Maddox, S. J., Madgwick, D., Peterson, B. A., Sutherland, W., & Taylor, K. 2004, MNRAS, 355, 769

Ellingson, E., Lin, H., Yee, H. K. C., & Carlberg, R. G. 2001, ApJ, 547, 609

Ellis, R. S., Smail, I., Dressler, A., Couch, W. J., Oemler, Jr., A., Butcher, H., & Sharples, R. M. 1997, ApJ, 483, 582

Ellison, S. L., Patton, D. R., Simard, L., McConnachie, A. W., Baldry, I. K., & Mendel, J. T. 2010, MNRAS, 407, 1514

Evrard, A. E., Summers, F. J., & Davis, M. 1994, ApJ, 422, 11

Fadda, D., Biviano, A., Marleau, F. R., Storrie-Lombardi, L. J., & Durret, F. 2008, ApJ, 672, L9

Fairley, B. W., Jones, L. R., Wake, D. A., Collins, C. A., Burke, D. J., Nichol, R. C., & Romer, A. K. 2002, MNRAS, 330, 755

Farouki, R. & Shapiro, S. L. 1981, ApJ, 243, 32

Fioc, M. & Rocca-Volmerange, B. 1997, A&A, 326, 950

Font, A. S., Bower, R. G., McCarthy, I. G., Benson, A. J., Frenk, C. S., Helly, J. C., Lacey, C. G., Baugh, C. M., & Cole, S. 2008, MNRAS, 389, 1619

Fontana, A., Pozzetti, L., Donnarumma, I., Renzini, A., Cimatti, A., Zamorani, G., Menci, N., Daddi, E., Giallongo, E., Mignoli, M., Perna, C., Salimbeni, S., Saracco, P., Broadhurst, T., Cristiani, S., D'Odorico, S., & Gilmozzi, R. 2004, A&A, 424, 23

Francis, P. J., Woodgate, B. E., Warren, S. J., Moller, P., Mazzolini, M., Bunker, A. J., Lowenthal, J. D., Williams, T. B., Minezaki, T., Kobayashi, Y., & Yoshii, Y. 1996, ApJ, 457, 490

Franzetti, P., Scodeggio, M., Garilli, B., Fumana, M., & Paioro, L. 2008, in Astronomical Society of the Pacific Conference Series, Vol. 394, Astronomical Data Analysis Software and Systems XVII, ed. R. W. Argyle, P. S. Bunclark, & J. R. Lewis, 642

Frayer, D. T., Ivison, R. J., Scoville, N. Z., Yun, M., Evans, A. S., Smail, I., Blain, A. W., & Kneib, J.-P. 1998, ApJ, 506, L7

Frye, B. L., Bowen, D. V., Hurley, M., Tripp, T. M., Fan, X., Holden, B., Guhathakurta, P., Coe, D., Broadhurst, T., Egami, E., & Meylan, G. 2008, ApJ, 685, L5

Fujita, Y. 2004, PASJ, 56, 29

Fukugita, M., Hogan, C. J., & Peebles, P. J. E. 1998, ApJ, 503, 518

Fukugita, M., Ichikawa, T., Gunn, J. E., Doi, M., Shimasaku, K., & Schneider, D. P. 1996, AJ, 111, 1748

Fukugita, M., Shimasaku, K., & Ichikawa, T. 1995, PASP, 107, 945

Gallazzi, A., Charlot, S., Brinchmann, J., White, S. D. M., & Tremonti, C. A. 2005, MNRAS, 362, 41

Gamow, G. 1948, Nature, 162, 680

Gavazzi, R., Treu, T., Rhodes, J. D., Koopmans, L. V. E., Bolton, A. S., Burles, S., Massey, R. J., & Moustakas, L. A. 2007, ApJ, 667, 176

Geach, J. E., Ellis, R. S., Smail, I., Rawle, T. D., & Moran, S. M. 2011, MNRAS, 413, 177

Gerke, B. F., Newman, J. A., Davis, M., Marinoni, C., Yan, R., Coil, A. L., Conroy, C., Cooper, M. C., Faber, S. M., Finkbeiner, D. P., Guhathakurta, P., Kaiser, N., Koo, D. C., Phillips, A. C., Weiner, B. J., & Willmer, C. N. A. 2005, ApJ, 625, 6

Gerke, B. F., Newman, J. A., Faber, S. M., Cooper, M. C., Croton, D. J., Davis, M., Willmer, C. N. A., Yan, R., Coil, A. L., Guhathakurta, P., Koo, D. C., & Weiner, B. J. 2007, MNRAS, 376, 1425

Gilbank, D. G., Bower, R. G., Castander, F. J., & Ziegler, B. L. 2004, MNRAS, 348, 551

Girardi, L., Bressan, A., Bertelli, G., & Chiosi, C. 2000, A&AS, 141, 371

Gladders, M. D. & Yee, H. K. C. 2000, AJ, 120, 2148

Glazebrook, K., Peacock, J. A., Collins, C. A., & Miller, L. 1994, MNRAS, 266, 65

Gómez, P. L., Nichol, R. C., Miller, C. J., Balogh, M. L., Goto, T., Zabludoff, A. I., Romer, A. K., Bernardi, M., Sheth, R., Hopkins, A. M., Castander, F. J., Connolly, A. J., Schneider, D. P., Brinkmann, J., Lamb, D. Q., SubbaRao, M., & York, D. G. 2003, ApJ, 584, 210

González, R. E., Padilla, N. D., Galaz, G., & Infante, L. 2005, MNRAS, 363, 1008

Goto, T., Sekiguchi, M., Nichol, R. C., Bahcall, N. A., Kim, R. S. J., Annis, J., Ivezić, Ž., Brinkmann, J., Hennessy, G. S., Szokoly, G. P., & Tucker, D. L. 2002, AJ, 123, 1807

Goto, T., Yamauchi, C., Fujita, Y., Okamura, S., Sekiguchi, M., Smail, I., Bernardi, M., & Gomez, P. L. 2003, MNRAS, 346, 601

Graham, A. W. & Driver, S. P. 2005, PASA, 22, 118

Gray, M. E., Taylor, A. N., Meisenheimer, K., Dye, S., Wolf, C., & Thommes, E. 2002, ApJ, 568, 141

Green, P. J., Silverman, J. D., Cameron, R. A., Kim, D.-W., Wilkes, B. J., Barkhouse, W. A., LaCluyzé, A., Morris, D., Mossman, A., Ghosh, H., Grimes, J. P., Jannuzi, B. T., Tananbaum, H., Aldcroft, T. L., Baldwin, J. A., Chaffee, F. H., Dey, A., Dosaj, A., Evans, N. R., Fan, X., Foltz, C., Gaetz, T., Hooper, E. J., Kashyap, V. L., Mathur, S., McGarry, M. B., Romero-Colmenero, E., Smith, M. G., Smith, P. S., Smith, R. C., Torres, G., Vikhlinin, A., & Wik, D. R. 2004, ApJS, 150, 43

Gregory, S. A. & Thompson, L. A. 1978, ApJ, 222, 784

Gunn, J. E. & Gott, III, J. R. 1972, ApJ, 176, 1

Gunn, J. E. & Stryker, L. L. 1983, ApJS, 52, 121

Haines, C. P., Gargiulo, A., & Merluzzi, P. 2008, MNRAS, 385, 1201

Haines, C. P., Merluzzi, P., Mercurio, A., Gargiulo, A., Krusanova, N., Busarello, G., La Barbera, F., & Capaccioli, M. 2006, MNRAS, 371, 55

Haines, C. P., Smith, G. P., Egami, E., Ellis, R. S., Moran, S. M., Sanderson, A. J. R., Merluzzi, P., Busarello, G., & Smith, R. J. 2009, ApJ, 704, 126

Hansen, S. M., Sheldon, E. S., Wechsler, R. H., & Koester, B. P. 2009, ApJ, 699, 1333

Heald, G., Józsa, G., Serra, P., Zschaechner, L., Rand, R., Fraternali, F., Oosterloo, T., Walterbos, R., Jütte, E., & Gentile, G. 2011, A&A, 526, A118

Heiderman, A., Jogee, S., Marinova, I., van Kampen, E., Barden, M., Peng, C. Y., Heymans, C., Gray, M. E., Bell, E. F., Bacon, D., Balogh, M., Barazza, F. D., Böhm, A., Caldwell, J. A. R., Häußler, B., Jahnke, K., Lane, K., McIntosh, D. H., Meisenheimer, K., Sánchez, S. F., Somerville, R. S., Taylor, A., Wisotzki, L., Wolf, C., & Zheng, X. 2009, ApJ, 705, 1433

Henriques, B. M. B., Thomas, P. A., Oliver, S., & Roseboom, I. 2009, MNRAS, 396, 535

Hill, D. T., Driver, S. P., Cameron, E., Cross, N., Liske, J., & Robotham, A. 2010, MNRAS, 404, 1215

Hodgkin, S. T., Irwin, M. J., Hewett, P. C., & Warren, S. J. 2009, MNRAS, 394, 675

Hogg, D. W. 1999, ArXiv Astrophysics e-prints

Hopkins, A. M. & Beacom, J. F. 2006, ApJ, 651, 142

Hoyle, F. 1953, ApJ, 118, 513

Huang, J.-S., Cowie, L. L., Gardner, J. P., Hu, E. M., Songaila, A., & Wainscoat, R. J. 1997, ApJ, 476, 12

Huchra, J. P. & Geller, M. J. 1982, ApJ, 257, 423

Irwin, M. J. 1985, MNRAS, 214, 575

Jõeveer, M., Einasto, J., & Tago, E. 1978, MNRAS, 185, 357

Jauzac, M., Jullo, E., Kneib, J.-P., Ebeling, H., Leauthaud, A., Ma, C.-J., Limousin, M., Massey, R., & Richard, J. 2012, MNRAS, 426, 3369

Jeltema, T. E., Mulchaey, J. S., Lubin, L. M., & Fassnacht, C. D. 2007, ApJ, 658, 865

Jensen, P. C. & Pimbblet, K. A. 2012, MNRAS, 422, 2841

Just, D. W., Zaritsky, D., Sand, D. J., Desai, V., & Rudnick, G. 2010, ApJ, 711, 192

Katz, N., Hernquist, L., & Weinberg, D. H. 1992, ApJ, 399, L109

Kauffmann, G., Colberg, J. M., Diaferio, A., & White, S. D. M. 1999, MNRAS, 303, 188

Kauffmann, G., Heckman, T. M., White, S. D. M., Charlot, S., Tremonti, C., Brinchmann, J., Bruzual, G., Peng, E. W., Seibert, M., Bernardi, M., Blanton, M., Brinkmann, J., Castander, F., Csábai, I., Fukugita, M., Ivezic, Z., Munn, J. A., Nichol, R. C., Padmanabhan, N., Thakar, A. R., Weinberg, D. H., & York, D. 2003a, MNRAS, 341, 33

Kauffmann, G., Heckman, T. M., White, S. D. M., Charlot, S., Tremonti, C., Peng, E. W., Seibert, M., Brinkmann, J., Nichol, R. C., SubbaRao, M., & York, D. 2003b, MNRAS, 341, 54

Kauffmann, G., White, S. D. M., & Guiderdoni, B. 1993, MNRAS, 264, 201

Kauffmann, G., White, S. D. M., Heckman, T. M., Ménard, B., Brinchmann, J., Charlot, S., Tremonti, C., & Brinkmann, J. 2004, MNRAS, 353, 713

Kawata, D. & Mulchaey, J. S. 2008, ApJ, 672, L103

Kennicutt, Jr., R. C. 1989, ApJ, 344, 685

—. 1998a, ARA&A, 36, 189

—. 1998b, ApJ, 498, 541

Kennicutt, Jr., R. C., Tamblyn, P., & Congdon, C. E. 1994, ApJ, 435, 22

Kimm, T., Somerville, R. S., Yi, S. K., van den Bosch, F. C., Salim, S., Fontanot, F., Monaco, P., Mo, H., Pasquali, A., Rich, R. M., & Yang, X. 2009, MNRAS, 394, 1131

Knop, R. A., Aldering, G., Amanullah, R., Astier, P., Blanc, G., Burns, M. S., Conley, A., Deustua, S. E., Doi, M., Ellis, R., Fabbro, S., Folatelli, G., Fruchter, A. S., Garavini, G., Garmond, S., Garton, K., Gibbons, R., Goldhaber, G., Goobar, A., Groom, D. E., Hardin, D., Hook, I., Howell, D. A., Kim, A. G., Lee, B. C., Lidman, C., Mendez, J., Nobili, S., Nugent, P. E., Pain, R., Panagia, N., Pennypacker, C. R., Perlmutter, S., Quimby, R., Raux, J., Regnault, N., Ruiz-Lapuente, P., Sainton, G., Schaefer, B., Schahmaneche, K., Smith, E., Spadafora, A. L., Stanishev, V., Sullivan, M., Walton, N. A., Wang, L., Wood-Vasey, W. M., & Yasuda, N. 2003, ApJ, 598, 102

Kodama, T., Arimoto, N., Barger, A. J., & Arag'on-Salamanca, A. 1998, A&A, 334, 99

Kodama, T., Smail, I., Nakata, F., Okamura, S., & Bower, R. G. 2001, ApJ, 562, L9

Koester, B. P., McKay, T. A., Annis, J., Wechsler, R. H., Evrard, A., Bleem, L., Becker, M., Johnston, D., Sheldon, E., Nichol, R., Miller, C., Scranton, R., Bahcall, N., Barentine, J., Brewington, H., Brinkmann, J., Harvanek, M., Kleinman, S., Krzesinski, J., Long, D., Nitta, A., Schneider, D. P., Sneddin, S., Voges, W., & York, D. 2007a, ApJ, 660, 239

Koester, B. P., McKay, T. A., Annis, J., Wechsler, R. H., Evrard, A. E., Rozo, E., Bleem, L., Sheldon, E. S., & Johnston, D. 2007b, ApJ, 660, 221

Komatsu, E., Dunkley, J., Nolta, M. R., Bennett, C. L., Gold, B., Hinshaw, G., Jarosik, N., Larson, D., Limon, M., Page, L., Spergel, D. N., Halpern, M., Hill, R. S., Kogut, A., Meyer, S. S., Tucker, G. S., Weiland, J. L., Wollack, E., & Wright, E. L. 2009, ApJS, 180, 330

Komatsu, E., Kogut, A., Nolta, M. R., Bennett, C. L., Halpern, M., Hinshaw, G., Jarosik, N., Limon, M., Meyer, S. S., Page, L., Spergel, D. N., Tucker, G. S., Verde, L., Wollack, E., & Wright, E. L. 2003, ApJS, 148, 119

Kormendy, J. & Kennicutt, Jr., R. C. 2004, ARA&A, 42, 603

Kotulla, R., Fritze, U., Weilbacher, P., & Anders, P. 2009, MNRAS, 396, 462

Kron, R. G. 1980, ApJS, 43, 305

Kroupa, P. 2001, MNRAS, 322, 231

Kull, A. & Böhringer, H. 1999, A&A, 341, 23

Lambas, D. G., Tissera, P. B., Alonso, M. S., & Coldwell, G. 2003, MNRAS, 346, 1189

Larson, R. B., Tinsley, B. M., & Caldwell, C. N. 1980, ApJ, 237, 692

Lawrence, A., Warren, S. J., Almaini, O., Edge, A. C., Hambly, N. C., Jameson, R. F., Lucas, P., Casali, M., Adamson, A., Dye, S., Emerson, J. P., Foucaud, S., Hewett, P., Hirst, P., Hodgkin, S. T., Irwin, M. J., Lodieu, N., McMahon, R. G., Simpson, C., Smail, I., Mortlock, D., & Folger, M. 2007, MNRAS, 379, 1599

Le Borgne, J.-F., Bruzual, G., Pelló, R., Lançon, A., Rocca-Volmerange, B., Sanahuja, B., Schaerer, D., Soubiran, C., & Vílchez-Gómez, R. 2003, A&A, 402, 433

Leitherer, C., Schaerer, D., Goldader, J. D., González Delgado, R. M., Robert, C., Kune, D. F., de Mello, D. F., Devost, D., & Heckman, T. M. 1999, ApJS, 123, 3

Lejeune, T., Cuisinier, F., & Buser, R. 1997, A&AS, 125, 229

—. 1998, A&AS, 130, 65

Lewis, I., Balogh, M., De Propris, R., Couch, W., Bower, R., Offer, A., Bland-Hawthorn, J., Baldry, I. K., Baugh, C., Bridges, T., Cannon, R., Cole, S., Colless, M., Collins, C., Cross, N., Dalton, G., Driver, S. P., Efstathiou, G., Ellis, R. S., Frenk, C. S., Glazebrook, K., Hawkins, E., Jackson, C., Lahav, O., Lumsden, S., Maddox, S., Madgwick, D., Norberg, P., Peacock, J. A., Percival, W., Peterson, B. A., Sutherland, W., & Taylor, K. 2002, MNRAS, 334, 673

Li, C., Gadotti, D. A., Mao, S., & Kauffmann, G. 2009, MNRAS, 397, 726

Li, I. H., Glazebrook, K., Gilbank, D., Balogh, M., Bower, R., Baldry, I., Davies, G., Hau, G., & McCarthy, P. 2011, MNRAS, 411, 1869

Li, I. H. & Yee, H. K. C. 2008, AJ, 135, 809

Li, I. H., Yee, H. K. C., Hsieh, B. C., & Gladders, M. 2012, ApJ, 749, 150

Lilly, S. J., Le Fevre, O., Hammer, F., & Crampton, D. 1996, ApJ, 460, L1

Lu, T., Gilbank, D. G., Balogh, M. L., & Bognat, A. 2009, MNRAS, 399, 1858

Lu, T., Gilbank, D. G., McGee, S. L., Balogh, M. L., & Gallagher, S. 2012, MNRAS, 420, 126

Lupton, R., Gunn, J. E., Ivezić, Z., Knapp, G. R., & Kent, S. 2001, in Astronomical Society of the Pacific Conference Series, Vol. 238, Astronomical Data Analysis Software and Systems X, ed. F. R. Harnden, Jr., F. A. Primini, & H. E. Payne, 269

Madau, P., Ferguson, H. C., Dickinson, M. E., Giavalisco, M., Steidel, C. C., & Fruchter, A. 1996, MNRAS, 283, 1388

Madau, P., Pozzetti, L., & Dickinson, M. 1998, ApJ, 498, 106

Makino, J. & Hut, P. 1997, ApJ, 481, 83

Maraston, C. 1998, MNRAS, 300, 872

—. 2005, MNRAS, 362, 799

Margoniner, V. E., de Carvalho, R. R., Gal, R. R., & Djorgovski, S. G. 2001, ApJ, 548, L143

Marigo, P. & Girardi, L. 2007, A&A, 469, 239

Marigo, P., Girardi, L., Bressan, A., Groenewegen, M. A. T., Silva, L., & Granato, G. L. 2008, A&A, 482, 883

Materne, J. 1978, A&A, 63, 401

Mather, J. C., Cheng, E. S., Eplee, Jr., R. E., Isaacman, R. B., Meyer, S. S., Shafer, R. A., Weiss, R., Wright, E. L., Bennett, C. L., Boggess, N. W., Dwek, E., Gulkis, S., Hauser, M. G., Janssen, M., Kelsall, T., Lubin, P. M., Moseley, Jr., S. H., Murdock, T. L., Silverberg, R. F., Smoot, G. F., & Wilkinson, D. T. 1990, ApJ, 354, L37

McCarthy, I. G., Frenk, C. S., Font, A. S., Lacey, C. G., Bower, R. G., Mitchell, N. L., Balogh, M. L., & Theuns, T. 2008, MNRAS, 383, 593

McGee, S. L., Balogh, M. L., Bower, R. G., Font, A. S., & McCarthy, I. G. 2009, MNRAS, 400, 937

McGee, S. L., Balogh, M. L., Henderson, R. D. E., Wilman, D. J., Bower, R. G., Mulchaey, J. S., & Oemler, Jr., A. 2008, MNRAS, 387, 1605

McGee, S. L., Balogh, M. L., Wilman, D. J., Bower, R. G., Mulchaey, J. S., Parker, L. C., & Oemler, A. 2011, MNRAS, 413, 996

McIntosh, D. H., Guo, Y., Hertzberg, J., Katz, N., Mo, H. J., van den Bosch, F. C., & Yang, X. 2008, MNRAS, 388, 1537

Mihos, J. C. & Hernquist, L. 1994, ApJ, 437, 611

—. 1996, ApJ, 464, 641

Milkeraitis, M., van Waerbeke, L., Heymans, C., Hildebrandt, H., Dietrich, J. P., & Erben, T. 2010, MNRAS, 406, 673

Miller, C. J., Nichol, R. C., Reichart, D., Wechsler, R. H., Evrard, A. E., Annis, J., McKay, T. A., Bahcall, N. A., Bernardi, M., Boehringer, H., Connolly, A. J., Goto, T., Kniazev, A., Lamb, D., Postman, M., Schneider, D. P., Sheth, R. K., & Voges, W. 2005, AJ, 130, 968

Mollá, M., García-Vargas, M. L., & Bressan, A. 2009, MNRAS, 398, 451

Moller, P. & Warren, S. J. 1998, MNRAS, 299, 661

Moore, B., Lake, G., & Katz, N. 1998, ApJ, 495, 139

Muzzin, A., Wilson, G., Yee, H. K. C., Gilbank, D., Hoekstra, H., Demarco, R., Balogh, M., van Dokkum, P., Franx, M., Ellingson, E., Hicks, A., Nantais, J., Noble, A., Lacy, M., Lidman, C., Rettura, A., Surace, J., & Webb, T. 2012, ApJ, 746, 188

Navarro, J. F., Frenk, C. S., & White, S. D. M. 1994, MNRAS, 267, L1

Navarro, J. F. & Steinmetz, M. 1997, ApJ, 478, 13

Negroponte, J. & White, S. D. M. 1983, MNRAS, 205, 1009

Noeske, K. G., Weiner, B. J., Faber, S. M., Papovich, C., Koo, D. C., Somerville, R. S., Bundy, K., Conselice, C. J., Newman, J. A., Schiminovich, D., Le Floc'h, E., Coil, A. L., Rieke, G. H., Lotz, J. M., Primack, J. R., Barmby, P., Cooper, M. C., Davis, M., Ellis, R. S., Fazio, G. G., Guhathakurta, P., Huang, J., Kassin, S. A., Martin, D. C., Phillips, A. C., Rich, R. M., Small, T. A., Willmer, C. N. A., & Wilson, G. 2007, ApJ, 660, L43

Oemler, Jr., A. 1974, ApJ, 194, 1

Oke, J. B. & Gunn, J. E. 1983, ApJ, 266, 713

Olsen, L. F., Benoist, C., Cappi, A., Maurogordato, S., Mazure, A., Slezak, E., Adami, C., Ferrari, C., & Martel, F. 2007, A&A, 461, 81

Oort, J. H. 1983, ARA&A, 21, 373

Oyaizu, H., Lima, M., Cunha, C. E., Lin, H., Frieman, J., & Sheldon, E. S. 2008, ApJ, 674, 768

Pacaud, F., Pierre, M., Adami, C., Altieri, B., Andreon, S., Chiappetti, L., Detal, A., Duc, P.-A., Galaz, G., Gueguen, A., Le Fèvre, J.-P., Hertling, G., Libbrecht, C., Melin, J.-B., Ponman, T. J., Quintana, H., Refregier, A., Sprimont, P.-G., Surdej, J., Valtchanov, I., Willis, J. P., Alloin, D., Birkinshaw, M., Bremer, M. N., Garcet, O., Jean, C., Jones, L. R., Le Fèvre, O., Maccagni, D., Mazure, A., Proust, D., Röttgering, H. J. A., & Trinchieri, G. 2007, MNRAS, 382, 1289

Panter, B., Heavens, A. F., & Jimenez, R. 2004, MNRAS, 355, 764

Papadopoulos, P., Ivison, R., Carilli, C., & Lewis, G. 2001, Nature, 409, 58

Papovich, C., Dickinson, M., & Ferguson, H. C. 2001, ApJ, 559, 620

Paz, D. J., Lambas, D. G., Padilla, N., & Merchán, M. 2006, MNRAS, 366, 1503

Pence, W. D., Seaman, R., & White, R. L. 2009, in Astronomical Society of the Pacific Conference Series, Vol. 411, Astronomical Data Analysis Software and Systems XVIII, ed. D. A. Bohlender, D. Durand, & P. Dowler, 25

Pence, W. D., White, R. L., & Seaman, R. 2010, PASP, 122, 1065

Peng, Y.-j., Lilly, S. J., Kovač, K., Bolzonella, M., Pozzetti, L., Renzini, A., Zamorani, G., Ilbert, O., Knobel, C., Iovino, A., Maier, C., Cucciati, O., Tasca, L., Carollo, C. M., Silverman, J., Kampczyk, P., de Ravel, L., Sanders, D., Scoville, N., Contini, T., Mainieri, V., Scodeggio, M., Kneib, J.-P., Le Fèvre, O., Bardelli, S., Bongiorno, A., Caputi, K., Coppa, G., de la Torre, S., Franzetti, P., Garilli, B., Lamareille, F., Le Borgne, J.-F., Le Brun, V., Mignoli, M., Perez Montero, E., Pello, R., Ricciardelli, E., Tanaka, M., Tresse, L., Vergani, D., Welikala, N., Zucca, E., Oesch, P., Abbas, U., Barnes, L., Bordoloi, R., Bottini, D., Cappi, A., Cassata, P., Cimatti, A., Fumana, M., Hasinger, G., Koekemoer, A., Leauthaud, A., Maccagni, D., Marinoni, C., McCracken, H., Memeo, P., Meneux, B., Nair, P., Porciani, C., Presotto, V., & Scaramella, R. 2010, ApJ, 721, 193

Peng, Y.-j., Lilly, S. J., Renzini, A., & Carollo, M. 2012, ApJ, 757, 4

Penzias, A. A. & Wilson, R. W. 1965, ApJ, 142, 419

Percival, W. J., Baugh, C. M., Bland-Hawthorn, J., Bridges, T., Cannon, R., Cole, S., Colless, M., Collins, C., Couch, W., Dalton, G., De Propris, R., Driver, S. P., Efstathiou, G., Ellis, R. S., Frenk, C. S., Glazebrook, K., Jackson, C., Lahav, O., Lewis, I., Lumsden, S., Maddox, S., Moody, S., Norberg, P., Peacock, J. A., Peterson, B. A., Sutherland, W., & Taylor, K. 2001, MNRAS, 327, 1297

Petrosian, V. 1976, ApJ, 209, L1

Pickles, A. J. 1998, PASP, 110, 863

Pier, J. R., Munn, J. A., Hindsley, R. B., Hennessy, G. S., Kent, S. M., Lupton, R. H., & Ivezić, Ž. 2003, AJ, 125, 1559

Pimbblet, K. A. & Drinkwater, M. J. 2004, MNRAS, 347, 137

Pimbblet, K. A., Drinkwater, M. J., & Hawkrigg, M. C. 2004, MNRAS, 354, L61

Pimbblet, K. A., Smail, I., Edge, A. C., O'Hely, E., Couch, W. J., & Zabludoff, A. I. 2006, MNRAS, 366, 645

Pimbblet, K. A., Smail, I., Kodama, T., Couch, W. J., Edge, A. C., Zabludoff, A. I., & O'Hely, E. 2002, MNRAS, 331, 333

Poggianti, B. M., Desai, V., Finn, R., Bamford, S., De Lucia, G., Varela, J., Aragón-Salamanca, A., Halliday, C., Noll, S., Saglia, R., Zaritsky, D., Best, P., Clowe, D., Milvang-Jensen, B., Jablonka, P., Pelló, R., Rudnick, G., Simard, L., von der Linden, A., & White, S. 2008, ApJ, 684, 888

Poggianti, B. M., von der Linden, A., De Lucia, G., Desai, V., Simard, L., Halliday, C., Aragón-Salamanca, A., Bower, R., Varela, J., Best, P., Clowe, D. I., Dalcanton, J., Jablonka, P., Milvang-Jensen, B., Pello, R., Rudnick, G., Saglia, R., White, S. D. M., & Zaritsky, D. 2006, ApJ, 642, 188

Popesso, P., Biviano, A., Böhringer, H., & Romaniello, M. 2007a, A&A, 461, 397

Popesso, P., Biviano, A., Romaniello, M., & Böhringer, H. 2007b, A&A, 461, 411

Popesso, P., Böhringer, H., Brinkmann, J., Voges, W., & York, D. G. 2004, A&A, 423, 449

Porter, S. C. & Raychaudhury, S. 2007, MNRAS, 375, 1409

Porter, S. C., Raychaudhury, S., Pimbblet, K. A., & Drinkwater, M. J. 2008, MNRAS, 388, 1152

Postman, M., Lubin, L. M., Gunn, J. E., Oke, J. B., Hoessel, J. G., Schneider, D. P., & Christensen, J. A. 1996, AJ, 111, 615

Pozzetti, L., Bolzonella, M., Lamareille, F., Zamorani, G., Franzetti, P., Le Fèvre, O., Iovino, A., Temporin, S., Ilbert, O., Arnouts, S., Charlot, S., Brinchmann, J., Zucca, E., Tresse, L., Scodeggio, M., Guzzo, L., Bottini, D., Garilli, B., Le Brun, V., Maccagni, D., Picat, J. P., Scaramella, R., Vettolani, G., Zanichelli, A., Adami, C., Bardelli, S., Cappi, A., Ciliegi, P., Contini, T., Foucaud, S., Gavignaud, I., McCracken, H. J., Marano, B., Marinoni, C., Mazure, A., Meneux, B., Merighi, R., Paltani, S., Pellò, R., Pollo, A., Radovich, M., Bondi, M., Bongiorno, A., Cucciati, O., de la Torre, S., Gregorini, L., Mellier, Y., Merluzzi, P., Vergani, D., & Walcher, C. J. 2007, A&A, 474, 443

Pozzetti, L., Bolzonella, M., Zucca, E., Zamorani, G., Lilly, S., Renzini, A., Moresco, M., Mignoli, M., Cassata, P., Tasca, L., Lamareille, F., Maier, C., Meneux, B., Halliday, C., Oesch, P., Vergani, D., Caputi, K., Kovač, K., Cimatti, A., Cucciati, O., Iovino, A., Peng, Y., Carollo, M., Contini, T., Kneib, J.-P., Le Févre, O., Mainieri, V., Scodeggio, M., Bardelli, S., Bongiorno, A., Coppa, G., de la Torre, S., de Ravel, L., Franzetti, P., Garilli, B., Kampczyk, P., Knobel, C., Le Borgne, J.-F., Le Brun, V., Pellò, R., Perez Montero, E., Ricciardelli, E., Silverman, J. D., Tanaka, M., Tresse, L., Abbas, U., Bottini, D., Cappi, A., Guzzo, L., Koekemoer, A. M., Leauthaud, A., Maccagni, D., Marinoni, C., McCracken, H. J., Memeo, P., Porciani, C., Scaramella, R., Scarlata, C., & Scoville, N. 2010, A&A, 523, A13

Prescott, M., Baldry, I. K., James, P. A., Bamford, S. P., Bland-Hawthorn, J., Brough, S., Brown, M. J. I., Cameron, E., Conselice, C. J., Croom, S. M., Driver, S. P., Frenk, C. S., Gunawardhana, M., Hill, D. T., Hopkins, A. M., Jones, D. H., Kelvin, L. S., Kuijken, K., Liske, J., Loveday, J., Nichol, R. C., Norberg, P., Parkinson, H. R., Peacock, J. A., Phillipps, S., Pimbblet, K. A., Popescu, C. C., Robotham, A. S. G., Sharp, R. G., Sutherland, W. J., Taylor, E. N., Tuffs, R. J., van Kampen, E., & Wijesinghe, D. 2011, MNRAS, 417, 1374

Press, W. H. & Davis, M. 1982, ApJ, 259, 449

Quadri, R., van Dokkum, P., Gawiser, E., Franx, M., Marchesini, D., Lira, P., Rudnick, G., Herrera, D., Maza, J., Kriek, M., Labbé, I., & Francke, H. 2007, ApJ, 654, 138

Raichoor, A. & Andreon, S. 2012, A&A, 543, A19

Rees, M. J. & Ostriker, J. P. 1977, MNRAS, 179, 541

Rines, K., Geller, M. J., Kurtz, M. J., & Diaferio, A. 2005, AJ, 130, 1482

Rubin, V. C., Ford, Jr., W. K., & D'Odorico, S. 1970, ApJ, 160, 801

Rubin, V. C., Thonnard, N., & Ford, Jr., W. K. 1978, ApJ, 225, L107

Salim, S., Rich, R. M., Charlot, S., Brinchmann, J., Johnson, B. D., Schiminovich, D., Seibert, M., Mallery, R., Heckman, T. M., Forster, K., Friedman, P. G., Martin, D. C., Morrissey, P., Neff, S. G., Small, T., Wyder, T. K., Bianchi, L., Donas, J., Lee, Y.-W., Madore, B. F., Milliard, B., Szalay, A. S., Welsh, B. Y., & Yi, S. K. 2007, ApJS, 173, 267

Salpeter, E. E. 1955, ApJ, 121, 161

Sanders, R. H. 1984, A&A, 140, 52

Scalo, J., Vazquez-Semadeni, E., Chappell, D., & Passot, T. 1998, ApJ, 504, 835

Schaller, G., Schaerer, D., Meynet, G., & Maeder, A. 1992, A&AS, 96, 269

Scharf, C., Donahue, M., Voit, G. M., Rosati, P., & Postman, M. 2000, ApJ, 528, L73

Schiavon, R. P. 2007, ApJS, 171, 146

Schindler, S. 2000, A&AS, 142, 433

Schindler, S. & Mueller, E. 1993, A&A, 272, 137

Schlafly, E. F. & Finkbeiner, D. P. 2011, ApJ, 737, 103

Schlegel, D. J., Finkbeiner, D. P., & Davis, M. 1998, ApJ, 500, 525

Schmidt, M. 1959, ApJ, 129, 243

Sersic, J. L. 1968, Atlas de galaxias australes

Silk, J. 1977, ApJ, 211, 638

Smail, I., Dressler, A., Couch, W. J., Ellis, R. S., Oemler, Jr., A., Butcher, H., & Sharples, R. M. 1997, ApJS, 110, 213

Smith, A. J., Loveday, J., & Cross, N. J. G. 2009, MNRAS, 397, 868

Smith, R. J., Lucey, J. R., & Carter, D. 2012, MNRAS, 426, 2994

Smoot, G. F., Bennett, C. L., Kogut, A., Aymon, J., Backus, C., de Amici, G., Galuk, K., Jackson, P. D., Keegstra, P., Rokke, L., Tenorio, L., Torres, S., Gulkis, S., Hauser, M. G., Janssen, M. A., Mather, J. C., Weiss, R., Wilkinson, D. T., Wright, E. L., Boggess, N. W., Cheng, E. S., Kelsall, T., Lubin, P., Meyer, S., Moseley, S. H., Murdock, T. L., Shafer, R. A., & Silverberg, R. F. 1991, ApJ, 371, L1

Solomon, P. M. & Sanders, D. B. 1980, in Giant Molecular Clouds in the Galaxy, ed. P. M. Solomon & M. G. Edmunds, 41–73

Stoughton, C., Lupton, R. H., Bernardi, M., Blanton, M. R., Burles, S., Castander, F. J., Connolly, A. J., Eisenstein, D. J., Frieman, J. A., Hennessy, G. S., Hindsley, R. B., Ivezić, Ž., Kent, S., Kunszt, P. Z., Lee, B. C., Meiksin, A., Munn, J. A., Newberg, H. J., Nichol, R. C., Nicinski, T., Pier, J. R., Richards, G. T., Richmond, M. W., Schlegel, D. J., Smith, J. A., Strauss, M. A., SubbaRao, M., Szalay, A. S., Thakar, A. R., Tucker, D. L., Vanden Berk, D. E., Yanny, B., Adelman, J. K., Anderson, Jr., J. E., Anderson, S. F., Annis, J., Bahcall, N. A., Bakken, J. A., Bartelmann, M., Bastian, S., Bauer, A., Berman, E., Böhringer, H., Boroski, W. N., Bracker, S., Briegel, C., Briggs, J. W., Brinkmann, J., Brunner, R., Carey, L., Carr, M. A., Chen, B., Christian, D., Colestock, P. L., Crocker, J. H., Csabai, I., Czarapata, P. C., Dalcanton, J., Davidsen, A. F., Davis, J. E., Dehnen, W., Dodelson, S., Doi, M., Dombeck, T., Donahue, M., Ellman, N., Elms, B. R., Evans, M. L., Eyer, L., Fan, X., Federwitz, G. R., Friedman, S., Fukugita, M., Gal, R., Gillespie, B., Glazebrook, K., Gray, J., Grebel, E. K., Greenawalt, B., Greene, G., Gunn, J. E., de Haas, E., Haiman, Z., Haldeman, M., Hall, P. B., Hamabe, M., Hansen, B., Harris, F. H., Harris, H., Harvanek, M., Hawley, S. L., Hayes, J. J. E., Heckman, T. M., Helmi, A.,

Henden, A., Hogan, C. J., Hogg, D. W., Holmgren, D. J., Holtzman, J., Huang, C.-H., Hull, C., Ichikawa, S.-I., Ichikawa, T., Johnston, D. E., Kauffmann, G., Kim, R. S. J., Kimball, T., Kinney, E., Klaene, M., Kleinman, S. J., Klypin, A., Knapp, G. R., Korienek, J., Krolik, J., Kron, R. G., Krzesiński, J., Lamb, D. Q., Leger, R. F., Limmongkol, S., Lindenmeyer, C., Long, D. C., Loomis, C., Loveday, J., MacKinnon, B., Mannery, E. J., Mantsch, P. M., Margon, B., McGehee, P., McKay, T. A., McLean, B., Menou, K., Merelli, A., Mo, H. J., Monet, D. G., Nakamura, O., Narayanan, V. K., Nash, T., Neilsen, Jr., E. H., Newman, P. R., Nitta, A., Odenkirchen, M., Okada, N., Okamura, S., Ostriker, J. P., Owen, R., Pauls, A. G., Peoples, J., Peterson, R. S., Petravick, D., Pope, A., Pordes, R., Postman, M., Prosapio, A., Quinn, T. R., Rechenmacher, R., Rivetta, C. H., Rix, H.-W., Rockosi, C. M., Rosner, R., Ruthmansdorfer, K., Sandford, D., Schneider, D. P., Scranton, R., Sekiguchi, M., Sergey, G., Sheth, R., Shimasaku, K., Smee, S., Snedden, S. A., Stebbins, A., Stubbs, C., Szapudi, I., Szkody, P., Szokoly, G. P., Tabachnik, S., Tsvetanov, Z., Uomoto, A., Vogeley, M. S., Voges, W., Waddell, P., Walterbos, R., Wang, S.-i., Watanabe, M., Weinberg, D. H., White, R. L., White, S. D. M., Wilhite, B., Wolfe, D., Yasuda, N., York, D. G., Zehavi, I., & Zheng, W. 2002, AJ, 123, 485

Strateva, I., Ivezić, Ž., Knapp, G. R., Narayanan, V. K., Strauss, M. A., Gunn, J. E., Lupton, R. H., Schlegel, D., Bahcall, N. A., Brinkmann, J., Brunner, R. J., Budavári, T., Csabai, I., Castander, F. J., Doi, M., Fukugita, M., Győry, Z., Hamabe, M., Hennessy, G., Ichikawa, T., Kunszt, P. Z., Lamb, D. Q., McKay, T. A., Okamura, S., Racusin, J., Sekiguchi, M., Schneider, D. P., Shimasaku, K., & York, D. 2001, AJ, 122, 1861

SubbaRao, M., Frieman, J., Bernardi, M., Loveday, J., Nichol, B., Castander, F., & Meiksin, A. 2002, in Society of Photo-Optical Instrumentation Engineers (SPIE) Conference Series, Vol. 4847, Society of Photo-Optical Instrumentation Engineers (SPIE) Conference Series, ed. J.-L. Starck & F. D. Murtagh, 452–460

Suhhonenko, I., Einasto, J., Liivamägi, L. J., Saar, E., Einasto, M., Hütsi, G., Müller, V., Starobinsky, A. A., Tago, E., & Tempel, E. 2011, A&A, 531, A149

Sun, M., Donahue, M., Roediger, E., Nulsen, P. E. J., Voit, G. M., Sarazin, C., Forman, W., & Jones, C. 2010, ApJ, 708, 946

Sunyaev, R. A. & Zeldovich, Y. B. 1972, A&A, 20, 189

Tago, E., Einasto, J., Saar, E., Tempel, E., Einasto, M., Vennik, J., & Müller, V. 2008, A&A, 479, 927

Tal, T., van Dokkum, P. G., Nelan, J., & Bezanson, R. 2009, AJ, 138, 1417

Tanaka, M., Kodama, T., Arimoto, N., Okamura, S., Umetsu, K., Shimasaku, K., Tanaka, I., & Yamada, T. 2005, MNRAS, 362, 268

Taylor, E. N., Hopkins, A. M., Baldry, I. K., Brown, M. J. I., Driver, S. P., Kelvin, L. S., Hill, D. T., Robotham, A. S. G., Bland-Hawthorn, J., Jones, D. H., Sharp, R. G., Thomas, D.,

Liske, J., Loveday, J., Norberg, P., Peacock, J. A., Bamford, S. P., Brough, S., Colless, M., Cameron, E., Conselice, C. J., Croom, S. M., Frenk, C. S., Gunawardhana, M., Kuijken, K., Nichol, R. C., Parkinson, H. R., Phillipps, S., Pimbblet, K. A., Popescu, C. C., Prescott, M., Sutherland, W. J., Tuffs, R. J., van Kampen, E., & Wijesinghe, D. 2011, MNRAS, 418, 1587

Tinker, J., Wetzel, A., & Conroy, C. 2011, ArXiv e-prints

Tinsley, B. M. & Gunn, J. E. 1976, ApJ, 203, 52

Tojeiro, R., Heavens, A. F., Jimenez, R., & Panter, B. 2007, MNRAS, 381, 1252

Toomre, A. & Toomre, J. 1972, ApJ, 178, 623

Treu, T., Ellis, R. S., Kneib, J.-P., Dressler, A., Smail, I., Czoske, O., Oemler, A., & Natarajan, P. 2003, ApJ, 591, 53

Turner, E. L. & Gott, III, J. R. 1976, ApJS, 32, 409

Urquhart, S. A., Willis, J. P., Hoekstra, H., & Pierre, M. 2010, MNRAS, 406, 368

Väisänen, P., Tollestrup, E. V., Willner, S. P., & Cohen, M. 2000, ApJ, 540, 593

van den Bosch, F. C., Aquino, D., Yang, X., Mo, H. J., Pasquali, A., McIntosh, D. H., Weinmann, S. M., & Kang, X. 2008, MNRAS, 387, 79

van Dokkum, P. G. & Conroy, C. 2012, ApJ, 760, 70

Verdugo, M., Lerchster, M., Böhringer, H., Hildebrandt, H., Ziegler, B. L., Erben, T., Finoguenov, A., & Chon, G. 2012, MNRAS, 421, 1949

Verdugo, M., Ziegler, B. L., & Gerken, B. 2008, A&A, 486, 9

von der Linden, A., Wild, V., Kauffmann, G., White, S. D. M., & Weinmann, S. 2010, MNRAS, 404, 1231

Wake, D. A., Collins, C. A., Nichol, R. C., Jones, L. R., & Burke, D. J. 2005, ApJ, 627, 186

Wake, D. A., Nichol, R. C., Eisenstein, D. J., Loveday, J., Edge, A. C., Cannon, R., Smail, I., Schneider, D. P., Scranton, R., Carson, D., Ross, N. P., Brunner, R. J., Colless, M., Couch, W. J., Croom, S. M., Driver, S. P., da Ângela, J., Jester, S., de Propris, R., Drinkwater, M. J., Bland-Hawthorn, J., Pimbblet, K. A., Roseboom, I. G., Shanks, T., Sharp, R. G., & Brinkmann, J. 2006, MNRAS, 372, 537

Walcher, C. J., Lamareille, F., Vergani, D., Arnouts, S., Buat, V., Charlot, S., Tresse, L., Le Fèvre, O., Bolzonella, M., Brinchmann, J., Pozzetti, L., Zamorani, G., Bottini, D., Garilli, B., Le Brun, V., Maccagni, D., Milliard, B., Scaramella, R., Scodeggio, M., Vettolani, G., Zanichelli, A., Adami, C., Bardelli, S., Cappi, A., Ciliegi, P., Contini, T., Franzetti, P., Foucaud, S., Gavignaud, I., Guzzo, L., Ilbert, O., Iovino, A., McCracken, H. J., Marano,

B., Marinoni, C., Mazure, A., Meneux, B., Merighi, R., Paltani, S., Pellò, R., Pollo, A., Radovich, M., Zucca, E., Lonsdale, C., & Martin, C. 2008, A&A, 491, 713

Weiner, B. J., Phillips, A. C., Faber, S. M., Willmer, C. N. A., Vogt, N. P., Simard, L., Gebhardt, K., Im, M., Koo, D. C., Sarajedini, V. L., Wu, K. L., Forbes, D. A., Gronwall, C., Groth, E. J., Illingworth, G. D., Kron, R. G., Rhodes, J., Szalay, A. S., & Takamiya, M. 2005, ApJ, 620, 595

Weinmann, S. M., Kauffmann, G., van den Bosch, F. C., Pasquali, A., McIntosh, D. H., Mo, H., Yang, X., & Guo, Y. 2009, MNRAS, 394, 1213

Weinmann, S. M., van den Bosch, F. C., Yang, X., & Mo, H. J. 2006a, MNRAS, 366, 2

Weinmann, S. M., van den Bosch, F. C., Yang, X., Mo, H. J., Croton, D. J., & Moore, B. 2006b, MNRAS, 372, 1161

Westera, P., Lejeune, T., Buser, R., Cuisinier, F., & Bruzual, G. 2002, A&A, 381, 524

Wetzel, A. R., Cohn, J. D., & White, M. 2009, MNRAS, 395, 1376

Wetzel, A. R., Tinker, J. L., & Conroy, C. 2012, MNRAS, 424, 232

White, M., Cohn, J. D., & Smit, R. 2010, MNRAS, 408, 1818

White, S. D. M. & Frenk, C. S. 1991, ApJ, 379, 52

White, S. D. M. & Rees, M. J. 1978, MNRAS, 183, 341

Wilman, D. J., Balogh, M. L., Bower, R. G., Mulchaey, J. S., Oemler, A., Carlberg, R. G., Morris, S. L., & Whitaker, R. J. 2005, MNRAS, 358, 71

Wilman, D. J., Oemler, Jr., A., Mulchaey, J. S., McGee, S. L., Balogh, M. L., & Bower, R. G. 2009, ApJ, 692, 298

Wilman, D. J., Pierini, D., Tyler, K., McGee, S. L., Oemler, Jr., A., Morris, S. L., Balogh, M. L., Bower, R. G., & Mulchaey, J. S. 2008, ApJ, 680, 1009

Wilman, D. J., Zibetti, S., & Budavári, T. 2010, MNRAS, 406, 1701

Wittman, D., Dell'Antonio, I. P., Hughes, J. P., Margoniner, V. E., Tyson, J. A., Cohen, J. G., & Norman, D. 2006, ApJ, 643, 128

Wittman, D., Tyson, J. A., Margoniner, V. E., Cohen, J. G., & Dell'Antonio, I. P. 2001, ApJ, 557, L89

Wolf, C., Aragón-Salamanca, A., Balogh, M., Barden, M., Bell, E. F., Gray, M. E., Peng, C. Y., Bacon, D., Barazza, F. D., Böhm, A., Caldwell, J. A. R., Gallazzi, A., Häusler, B., Heymans, C., Jahnke, K., Jogee, S., van Kampen, E., Lane, K., McIntosh, D. H., Meisenheimer, K., Papovich, C., Sánchez, S. F., Taylor, A., Wisotzki, L., & Zheng, X. 2009a, in Astronomical Society of the Pacific Conference Series, Vol. 408, The Starburst-AGN Connection, ed. W. Wang, Z. Yang, Z. Luo, & Z. Chen, 248

Wolf, C., Aragón-Salamanca, A., Balogh, M., Barden, M., Bell, E. F., Gray, M. E., Peng, C. Y., Bacon, D., Barazza, F. D., Böhm, A., Caldwell, J. A. R., Gallazzi, A., Häußler, B., Heymans, C., Jahnke, K., Jogee, S., van Kampen, E., Lane, K., McIntosh, D. H., Meisenheimer, K., Papovich, C., Sánchez, S. F., Taylor, A., Wisotzki, L., & Zheng, X. 2009b, MNRAS, 393, 1302

Yang, X., Mo, H. J., & van den Bosch, F. C. 2008, ApJ, 676, 248

Yang, X., Mo, H. J., van den Bosch, F. C., & Jing, Y. P. 2005, MNRAS, 356, 1293

Yang, X., Mo, H. J., van den Bosch, F. C., Pasquali, A., Li, C., & Barden, M. 2007, ApJ, 671, 153

Yasuda, N., Fukugita, M., Narayanan, V. K., Lupton, R. H., Strateva, I., Strauss, M. A., Ivezić, Ž., Kim, R. S. J., Hogg, D. W., Weinberg, D. H., Shimasaku, K., Loveday, J., Annis, J., Bahcall, N. A., Blanton, M., Brinkmann, J., Brunner, R. J., Connolly, A. J., Csabai, I., Doi, M., Hamabe, M., Ichikawa, S.-I., Ichikawa, T., Johnston, D. E., Knapp, G. R., Kunszt, P. Z., Lamb, D. Q., McKay, T. A., Munn, J. A., Nichol, R. C., Okamura, S., Schneider, D. P., Szokoly, G. P., Vogeley, M. S., Watanabe, M., & York, D. G. 2001, AJ, 122, 1104

Yee, H. K. C. & Ellingson, E. 2003, ApJ, 585, 215

York, D. G., Adelman, J., Anderson, Jr., J. E., Anderson, S. F., Annis, J., Bahcall, N. A., Bakken, J. A., Barkhouser, R., Bastian, S., Berman, E., Boroski, W. N., Bracker, S., Briegel, C., Briggs, J. W., Brinkmann, J., Brunner, R., Burles, S., Carey, L., Carr, M. A., Castander, F. J., Chen, B., Colestock, P. L., Connolly, A. J., Crocker, J. H., Csabai, I., Czarapata, P. C., Davis, J. E., Doi, M., Dombeck, T., Eisenstein, D., Ellman, N., Elms, B. R., Evans, M. L., Fan, X., Federwitz, G. R., Fiscelli, L., Friedman, S., Frieman, J. A., Fukugita, M., Gillespie, B., Gunn, J. E., Gurbani, V. K., de Haas, E., Haldeman, M., Harris, F. H., Hayes, J., Heckman, T. M., Hennessy, G. S., Hindsley, R. B., Holm, S., Holmgren, D. J., Huang, C.-h., Hull, C., Husby, D., Ichikawa, S.-I., Ichikawa, T., Ivezić, Ž., Kent, S., Kim, R. S. J., Kinney, E., Klaene, M., Kleinman, A. N., Kleinman, S., Knapp, G. R., Korienek, J., Kron, R. G., Kunszt, P. Z., Lamb, D. Q., Lee, B., Leger, R. F., Limmongkol, S., Lindenmeyer, C., Long, D. C., Loomis, C., Loveday, J., Lucinio, R., Lupton, R. H., MacKinnon, B., Mannery, E. J., Mantsch, P. M., Margon, B., McGehee, P., McKay, T. A., Meiksin, A., Merelli, A., Monet, D. G., Munn, J. A., Narayanan, V. K., Nash, T., Neilsen, E., Neswold, R., Newberg, H. J., Nichol, R. C., Nicinski, T., Nonino, M., Okada, N., Okamura, S., Ostriker, J. P., Owen, R., Pauls, A. G., Peoples, J., Peterson, R. L., Petravick, D., Pier, J. R., Pope, A., Pordes, R., Prosapio, A., Rechenmacher, R., Quinn, T. R., Richards, G. T., Richmond, M. W., Rivetta, C. H., Rockosi, C. M., Ruthmansdorfer, K., Sandford, D., Schlegel, D. J., Schneider, D. P., Sekiguchi, M., Sergey, G., Shimasaku, K., Siegmund, W. A., Smee, S., Smith, J. A., Snedden, S., Stone, R., Stoughton, C., Strauss, M. A., Stubbs, C., SubbaRao, M., Szalay,

A. S., Szapudi, I., Szokoly, G. P., Thakar, A. R., Tremonti, C., Tucker, D. L., Uomoto, A., Vanden Berk, D., Vogeley, M. S., Waddell, P., Wang, S.-i., Watanabe, M., Weinberg, D. H., Yanny, B., Yasuda, N., & SDSS Collaboration. 2000, AJ, 120, 1579

Zabludoff, A. I. & Mulchaey, J. S. 1998, ApJ, 496, 39

Zeldovich, I. B., Einasto, J., & Shandarin, S. F. 1982, Nature, 300, 407

Zhang, B., Sun, M., Ji, L., Sarazin, C., Lin, X. B., Nulsen, P. E. J., Roediger, E., Donahue, M., Forman, W., Jones, C., Voit, G. M., & Kong, X. 2013, ApJ, 777, 122

Zheng, X. Z., Bell, E. F., Papovich, C., Wolf, C., Meisenheimer, K., Rix, H.-W., Rieke, G. H., & Somerville, R. 2007, ApJ, 661, L41

Zibetti, S., Charlot, S., & Rix, H.-W. 2009, MNRAS, 400, 1181